Physical Organic Approach Towards High-Performance Materials for Non-Aqueous Redox Flow Battery

by

Yichao Yan

A dissertation submitted in partial fulfillment
of the requirements for the degree of
Doctor of Philosophy
(Chemistry)
in the University of Michigan
2021

Doctoral Committee:

Professor Melanie S. Sanford, Chair
Professor Stephen Maldonado
Professor John Montgomery
Professor Nirala Singh

Yichao Yan

ychyan@umich.edu

ORCID iD: 0000-0003-0152-9312

Dedication

Dedicated to my family.

Acknowledgements

First of all, I would like to thank the mentorship and support from my advisor, Prof. Melanie Sanford. Without her, all these projects would not be made possible. I would also like to thank the help and support from my long-term collaborator, Prof. Matthew Sigman and his group (U of Utah). A lot of projects in this thesis were significantly improved with his help. I also thank help and support from my committee members during my graduate study, Prof. John Montgomery (for letting me do rotation in his group), Prof. Stephen Maldonado (for teaching me electrochemistry) and Prof. Nirala Singh (for providing a lot of insights in both science and career development). Thank my initial mentor in Sanford lab, Dr. Koen Hendriks (now at Dutch Institute for Fundamental Energy Research) for teaching me everything about redox flow batteries and guiding me on research idea and design. Thank my close colleagues in Sanford lab, Dr. Anushka Shrestha, Dr. Thomas Vaid, Ryan Walser-Kuntz and many others for their help, suggestions and support during my graduate study. I would also thank all the departmental staff for their hard working and help to facilitate my graduate study. Last but not least, I would like to thank my family, especially my parents for long-term support, understanding and help.

Table of Contents

List of Tables

List of Figures

List of Schemes

Abstract

Redox flow batteries (RFBs) are a promising technology for grid-scale energy storage of renewable energy resources. Aqueous RFBs have been studied extensively and have resulted in the development of promising commercial batteries. However, aqueous systems suffer from a narrow thermodynamic cell voltage window of 1.5 V. Switching from water to a non-aqueous solvent expands the theoretical cell voltage window from 1.5 V up to 5 V, drastically increasing the energy that can be stored. One of the major research efforts has been focusing on the discovery of proper catholyte and anolyte materials for this application. Molecules that are stable at all redox states, but also electrochemically active and soluble, are required to develop RFBs that take full advantage of the non-aqueous solvent. My research focuses on addressing these challenges in the context of developing new materials for non-aqueous RFBs using basic principles of physical organic chemistry. The Chapter 1 will give an introduction on the background of the thesis research. Chapter 2-7 focus on the development of promising catholyte candidates based on cyclopropenium through molecular engineering of their vital properties including redox potentials, solubility, stability and number of electron transfer. Chapter 8 discusses the development of a new anolyte based on benzotriazole with extreme low reduction potential and its molecular engineering for stable cycling in a flow cell setup.

Chapter 1 Introduction

Current electricity demands heavily rely on energy produced from fossil fuels, which leads to an adverse impact on the environment.[1] Burning fossil fuels to generate energy releases a large amount of carbon dioxide, which is a leading cause of global warming. Furthermore, other pollutants, including heavy metals and fine dust, are released by burning these fossil fuels, which threatens human health. [1,2] Therefore, increasing the use of green and renewable sources of energy, such as solar energy and wind power, has received tremendous support in recent years. However, unlike fossil fuels, solar energy and wind power generate electricity discontinuously.[1,2] Because of this, these alternative sources of energy do not meet requirements to sustain the grid system that currently provides energy for cities. To address this issue, energy storage technologies are needed to provide continuity between energy production and consumption. Redox flow batteries (RFBs) are a promising technology for such grid-scale energy storage.[3,4] The design feature of RFBs, that sets them apart from traditional solid-state batteries (e.g., Li-ion batteries) is that energy is stored in soluble redox active molecules, termed anolytes (reduced during charging) and catholytes (oxidized during charging), in external reservoirs (Figure 1.1). Thus, RFBs enable straightforward scaling of energy capacity or power by independently increasing the size of the external tanks or the size of the electrodes. In this regard, aqueous RFBs have been studied extensively and have resulted in the development of promising commercial batteries. However, aqueous systems suffer from a narrow thermodynamic cell voltage window of 1.23 V. Switching from water to a non-aqueous solvent expands the theoretical cell voltage window from 1.23 V up to 5 V, drastically

increasing the energy that can be stored. However, this field of non-aqueous redox flow batteries is currently in its infancy.[5] One of the major research efforts has been focusing on the discovery of proper catholyte and anolyte materials for this application. Organic molecules attract tremendous interests for this purpose due to its diversity, structure-property tunability and modular synthesis from cheap raw materials.

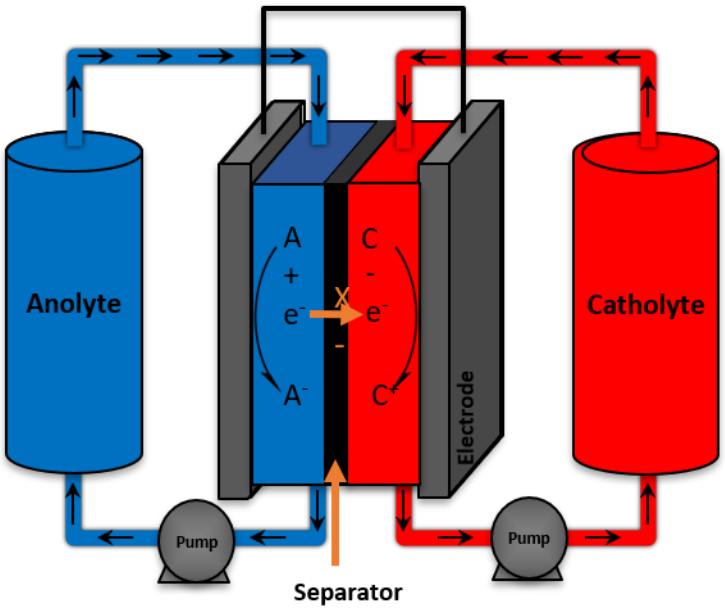

Figure 1.1. Schematic Representation of an RFB

A number of properties are crucial for redox active molecules that store energy in RFBs. Most importantly, the redox potential, numbers of electron transfer, and solubility of a molecule dictate its total energy storage capability (see figure 1.2). Redox potential and numbers of electron transfer determines how much energy each molecule can store and release, while solubility defines the maximum quantity of the molecule present in a given volume. Current state-of-the-art compounds exhibits cycling solubility up to 1 M, catholyte potential as high as 1.3 V vs Fc/Fc^+, and anolyte potential as low as -2.0 V vs Fc/Fc^+.[6,7] However, there is still lots of room for advancement considering the potential window of non-aqueous solvents and the tunability of properties of

organic molecules. Additionally, the oxidation or reduction of organic molecules often leads to reactive species that are susceptible to undesired decomposition processes. Thus, molecules that are stable at all redox states, but also electrochemically active and soluble, are required in order to develop RFBs. Due to the infancy of the non-aqueous RFB, current materials only showed reasonable cycling for relatively short period of time ranging from hours to days while a commercial battery would potentially be in place and cycling for at least months.

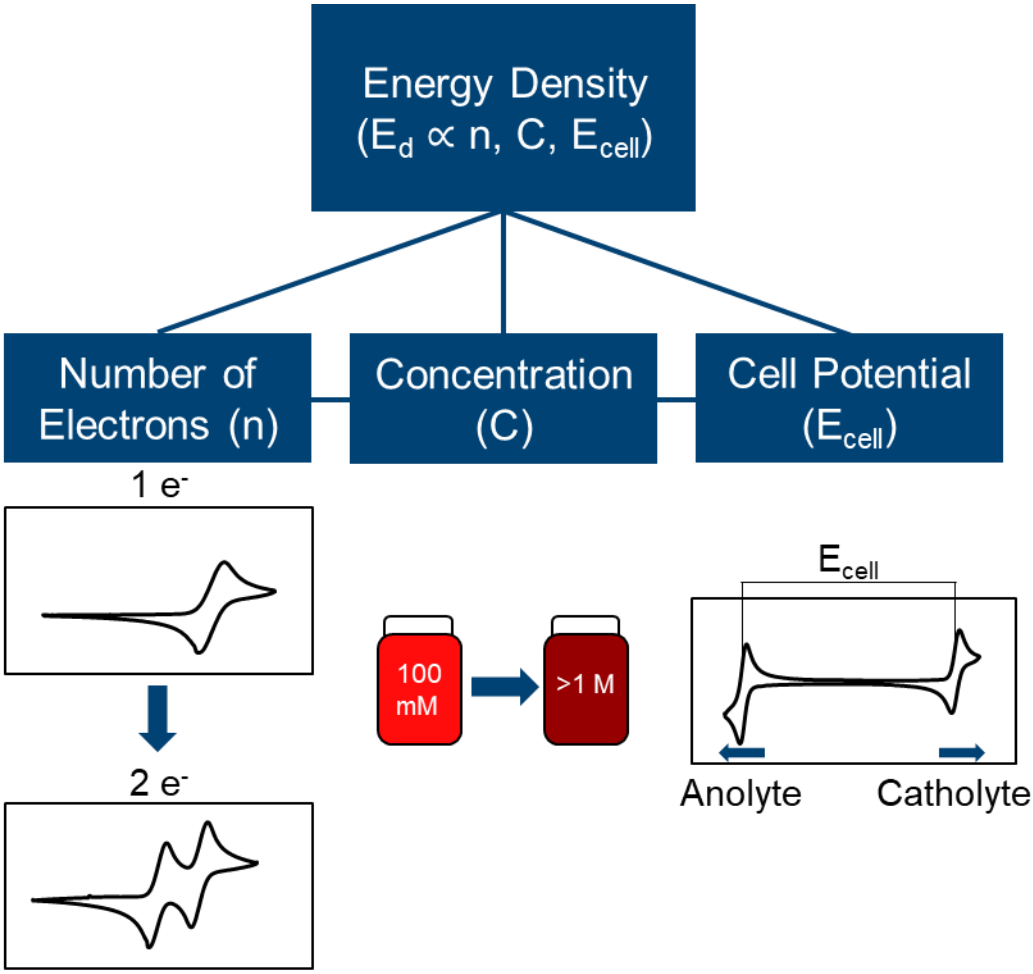

Figure 1.2. Targeted properties for improved energy densities.

In addition to these properties, cross-over of active species in a battery setup is another critical factor influencing the performance of the battery. Cross-over of redox active molecules between

the anolyte and catholyte chambers can cause mechanical energy capacity and efficiency loss by unbalanced active species concentrations. The irreversible energy capacity and efficiency loss by unexpected side reactions and cross-over needs to be addressed when developing new redox active molecules.

While various organic catholytes and anolytes have been discovered, most of them have not met all the requirements mentioned above. An ideal catholyte material would be stable in its oxidized form, highly soluble in all redox states, and have a high redox potential and same requirements also applied to an ideal anolyte with low redox potential.[6] Chapter 2-8 focuses on synthetic strategies used to address these challenges in the context of developing cyclopropenium as a catholyte for non-aqueous RFBs (NRFBs).

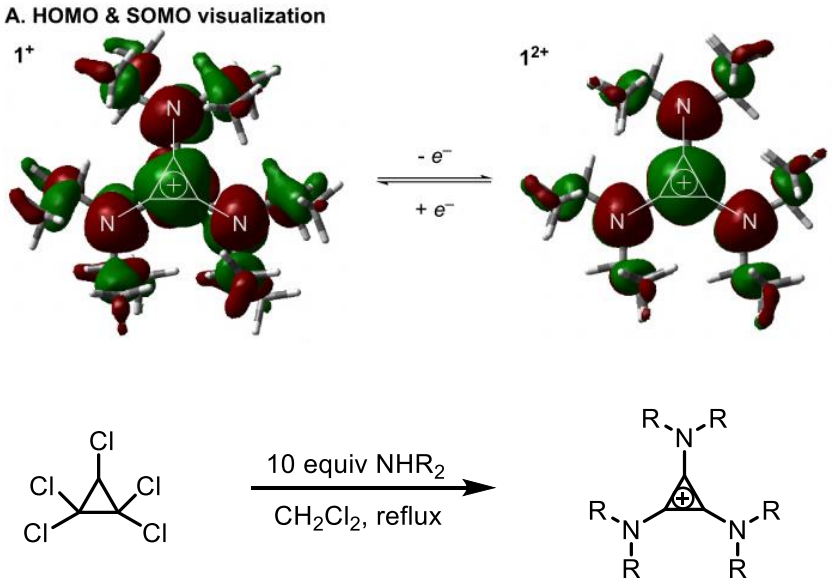

Figure 1.3. HOMO SOMO; and synthesis

Triphenyl-cyclopropenium ion was first discovered by Breslow in 1957 as the smallest aromatic system with two π-electrons.[7] Amino-substituted cyclopropenium ions possess a number of useful properties including high cation stability, reversible redox activity, and an unusual reactivity profile as a consequence of the resonance-donating ability of the amino substituents and

the aromaticity of the cyclic core.[8] It has been widely used as ionic liquids, transition-metal ligands, Bronsted bases and organocatalysts since it was first discovered in the early 1970s.[8] The HOMO orbital is a combination of the C_3 and the nitrogen ligands symmetric group orbitals in an antibonding fashion, and is thus quite a high energy HOMO orbital. While the oxidation of organic cations is challenging, the high energy HOMO of tris(dialkyl)aminocyclopropenium(CP) ions indicates these compounds could potentially undergo facile oxidation.[9] Weiss and Schloter first reported the synthesis and isolation of CP radical dication by chemical oxidation noting moderate air stability.[9] Further electrochemistry study of CP ions reveals its first oxidation to radical cations occurs at 1.12 V (vs SCE, Pt anode transfer to ~0.8 vs Fc/Fc^+) and is reversible.[10] This early discovery attracted our interest as no organic catholytes with oxidation potential > 0.7 V vs Fc/Fc^+ had been reported at that time.[11] Meanwhile, CP derivatives and their oxidized forms with different amino substitution groups can be easily generated through one-step synthetic process, allowing for systematic studies on numerous properties at different oxidation states. Moreover, because of the permanent cation on cyclopropenium core, CP shows the possibility to reduce crossover when coupled with an anion-exchange membrane. Chapter 2-7 focus on the development of promising catholyte candidates based on cyclopropenium through molecular engineering of their vital properties including redox potentials, solubility, stability and number of electron transfer.

In the last chapter, a new anolyte based on benzotriazole was developed. Using a combination of iterative molecular design, organic synthesis, and electrochemical evaluation, a 2-aryl benzotriazole derivative is identified that exhibits a redox potential below -2 V (-2.3 V vs Fc/Fc^+), while maintaining stable electrochemical cycling (~90% capacity retention over 100 cycles) at both low (0.1 M) and high (0.3 M) concentration.

Reference

(1) Rugolo, J.; Aziz, M. J. Electricity Storage for Intermittent Renewable Sources. *Energy Environ. Sci.* **2012**, *5* (5), 7151–7160. https://doi.org/10.1039/C2EE02542F.

(2) Barnhart, C. J.; Dale, M.; Brandt, A. R.; Benson, S. M. The Energetic Implications of Curtailing versus Storing Solar- and Wind-Generated Electricity. *Energy Environ. Sci.* **2013**, *6* (10), 2804–2810. https://doi.org/10.1039/C3EE41973H.

(3) Dunn, B.; Kamath, H.; Tarascon, J.-M. Electrical Energy Storage for the Grid: A Battery of Choices. *Science* **2011**, *334* (6058), 928–935. https://doi.org/10.1126/science.1212741.

(4) Soloveichik, G. L. Flow Batteries: Current Status and Trends. *Chem. Rev.* **2015**, *115* (20), 11533–11558. https://doi.org/10.1021/cr500720t.

(5) Schon, T. B.; McAllister, B. T.; Li, P.-F.; Seferos, D. S. The Rise of Organic Electrode Materials for Energy Storage. *Chem. Soc. Rev.* **2016**, *45* (22), 6345–6404. https://doi.org/10.1039/C6CS00173D.

(6) Yan, Y.; Robinson, S. G.; Sigman, M. S.; Sanford, M. S. Mechanism-Based Design of a High-Potential Catholyte Enables a 3.2 V All-Organic Nonaqueous Redox Flow Battery. *J. Am. Chem. Soc.* **2019**, *141* (38), 15301–15306. https://doi.org/10.1021/jacs.9b07345.

(7) Sevov, C. S.; Fisher, S. L.; Thompson, L. T.; Sanford, M. S. Mechanism-Based Development of a Low-Potential, Soluble, and Cyclable Multielectron Anolyte for Nonaqueous Redox Flow Batteries. *J. Am. Chem. Soc.* **2016**, *138* (47), 15378–15384. https://doi.org/10.1021/jacs.6b07638.

(8) Luo, J.; Hu, B.; Hu, M.; Zhao, Y.; Liu, T. L. Status and Prospects of Organic Redox Flow Batteries toward Sustainable Energy Storage. *ACS Energy Lett.* **2019**, *4* (9), 2220–2240. https://doi.org/10.1021/acsenergylett.9b01332.

(9) Breslow, R. SYNTHESIS OF THE S-TRIPHENYLCYCLOPROPENYL CATION. *J. Am. Chem. Soc.* **1957**, *79* (19), 5318–5318. https://doi.org/10.1021/ja01576a067.

(10) Bandar, J. S.; Lambert, T. H. Aminocyclopropenium Ions: Synthesis, Properties, and Applications. *Synthesis* **2013**, *45* (18), 2485–2498. https://doi.org/10.1055/s-0033-1338516.

(11) Weiss, R.; Schloter, K. Stable Radical Dications. *Tetrahedron Letters* **1975**, *16* (40), 3491–3494. https://doi.org/10.1016/S0040-4039(00)91392-3.

(12) Johnson, R. W. Electrochemistry of Heterosubstituted Cyclopropenyl Cations. *Tetrahedron Letters* **1976**, *17* (8), 589–592. https://doi.org/10.1016/S0040-4039(00)77918-4.

(13) Sevov, C. S.; Samaroo, S. K.; Sanford, M. S. Cyclopropenium Salts as Cyclable, High-Potential Catholytes in Nonaqueous Media. *Adv. Energy Mater.* **2017**, *7* (5), 1602027. https://doi.org/10.1002/aenm.201602027.

Chapter 2

Developing a Predictive Solubility Model for Monomeric and Oligomeric Cyclopropenium-Based Flow Battery Catholytes

(published as *J. Am. Chem. Soc.* 2019, 141, 26, 10171–10176)

2.1. Introduction

Redox-active organic molecules (ROMs) have emerged as attractive electrolyte candidates for nonaqueous redox flow batteries (NRFBs).[1] Recent studies have demonstrated that both empirical design and predictive models are effective for identifying ROMs with high (catholyte) or low (anolyte) potentials and robust stability to redox cycling.[2] However, an unmet challenge is the ability to predictably design ROMs that exhibit high solubility in non-aqueous supporting electrolytes in all redox states. Importantly, technoeconomic models show that solubilities of >1 M are essential for achieving energy densities that are superior to existing aqueous RFB systems.[3] While many ROMs have the requisite solubility in their discharged states, relatively few maintain this high solubility upon charging.[4-7] In addition, the solubility of both the charged and uncharged ROMs typically decreases precipitously upon the addition of supporting salts that are generally required for electrochemical cycling.[8-10] As such, nearly all non-aqueous electrochemical cycling studies are performed at concentrations significantly lower than 1 M.[11,12]

To date, investigations of ROM solubility have been largely empirical. Over the past 20 years, there have been major advancements in the prediction of the aqueous solubility of organic molecules for pharmaceutical applications.[13-15] In contrast, insight into the structural features contributing to solubility in nonaqueous solvents remains limited.[5] Herein we report a workflow

that utilizes computationally-derived structural parameters that account for conformational dynamics to build statistical models describing the solubility of tris-(dialkylamino)cyclopropenium (CP) radical dications in acetonitrile. These mathematical correlations are used to predict new, highly soluble monomeric and dimeric derivatives of this catholyte. This approach identified multiple novel derivatives with solubilities of >1 M, and one such derivative was deployed in a high concentration supporting electrolyte-free symmetrical flow cell.

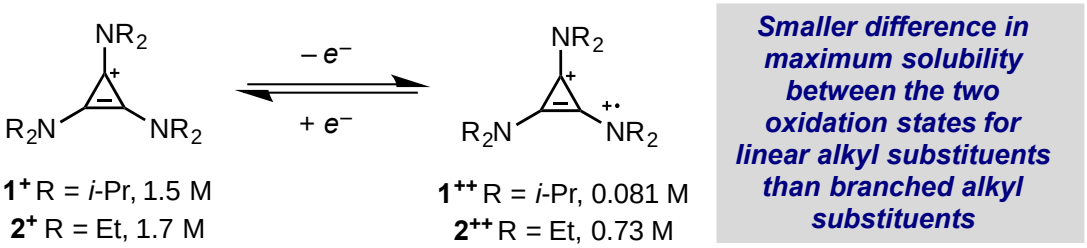

Scheme 2.1 Solubility drastically decreases upon oxidation for tris(dialkylamino)cyclopropenium ions.

2.2. Results and Discussion

CP ion catholytes were selected as the model system for this study for several reasons. First, this class of molecules undergo reversible single electron oxidation to a CP radical dication at relatively high potentials (≥0.8 V vs. Fc/Fc^+) and are stable for more than 200 electrochemical charge-discharge cycles.[16] However, earlier studies demonstrated that variation of both the redox state of the molecule and the substituents on nitrogen lead to dramatic changes in solubility. For instance, the solubility of $\mathbf{1}^+$, $\mathbf{1}^{++}$, $\mathbf{2}^+$, and $\mathbf{2}^{++}$ as hexafluorophosphate salts in MeCN ranges from 0.08 M to 1.7 M. This suggests that statistical modeling could be effective for identifying new, highly soluble derivatives. Finally, CP derivatives possess a cationic charge in both battery-

relevant redox states. As such, high solubility derivatives could, in principle, be deployed without added supporting electrolyte salts, which are known to detrimentally impact solubility.[8-9]

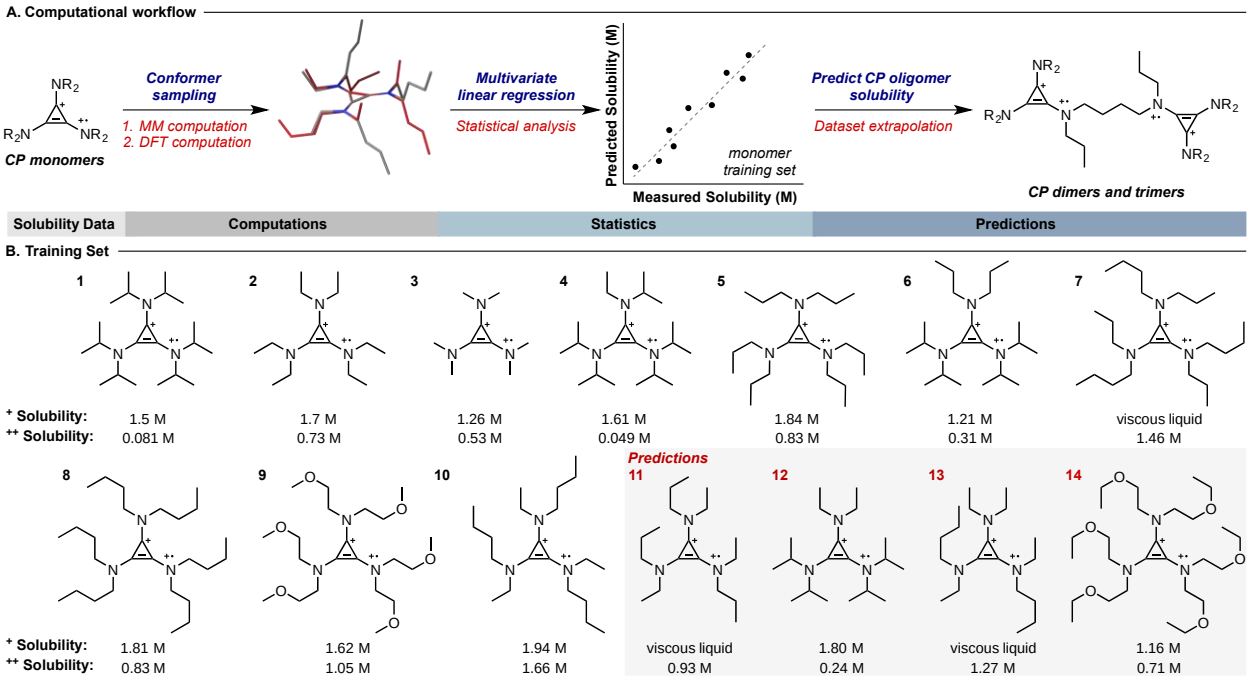

Figure 2.1 (A) Computational workflow. (B) Acetonitrile solubility of 1-14. PF_6 (counterions excluded for clarity).

A combined experimental and computational approach was applied to develop a predictive model for CP solubility. A training set of ten CP derivatives was used to provide requisite structural changes as a function of solubility, but also incorporate sufficient overlapping features for modeling (see experimental sections for details on MLR model development). All of the CP monocations (**1**$^{+}$-**10**$^{+}$; PF_6^- salts) have solubilities of >1.1 M in MeCN. As such, the corresponding dications (**1**$^{++}$-**10**$^{++}$; PF_6^- salts) are the solubility-limiting species, and among these there is more than an order of magnitude variation in solubility. Notably, the **10**$^{+}$/**10**$^{++}$ pair has remarkably high solubility (1.94 M/1.66 M), making this an attractive candidate for high concentration electrochemical cycling (*vide infra*). However, overall this data set reveals no intuitive, global trends regarding the features that impact solubility. While higher solubilities were generally

observed with linear alkyl amino substituents, increasing the length of the alkyl chain did not always produce the most soluble CP radical dication (compare $\mathbf{8}^{++}$ to $\mathbf{10}^{++}$).

The ten radical dications were used as a training set for molecular parameterization and statistical model development. Derivatives containing *n*-alkyl substituents (*e.g.* $\mathbf{5}^{++}$-$\mathbf{10}^{++}$) present computational challenges due to their high conformational flexibility. These molecules have numerous energetically clustered ground state conformations, which require exhaustive sampling for comprehensive analysis and parameter acquisition.[17] Thus, we envisioned a computational platform that would incorporate a collection of descriptors from different conformations. Energetically relevant conformations for each CP were identified by a conformational search using the OPLS3 force field.[18] These conformations were then optimized at the B3LYP/6-31G(d) level of theory.[19] Next, the lowest energy conformer was identified by a single point energy calculation at the M06-2X/def2-TZVP level of theory.[20,21] All calculations were performed in the gas phase without including counterions.

Multiple solution conformations are likely to contribute to a bulk property like solubility. To address this point, we selected three conformer classes from which to acquire parameters: (I) the lowest energy conformer, (II) the maximum and minimum width conformers (determined by B5 Sterimol values), and (III) a Boltzmann averaged set.[22] We reasoned that II and III would be critical for capturing the ensemble of conformers responsible for solubility. From the optimized structures in each subclass (I-III), we collected a variety of steric and electronic parameters (*e.g.*, Sterimol values, dipoles, IR stretches, NBO charges) to probe structural effects.[23]

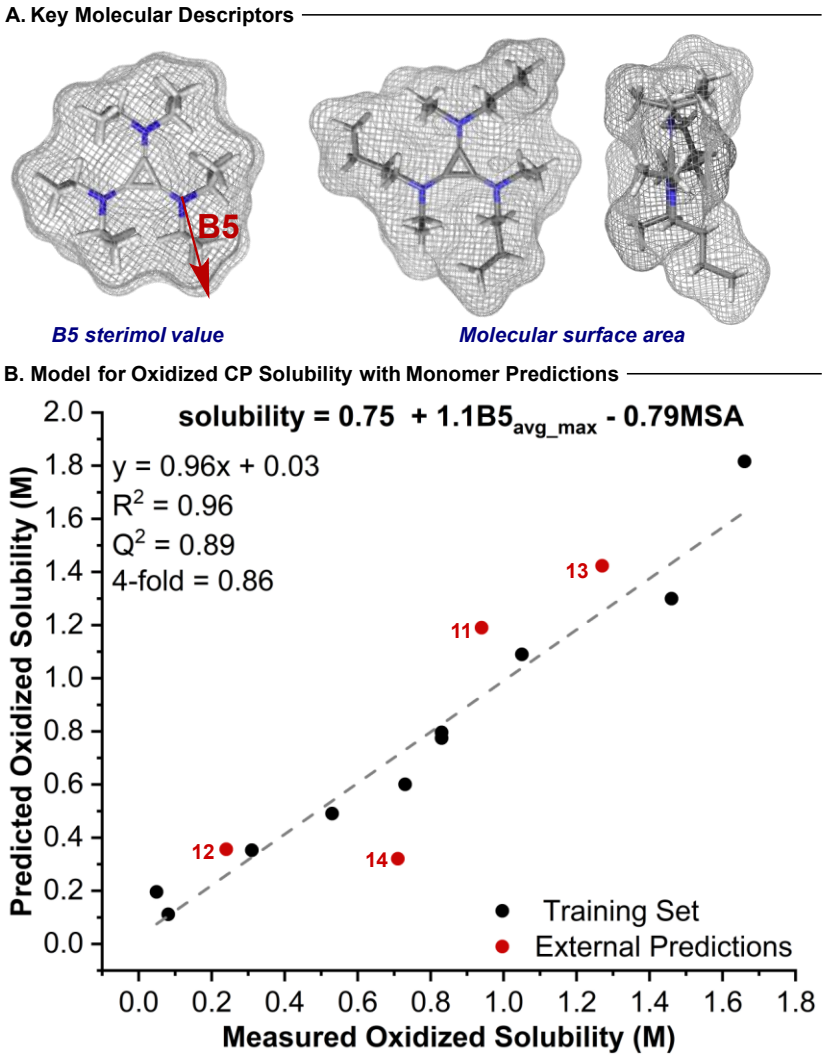

Figure 2.2 (A) B5 sterimol value and molecular surface area. (B) Statistical model for CP^{++} solubility developed with conformationally sampled parameters. An $R^2 = 0.56$ is found for four external monomer predictions (excluding **14**, while an $R^2 = 0.83$ is observed for external validations).

Using these parameters in combination with the measured solubility values for $\mathbf{1}^{++}$ to $\mathbf{10}^{++}$, a forward stepwise linear regression algorithm was applied to reveal a statistical model comprised of two terms (Figure 2.2 A).[24] The model consists of parameters acquired from two of the conformer classes: the average of the three Sterimol B5 values ($B5_{avg\_max}$) of the amine substituents

from the maximum Sterimol conformation of each CP dication and the molecular surface area (MSA) of the lowest energy conformer for each CP dication. As shown in Figure 2A, this model has an R^2 value of 0.96, a slope near unity, and an intercept close to zero, indicating a high degree of model accuracy. Model robustness was assessed using both internal (Leave-one-out Q^2 of 0.89 and *4*-fold of 0.86) and external validation techniques, involving predictions of solubility determined to be in good agreement with experimental values for four new catholytes, **11**-**14** (Figure 2.2B). The leave-one-out (LOO) validation technique involves exclusion of a single data point from the training set wherein the coefficients of the two parameters are adjusted to best fit the remaining training set points. The resulting model is then used to predict the value of the excluded point. This is performed in an iterative fashion for each data point. The leave-one-out values are then plotted against the experimental values and the R^2 for the linear regression fit of these points is defined as Q^2 (see experimental sections for models with LOO predictions included). The high Q^2 demonstrates accurate prediction of the entire training set and that the model is not biased toward specific data points in the training set.[25]

The inclusion of intrinsically related but inversely contributing steric terms proved critical for capturing the impact of substituents on solubility. For instance, the $B5_{avg\_max}$ descriptor involves the most extended conformation of the alkyl chains, describing the crucial role of a preferred geometry. The molecular surface area likely provides a description of the positioning of the alkyl chains about the CP core, with more compact arrangements enhancing solubility. Overall, this balance between the MSA and the $B5_{avg\_max}$ clarifies the non-intuitive trend that longer alkyl chains do not always afford increased solubility in these systems.

The model development workflow identified several CP derivatives with mono- and di-cation solubilities of >1 M, with $\mathbf{10}^{+}/\mathbf{10}^{++}$ exhibiting the highest values. Shelf life studies demonstrate

that 1 M solutions of the radical dication $\mathbf{10}^{++}$ are stable for more than 3 days at room temperature (see experimental sections for experimental details). Furthermore, a 1 M acetonitrile solution of monocation $\mathbf{10}^{+}$ shows a conductivity of 34.0 mS/cm without the addition of supporting electrolyte.[10] As such, this was selected as a candidate for pursuing high concentration electrochemical cycling. Cycling was performed in a symmetrical flow cell using a 1 M MeCN solution of **10** without added supporting electrolyte.[10,26] The flow cell contains graphite charge collecting plates with an interdigitated flow field, in combination with 400 μm thick carbon-felt electrodes, and Fumasep FAP-375-PP as the separator.[12,27] The solution was flowed through the cell at 10 mL/min and was subjected to galvanostatic cycling at 10 mA/cm^2. Cycling was conducted for 7 days (18 cycles) and proceeded with 78% material utilization and 99% columbic efficiency. Overall, 87% capacity retention was observed. Cyclic voltammograms before and after cycling indicate there is <5% decomposition of **10**, suggesting that capacity decay arises from issues related to flow cell engineering.[28] Overall, **10** exhibits outstanding cyclability and stability during this high-concentration and long-duration cycling. Considering that supporting electrolyte limits the solubility of active species and contributes significant additional cost to these systems, molecules like **10** that effectively cycle at high concentrations without supporting electrolyte are attractive for future development.[10]

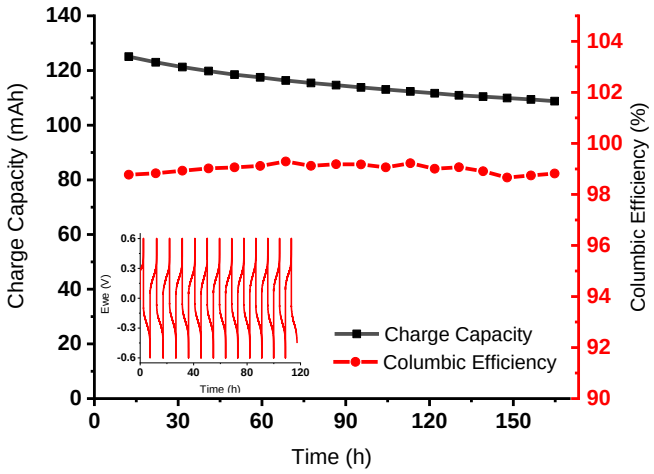

Figure 2.3 Symmetrical cycling of a 1.0 M solution of **10** in anhydrous acetonitrile at 10 mA/cm^2 using a flow cell prototype. (Inset: selected charge/discharge profiles).

A final set of studies focused on predicting the solubility of oligomeric CP derivatives. Such oligomeric ROMs are highly desirable for limiting the crossover of active species between the catholyte and anolyte compartments of a NRFB.[29-33] Oligomers would be even more attractive if they exhibited comparable solubility (and hence enhanced maximum charge capacity) relative to their monomeric counterparts. However, our previous work demonstrated that oligomer solubility generally decreases relative to the corresponding monomeric species. For instance, monomer **6**$^{++}$, dimer **15**$^{+4}$, and trimer **16**$^{+6}$ have 0.31 M, 0.19 M, and 0.14 M solubility in acetonitrile, respectively, resulting in similar maximum charge capacity across the series. We sought to use the statistical model features derived from the CP monomers to predict oligomer solubility, a significant dataset extrapolation.

As summarized in Figure 4A, we acquired the relevant molecular parameters for each CP subunit in the oligomer individually, and then averaged them (see experimental sections for complete details). This approach was initially validated by predicting the solubility of the previously reported dimer **15**$^{4+}$ (predicted: 0.28 M, measured: 0.19 M) and trimer **16**$^{6+}$ (predicted: 0.14 M,

measured: 0.14 M). As a challenging final case, we sought to identify a dimer with a solubility of >1 M. Virtual assessment of a variety of dimer structures identified **17**$^{4+}$ as a promising candidate, with a predicted solubility of 1.04 M. In agreement with prediction, the measured solubility of dimer **17**$^{4+}$ was 1.1 M. Notably, by virtue of the fact that **17**$^{4+}$ is a two electron catholyte with 1.1 M solubility, it has a higher maximum charge capacity (59.0 Ah/L) than the parent monomer **10**$^{++}$ (44.5 Ah/L). The success of this parameter acquisition platform suggests that, in this system, highly compact molecular arrangements in which the size of the oligomer can be distilled into a singular, averaged CP parameter set. Because the oligomer CP subunits are well represented in the training set (*i.e.*, **6**$^{++}$ and **10**$^{++}$), the model is able to predict their solubility with excellent accuracy. This showcases that the workflow can translate monomer behavior to quantitatively predict CP oligomer outputs.

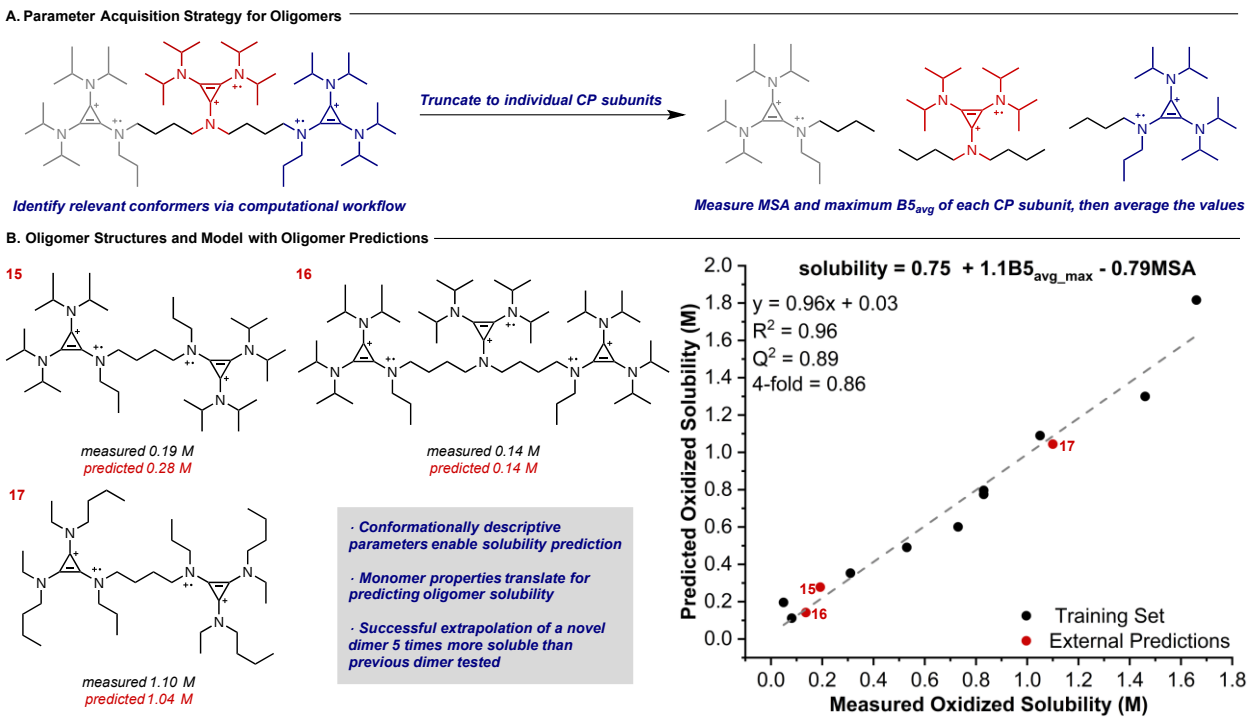

Figure 2.4 (A) Summary of truncations performed on CP oligomers for parameter acquisition. (B) CP oligomer structures with measured and predicted solubilities and the CP solubility model

developed based on monomer training set with oligomer predictions. Predicted $R^2 = 0.99$ for all external dimer predictions.

2.3. Conclusions

In summary, we demonstrate the successful development of a statistical model for predicting the MeCN solubility of conformationally flexible CP radical dications. Strategic consideration of conformer space was key to model development. This study identified a CP monomer that is soluble at >1.6 M in both redox states and undergoes stable electrochemical cycling at 1 M concentration in a supporting electrolyte free symmetric flow cell. Finally, the model was effectively extrapolated to predict the solubilities of related oligomeric species. This ultimately enabled the prediction of a CP dimer that has a solubility of >1.1 M, and thus more than 30% higher charge capacity than the parent monomer. Ongoing work is focused on applying analogous approaches to other catholyte and anolyte candidates for NRFBs.

2.4. Experimental Procedures and Characterization of Compounds

2.4.1 Computation Methods

Full list of authors in the Gaussian09 reference

M. J. Frisch, G. W. Trucks, H. B. Schlegel, G. E. Scuseria, M. A. Robb, J. R. Cheeseman, G. Scalmani, V. Barone, B. Mennucci, G. A. Petersson, H. Nakatsuji, M. Caricato, X. Li, H. P. Hratchian, A. F. Izmaylov, J. Bloino, G. Zheng, J. L. Sonnenberg, M. Hada, M. Ehara, K. Toyota, R. Fukuda, J. Hasegawa, M. Ishida, T. Nakajima, Y. Honda, O. Kitao, H. Nakai, T. Vreven, J. A. Montgomery, Jr., J. E. Peralta, F. Ogliaro, M. Bearpark, J. J. Heyd, E. Brothers, K. N. Kudin, V. N. Staroverov, T. Keith, R. Kobayashi, J. Normand, K. Raghavachari, A. Rendell, J. C. Burant, S. S. Iyengar, J. Tomasi, M. Cossi, N. Rega, J. M. Millam, M. Klene, J. E. Knox, J. B. Cross, V. Bakken, C. Adamo, J. Jaramillo, R. Gomperts, R. E. Stratmann, O. Yazyev, A. J. Austin, R. Cammi,

C. Pomelli, J. W. Ochterski, R. L. Martin, K. Morokuma, V. G. Zakrzewski, G. A. Voth, P. Salvador, J. J. Dannenberg, S. Dapprich, A. D. Daniels, O. Farkas, J. B. Foresman, J. V. Ortiz, J. Cioslowski, and D. J. Fox, Gaussian, Inc., Wallingford CT, 2013.

Computational Methods

Conformational searches were performed with MacroModel version 11.7[34] and the OPLS3 force field.[35] To keep the number of conformers reasonable, an energy window of 10 kJ/mol relative to the minimum and a hard limit of 100 conformers was set. All of the conformers within these limits were optimized with DFT.

All structures were optimized in the gas-phase with the B3LYP density functional[36,37] and the 6-31G(d) basis set as implemented in Gaussian09 (revision D.01).[38] Single point energies were performed on these geometries with the M06-2X density functional[39] and the triple-ζ valence quality def2-TZVP basis set of Weigend and Ahlrichs.[40] This energy was used to identify the lowest energy conformer, which was then re-optimized in the gas-phase with the M06-2X density functional and the triple-ζ valence quality def2-TZVP basis set. All of the optimized geometries were verified by frequency computations as minima (zero imaginary frequencies). Gaussian input files were written using a Python script.[41] Parameters were acquired from these ground state structures optimized at both levels of theory.

Multivariate Correlation Analyses

Parameters Collected

To explore the different geometries that could be contributing to the output, parameters were collected from four conformer classes defined as follows: the lowest energy conformer, the

maximum and minimum width conformers (determined by B5 Sterimol values), and a Boltzmann averaged set (considering those below a 2.5 kcal/mol energy cut-off). Sterimol values were calculated using a modified version of Paton's Python script with CPK radii.[42] The average B5 Sterimol value measured from each cyclopropenium carbon to the bonded nitrogen was used to identify the minimum and maximum width conformers for each cyclopropenium (Figure 2.5). Parameters were acquired from these ground state structures for each of the three conformer classes. The molecular surface area (MSA) was measured using Maestro. Boltzmann-weighting of the conformers' MSA and $B5_{avg\_max}$ parameters was performed with a 2.5 kcal/mol cutoff (T = 298.15 K). Multidimensional regression analyses were performed using MATLAB®.[43]

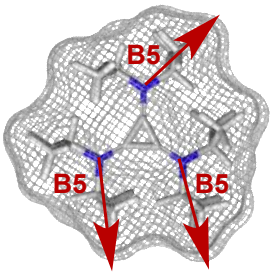

Figure 2.5. Vectors showing how the B5 Sterimol value measurement was performed. Three B5 Sterimol values were measured for each CP monomer; these values were then averaged into a singular value.

Model Development

Linear regression models were developed using an in-house script implemented in MATLAB® (version R2017b) to obtain the predicted oxidized solubility.[44] Using this previous published algorithm,[44] multiple linear regression models were developed using forward linear regression to correlate structural descriptors to the solubility output. A good linear correlation (R^2 approaching 1.0 and intercept near 0.0) between the predicted oxidized solubility and the measured oxidized

solubility indicates that the obtained model adequately approximates the system under study. Cross validation techniques, specifically leave-one-out, were utilized to ensure the model was not an overfit. This leave-one-out process involves exclusion of a single data point from the training set, the remaining training set points are then used to adjust the coefficients of the model. This new model is then employed to predict the solubility of the excluded data point. This is performed in an iterative fashion such that a leave-one-out (LOO) prediction point is obtained for every data point in the training set. These LOO predictions are then plotted against the experimental values and a linear regression is performed to obtain the R^2, termed Q^2. A Q^2 close to the R^2 of the model suggests that the model is able to predict the points in the training set and is not weighted toward a specific point or set of points. The LOO plots are included on the models presented in the experimental sections.

At the onset of this study, given the nature of the output and the number of conformers to be calculated for proper analysis, it was unclear which parameters (*e.g.*, electronic, steric, hybrid, or some combination) and structures (one structure or an averaged set) would best describe the systems under study. To this end, our computational workflow was properly vetted during model development. The first approach focused on a low-level conformers optimization/reordering followed by a high-level optimization strategy. This involved optimizing all candidate structures identified by conformational searches within the defined restrictions at the B3LYP/6-31G(d) level of theory. Single point energy calculations were performed on these structures at the M06-2X/def2-TZVP level of theory. From this energy calculation, the lowest energy conformer was identified and reoptimized at the M06-2X/def2-TZVP level of theory. A promising model was developed using parameters collected from the lowest energy structure determined by this process

(M06-2x/def2-TZVP optimized, Figure 2.6, A) consisting of two steric terms. As a consequence, we next examined if a model could be obtained using the same parameters from the B3LYP/6-31G(d) optimized structures (Figure 2.6, B), since it was likely that the method change would have a minor impact on the geometries. As expected, a similar statistical model could be developed and encouraged further investigation of using parameters acquired from optimized structures defined with the lower level of theory.

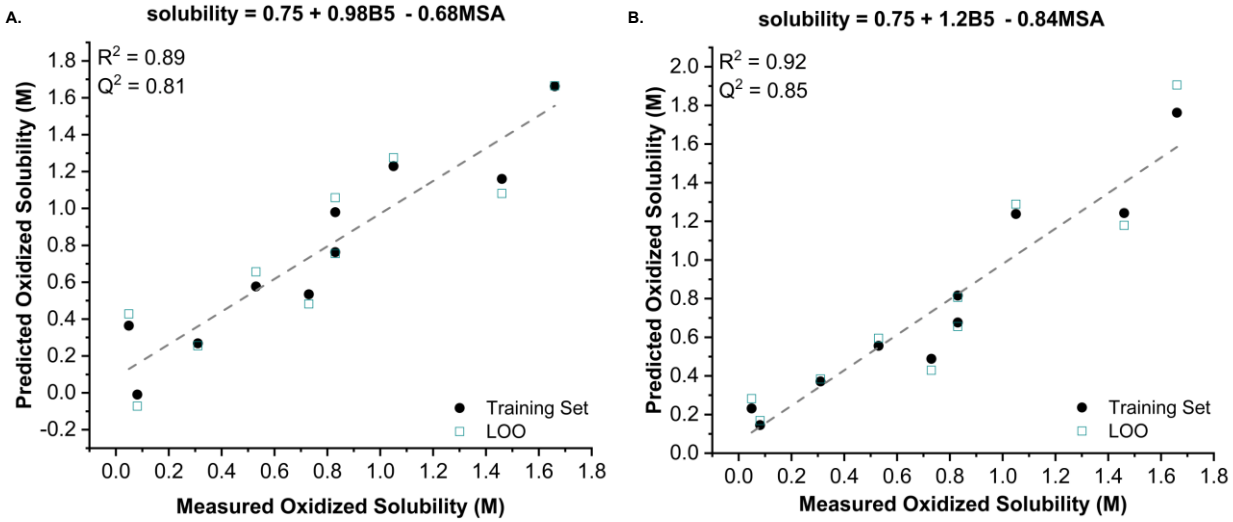

Figure 2.6. Models derived from lowest energy conformers of cyclopropeniums optimized at the A.) M06-2X/def2-TZVP level of theory and, B.) B3LYP/6-31G(d) level of theory. Q^2 = LOO = leave-one-out.

Table 2.1. Values for model (Figure 2.6, A) consisting of $B5_{avg}$ Sterimol values and MSAs acquired from CP structures optimized at the M06-2X/def2-TZVP level of theory.

measured solubility	predicted solubility	LOO
0.83	0.76	0.75
0.081	-0.01	-0.07
0.53	0.58	0.66
0.73	0.53	0.48
1.66	1.66	1.67
0.83	0.98	1.06
1.05	1.23	1.27

0.31	0.27	0.26
0.049	0.36	0.43
1.46	1.16	1.08

Table 2.2. Values for model (Figure 2.6, A) consisting of $B5_{avg}$ Sterimol values and MSAs acquired from CP structures optimized at the B3LYP/6-31G(d) level of theory.

measured solubility	predicted solubility	LOO
0.83	0.68	0.66
0.081	0.15	0.17
0.53	0.56	0.59
0.73	0.49	0.43
1.66	1.76	1.91
0.83	0.82	0.81
1.05	1.24	1.29
0.31	0.37	0.38
0.049	0.23	0.28
1.46	1.24	1.18

We next explored acquiring the statistically relevant parameters, B5 and MSA, from the aforementioned conformer classes. These were defined as I.) the lowest energy conformer, II.) the minimum and maximum width conformer based on B5 Sterimol values, and III.) the Boltzmann averaged set. The relevant conformer of each cyclopropenium was identified for each conformational class and the MSA and B5 were measured for each. Various combinations of these parameters were explored to identify the optimal model. The result of combining different combinations was highly variable, with some combinations providing models nearly as strong as the model presented in the manuscript and others with quite poor statistics. The Boltzmann weighted MSA and $B5_{avg\_max}$ model (Figure 2.7, A) had comparable statistics, but the process through which parameters are measured for the oligomers rendered Boltzmann weighting rather arduous. Using the Boltzmann weighted $B5_{avg}$ Sterimol values or $B5_{avg\_min}$ Sterimol values rather

than the $B5_{avg\_max}$ Sterimol values had detrimental effects to the statistics of the model (Figure 2.7, B-D).

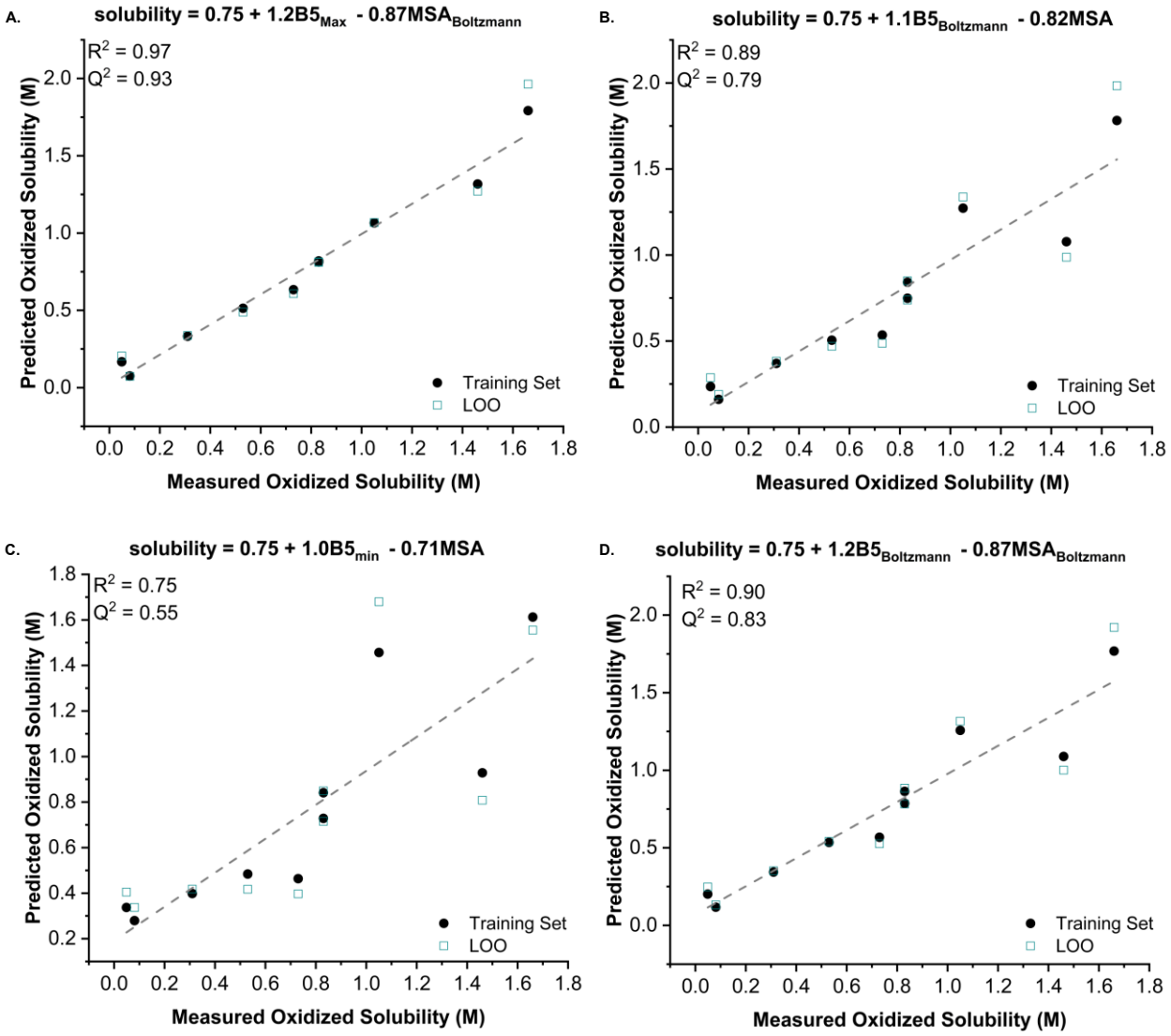

Figure 2.7. Models derived from different conformers of cyclopropeniums optimized at the B3LYP/6-31G(d) level of theory: A.) $B5_{avg\_max}$ Sterimol values and Boltzmann weighted MSAs, B.) Boltzmann weighted $B5_{avg}$ Sterimol values and lowest energy MSAs, C.) $B5_{avg\_min}$ Sterimol values and lowest energy MSAs, and D.) Boltzmann weighted $B5_{avg}$ Sterimol values and Boltzmann weighted MSAs. LOO = leave-one-out

Table 2.3. Values for model (Figure 2.7, A) consisting of $B5_{avg\_max}$ Sterimol values and Boltzmann weighted MSAs.

measured solubility	predicted solubility	LOO
0.83	0.81	0.81
0.081	0.08	0.07
0.53	0.51	0.49
0.73	0.63	0.61
1.66	1.79	1.96
0.83	0.82	0.81
1.05	1.07	1.07
0.31	0.33	0.34
0.049	0.17	0.20
1.46	1.32	1.27

Table 2.4. Values for model (Figure 2.7, B) consisting of Boltzmann weighted $B5_{avg}$ Sterimol values and lowest energy MSAs.

measured solubility	predicted solubility	LOO
0.83	0.75	0.74
0.081	0.16	0.19
0.53	0.51	0.47
0.73	0.53	0.49
1.66	1.78	1.98
0.83	0.84	0.85
1.05	1.27	1.34
0.31	0.37	0.38
0.049	0.24	0.29
1.46	1.08	0.99

Table 2.5. Values for model (Figure 2.7, C) consisting of $B5_{avg\_min}$ Sterimol values and lowest energy MSAs

measured solubility	predicted solubility	LOO
0.83	0.73	0.72

0.081	0.28	0.34
0.53	0.48	0.42
0.73	0.46	0.40
1.66	1.61	1.56
0.83	0.84	0.85
1.05	1.46	1.68
0.31	0.40	0.42
0.049	0.34	0.40
1.46	0.93	0.81

Table 2.6. Values for model (Figure 2.7, D) consisting of Boltzmann weighted $B5_{avg}$ Sterimol values and Boltzmann weighted MSAs.

measured solubility	**predicted solubility**	**LOO**
0.83	0.79	0.78
0.081	0.12	0.13
0.53	0.53	0.54
0.73	0.57	0.53
1.66	1.77	1.92
0.83	0.86	0.88
1.05	1.26	1.32
0.31	0.34	0.35
0.049	0.20	0.25
1.46	1.09	1.00

Finally, a statistically comparable model was obtained using the combination of $B5_{avg\_max}$ Sterimol values and the minimum width conformer MSAs (Figure 2.8 B). However, this model was less accurate for predicting solubility (predicted $R^2 = 0.6$) than the final model composed of $B5_{avg\_max}$ Sterimol values and the lower energy conformer MSAs (predicted $R^2 = 0.81$) (Figure 2.8 A). The slight difference in the statistics is a consequence of weighting toward how well the model can predict the most soluble CP, **10.** The model using the minimum width MSAs is somewhat better at predicting **10** but not advantageous for any of the other points in the training set, and ultimately is less accurate at predicting solubility outside of the training set given the predicted R^2 values.

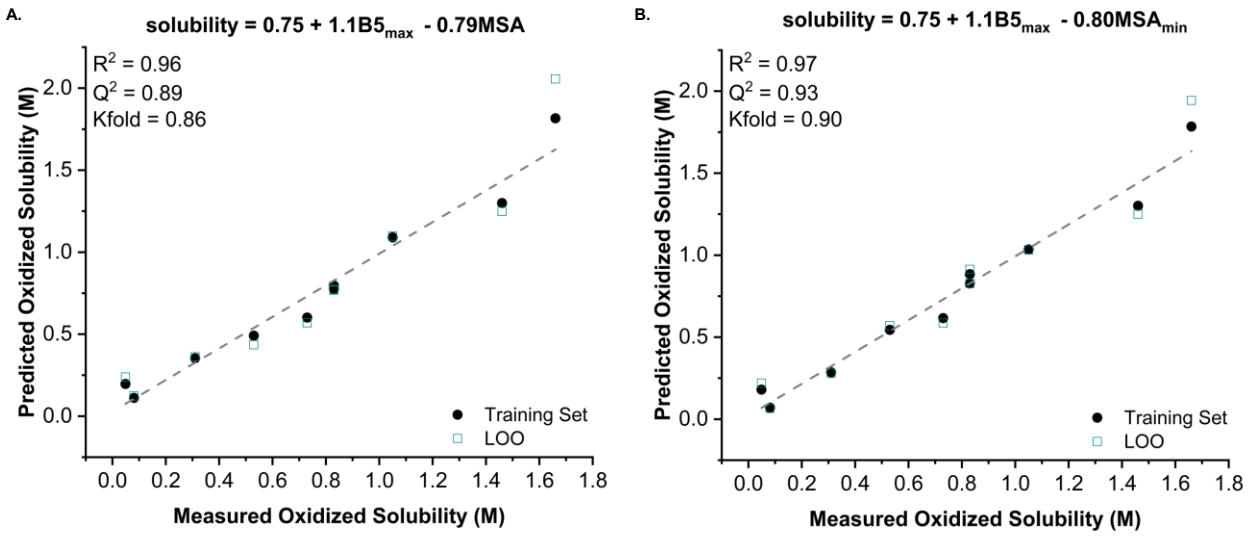

Figure 2.8. Models derived from different conformers of cyclopropeniums optimized at the B3LYP/6-31G(d) level of theory: A.) $B5_{avg\_max}$ Sterimol values and lowest energy conformer MSAs (Finalized model, predicted $R^2 = 0.81$), and B.) $B5_{avg\_max}$ Sterimol values and and minimum width conformer MSAs (predicted $R^2 = 0.67$). LOO = leave-one-out.

Table 2.7. Values for final model (Figure 2.8, A) consisting of $B5_{avg\_max}$ Sterimol values and lowest energy MSAs

measured solubility	predicted solubility	LOO
0.83	0.78	0.77
0.081	0.11	0.12
0.53	0.49	0.44
0.73	0.60	0.57
1.66	1.82	2.06
0.83	0.80	0.77
1.05	1.09	1.10
0.31	0.35	0.36
0.049	0.20	0.24
1.46	1.30	1.25

Table 2.8. Values for model (Figure 2.8, B) consisting of $B5_{avg\_max}$ Sterimol values and minimum width conformer MSAs.

measured solubility	predicted solubility	LOO
0.83	0.83	0.83
0.081	0.07	0.07
0.53	0.54	0.57
0.73	0.62	0.59
1.66	1.78	1.94
0.83	0.88	0.91
1.05	1.04	1.03
0.31	0.29	0.28
0.049	0.18	0.22
1.46	1.30	1.25

External Validation

Upon identification of a statistical model we carry out external validation to further assess model robustness. In this study, the external validation of the model was performed after the model had been developed with the ten training set points. Our virtual screen involved calculations of over fifteen novel cyclopropenium structures through the computational workflow outlined above. The structures computed for the virtual screen were designed based on the model parameters and observed training set trends. The model was then employed to predict the solubility of these species using the computationally derived parameters. From the virtual screen we selected four species for experimental testing. These species were selected for various reasons; one being that the predicted solubilities spanned the solubility output range of the training set. Monomers **11** and **13** were specifically evaluated because they were a clear extension of the most soluble CP **10**, and thus allowed us to further probe the effect of two different alkyl chains on the amines and also assess if atom count could be lowered while maintaining high levels of solubility. We tested CP **14** because it was intriguing that the model could so accurately describe CP **9** given that it was the only species in the training set that contained heteroatoms in the alkyl chains.

RMSD Analysis

The RMSD of a subset of CPs was analyzed for different optimized structures to quantify the differences in the geometry of the DFT optimized structures. RMSD analysis was performed in Maestro. The geometries were aligned using the superposition feature and atom pairwise tool as defined by the CP ring common substructure. The RMSD was calculated from these aligned structures using all atoms.

Table 2.9. RMSD comparison for a subset of CPs of the two conformer classes in the final model in the manuscript (Figure 2.8, A) and for the structures optimized with different levels of theory.

	CP	RMSD (Å)
B5max conformer vs Low E conformer, both optimized with B3LYP/6-31G(d)	**8**$^{++}$	1.46
	2^{++}	4.34
	4^{++}	1.41
	6^{++}	1.60
	5^{++}	2.28
Lowest E conformers optimized at B3LYP/6-31G(d) vs M06-2X/def2-TZVP	**8**$^{++}$	0.38
	2^{++}	0.09
	4 $^{++}$	0.22
	6 $^{++}$	0.35
	5 $^{++}$	0.19

Parameter Tables

To identify the most robust model, parameters acquired from different conformer classes were used to construct a variety of models (vide supra). These parameters, as well as the parameters used to develop the best model and make predictions of oxidized solubility, are presented in the tables below.

Table 2.10. B5 Sterimol values for all conformer classes of the CPs in the training set

	Optimized at the B3LYP/6-31G(d) Level of Theory							Optimized at the M06-2X/def2-TZVP Level of Theory			
				Lowest Energy Conformer				Lowest Energy Conformer			
CP	B5max	B5min	Boltzmann weighted B5 avg	B5	B5	B5	Average B5	B5	B5	B5	Average B5
1^{++}	4.21	4.17	4.20	4.19	4.19	4.19	4.19	4.28	4.27	4.28	4.28
2^{++}	4.15	3.86	4.01	3.96	3.95	3.96	3.96	3.98	3.98	3.98	3.98
3^{++}	3.10	3.10	3.10	3.11	3.11	3.11	3.11	3.10	3.10	3.10	3.10
4^{++}	4.22	4.16	4.19	4.17	4.20	4.22	4.20	4.27	4.26	4.28	4.27
5^{++}	5.34	4.97	5.17	5.12	5.12	5.14	5.13	5.19	5.24	5.27	5.23
6^{++}	4.61	4.41	4.54	4.23	5.20	4.23	4.55	4.22	5.44	4.27	4.64
7^{++}	6.40	5.60	5.97	6.14	6.22	6.18	6.18	6.12	6.34	6.19	6.22
8^{++}	6.43	5.99	6.28	6.19	6.52	6.24	6.32	6.32	6.65	6.62	6.53
9^{++}	6.05	6.02	6.04	5.85	6.43	5.87	6.05	5.79	6.55	5.79	6.04
10^{++}	6.42	5.83	6.16	6.15	6.16	6.20	6.17	6.24	6.23	6.35	6.27

Table 2.11. MSA values for all conformer classes of the CPs in the training set

	Optimized at the B3LYP/6-31G(d) Level of Theory				Optimized at the M06-2X/def2-TZVP Level of Theory
CP	Lowest energy conformer MSA	Minimum width conformer MSA	Maximum width conformer MSA	Boltzmann weighted MSA	Lowest energy conformer MSA
1^{++}	358.3	361.8	360.9	359.1	384.8
2^{++}	301.9	301.5	294.6	298.9	296.4
3^{++}	211.5	211.5	211.5	211.5	209.5
4^{++}	350.6	351.8	351.1	351.0	342.5
5^{++}	399.6	393.0	391.1	394.3	388.1

6^{++}	372.4	378.2	369.5	372.0	388.1
7^{++}	448.9	446.4	435.5	446.1	435.6
8^{++}	503.9	491.1	493.7	497.4	485.0
9^{++}	436.5	439.8	436.6	437.4	411.8
10^{++}	397.5	399.9	399.8	401.7	385.0

Table 2.12. Parameter values used to develop optimal model and make predictions

	CP	Lowest Energy MSA	B5max
Training Set	1^{++}	358.3	4.21
	2^{++}	301.9	4.15
	3^{++}	211.5	3.10
	4^{++}	350.6	4.22
	5^{++}	399.6	5.34
	6^{++}	372.4	4.61
	7^{++}	448.9	6.40
	8^{++}	503.9	6.43
	9^{++}	436.5	6.05
	10^{++}	397.5	6.42
Prediction Set	11^{++}	352.4	5.29
	12^{++}	338.3	4.26
	13^{++}	367.3	5.69
	14^{++}	498.3	5.87
	15^{++++}	391.5	4.73
	16^{++++++}	397.1	4.64
	17^{++++}	419.0	5.82

Method for Oligomer Parameter Acquisition

The workflow was adapted in order to handle CP oligomers and demonstrate property transfer from the monomeric components. Following the standard workflow, DFT optimized structures of all relevant conformers were obtained. The average B5 sterimol value measured from each cyclopropenium carbon to the bonded nitrogen was used to identify the minimum and maximum width conformers for each CP oligomer (*i.e.*, an average of six B5 Sterimol values for dimers, and

an average of nine B5 Sterimol values for the trimer). Once the appropriate conformer for each conformational class was identified for each oligomer, the oligomer was iteratively truncated to each individual CP unit in GaussView (Figure 2.9). Parameter measurements ($B5_{avg}$ and MSA) were taken of each individual CP unit (*i.e.*, two values for dimers, three values for the trimer), and these values were averaged into a singular value. This averaged, singular value was then used in the model to predict oxidized solubility.

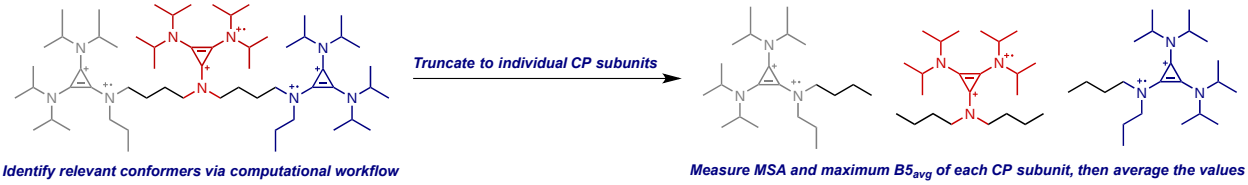

Figure 2.9. General truncation strategy for parameter acquisition from oligomeric structures.

2.4.2 Synthetic Methods

General Information: All commercial chemicals were used as received unless stated otherwise. Anhydrous DCM and ether were obtained from an SDS solvent system. All reactions were performed under nitrogen atmosphere unless stated otherwise. Compound **3**,[16] 1-chloro-2,3-bis(diisopropylamino)cyclopropenium chloride,[45] N,N'-di(n-propyl)butylenediamine,[45] and 1-chloro-2,3-bis(butyl(ethyl)amino) cyclopropenium chloride[45] were synthesized according to literature procedures. All other chemicals were purchased from commercial sources and used as received. Solubility limits of oxidized cyclopropenium oligomers were determined using a previously reported method,[16] which is also outlined below. NMR spectra were obtained on Varian VNMRs 700, Varian VNMRs 500, Varian Inova 500, or Varian MR400 spectrometers. ^{1}H and ^{13}C chemical shifts are reported in parts per million (ppm) relative to TMS, with the residual solvent peak used as an internal reference. High resolution mass spectroscopy was performed on a

Micromass AutoSpec Ultima Magnetic Sector Mass Spectrometer using ESI. Elemental analyses were obtained by Midwest Microlab.

Synthesis of New Cyclopropeniums

General Procedure A: Synthesis of tris(dialkylamino)cyclopropenium hexafluorophosphate: Under atmospheric conditions, a 20 mL vial with Teflon cap was charged with pentachlorocyclopropane (430 mg, 2 mmol), dichloromethane (10 mL), and a magnetic stir bar. Dialkylamine (10 mmol) was then added dropwise at 0 ℃. The mixture was allowed to stir for 15 minutes at 0 ℃ and then warmed to room temperature and stirred for another 30 minutes. After this time, the resulting solution was heated to 40 ℃ for overnight. The solution was cooled down and transferred to a separatory funnel with 20 mL 1:1 2M HCl:brine. The aqueous layer was extracted twice with 30 mL dichloromethane. The combined organic fractions were reduced and dissolved in 10 mL water. An aqueous solution of NH_4PF_6 (0.65 g, 4 mmol in 4 mL water) was subsequently added while stirring vigorously. The resulting suspension was extracted three times with 30 mL dichloromethane. The organic layers collected, dried over $MgSO_4$, and concentrated via rotary evaporation. The crude material was purified by silica gel column chromatography with gradient elution (1 – 5% acetonitrile in dichloromethane).

General Procedure B: Synthesis of mixed (dialkylamino)cyclopropenium Salts and Dimer (4, 6, 11, 12, 17): A solution of 1-chloro-2,3-bis(diisopropylamino)cyclopropenium chloride or 1-chloro-2,3-bis(butyl(ethyl)amino) cyclopropenium chloride (2 mmol, 1 equiv) and triethylamine (6mmol, 3 equiv) in DCM (10 mL) was cooled to 0 °C and one or half (for dimer) equivalent of

the selected amine was added dropwise. After stirring for 15 minutes, the solution was allowed to warm to room temperature and subsequenty heated to 40 °C. After 16 hours, the solution was cooled down and washed with a 1:1 brine and 2 M HCl solution (20 mL). The aqueous layer was further extracted with DCM (2 × 30 mL) and the combined organic fractions were reduced in vacuo. The residue was dissolved in water (20 mL) and under vigorous stirring, a solution of ammonium hexafluorophosphate (652 mg, 4.0 mmol) in water (5 mL) was added. The resulting white precipitate was extracted with DCM (3 × 30 mL) and the combined organic fractions were dried with MgSO4 and reduced. The compound was subsequently purified by silica gel column chromatography with gradient elution (1 – 5% acetonitrile in dichloromethane; 2-8% acetonitrile in dichloromethane for dimer).

General Procedure C: Chemical Oxidation of Cyclopropenium Salts: In a nitrogen filled glovebox, a 20 mL vial with septum was charged with cyclopropenium salts (300 mg, 1 equiv), acetonitrile (3 mL), and a magnetic stir bar. The resulting solution was cooled to -30 °C for half an hour. $NOPF_6$ (1 equiv) was dissolved in 3 mL acetonitrile in a syringe and cooled to -30 °C for half an hour. After cooling, the $NOPF_6$ solution was added dropwise to the stirred solution of cyclopropenium salts while a partial vacuum was applied to the vial in order to remove evolved NO gas. The reaction proceeded instantaneous, apparent by the formation of a deep red solution. After addition was complete, the vial remained under vacuum for another 15 minutes until the total volume was reduced to approximately 2 mL. 15 mL diethyl ether was then added and the resulting red suspension centrifuged at 2000 RPM for 5 min and decanted. The resulting red compound was further purified by two additional precipitations from acetonitrile and diethyl ether, dried and stored under nitrogen at –30 °C.

Synthesis of **4**$^{+}$**:** Prepared by **General Procedure B** using *N*-ethylisopropylamine and 1-chloro-2,3-bis(di-isopropylamino)cyclopropenium chloride, followed by ion-exchange with NH_4PF_6 to yield a white powder (450 mg, 64% yield). ^{1}H NMR (400 MHz, Chloroform-*d*) δ 4.04 (hept, *J* = 6.7 Hz, 1H), 3.82 (hept, *J* = 6.9 Hz, 4H), 3.38 (q, *J* = 7.2 Hz, 2H), 1.33 (d, *J* = 6.9 Hz, 24H), 1.28 (d, *J* = 6.8 Hz, 6H), 1.19 (t, *J* = 7.2 Hz, 3H). ^{13}C NMR (100 MHz, Chloroform-*d*) δ 118.39, 118.34, 54.17, 51.47, 39.67, 21.90, 21.06, 16.89. HRMS (ESI) *m/z* calcd for $C_{20}H_{40}N_3$ $(M-PF_6)^+$: 322.3217, found 322.3215.

Synthesis of **5**$^{+}$**:** Prepared by **General Procedure A** using dipropylamine, white powder (716 mg, 74% yield). ^{1}H NMR (400 MHz, Chloroform-*d*) δ 3.30-3.15 (m, 12H), 1.65 (dt, *J* = 15.7, 7.6 Hz, 12H), 0.91 (t, *J* = 7.4 Hz, 18H).^{13}C NMR (100 MHz, Chloroform-*d*) δ 116.59, 54.52, 22.05, 10.90. HRMS (ESI) *m/z* calcd for $C_{21}H_{42}N_3$ $(M-PF_6)^+$: 336.3373, found 336.3369.

Synthesis of **7**$^{+}$**:** Prepared by **General Procedure A** using *N*-propylbutylamine, light yellow oil (653 mg, 62% yield). ^{1}H NMR (400 MHz, Chloroform-*d*) δ 3.32-3.18 (m, 1H), 1.75-1.50 (m, 1H), 1.33 (h, *J* = 7.4 Hz, 1H), 0.96 (t, *J* = 7.4 Hz, 1H), 0.94 (t, *J* = 7.5 Hz, 1H).^{13}C NMR (126 MHz, Chloroform-*d*) δ 116.88, 54.64, 52.93, 30.99, 22.10, 20.06, 13.92, 11.02. HRMS (ESI) *m/z* calcd for $C_{24}H_{48}N_3$ $(M-PF_6)^+$: 378.3843, found 378.3837.

Synthesis of **8**$^{+}$**:** Prepared by **General Procedure A** using dibutylamine, white powder (894 mg, 79% yield). ^{1}H NMR (400 MHz, Chloroform-d) δ 3.31-3.23 (m, 12H), 1.67-1.53 (m, 12H), 1.32 (h, J = 7.4 Hz, 12H), 0.96 (t, J = 7.3 Hz, 18H). ^{13}C NMR (100 MHz, Chloroform-*d*) δ 116.97,

52.92, 30.98, 20.08, 13.93. HRMS (ESI) *m/z* calcd for $C_{27}H_{54}N_3$ $(M-PF_6)^+$: 420.4312, found 420.4310.

Synthesis of **9⁺:** Prepared by **General Procedure A** using bis(2-methoxyethyl)amine, white powder (1035 mg, 90% yield).^{1}H NMR (400 MHz, Chloroform-*d*) δ 3.64-3.50 (m, 24H), 3.34 (s, 18H). ^{13}C NMR (100 MHz, Chloroform-*d*) δ 117.57, 70.50, 59.95, 59.17, 52.58. HRMS (ESI) *m/z* calcd for $C_{21}H_{42}N_3O_6$ $(M-PF_6)^+$: 432.3068, found 432.3065.

Synthesis of **10⁺:** Prepared by **General Procedure A** using *N*-ethylbutylamine, white powder (694 mg, 72% yield).^{1}H NMR (401 MHz, Chloroform-*d*) δ 3.38 (q, *J* = 7.2 Hz, 6H), 3.28 (t, *J* = 9.1, 6.9 Hz, 6H), 1.62 (dd, *J* = 9.3, 6.5 Hz, 6H), 1.40 – 1.23 (m, 15H), 0.96 (t, *J* = 7.4 Hz, 9H).^{13}C NMR (100 MHz, Chloroform-*d*) δ 116.84, 60.05, 52.31, 47.68, 31.01, 20.07, 14.11, 13.91. HRMS (ESI) *m/z* calcd for $C_{21}H_{42}N_3$ $(M-PF_6)^+$: 336.3373, found 336.3375.

Synthesis of **11⁺:** Prepared by **General Procedure A** using *N*-ethylpropylamine, yellow liquid (779 mg, 89% yield).^{1}H NMR (500 MHz, Chloroform-*d*) δ 3.38 (q, *J* = 7.2 Hz, 6H), 3.24 (t, *J* = 9.5, 6.4 Hz, 6H), 1.68 (h, *J* = 15.5, 7.5 Hz, 6H), 1.28 (t, *J* = 7.2 Hz, 9H), 0.94 (t, *J* = 7.3 Hz, 9H).^{13}C NMR (126 MHz, Chloroform-*d*) δ 116.71, 54.04, 47.68, 22.19, 14.10, 11.01. HRMS (ESI) *m/z* calcd for $C_{18}H_{36}N_3$ $(M-PF_6)^+$: 294.2904, found 294.2902.

Synthesis of **12⁺:** Prepared by **General Procedure B** using diethylamine and 1-chloro-2,3-*bis*(di-isopropylamino)cyclopropenium chloride, followed by ion-exchange with NH_4PF_6 to yield a white powder (240 mg, 54% yield). ^{1}H NMR (401 MHz, Chloroform-*d*) δ 3.84 (hept, *J* = 6.9 Hz, 4H),

3.51 (q, *J* = 7.2 Hz, 4H), 1.36 (d, *J* = 6.9 Hz, 24H), 1.26 (t, *J* = 7.2 Hz, 6H). ^{13}C NMR (126 MHz, cdcl$_3$) δ 118.66, 117.79, 51.62, 45.94, 22.06, 14.09. HRMS (ESI) *m/z* calcd for $C_{19}H_{38}N_3$ $(M-PF_6)^+$: 308.3060, found 308.3060.

Synthesis of **13$^+$:** Prepared by **General Procedure B** using diethylamine and 1-chloro-2,3-bis(butyl(ethyl)amino)cyclopropenium chloride, followed by ion-exchange with NH_4PF_6 to yield a light pink oil (403 mg, 63% yield). ^{1}H NMR (400 MHz, Chloroform-*d*) δ 3.38 (q, *J* = 7.2, 1.0 Hz, 8H), 3.28 (t, *J* = 7.9 Hz, 4H), 1.68-1.51 (m, 4H), 1.39-1.17 (m, 16H), 0.96 (t, *J* = 7.3 Hz, 6H). ^{13}C NMR (126 MHz, Chloroform-*d*) δ 116.67, 116.58, 52.30, 47.68, 47.05, 31.01, 20.01, 14.06. HRMS (ESI) *m/z* calcd for $C_{19}H_{38}N_3$ $(M-PF_6)^+$: 308.3060, found 308.3058.

Synthesis of **14$^+$:** Prepared by **General Procedure A** using bis(2-ethoxyethyl)amine, light yellow powder. (1012 mg, 76% yield). ^{1}H NMR (400 MHz, Chloroform-*d*) δ 3.70-3.63 (m, 12H), 3.63-3.53 (m, 12H), 3.47 (q, *J* = 7.0 Hz, 12H), 1.14 (t, *J* = 7.0 Hz, 18H). ^{13}C NMR (126 MHz, Chloroform-*d*) δ 117.20, 68.56, 66.92, 52.48, 15.15. HRMS (ESI) *m/z* calcd for $C_{27}H_{54}N_3O_6$ $(M-PF_6)^+$: 516.4007, found 516.4001.

Synthesis of **17$^+$:** Prepared by **General Procedure B** using *N,N'-di*(*n*-propyl)butylenediamine and 1-chloro-2,3-bis(butyl(ethyl)amino) cyclopropenium chloride, followed by ion-exchange with NH_4PF_6 to yield a colorless solid (181 mg, 31% yield).^{1}H NMR (401 MHz, Chloroform-*d*) δ 3.40-3.32 (m, 12H), 3.30-3.22 (m, 12H), 1.74-1.54 (m, 16H), 1.35-1.21 (m, 20H), 0.97-0.87 (m, 18H). ^{13}C NMR (176 MHz, cdcl$_3$) δ 116.75, 116.65, 54.02, 52.51, 52.11, 47.50, 30.80, 25.48, 22.06,

19.92, 13.88, 13.76, 10.71. HRMS (ESI) *m/z* calcd for $C_{40}H_{78}N_6$ (M−2 PF_6) $^{2+}$: 321.3138, found 321.3144.

Compound $\mathbf{3}^{\bullet+}$

According to **General Procedure C**, $\mathbf{3}^{+}$ (163 mg) is oxidized to form $\mathbf{3}^{\bullet+}$ as a red powder (170 mg, 71% yield). Anal. Calcd for $C_9H_{18}F_{12}N_3P_2^{\bullet}$: C 23.59%, H 3.96%, N 9.17%; found: C 24.09%, H 4.02%, N 9.16%.

Compound $\mathbf{4}^{\bullet+}$

According to **General Procedure C**, $\mathbf{4}^{+}$ (108 mg) is oxidized to form $\mathbf{4}^{\bullet+}$ as a red powder (45 mg, 32% yield). Anal. Calcd for $C_{20}H_{40}F_{12}N_3P_2^{\bullet}$: C 39.22%, H 6.58%, N 6.86%; found: C 39.39%, H 6.46%, N 6.91%.

Compound $\mathbf{5}^{\bullet+}$

According to **General Procedure C**, $\mathbf{5}^{+}$ (151 mg) is oxidized to form $\mathbf{5}^{\bullet+}$ as a red powder (100 mg, 51% yield). Anal. Calcd for $C_{21}H_{42}F_{12}N_3P_2^{\bullet}$: C 40.26%, H 6.76%, N 6.71%; found: C 40.31%, H 6.84%, N 6.80%.

Compound $\mathbf{7}^{\bullet+}$

According to **General Procedure C**, $\mathbf{7}^{+}$ (300 mg) is oxidized to form $\mathbf{7}^{\bullet+}$ as a red powder (152 mg, 61% yield). Anal. Calcd for $C_{27}H_{54}F_{12}N_3P_2^{\bullet}$: C 45.63%, H 7.66%, N 5.91%; found: C 46.38%, H 7.86%, N 5.93%.

Compound **8**$^{++}$

According to **General Procedure C**, **8**$^{+}$ (300 mg) is oxidized to from **8**$^{++}$ as a red powder (188 mg, 49% yield). Anal. Calcd for $C_{24}H_{48}F_{12}N_3P_2^{\bullet}$: C 43.11%, H 7.24%, N 6.28%; found: C 43.39%, H 7.23%, N 6.40%.

Compound **9**$^{++}$

According to **General Procedure C**, **9**$^{+}$ (300 mg) is oxidized to form **9**$^{++}$ as a red powder (172 mg, 46% yield). Anal. Calcd for $C_{21}H_{42}F_{12}N_3O_6P_2^{\bullet}$: C 34.91%, H 5.86%, N 5.82%; found: C 35.02%, H 5.94%, N 5.93%.

Compound **10**$^{++}$

According to **General Procedure C**, **10**$^{+}$ (300 mg) is oxidized to form **10**$^{++}$ as a red powder (218 mg, 56% yield). Anal. Calcd for $C_{21}H_{42}F_{12}N_3P_2^{\bullet}$: C 40.26%, H 6.76%, N 6.71%; found: C 40.17%, H 6.87%, N 6.98%.

Compound **11**$^{++}$

According to **General Procedure C**, **11**$^{+}$ (300 mg) is oxidized to form **11**$^{++}$ as a red powder (208 mg, 52% yield). Anal. Calcd for $C_{18}H_{36}F_{12}N_3P_2^{\bullet}$: C 36.99%, H 6.21%, N 7.19%; found: C 36.83%, H 6.03%, N 7.13%.

Compound **12**$^{++}$

According to **General Procedure C**, **12**$^{+}$ (300 mg) is oxidized to form **12**$^{++}$ as a red powder (160 mg, 73% yield). Anal. Calcd for $C_{19}H_{38}F_{12}N_3P_2^{\bullet}$: C 38.13%, H 6.40%, N 7.02%; found: C 38.39%, H 6.44%, N 7.15%.

Compound **13**$^{++}$

According to **General Procedure C**, **13**$^{+}$ (314 mg) is oxidized to form **13**$^{++}$ as a red powder (146 mg, 35% yield). Anal. Calcd for $C_{19}H_{38}F_{12}N_3P_2^{\bullet}$: C 38.13%, H 6.40%, N 7.02%; found: C 37.88%, H 6.28%, N 6.87%

Compound **14**$^{++}$

According to **General Procedure C**, **14**$^{+}$ (300 mg**)** is oxidized to form **14**$^{++}$ as a red powder (271 mg, 74% yield). Anal. Calcd for $C_{27}H_{54}F_{12}N_3O_6P_2^{\bullet}$: C 40.20%, H 6.75%, N 5.21%; found: C 40.28%, H 6.63%, N 5.35%

Compound **17**$^{++++}$

According to **General Procedure C**, **17**$^{++}$ (160 mg) is oxidized to **17**$^{++++}$ as a red powder (112 mg, 54% yield). Anal. Calcd for $C_{40}H_{78}F_{24}N_6P_4^{2\bullet}$: C 39.28%, H 6.43%, N 6.87%; found: C 40.88%, H 6.51%, N 7.20%

Solubility Measurements

Using a published method,[16] the appropriate CP derivative was added to a 1 mL vial containing acetonitrile (0.3 mL) until a solid persisted. A piece of an ultrafine glass frit (GE Healthcare

Whatman™ Binder-Free Glass Microfiber Filters, Grade GF/A) was put inside a needle to make a mini-filter. The suspension was filtered through the needle-filter to remove the solids, and the saturated solution was collected. 25 μL of this saturated solution were dispensed to 4-5 pre-tared 1 mL vials. After over-night high vacuum, the increase in mass from vial mass represents the mass of CP that is dissolved in the dispensed volume.

Table 2.13. Maximum solubility of cyclopropenium monocation and dication salts in acetonitrile. Solubility measurements for $\mathbf{1}^{+}$, $\mathbf{1}^{++}$, $\mathbf{2}^{+}$, $\mathbf{2}^{++}$, $\mathbf{6}^{+}$, $\mathbf{6}^{++}$, $\mathbf{15}^{++}$, $\mathbf{15}^{++++}$, $\mathbf{16}^{+++}$, and $\mathbf{16}^{++++++}$ were taken from the literature.[16,29]

Compound	Reduced Species in MeCN (M)	Oxidized Species in MeCN (M)
1[10]	1.5	0.081
2[12]	1.7	0.73
3	1.26 ± 0.12	0.53 ± 0.06
4	1.61 ± 0.05	0.049 ± 0.008
5	1.84 ± 0.09	0.83 ± 0.02
6[14]	1.21 ± 0.06	0.31 ± 0.01
7	viscous liquid	1.46 ± 0.12
8	1.81 ± 0.07	0.83 ± 0.20
9	1.62 ±0.06	1.05 ±0.07
10	1.94 ± 0.02	1.66 ± 0.07
11	viscous liquid	0.93 ± 0.05
12	1.80 ±0.09	0.24 ± 0.02
13	viscous liquid	1.27 ± 0.05
14	1.16 ±0.07	0.71 ± 0.04
15[14]	0.80 ± 0.02	0.192 ± 0.008
16[14]	0.46 ± 0.01	0.136 ± 0.008
17	viscous liquid	1.10 ± 0.07

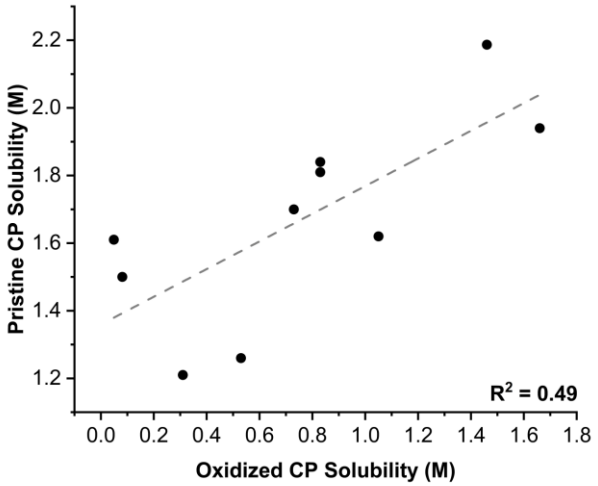

Figure 2.10. Plot of CP^{+} (pristine) versus CP^{++} (oxidized) solubility demonstrates there is not a strong correlation between CP solubility in the two redox states.

2.4.3 Electrochemistry and Cycling Studies

General remarks

Acetonitrile (99.8%, anhydrous) was obtained from Sigma Aldrich and used as received. Potassium hexafluorophoshate (≥99%) was obtained from Sigma Aldrich and was dried under high vacuum for 48 h before being transferred to a nitrogen-filled glovebox. A 0.5 M stock solution of the supporting electrolyte in acetonitrile was prepared in a glovebox and dried over 3Å molecular sieves for at least two days prior to use. A Fumasep® FAP-375-PP membrane was obtained from Fumatech and ion-exchanged in saturated KPF_6 before use and then dried under high vacuum overnight before use. Conductivity measurements was acquired using an Orion Star™ A215 pH/Conductivity Benchtop Multiparameter Meter. Shelf life studies were conducted in a Teflon vial at room temperature in a nitrogen-filled glovebox.

Cyclic Voltammetry

Cyclic voltammetry was performed in a nitrogen-filled glovebox with a Biologic VSP multichannel potentiostat/galvanostat using a three-electrode electrochemical cell, consisting of a glassy carbon disk working electrode (0.07 cm^2, BASi), a Ag/Ag+ quasi-reference electrode (BASi) with 0.01 M $AgBF_4$ (Sigma) in acetonitrile, and a platinum wire counter electrode (ALS). The glassy carbon disk electrode was polished in a nitrogen-filled glovebox using aluminum oxide polishing paper (9 micron and 0.3 micron, Fiber Instrument) and anhydrous acetonitrile. All experiments were run in the 0.5 M KPF_6 stock electrolyte solution.

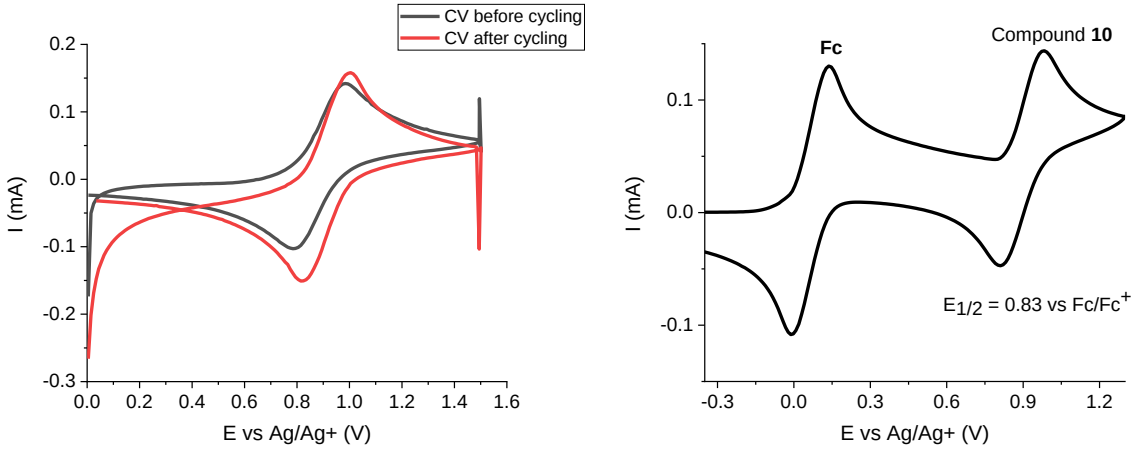

Figure 2.11. (left) CV before and after cycling of 1 M **10** shows no detectable decomposition $\frac{ip\ after}{ip\ before} = 1.1$ (due to solvent evaporation); (right) CV of 5 mM Compound **10** in 0.5 M KPF_6 acetonitrile solution with ferrocene as an internal standard

Flow Cell Cycling

Cycling under flow conditions was performed with a zero-gap flow cell[12] comprised of graphite charge collecting plates containing an interdigitated flow field in combination with two layers of non-woven carbon felt electrodes (Sicracet 29AA) on each side. ePTFE gaskets were used to

achieve ~20% compression of the felt. A Fumasep® FAP-375-PP anion-exchange membrane separated the two half cells, and the exposed area of the membrane in the gasket window was used as the active area (2.55 cm^2). After assembly, the catholyte and anolyte sides of the cell were both loaded with a 6 mL mixture of 0.5 M $\mathbf{10}^{+}$ and 0.5 M $\mathbf{10}^{++}$ in acetonitrile. The cell was pretreated by continuously flowing the solution at 10 mL/min for 1 h without any charging process using a peristaltic pump (Cole-Parmer) with Solveflex and PFA tubing. After this step, using the same flow rate, galvanostatic charge/discharge cycling was performed using a BioLogic VSP galvanostat employing a charging current of 10 mA cm^{-2} and a discharging current of -10 mA/cm^{-2} with +0.6 V and -0.6 V voltage limits. EIS was performed at 50% SOC from 500 kHz to 1 Hz at OCV using a 10 mV sine perturbation. Polarization measurements were collected at 50% SOC in alternating 50 mV steps over the range of 0.5 to 0.5 V

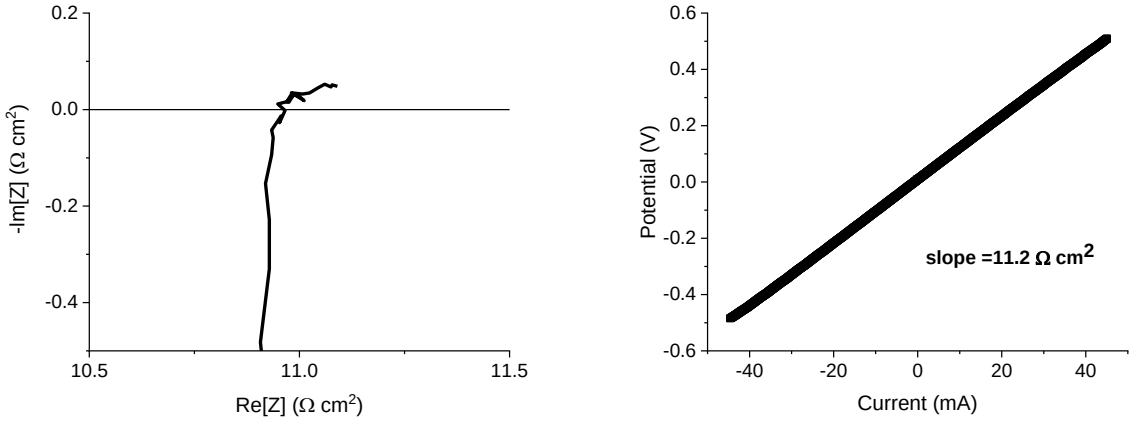

Figure **2.12**. (left) Nyquist plot from EIS measurement and (right) Polarization curve at 50% SOC

2.5 References

(1) For recent reviews on ROMs in NRFBs see: (a) Soloveichik, G. L. Flow Batteries: Current Status and Trends. *Chem. Rev.* **2015**, *115*, 11533. (b) Winsberg, J.; Hagemann, T.; Janoschka, T.;

Hager, M. D.; Schubert, U. S. Redox-Flow Batteries: From Metals to Organic Redox-Active Materials. *Angew. Chem. Int. Ed.* **2016**, *56*, 686. (c) Gong, K.; Fang, Q.; Gu, S.; Li, S. F. Y.; Yan, Y. Nonaqueous Redox-Flow Batteries: Organic Solvents, Supporting Electrolytes, and Redox Pairs. *Energy Environ. Sci.* **2015**, *8*, 3515. (d) Wei, X.; Pan, W.; Duan, W.; Hollas, A.; Yang, Z.; Li, B.; Nie, Z.; Liu, J.; Reed, D.; Wang, W.; Sprenkle, V. Materials and Systems for Organic Redox Flow Batteries: Status and Challenges. *ACS Energy Lett.* **2017**, *2*, 2187. (e) Zhang, C.; Zhang, L.; Ding, Y.; Peng, S.; Guo, X.; Zhao, Y.; He, G.; Yu, G. "Progress and Prospects of Next-Generation Redox Flow Batteries. *Energy Storage Materials* **2018**, *15*, 324. (2) For some previous ROM electrolyte examples see: (a) Duan, W.; Huang, J.; Kowalski, J. A.; Shkrob, I. A.; Vijayakumar, M.; Walter, E.; Pan, B.; Yang, Z.; Milshtein, J. D.; Li, B.; Liao, C.; Zhang, Z.; Wang, W.; Liu, J.; Moore, J. S.; Brushett, F. R.; Zhang, L.; Wei, Z. "Wine-Dark Sea" in an Organic Flow Battery: Storing Negative Charge in 2,1,3-Benzothiadiazole Radicals Leads to Improved Cyclability. *ACS Energy Lett.* **2017**, *2*, 1156. (b) Huang, J.; Duan, W.; Zhang, J.; Shkrob, I. A.; Assary, R. S.; Pan, B.; Liao, C.; Zhang, Z.; Wei, X.; Zhang, L. Substituted Thiadiazoles as Energy-Rich Anolytes for Nonaqueous Redox Flow Cells. *J. Mater. Chem. A* **2018**, *6*, 6251. (c) Kwon, G.; Lee, S.; Hwang, J.; Shim, H.-S.; Lee, B.; Lee, M. H.; Ko, Y.; Jung, S.-K.; Ku, K.; Hong, J.; Kang, K. Multi-Redox Molecule for High-Energy Redox Flow Batteries. *Joule* **2018**, *2*, 1771. (d) Lin, K.; Chen, Q.; Gerhardt, M. R.; Tong, L.; Kim, S. B.; Eisenach, L.; Valle, A. W.; Hardee, D.; Gordon, R. G.; Aziz, M. J.; Marshak, M. P. Alkaline Quinone Flow Battery. *Science* **2015**, *349*, 1529. (e) Sevov, C. S.; Brooner, R. E. M.; Chenard, E.; Assary, R. S.; Moore, J. S.; Rodriguez-Lopez, J.; Sanford, M. S. Evolutionary Design of Low Molecular Weight Organic Anolyte Materials for Applications in Nonaqueous Redox Flow Batteries. *J. Am. Chem. Soc.* **2015**, *137*, 14465. (f) Sevov, C. S.; Hickey, D. P.; Cook, M. E.; Robinson, S. G.;

Barnett, S.; Minteer, S. D.; Sigman, M. S.; Sanford, M. S. Physical Organic Approach to Persistent, Cyclable, Low-Potential Electrolytes for Flow Battery Applications. *J. Am. Chem. Soc.* **2017**, *139*, 2924. (g) Wei, X.; Wu, X.; Vijayakumar, M.; Cosimbescu, L.; Liu, T.; Sprenkle, V.; Wang, W. TEMPO-Based Catholyte for High-Energy Density Nonaqueous Redox Flow Batteries. *Adv. Mater.* **2014**, *26*, 7649. (h) Winsberg, J.; Hagemann, T.; Muench, S.; Friebe, C.; Haupler, B.; Janoschka, T.; Morgenstern, S.; Hager, M. D.; Schubert, U. S. Poly(boron-dipyrromethene)-A Redox-Active Polymer Class for Polymer Redox-Flow Batteries. *Chem. Mater.* **2016**, *28*, 3401. (i) Zhang, J.; Yang, Z.; Shkrob, I. A.; Assary, R. S.; Tung, S.; Silcox, B.; Duan, W.; Zhang, J.; Su, C. C.; Hu, B.; Pan, B.; Liao, C.; Zhang, Z.; Wang, W.; Curtiss, L. A.; Thompson, L. T.; Wei, X.; Zhang, L. Annulated Dialkoxybenzenes as Catholyte Materials for Non-Aqueous Redox Flow Batteries: Achieving High Chemical Stability through Bicyclic Substitution. *Adv. Energy Mater.* **2017**, *7*, 1701272.

(3) Darling, R. M.; Gallagher, K. G.; Kowalski, J. A.; Ha, S.; Brushett, F. R. Pathways to Low-Cost Electrochemical Energy Storage: A Comparison of Aqueous and Nonaqueous Flow Batteries. *Energy Environ. Sci.* **2014**, *7*, 3459.

(4) Chen, H.; Zhou, Y.; Lu, Y.-C. Lithium-Organic Nanocomposite Suspension for High-Energy-Density Redox Flow Batteries. *ACS Energy Lett.* **2018**, *3*, 1991.

(5) Ding, Y.; Zhang, C.; Zhang, L.; Zhou, Y.; Yu, G. Molecular Engineering of Organic Electroactive Materials for Redox Flow Batteries. *Chem. Soc. Rev.* **2018**, *47*, 69.

(6) Huang, J.; Su, L.; Kowalski, J. A.; Barton, J. L.; Ferrandon, M.; Burrell, A. K.; Brushett, F. R.; Zhang, L. A Substractive Approach to Molecular Engineering of Dimethoxybenzene-Based Redox Materials for Non-Aqueous Flow Batteries. *J. Mater. Chem. A* **2015**, *3*, 14971.

(7) Zhang, C.; Qian, Y.; Ding, Y.; Zhang, L.; Guo, X.; Zhao, Y.; Yu, G. Biredox Eutectic Electrolytes Derived from Organic Redox-Active Molecules: High-Energy Storage Systems. *Angew. Chem. Int. Ed.* **2019**, *58*, 7045..

(8) Laramie, S. M.; Milshtein, J. D.; Breault, T. M.; Brushett, F. R.; Thompson, L. T. Performance and Cost Characteristics of Multi-Electron Transfer, Common Ion Exchange Non-Aqueous Redox Flow Batteries. *J. Power Sources* **2016**, *327*, 681.

(9) Shinkle, A. A.; Pomaville, T. J.; Sleightholme, A. E. S.; Thompson, L. T.; Monroe, C. W. Solvents and Supporting Electrolytes for Vanadium Acetylacetonate Flow Batteries. *J. Power Sources* **2014**, *248*, 1299.

(10) Zhang, J.; Corman, R. E.; Schuh, J. K.; Ewoldt, R. H.; Shkrob, I. A.; Zhang, L. Solution Properties and Practical Limits of Concentrated Electrolytes for Nonaqueous Redox Flow Batteries. *J. Phys. Chem. C.* **2018**, *122*, 8159.

(11) Xing, X.; Liu, Q.; Xu, W.; Liang, W.; Liu, J.; Wang, B.; Lemmon, J. P. All-Liquid Electroactive Materials for High Energy Density Organic Flow Battery. *ACS Appl. Energy Mater.* **2019**, *2*, 2364.

(12) Milshtein, J. D.; Kaur, A. P.; Casselman, M. D.; Kowalski, J. A.; Modekrutti, S.; Zhang, P. L.; Attanayake, N. H.; Elliott, C. F.; Parkin, S. R.; Risko, C.; Brushett, F. R.; Odom, S. A. High Current Density, Long Duration Cycling of Soluble Organic Active Species for Non-Aqueous Redox Flow Batteries. *Energy Environ. Sci.* **2016**, *9*, 3531.

(13) Wang, J.; Hou, T. Recent Advances on Aqueous Solubility Prediction. *Comb. Chem. High Throughput Screen* **2011**, *14*, 328.

(14) Bergstrom, C. A. S.; Larsson, P. Computational Prediction of Drug Solubility in Water-Based Systems: Qualitative and Quantitative Approaches Used in the Current Drug Discovery and Development Setting. *International Journal of Pharmaceutics* **2018**, *540*, 185.

(15) Llinas, A.; Glen, R. C.; Goodman, J. M. Solubility Challenge: Can You Predict Solubilities of 32 Molecules Using a Database of 100 Reliable Measurements? *J. Chem. Inf. Model.* **2008**, *48*, 1289.

(16) Sevov, C. S.; Samaroo, S.; Sanford, M. S. Cyclopropenium Salts as Cyclable, High-Potential Catholytes in Nonaqueous Media. *Adv. Energy Mater.* **2016**, 1602027.

(17) Brethome, A. V.; Fletcher, S. P.; Paton, R. S. Conformational Effects on Physical-Organic Descriptors: The Case of Sterimol Steric Parameters. *ACS Catal.* **2018**, *9*, 2313.

(18) Harder, E.; Damm, W.; Maple, J.; Wu, C.; Reboul, M.; Xiang, J. Y.; Wang, L.; Lupyan, D.; Dahlgren, M. K.; Knight, J. L.; Kaus, J. W.; Cerutti, D. S.; Krilov, G.; Jorgensen, W. L.; Abel, R.; Friesner, R. A. OPLS3: A Force Field Providing Broad Coverage of Drug-like Small Molecules and Proteins. *J. Chem. Theory Comput.* **2016**, *12*, 281.

(19) Becke, A. D. Density-Functional Exchange-Energy Approximation with Correct Asymptotic Behavior. *Phys. Rev. A* **1988**, *38*, 3098.

(20) Zhao, Y.; Truhlar, D. G. The M06 Suite of Density Functionals for Main Group Thermochemistry, Thermochemical Kinetics, Noncovalent Interactions, Excited States, and Transition Elements: Two New Functionals and Systematic Testing of Four M06-Class Functionals and 12 Other Functionals. *Theor. Chem. Acc.* **2008**, *120*, 215.

(21) Weigend, F.; Ahlrichs, R. Balanced Basis Sets of Split Valence, Triple Zeta Valence and Quadruple Zeta Valence Quality for H to Rn: Design and Assessment of Accuracy. *Phys. Chem. Chem. Phys.* **2005**, *7*, 3297.

(22) Verloop, A.; Hoogenstraaten, W.; Tipker, J. *Development and Application of New Steric Substituent Parameters in Drug Design*; Academic Press: New York, 1976; Vol. VII.

(23) Santiago, C. B.; Guo, J.-Y.; Sigman, M. S. Predictive and Mechanistic Multivariate Linear Regression Models for Reaction Development. *Chem. Sci.* **2018**, *9*, 2398.

(24) Guo, J.-Y.; Minko, Y.; Santiago, C. B.; Sigman, M. S. Developoing Comprehensive Computational Parameter Sets to Describe the Performance of Pyridine-Oxazoline and Related Ligands. *ACS Catal.* **2017**, *7*, 4144.

(25) Models could also be developed using various combinations of these same parameters acquired from different conformer classes; however, the most robust model identified is presented (see experimental sections for complete details).

(26) Milshtein, J. D.; Fisher, S. L.; Breault, T. M.; Thompson, L. T.; Brushett, F. R. Feasibility of a Supporting-Salt-Free Nonaqueous Redox Flow Battery Utilizing Ionic Active Materials. *ChemSusChem* **2017**, *10*, 2080.

(27) Milshtein, J. D.; Barton, J. L.; Darling, R. M.; Brushett, F. R. 4-Acetamido-2,2,6,6-tetramethylpiperidine-1-oxyl as a Model Organic Redox Active Compound for Nonaqueous Redox Flow Batteries. *J. Power Sources* **2016**, *327*, 151.

(28) Barton, J. L.; Wixtrom, A. I.; Kowalski, J. A.; Brushett, F. R.; Spokoyny, A. M. Perfunctionalized Dodecaborate Clusters as Stable Metal-Free Active Materials for Charge Storage. *ChemRxiv Preprint* **2019**, DOI:10.26434/chemrxiv.7472921.v1.

(29) Hendriks, K. H.; Robinson, S. G.; Braten, M. N.; Sevov, C. S.; Helms, B. A.; Sigman, M. S.; Minteer, S. D.; Sanford, M. S. High-Performance Oligomeric Catholytes for Effective Macromolecular Separation in Nonaqueous Redox Flow Batteries. *ACS Cent. Sci.* **2018**, *4*, 189.

(30) Montoto, E. C.; Nagarjuna, G.; Moore, J. S.; Rodriguez-Lopez, J. Redox Active Polymers for Non-Aqueous Redox Flow Batteries: Validation of the Size-Exclusion Approach. *J. Electrochem. Soc.* **2017**, *164*, A1688.

(31) Nagarjuna, G.; Hui, J.; Cheng, K. J.; Lichtenstein, T.; Shen, M.; Moore, J. S.; Rodriguez-Lopez, J. Impact of Redox-Active Polymer Molecular Weight on the Electrochemical Properties and Transport Across Porous Separators in Nonaqueous Solvents. *J. Am. Chem. Soc.* **2014**, *136*, 16309.

(33) Doris, S. E.; Ward, A. L.; Baskin, A.; Frischmann, P. D.; Gavvalapalli, N.; Chenard, E.; Sevov, C. S.; Prendergast, D.; Moore, J. S.; Helms, B. A. Macromolecular Design Strategies for Preventing Active-Material Crossover in Non-Aqueous All-Organic Redox-Flow Batteries. *Angew. Chem. Int. Ed.* **2017**, *56*, 1595.

(33) Baran, M. J.; Braten, M. N.; Montoto, E. C.; Gossage, Z. T.; Ma, L.; Chenard, E.; Moore, J. S.; Rodriguez-Lopez, J.; Helms, B. A.

(34) MacroModel; version 11.7 ed.; Schrödinger, LLC: New York, NY, 2017.

(35) Harder, E.; Damm, W.; Maple, J.; Wu, C.; Reboul, M.; Xiang, J. Y.; Wang, L.; Lupyan, D.; Dahlgren, M. K.; Knight, J. L.; Kaus, J. W.; Cerutti, D. S.; Krilov, G.; Jorgensen, W. L.; Abel, R.; Friesner, R. A. *CJ. Chem. Theory Comput.* **2016**, *12*, 281.

(36) Becke, A. D. *Phys. Rev. A* **1988**, *38*, 3098.

(37) Lee, C.; Yang, W.; Parr, R. G. *Phys. Rev. B* **1988**, *37*, 785.

(38) Frisch, M. J. *et al. Gaussian 09, Revision D.01*; Gaussian, Inc.: Wallingford, CT, 2013.

(39) Zhao, Y.; Truhlar, D. G. *Theor. Chem. Acc.* **2008**, *120*, 215.

(40) Weigend, F.; Ahlrichs, R. *Phys. Chem. Chem. Phys.* **2005**, *7*, 3297.

(41) Ermanis, K.; Parkes, K. E. B.; Agback, T.; Goodman, J. M. *Org. Biomol. Chem.* **2016**, *14*, 3943.

(42) Piou, T.; Romanov-Michailidis, F.; Romanova-Michaelides, M.; Jackson, K. E.; Semakul, N.; Taggart, T. D.; Newell, B. S.; Rithner, C. D.; Paton, R. S.; Rovis, T. *J. Am. Chem. Soc.* **2017**, *139*, 1296.

(43) MATLAB and Statistics Toolbox Release 2017b, The MathWorks, Inc.: Natick, Massachusetts, United States.

(44) Guo, J.-Y.; Minko, Y.; Santiago, C. B.; Sigman, M. S. *ACS Catal.* **2017**, *7*, 4144.

(45) Freyer, J. L.; Brucks, S. D.; Gobieski, G. S.; Russell, S. T.; Yozwiak, C. E.; Sun, M.; CHen, Z.; Jiang, Y.; Bandar, J. S.; Stockwell, B. R.; Lambert, T. H.; Campos, L. M. *Angew. Chem. Int. Ed.* **2016**, *55*, 12382.

Chapter 3

Mechanism-Based Design of a High-Potential Catholyte Enables a 3.2 V All-Organic Non-Aqueous Redox Flow Battery

(published as *J. Am. Chem. Soc.* 2019, 141, 38, 15301–15306)

3.1. Introduction

Redox flow batteries (RFBs) are attractive targets for storing energy generated from intermittent renewable energy sources.[1,2] These batteries consist of solutions of redox active electrolytes (termed anolytes and catholytes) that store energy via reversible reduction of the anolyte and oxidation of the catholyte at inert electrodes. While aqueous RFBs have already been commercialized,[3,4] the energy density of these systems remains limited, largely due to the narrow stability window of water (<1.5 V). Organic solvents like acetonitrile have stability windows of >4 V;[5–8] as such, non-aqueous RFBs offer opportunities for dramatically enhanced energy densities. However, the move to non-aqueous systems presents numerous scientific challenges with respect to electrolyte chemistry.[9–11] One key obstacle is a lack of molecules that undergo reversible redox reactions at potentials approaching the anodic limit of acetonitrile (approximately +2 V versus Fc/Fc^+). To date, the highest potential molecules are ~1 V vs Fc/Fc^+.[12–24]

Tris(dialkyl)aminocyclopropenium (CP) cations (*e.g.*, $\mathbf{1}^+$) recently emerged as promising catholytes for non-aqueous RFBs (Figure 3.1).[25,26] The resonance-donating ability of the three amino substituents and their conjugation with the cyclic core impart numerous desirable properties on these molecules.[27–33] For instance, $\mathbf{1}^+$ undergoes a reversible, single-electron oxidation at relatively high potential (+0.86 V vs Fc/Fc^+). The resulting radical dication ($\mathbf{1}^{2+}$) exhibits high

shelf stability and undergoes electrochemical charge-discharge cycling with minimal loss of capacity over 200 cycles.[25] Compared to other widely studied non-aqueous RFB catholytes (for example, (2,2,6,6-tetramethylpiperidin-1-yl)oxyl (TEMPO)[14,34,35] and dialkoxybenzene derivatives),[36–38] **1**$^{+}$ offers significant advantages with respect to redox potential and/or electrochemical cyclability. However, as mentioned above, the anodic limit of the acetonitrile solvent is greater than 2 V vs Fc/Fc^{+}; as such, opportunities remain to identify catholytes with much higher redox potentials.[13] Herein, we demonstrate that a combination of computations, chemical synthesis, and mechanistic analysis can be used to rationally design a new class of catholytes (**2**$^{+}$) with dramatically higher redox potentials as well as promising cyclability (Scheme 3.1). These molecules are optimized by varying the substituent on sulfur I, and the best catholyte candidate is deployed in a proof-of-principle 3.2 V all-organic RFB.

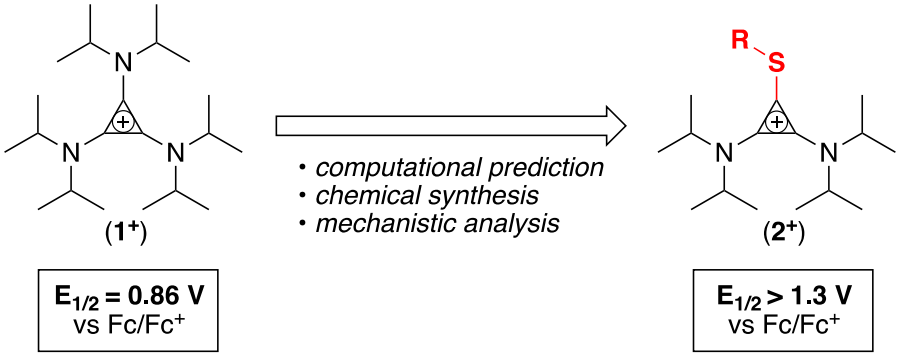

Scheme 3.1. Development of new high potential thiocy-clopropenium catholyte

3.2. Results and Discussion

As a first step, computational optimizations of the tris(dialkyl)aminocyclopropenium cation **1**$^{+}$ and the corresponding radical dication **1**$^{2+}$ were performed at the M06-2x/def2-TZVP level of theory with IEFPCM(acetonitrile) solvation. As described previously by Yoshida and Weiss,[27,28,30,31] the HOMO of **1**$^{+}$ and the SOMO of **1**$^{2+}$ show high symmetry and extensive resonance delocalization of electrons over the three nitrogen substituents (Figure 3.1A). As

summarized in Figure 3.1B, the three nitrogens and three cyclopropyl carbons have identical NBO and Mulliken charges. Furthermore, the spin densities in $\mathbf{1}^{2+}$ show that the radical is symmetrically delocalized across the three nitrogen atoms. The calculated redox potential for $\mathbf{1}^{+}$ (+0.82 V vs Fc/Fc^{+}) corresponds closely to the experimental value (+0.86 V vs Fc/Fc^{+}).

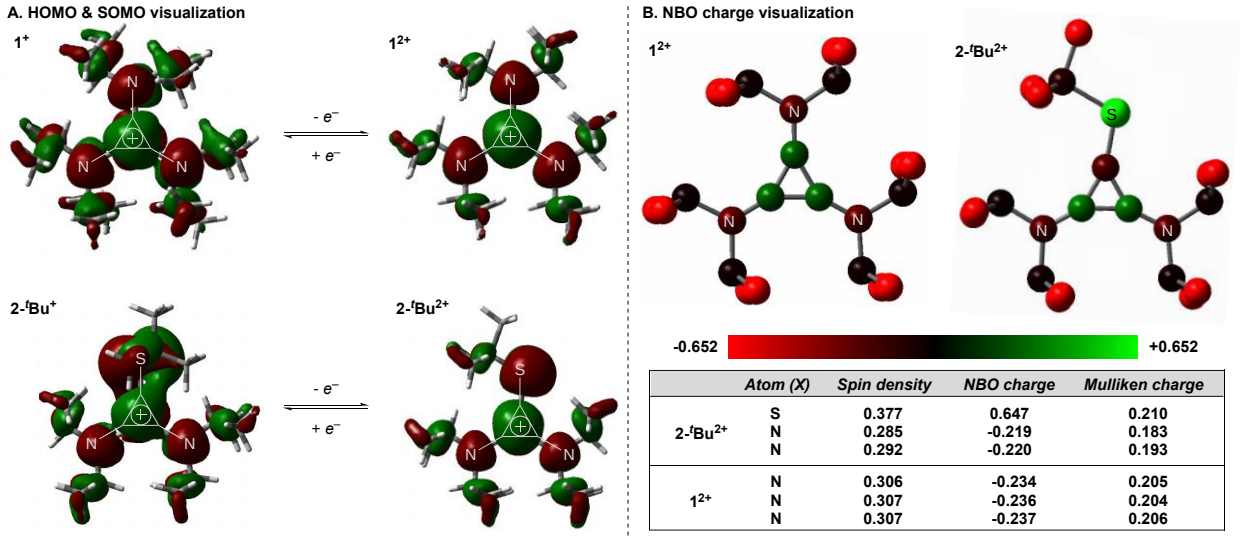

	Atom (X)	Spin density	NBO charge	Mulliken charge
$2\text{-}^{t}Bu^{2+}$	S	0.377	0.647	0.210
	N	0.285	-0.219	0.183
	N	0.292	-0.220	0.193
1^{2+}	N	0.306	-0.234	0.205
	N	0.307	-0.236	0.204
	N	0.307	-0.237	0.206

Figure 3.1. (A) HOMO and SOMO for $\mathbf{1}^{+}/\mathbf{1}^{2+}$ and $\mathbf{2}\text{-}^{t}\mathbf{Bu}^{+}/\mathbf{2}\text{-}^{t}\mathbf{Bu}^{2+}$. (B) Visualization of NBO charges for $\mathbf{1}^{2+}$ and $\mathbf{2}\text{-}^{t}\mathbf{Bu}^{2+}$ (hydrogens excluded for clarity), and tabulated values demonstrating differences in electronic symmetry between $\mathbf{1}^{2+}$ and $\mathbf{2}\text{-}^{t}\mathbf{Bu}^{2+}$

We hypothesized that replacing one strongly π-donating nitrogen with a weaker π-donating sulfur substituent[39] would result in an increase in the redox potential. This hypothesis was evaluated computationally by comparing **1** to the sulfur analogue $\mathbf{2}\text{-}^{t}\mathbf{Bu}^{+}$. As shown in Figure 3.1A, the HOMO of $\mathbf{2}\text{-}^{t}\mathbf{Bu}^{+}$ and the SOMO of $\mathbf{2}\text{-}^{t}\mathbf{Bu}^{2+}$ reflect the predicted electronic asymmetry induced by the introduction of sulfur. The electron density on sulfur in the HOMO of $\mathbf{2}\text{-}^{t}\mathbf{Bu}^{+}$ is significantly larger than that on either of the nitrogen atoms. Furthermore, the spin densities for $\mathbf{2}\text{-}^{t}\mathbf{Bu}^{2+}$ demonstrate that the sulfur has more radical character than either nitrogen. The NBO charges for $\mathbf{2}\text{-}^{t}\mathbf{Bu}^{2+}$ show that the sulfur is positively charged (+0.647) while the carbon attached to the sulfur

is negatively charged (-0.209). In contrast, the nitrogen atoms (-0.219) and other two cyclopropyl carbons (+0.282) possess similar NBO charges to those in $\mathbf{1}^{2+}$. Overall, this substitution has the predicted effect on redox potential, with the oxidation of $\mathbf{2\text{-}^{t}Bu}^{+}$ to $\mathbf{2\text{-}^{t}Bu}^{2+}$ calculated to occur at +1.34 V vs Fc/Fc^{+}. This constitutes a 480 mV increase relative to $\mathbf{1}^{+}/\mathbf{1}^{2+}$.[40]

Therefore, compound $\mathbf{2\text{-}^{t}Bu}^{+}$ was synthesized via the treatment of precursor **3**[41] with ^{t}BuSH in the presence of Net_3 (Figure 3.2A). The product was characterized by NMR spectroscopy, mass spectrometry, and cyclic voltammetry (CV). CV experiments were conducted using 5 mM solutions of $\mathbf{2\text{-}^{t}Bu}^{+}$ in 0.5 M Nbu_4PF_6/MeCN using a glassy carbon working electrode (0.07 cm^2, BASi) and a scan rate of 100 mV/s. Consistent with the DFT calculations, the oxidation of $\mathbf{2\text{-}^{t}Bu}^{+}$ occurs at a much higher potential than that of the parent compound $\mathbf{1}^{+}$, with a peak potential of +1.40 V vs Fc/Fc^{+}. However, as depicted in Figure 2B, this redox event is irreversible, suggesting that the radical dication $\mathbf{2\text{-}^{t}Bu}^{2+}$ is unstable.

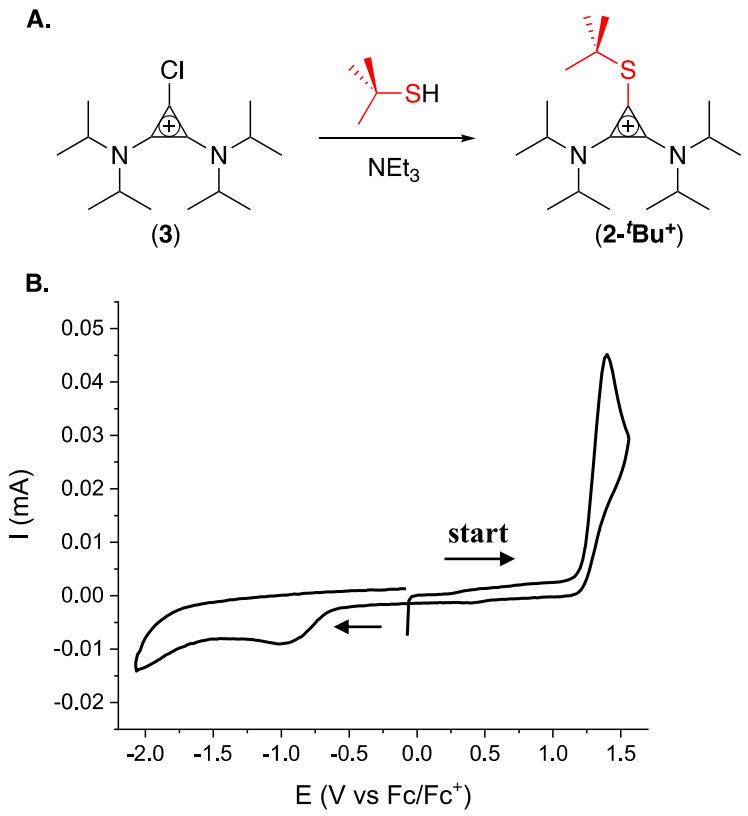

Figure 3.2. (A) Synthesis of **2-^{t}Bu$^+$**. (B) CV of **2-^{t}Bu$^+$** (5 mM in 0.5 M $TBAPF_6$/MeCN with a glassy carbon work-ing electrode (0.07 cm^2, BASi); 100 mV/s.

On the basis of reported studies of related compounds, we hypothesized that **2-^{t}Bu^{2+}** decomposes via S–C bond cleavage to release **4** and *tert*-butyl cation (Figure 3.3A).[42] Compound **4** then likely dimerizes to form **5**. To experimentally test for this possibility, we independently synthesized the proposed decomposition product **5**. Cyclic voltammetry of **5** shows a peak at around -1 V (Figure 3.3B) that is analogous to that observed in the CV of **2-^{t}Bu$^+$**. This provides support for the decay mechanism depicted in Figure 3.3A.

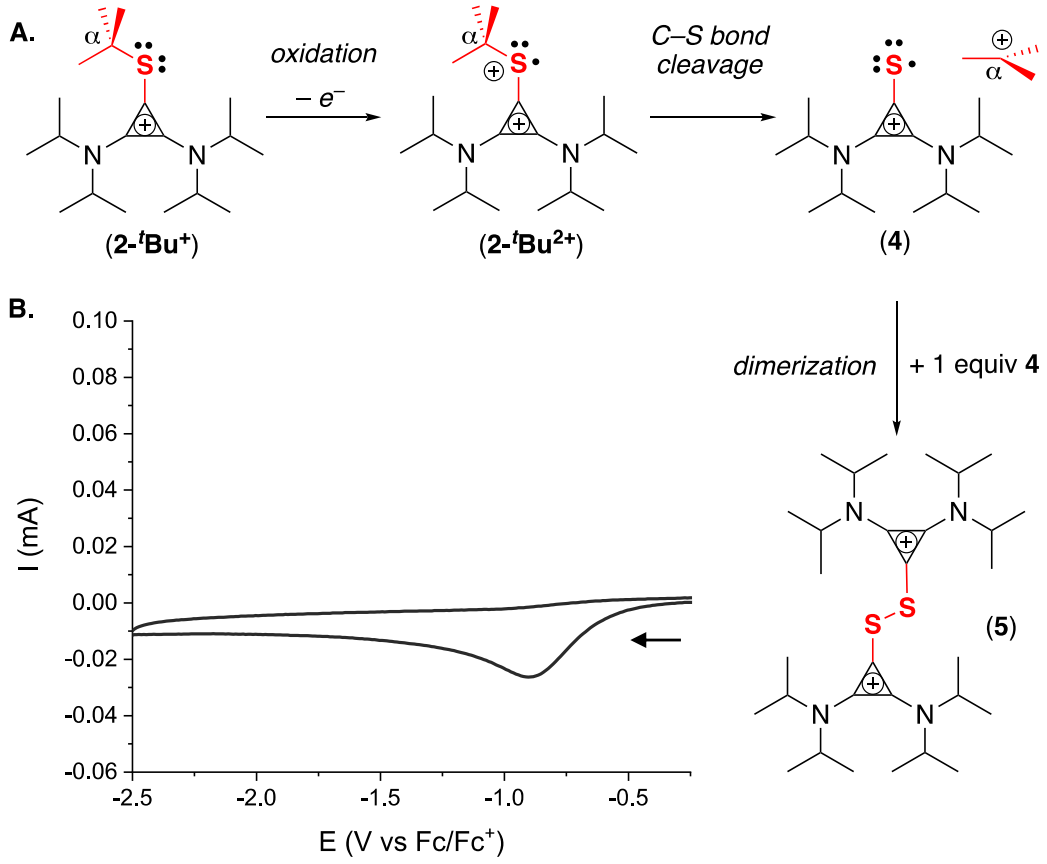

Figure 3.3. (A) Proposed decomposition pathway for **2-^{t}Bu^{2+}**. (B) CV of authentic sample of compound **5**

To mitigate this decomposition process, we next examined the derivatives **2-^{i}Pr$^+$**, **2-Oct$^+$**, and **2-Me$^+$** (Figure 3.4).[43] This series enables a direct comparison of 3º (**2-^{t}Bu$^+$**), 2º (**2-^{i}Pr$^+$**), 1º (**2-Oct$^+$**), and methyl (**2-Me$^+$**) substituents on sulfur. Founded on the proposed decomposition pathway, we anticipated that less substituted alkyl groups I would slow the decomposition of **2^{2+}** by raising the barrier for C–S cleavage to generate R^+ and **4**.[31] Consistent with this proposal, DFT calculations of the four radical dications demonstrate that the NBO charge at Cα decreases dramatically upon moving from 3º to 2º to 1º to methyl substitution (from -0.102 in **2-^{t}Bu^{2+}** to -0.758 in **2-Me^{2+}**; Figure 3.4). This suggests that there is significantly less carbocation character at

C_α in **2-Me**$^{2+}$ versus **2-**^{t}**Bu**$^{2+}$. Interestingly, despite these electronic changes, DFT predicts comparable redox potentials for all four derivatives, ranging from +1.32 to +1.43 V vs Fc/Fc^{+}.

Our calculations provide some insight into the insensitivity of redox potential to the alkyl substituent R. Although the identity of R has a substantial effect on the electron density at C_α in the radical dications, it has only a minor impact on the radical localization at sulfur in these oxidized species. As such, the relative energy difference between the cation and radical dication is comparable for these four molecules. It is worth noting that for the *tris*(dialkylamino)cyclopropenium analogues alkyl group substitution has a similarly modest impact on redox potential.[25]

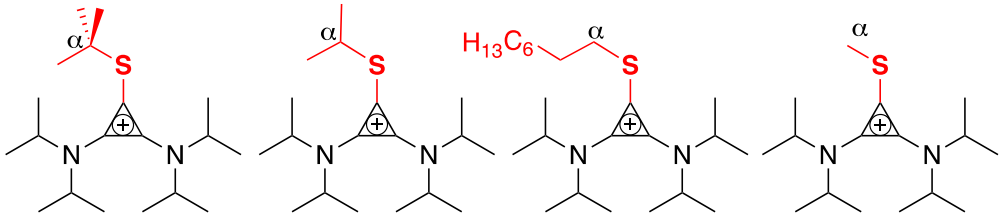

	(2-^{t}Bu^{+})	(2-^{i}Pr^{+})	(2-Oct^{+})	(2-Me^{+})
Redox potential (DFT)	+1.34 V	+1.34 V	+1.43 V	+1.32 V
NBO charge at C_α (DFT)	-0.102	-0.316	-0.509	-0.758

Figure 3.4. Derivatives to investigate impact of alkyl substitution on catholyte properties

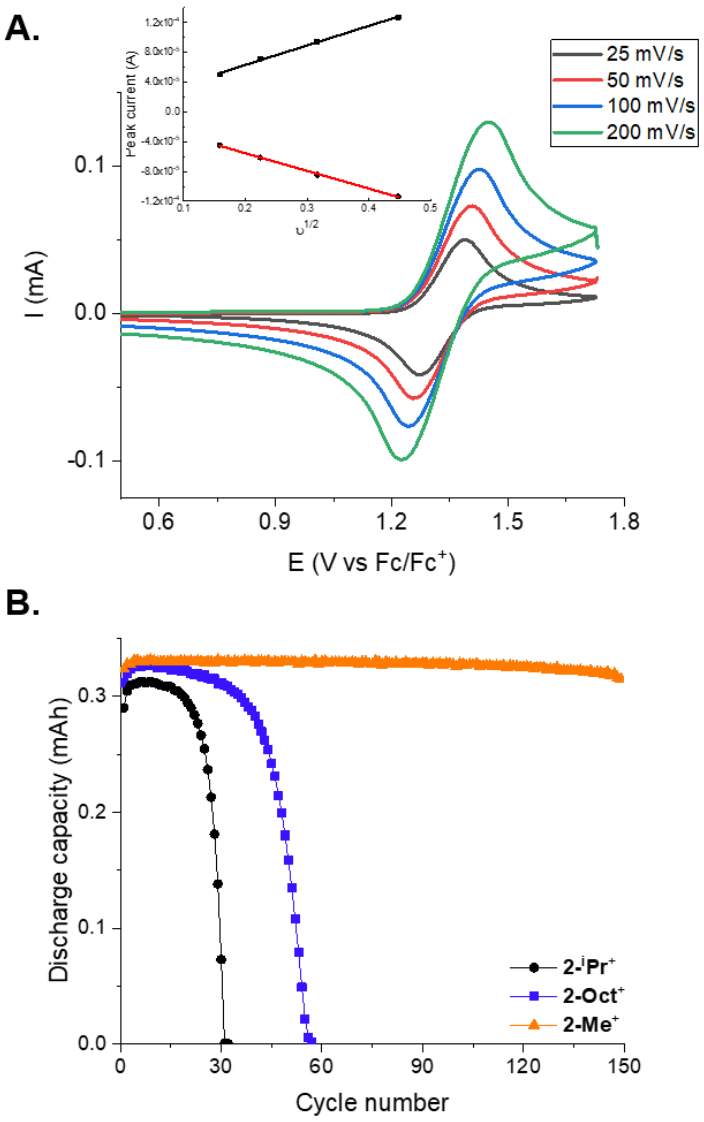

Figure 3.5. (A) Scan-rate dependent CVs of **2-^{i}Pr^{+}** (5 mM in 0.5 M $TBAPF_6$/MeCN). Inset: peak current versus square root of scan rate. (B) Capacity versus cycle number for bulk electrolysis cycling of **2-^{i}Pr^{+}**, **2-Oct^{+}**, and **2-Me^{+}** (5 mM in 0.5 M $TBAPF_6$/MeCN)

Electrochemical characterization of this series commenced with the isopropyl derivative **2-^{i}Pr^{+}**. As shown in Figure 3.5A, the scan rate-dependent CVs of **2-^{i}Pr^{+}** in 0.5 M $TBAPF_6$/acetonitrile show a quasi-reversible redox couple at +1.35 V versus Fc/Fc^{+}. This potential is within 10 mV of that predicted by DFT. Galvanostatic charge-discharge cycling of **2-^{i}Pr^{+}** (5

mM in 0.5 M $TBAPF_6$/acetonitrile) was conducted in a three-electrode H-cell separated with a fine glass frit with reticulated vitreous carbon (RVC) working and counter electrodes. Using a stability assessment protocol developed by Zhang *et al.*,[38,44] **2-^{i}Pr$^+$** was charged at 2.5 C to 50% theoretical capacity or until a voltage cutoff of 1.75 V was reached. Under these conditions, **2-^{i}Pr$^+$** underwent approximately 20 charge-discharge cycles in ~90% coulombic efficiency before the capacity began to fade (Figure 3.5B, black). The working side of the cell could no longer be charged/discharged after 30 cycles. CV of the solution after bulk electrolysis showed complete decomposition of **2-^{i}Pr$^+$** (Figure 3.7).

The mass transport and electrokinetics of **2-Me$^+$** were next evaluated. These properties are important for flow battery applications because fast diffusional and electron-transfer processes are critical for achieving high current densities and low overpotentials.[45] The diffusion coefficient was determined by varying the CV scan rate from 20 to 700 mV/s and then applying the Randles-Sevcik equation (Figure 3.7). The observed value of $(5.2 \pm 0.3) \times 10^{-6}$ cm^2 s^{-1} is comparable to that for other organic catholyte materials, including ferrocene derivative Fc1N112-TFSI (4.25×10^{-7} cm^2 s^{-1})[46] and dialkoxybenzene derivative DBMMB (5.77×10^{-6} cm^2 s^{-1}).[37] The heterogeneous electron-transfer rate was determined to be $(1.9 \pm 0.1) \times 10^{-3}$ cm s^{-1} using the Nicholson method[47] (Figure 3.9). This is very similar to that for a first generation CP [$(2.2 \pm 0.1) \times 10^{-3}$ cm s^{-1}][48] and comparable to that for other catholyte materials, including 5,10-dihydro-5,10-dimethyl phenazine (5.53×10^{-3} cm s^{-1})[12] and $V(acac)_3$ (6.5×10^{-4} cm s^{-1}).[45,49]

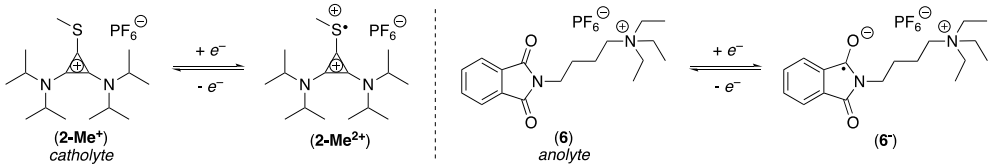

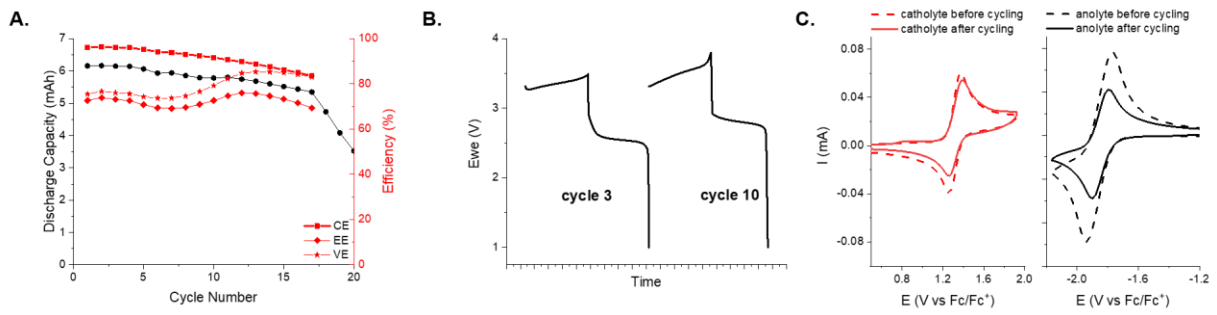

Figure 3.6. (A) Capacity and coulombic efficiency versus cycle number for a 3.2 V flow battery with **2-Me**$^+$/**5**. (B) Nernst curves for cycle 3 and cycle 10. (C) CV of spent anolyte and catholyte solutions after cycle 30.

Finally, we focused on deploying **2-Me**$^+$ in a full flow battery. As discussed above, a key advantage of non-aqueous RFBs is the large potential window of solvents like acetonitrile. However, due to a lack of suitable electrolytes, cell potentials of greater than 3 V have yet to be realized in an all-organic RFB.[50,51] To achieve this goal, it was critical to identify a low potential anolyte to pair with **2-Me**$^+$. After some investigation (see experimental sections for details), *N*-alkylphthalimide **6** was selected, based on its low redox potential (-1.85 V vs Fc/Fc$^+$) and reasonable compatibility with **2-Me**$^+$, as determined by CV (Figure 3.13).[37] This catholyte/anolyte pair was cycled in a Fumasep FAPQ-375-PP-separated asymmetric redox flow battery containing a 100 mM solution of **6** (anolyte) and a 50 mM solution of **2-Me**$^+$ (catholyte) in 0.5 M $TBAPF_6$/MeCN.[52,53] The flow cell contains graphite charge collecting plates with an interdigitated flow field, in combination with 400 µm thick carbon-felt electrodes. The electrolyte solutions were flowed through the cell at 10 mL/min and were subjected to galvanostatic cycling at 10 mA/cm^2, achieving 77% state of charge and an open circuit voltage of 3.2 V.[54] As shown in Figure 6A, the battery shows >86% capacity retention over 17 cycles with relatively high efficiency (columbic efficiency > 83%; energy efficiency > 70%; voltaic efficiency > 74%). However, rapid capacity

fade commenced at cycle 17, and 87% of the capacity was lost by cycle 30. Cyclic voltammetry was conducted on the spent anolyte and catholyte solutions after 30 cycles in order to assess the origin of the fade in this system. *As shown in Figure 6C, >90% of the catholyte **2-Me**$^+$ remained, indicating that this material is stable during the cycling experiment.* In contrast, ~42% of the CV signal associated with **6** was lost after cycling, and this was accompanied by the observation of one additional CV peak at ~0.3 V. These results demonstrate that capacity fade in this system is primarily driven by decay of the anolyte. Nonetheless, this experiment provides proof-of-principle that **2-Me**$^+$ delivers access to unprecedented high potential windows (>3 V), and ongoing work is focused on identifying more stable anolytes to pair with this molecule.

3.3. Conclusions

In summary, this article describes the development of a new high potential organic catholyte for non-aqueous RFBs. Mechanism-based design using a combination of theory and experiment enabled the identification of a methylthioether-substituted cyclopropenium (**2-Me**$^+$) that undergoes half-cell electrochemical cycling at nearly +1.4 V vs Fc/Fc$^+$. Pairing this material with an unoptimized organic anolyte enabled the demonstration of a 3.2 V all-organic non-aqueous flow battery.

3.4. Experimental Procedures and Characterization of Compounds

3.4.1 Synthesis

General Information: All commercial chemicals were used as received unless stated otherwise. Anhydrous DCM was obtained from an SDS solvent system. All reactions were performed under a nitrogen atmosphere unless stated otherwise. 1-Chloro-2,3-bis(diisopropylamino) cyclopropenium chloride[41], N-(N',N'-diethylaminobutyl)phthalamide[55] and **5**[43] were synthesized according to literature procedures. All other chemicals were purchased from commercial sources

and used as received. Solubility limits of compound **2-Me$^+$** were determined using a previously reported method.[25] Since 2-Me^{2+} was not stable for isolation (due to discharge to the parent compound in solution, vide infra) we could not obtain an exact solubility value for this compound. However, its solubility was measured to be >0.2 M in 0.5 M TBAPF6 acetonitrile (this estimate was based on a via bulk electrolysis of a 0.2 M solution to 100% SOC, which showed no precipitation). NMR spectra were obtained on Varian VNMRs 700, Varian VNMRs 500, Varian Inova 500, or Varian MR400 spectrometers. ^{1}H and ^{13}C chemical shifts are reported in parts per million (ppm) relative to TMS, with the residual solvent peak used as an internal reference. High resolution mass spectroscopy was performed on a Micromass AutoSpec Ultima Magnetic Sector Mass Spectrometer using ESI.

General procedure for synthesis of 2-^{t}Bu$^+$, 2-^{i}Pr$^+$, 2-Oct$^+$. A solution of 1-chloro-2,3-bis(diisopropylamino)cyclopropenium chloride[41] (0.5 mmol, 1 equiv) and triethylamine (1.5 mmol, 3 equiv) in DCM (5 mL) was cooled to 0 °C, and the appropriate thiol (0.75 mmol, 1.5 equiv) was added dropwise. After stirring for 15 min, the reaction mixture was allowed to warm to room temperature and then heated at 45 °C for 16 h. The resulting solution was washed with a 1:1 solution of brine and 2 M HCl (10 mL). The aqueous layer was further extracted with dichloromethane (2 × 15 mL), and the combined organic fractions were concentrated under vacuum. The resulting residue was dissolved in water (5 mL), and an aqueous solution of ammonium hexafluorophosphate (334 mg, 2 mmol in 2 mL H_2O) was added with vigorous stirring. A white precipitate formed, and this material was extracted into dichloromethane (3 × 15 mL). The organic extracts were dried over $MgSO_4$ and concentrated under vacuum. The product was then purified by chromatography on silica gel with gradient elution (1-8% acetonitrile in dichloromethane).

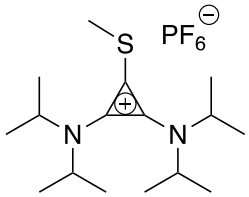

Synthesis of **2-Me$^+$.** Bis-diisopropylaminocyclopropenethione[43] (237 mg, 0.88 mmol, 1 equiv) was dissolved in neat dimethyl sulfate (0.12 mL, 1.3 mmol, 1.5 equiv) and the resulting mixture was stirred at 25 ºC for 2 h. Dichloromethane (5 mL) was added. With vigorous stirring, an aqueous solution of ammonium hexafluorophosphate (334 mg, 2 mmol in 2 mL of H_2O) was added. A white precipitate formed, and this material was extracted into dichloromethane (3 × 15 mL). The organic extracts were dried over $MgSO_4$ and concentrated under vacuum. The product was then purified by chromatography on silica gel with gradient elution (1-8% acetonitrile in dichloromethane). Product 2-Me was obtained as a white powder (287 mg, 76% yield). R_F = 0.30 in 10% acetonitrile/ dichloromethane. Mp = 222-224 ºC. ^{1}H NMR (700 MHz, CD_3NO_2 at 90 ºC) δ 4.13 (hept, *J* = 6.8 Hz, 4H), 2.78 (s, 3H), 1.45 (dd, *J* = 6.8, 1.5 Hz, 24H). ^{13}C NMR (700 MHz, CD_3NO_2 at 90 ºC) δ 134.21, 105.73, 52.83, 20.36, 15.75. HRMS (ESI) *m/z* calcd for $C_{16}H_{31}N_2S$ $(M - PF_6)^+$: 283.2202, found 283.2197.

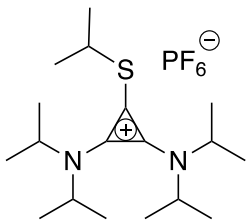

Synthesis of **2-^{i}Pr$^+$:** Prepared by general procedure using isopropyl thiol, followed by ion-exchange with NH_4PF_6 to yield a white powder (110 mg, 50% yield). R_F = 0.32 in 10% acetonitrile/ dichloromethane. Mp = 123-125 ºC. ^{1}H NMR (700 MHz, CD_3NO_2 at 90 ºC) δ 4.15 (hept, *J* = 6.8

Hz, 4H), 3.92 (hept, *J* = 6.7 Hz, 1H), 1.48 (d, *J* = 6.7, 1.5 Hz, 6H), 1.46 (d, *J* = 6.8, 1.6 Hz, 24H). ^{13}C NMR (700 MHz, CD_3NO_2 at 90 ºC) δ 135.75, 103.80, 52.93, 40.38, 22.68, 20.44. HRMS (ESI) *m/z* calcd for $C_{18}H_{35}N_2S$ $(M - PF_6)^+$: 311.2515, found 311.2487.

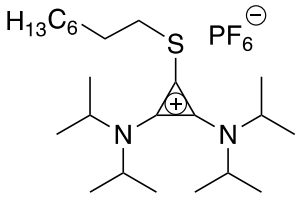

Synthesis of **2-Oct$^+$:** Prepared by general procedure using 1-octanethiol, followed by ion-exchange with NH_4PF_6 to yield a white powder (122.4 mg, 47% yield). R_F = 0.40 in 10% acetonitrile/ dichloromethane. Mp = 59-62 ºC. ^{1}H NMR (700 MHz, CD_3NO_2 at 90 ºC) δ 4.14 (hept, *J* = 6.9 Hz, 4H), 3.28 (t, *J* = 7.3 Hz, 2H), 1.81 (m, 2H), 1.53 (m, 2H), 1.45 (m, 24H), 1.37 (m, 8H), 0.91 (t, *J* = 6.9 Hz, 3H). ^{13}C NMR (700 MHz, CD_3NO_2 at 90 ºC) δ 134.90, 104.79, 52.76, 34.24, 31.33, 29.70, 28.59, 28.50, 27.88, 22.09, 20.44, 12.80. HRMS (ESI) *m/z* calcd for $C_{23}H_{45}N_2S$ $(M - PF_6)^+$: 381.3298, found 381.3294

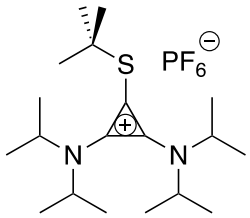

Synthesis of **2-^{t}Bu$^+$:** Prepared by general procedure using 2-methyl-2-propanethiol, followed by ion-exchange with NH_4PF_6 to yield a white powder (148 mg, 64% yield). R_F = 0.32 in 10% acetonitrile/ dichloromethane. Mp = 120-122 ºC. ^{1}H NMR (401 MHz, CD_3NO_2) δ 4.21 (hept, *J* = 6.8 Hz, 4H), 1.53 (s, 9H), 1.43 (d, *J* = 6.8 Hz, 24H). ^{13}C NMR (500 MHz, CD_3NO_2) δ 139.01, 99.22, 53.50, 52.55, 31.19, 20.14. HRMS (ESI) *m/z* calcd for $C_{20}H_{39}N_2S$ $(M - PF_6)^+$: 325.2672, found 325.2670.

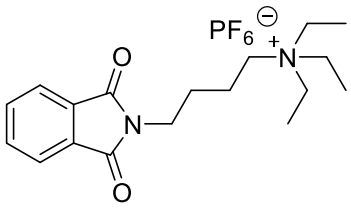

Synthesis of **6.** In a nitrogen-filled box, N-(N',N'-diethylaminobutyl)phthalimide[55] (548 mg, 2 mmol, 1 equiv) was dissolved in dichloromethane (5 mL). Triethyloxonium tetrafluoroborate (570 mg, 3 mmol, 1.5 equiv) was added, and the resulting mixture was stirred for 2 h at room temperature. With vigorous stirring, an aqueous solution of ammonium hexafluorophosphate (640 mg, 4 mmol in 3 mL H_2O) was added. After 1 hour, the reaction mixture was extracted with a solution of 2.5 % acetonitrile in dichloromethane (3 x 10 mL). The organic extracts were dried over $MgSO_4$ and concentrated under vacuum. The product was recrystallized three times from from MeCN/diethyl ether to afford 5 as a white powder (760 mg, 85% yield). Mp = 169-172 ºC. ^{1}H NMR (401 MHz, CD_3CN) δ 7.88-7.77 (m, 4H), 3.67 (t, *J* = 6.4 Hz, 2H), 3.21-3.05 (m, 8H), 1.68 (m, 4H), 1.20 (tt, *J* = 7.2, 1.9 Hz, 9H). ^{13}C NMR (401 MHz, CD_3CN) δ 168.46, 134.21, 132.28, 122.87, 56.38, 52.77, 36.82, 25.09, 18.82, 6.76.

3.4.2 Comparison of catholyte material

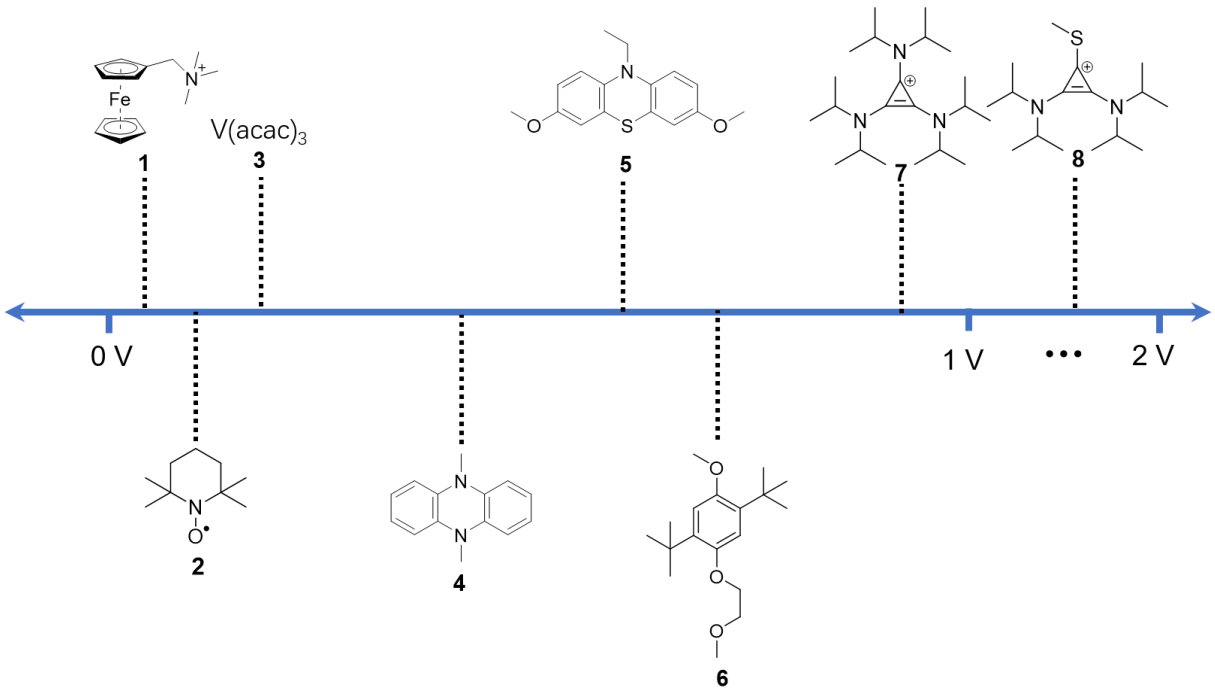

Compound	Redox Potential	Cyclability	Solubility
1[56]	0.27 V vs . Fc/Fc^+	91.8% capacity at 100 cycles	neutral: 0.98 M in pure MeCN
2[14]	0.3 V vs Ag/Ag^+	82% capacity at 100 cycles	neutral: 5.2 M in EC/PC/EMC
3[57,21]	0.45 V vs Ag/Ag^+	< 20% capacity at 10 cycles	Neutral: 0.58 M in MeCN
4[12]	1^{st}: -0.15 V; 2^{nd} : 0.6 V vs Ag/Ag^+	90% capacity at 80 cycles	neutral: 60 mM in pure MeCN
5[20]	1^{st}: 0.068 V; 2^{nd} : 0.63 V vs Fc/Fc^+	93% capacity at 50 cycles	neutral: 0.05 M; cation: 0.15 M; dication: 0.1 M in 1 M LiTFSI in PC
6[38]	0.69 V vs Ag/Ag^+	75% capacity at 30 cycles	Oil
7[25]	0.82 V vs Fc/Fc^+	>97% capacity at 200 cycles	cation: 1.5 M, dication: 0.081 M in pure MeCN
8	1.33 V vs Fc/Fc^+	90% capacity at 156 cycles	cation: 0.58 M in pure MeCN, dication: > 0.2 M in 0.5 M Nbu_4PF_6

Table 3.1. An overview of representative published catholytes

3.4.3 Electrochemical experiments

General

Acetonitrile (99.8%, anhydrous) was obtained from Sigma Aldrich and used as received. Tetrabutylammonium hexafluorophosphate (electrochemical grade) was obtained from Sigma Aldrich and was dried under high vacuum for 48 h before being transferred to a nitrogen-filled glovebox. A 0.5 M stock solution of the supporting electrolyte in acetonitrile was prepared in a N_2-filled glovebox and was dried over 3Å molecular sieves for at least two days prior to use. A Fumasep® FAP-375-PP membrane was obtained from Fumatech and was ion-exchanged in saturated KPF_6 and then dried under high vacuum overnight before use.

Cyclic Voltammetry. Cyclic voltammetry was performed in a nitrogen-filled glovebox with a Biologic VSP multichannel potentiostat/galvanostat using a three-electrode electrochemical cell, consisting of a glassy carbon disk working electrode (0.07 cm^2, BASi), a Ag/Ag^+ quasi-reference electrode (BASi) with 0.01 M $AgBF_4$ (Sigma) in acetonitrile, and a platinum wire counter electrode (ALS). The glassy carbon disk electrode was polished in a nitrogen-filled glovebox using aluminum oxide polishing paper (9 micron and 0.3 micron, Fiber Instrument) and anhydrous acetonitrile. All experiments were conducted in a 0.5 M Nbu_4PF_6 stock electrolyte solution.

Half-cell cycling. Charge/discharge measurements were carried out in a nitrogen-filled glovebox with a BioLogic VSP galvanostat in a custom glass H-cell with reticulated vitreous carbon electrodes (100 ppi, ~70 cm^2 surface area, Duocell). An Ag/Ag^+ quasi-reference electrode (BASi) with 0.01 M $AgBF_4$ was used on the working side of the H-cell. A porous glass frit (P5, Adams and Chittenden) was used as the separator. The electrolyte contained 5 mM active species and 0.5 M Nbu_4PF_6 in acetonitrile. The working chamber of the H-cell was loaded with 5 mL of the electrolyte solution, and the counter side was loaded with 5 mL of a solution containing methyl viologen hexafluorophosphate. Both chambers were stirred continuously during cycling at a current of 5 mA. Voltage cutoffs of +1.75 V and +0.5 V were employed.

Flow Cell Cycling. Cycling under flow conditions was performed with a zero-gap flow cell comprised of graphite charge collecting plates containing an interdigitated flow field in combination with two layers of non-woven carbon felt electrodes (Sicracet 29AA) on each side. ePTFE gaskets were used to achieve ~20% compression of the felt. A Fumasep® FAP-375-PP anion-exchange membrane separated the two half cells, and the exposed area of the membrane in the gasket window was used as the active area (2.55 cm^2). After assembly, the catholyte side of the cell was loaded with a 0.05 M solution of 2-Me^+ in 0.5 M Nbu_4PF_6/acetonitrile and the anolyte side of the cell was loaded with a 0.1 M solution of 6 in 0.5 M Nbu_4PF_6/acetonitrile. The cell was pretreated by continuously flowing the solution above at 10 mL/min for 1 h without any charging process using a peristaltic pump (Cole-Parmer) with Solveflex and PFA tubing. After this step, using the same flow rate, galvanostatic charge/discharge cycling was performed using a BioLogic VSP galvanostat employing a charging current of 10 mA/cm^2 and a discharging current of -10 mA/cm^2 with +3.8 V and 1 V voltage limits.

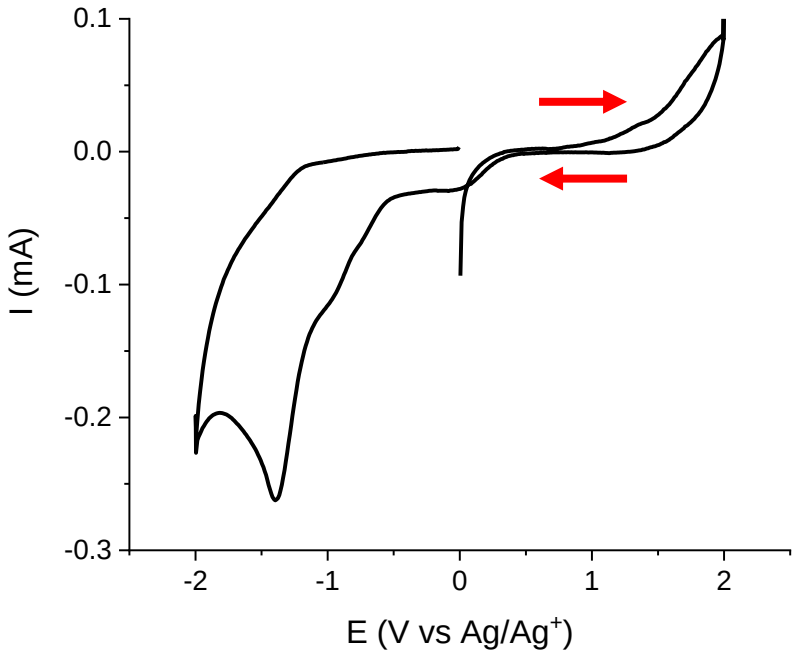

Figure 3.7. CV of **2-^{i}Pr^{+}** after 80 cycles of charge-discharge cycling in an H-Cell

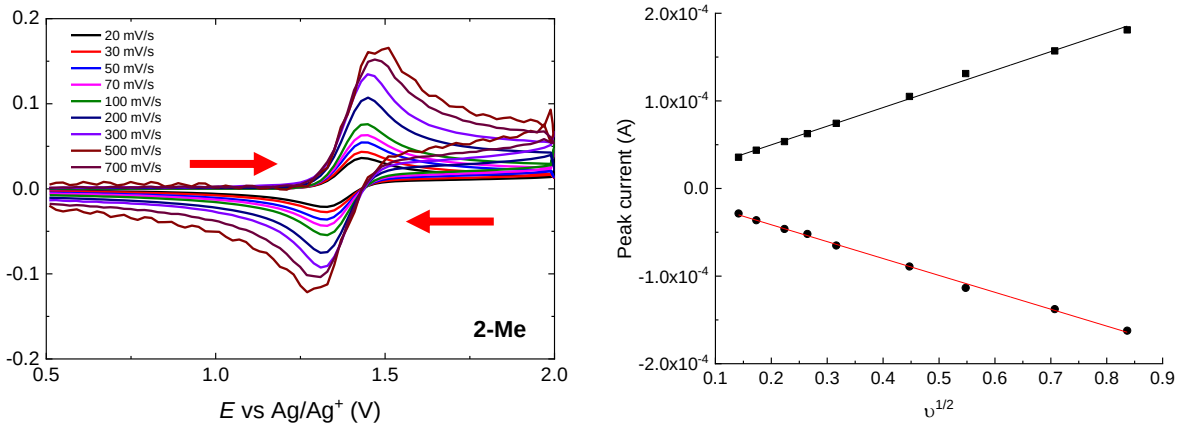

Figure 3.8. Cyclic voltammograms at various scan rates for **2-Me** (left). Peak current vs square root of the scan rate and linear fits used to determine diffusion coefficients (right).

Diffusion coefficients were determined by varying the scan rate of the cyclic voltammetry measurements between 20 and 700 mV/s (Figure 3.8, left). Plotting the cathodic and anodic peak height currents versus the square root of the scan rate showed a linear relationship, indicating a

transport-limited redox process (Figure 3.8, right). The slope of this linear relation was used in the Randles-Sevcik equation (*1*) to determine the diffusion coefficients.

$$i_p = 0.4463\, nFAC\sqrt{\frac{nF\nu D}{RT}} \qquad (1)$$

With i_p the peak current in A, *n* the number of electrons transferred, F equals Faraday's constant, A the area of the electrode in cm^2, C the concentration of redox active species in mol cm^{-3}, D the diffusion coefficient in $cm^2\ s^{-1}$, v the scan rate in V s^{-1}, R the gas constant and T the temperature in K.

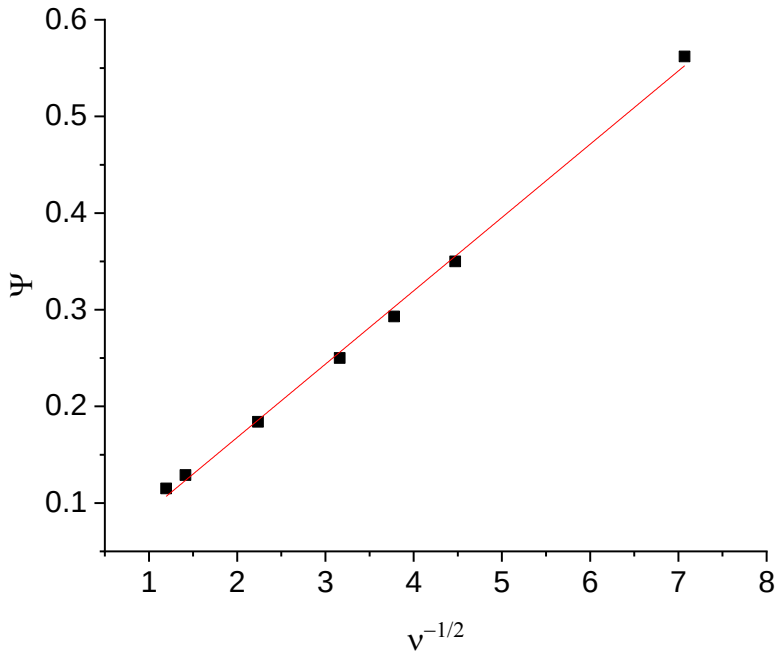

Figure 3.9. Plot of Ψ versus inverse of the scan rate. Linear fit used to determine heterogeneous electron transfer rates

Heterogeneous electron transfer rates were determined following the Nicholson method.[58] In short, the peak separations between the cathodic and anodic peaks at various scan rates were fitted to a

working curve. Plotting the resulting values of Ψ versus the inverse of the scan rate (Figure 3.9) gave a linear relationship from which the slope was used to determine k_0 according to (*2*).

$$\Psi = \frac{\gamma k_0}{\sqrt{\pi a D_0}} \quad (2)$$

Anolyte identification. Cyclic voltammograms of a 1:1 mixture of **2-Me** and anolyte molecules were acquired under the following conditions: 5 mM **1-Me**, 5 mM anolyte in 0.5 M Nbu_4PF_6 in MeCN. The experiments were performed in a nitrogen-filled glovebox with a Biologic VSP multichannel potentiostat/galvanostat using a three-electrode electrochemical cell, consisting of a glassy carbon disk working electrode (0.07 cm2, BASi), a Ag/Ag^+ quasi-reference electrode (BASi) with 0.01 M $AgBF_4$ (Sigma) in acetonitrile, and a platinum wire counter electrode (ALS). The glassy carbon disk electrode was polished in a nitrogen-filled glovebox using aluminum oxide polishing paper (9 micron and 0.3 micron, Fiber Instrument) and anhydrous acetonitrile. The scan rate is 100 mV/s. These experiments were conducted to preliminarily screen for compatible anolytes (i.e., those that maintain CV peaks associated with both the anolyte and catholyte under these conditions).

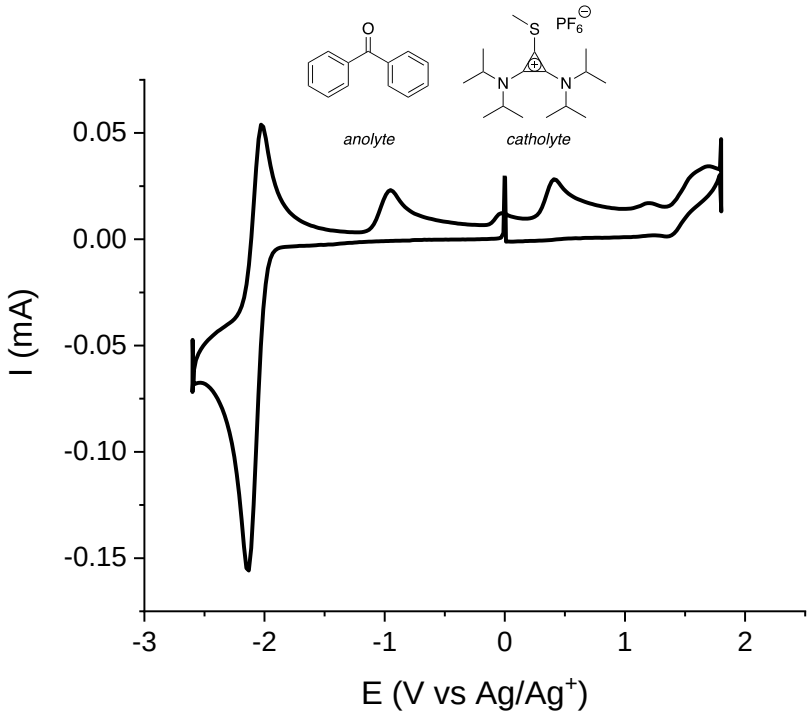

Figure 3.10. CV of a **2-Me**$^{+}$ and benzophenone, demonstrating that this catholyte/anolyte pair is incompatible

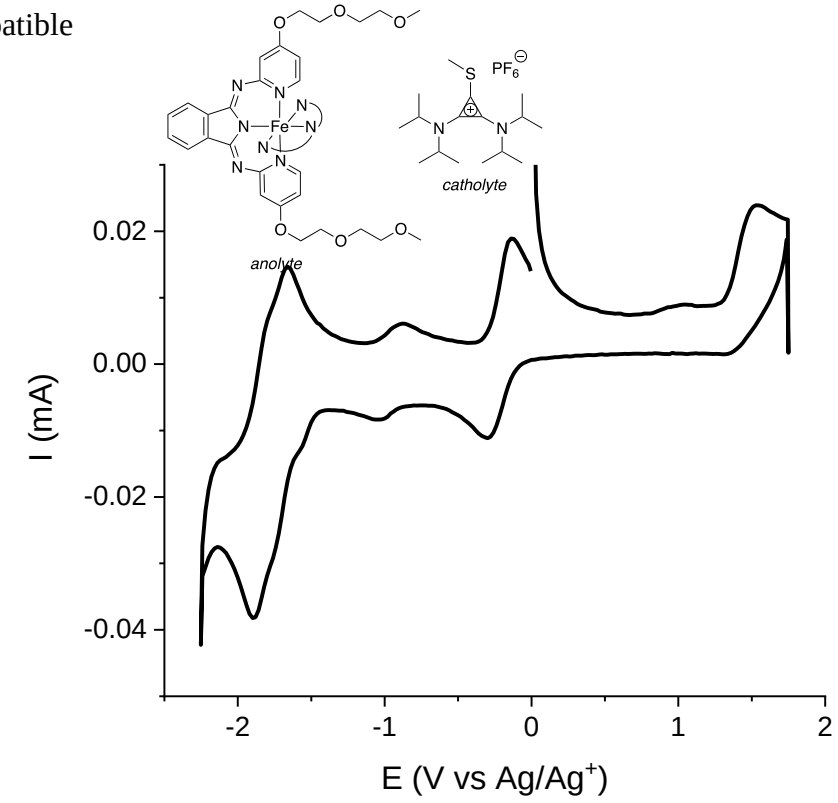

Figure 3.11. CV of **2-Me**$^{+}$ and Fe-based anolyte[59] demonstrating that this catholyte/anolyte

pair is incompatible

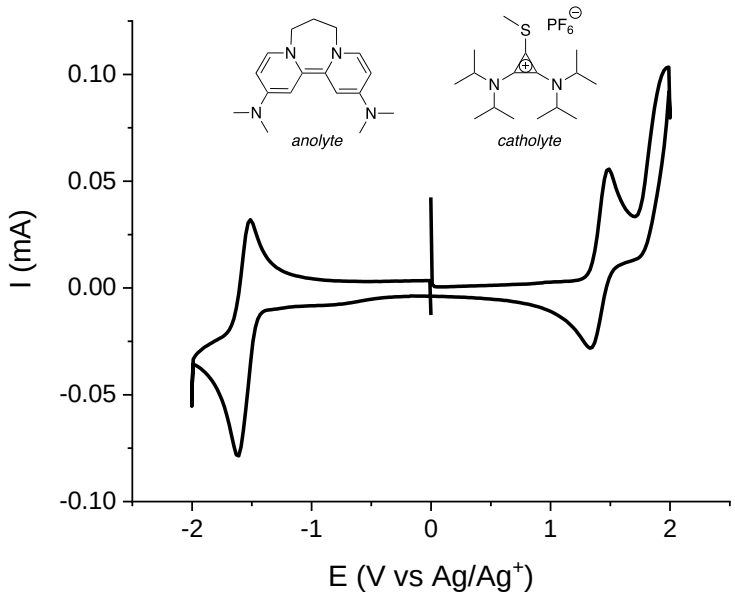

Figure 3.12. CV of **2-Me**$^{+}$ and 4,4'-bis(dimethylamino)-bispyridinylidene,[60] demonstrating that this catholyte/anolyte pair is moderately compatible. 4,4'-bis(dimethylamino)-bispyridinylidene has a very close irreversible oxidation peak to our catholyte 2-Me^{+}. As 4,4'-bis(dimethylamino)-bispyridinylidene is a neutral compound and the anion-exchange membrane would not be able to separate two electrolytes well. A 1:1 catholyte/anolyte mixture solution would be used for this case and that would lead to easily charging of the irreversible oxidation peak of 4,4'-bis(dimethylamino)-bispyridinylidene.

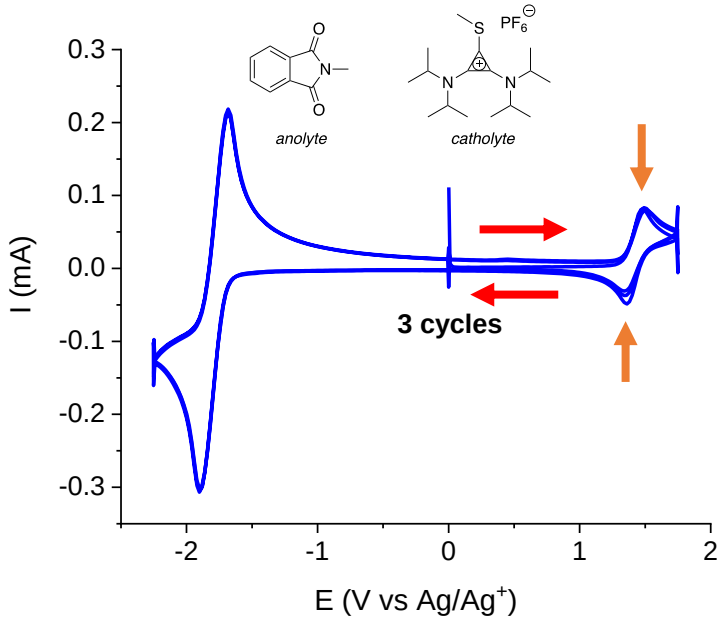

Figure 3.13. CV of **2-Me**$^{+}$ (5 mM) and *N*-methylphthalimide (10 mM) (3 cycles), demonstrating that this catholyte/anolte pair is moderately compatible. The peak current of catholyte slowly decreased within 3 continuous CV cycles with the presence of anolyte in the same solution.

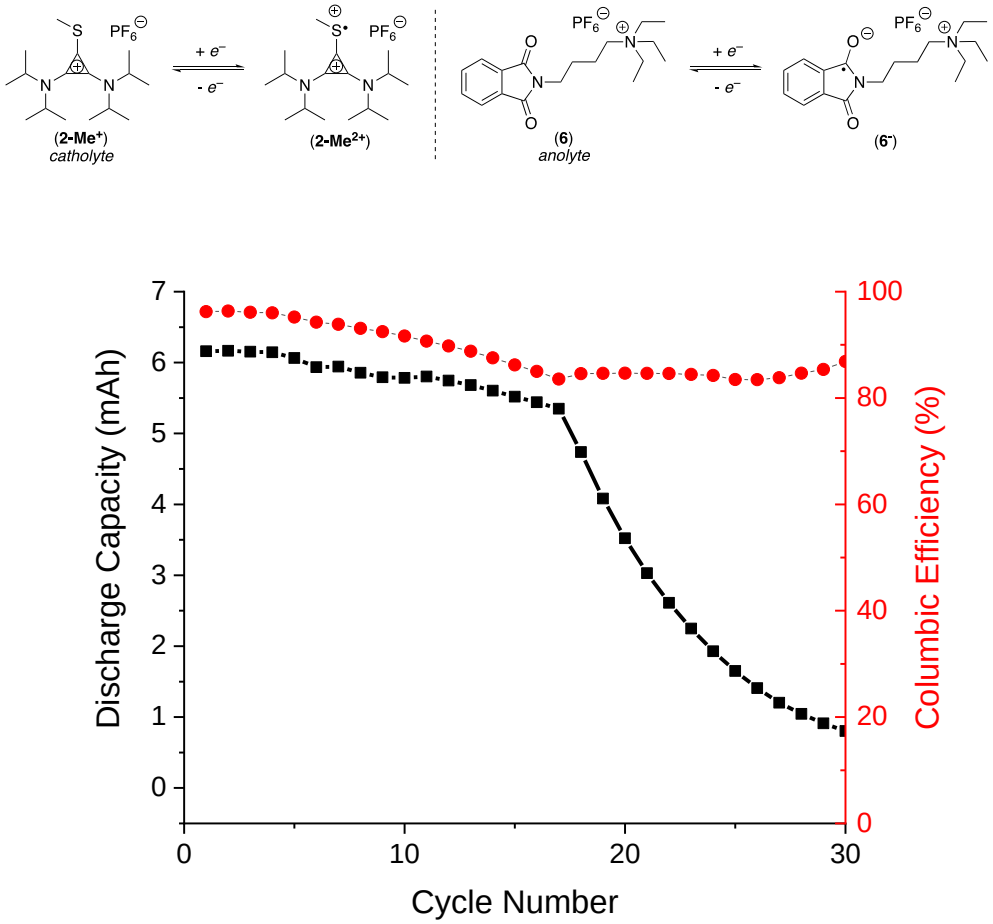

Figure 3.14. Full cycling performance of the asymmetric battery

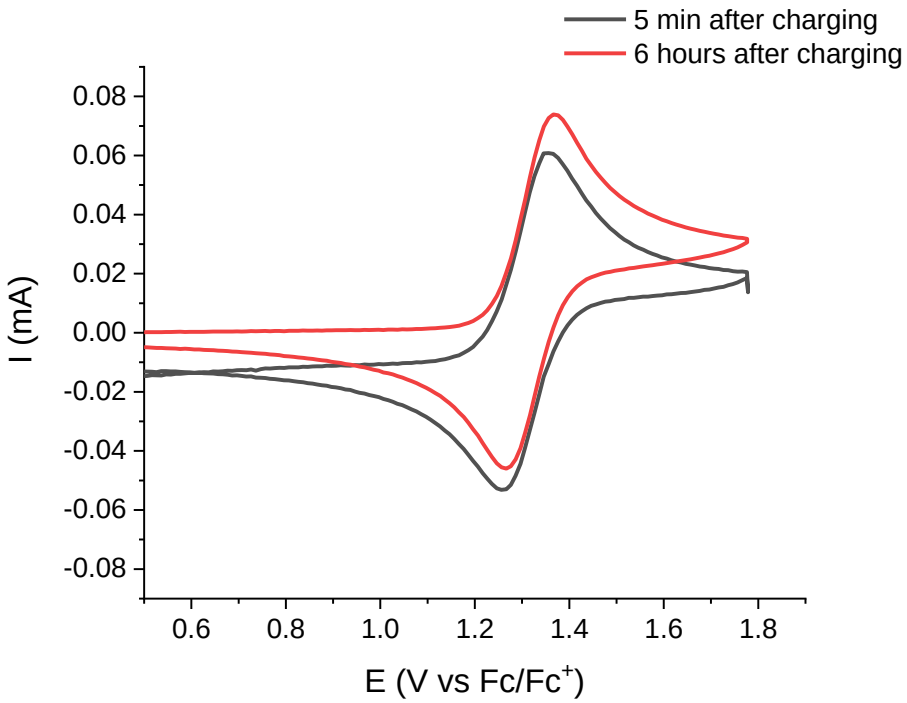

Figure 3.15. Shelf life study of **2-Me**$^{+}$ (5 mM of **2-Me**$^{+}$ in 0.5 M $TBAPF_6$ was charged to 100% SOC in an H-cell and the solution was stored in a Teflon vial; active species concentration was monitored by CV. The color of **2-Me**$^{2+}$ faded after about 6 h (with the solution changing from violet to colorless), indicating loss of **2-Me**$^{2+}$. However, the CV shows no obvious decomposition.

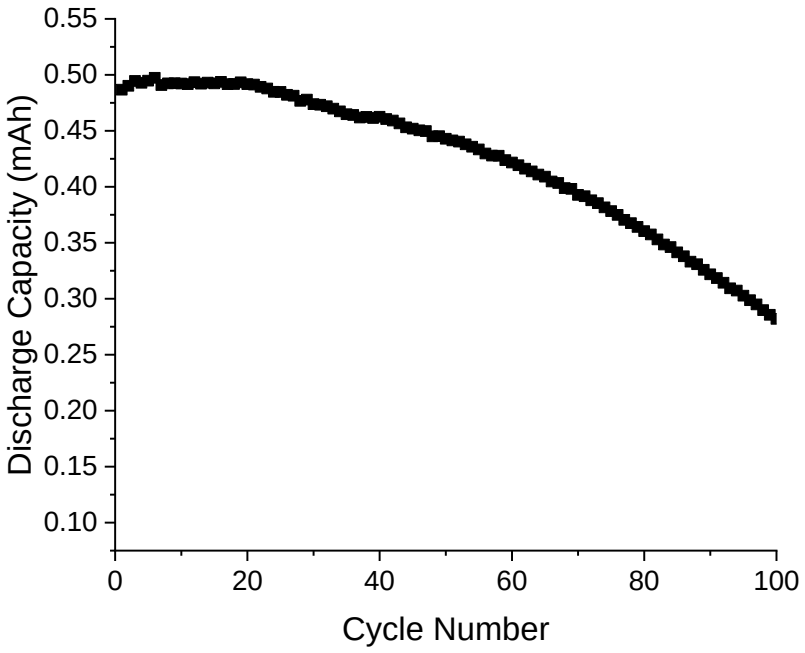

Figure 3.16. Discharge capacity versus cycle number for **2-Me**$^{+}$ at 75% theoretical capacity cut-off in an H-cell

H-cell cycling performance comparison

H-cell experiments were conducted using the procedure reported by Shkrob *et al*. Details can be found in their recent paper.[23] A brief comparison of some published catholyte materials tested by this method is provided below.

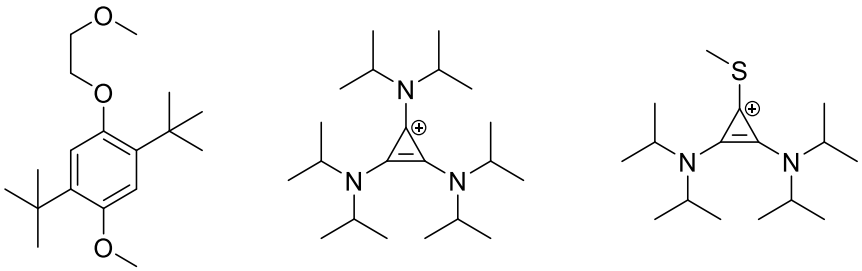

1 **2** **3**

Compound	Redox Potential	N_{90}*
1[23,37,38]	0.69 V vs Ag/Ag^+	64
2[25]	0.84 V vs Fc/Fc^+	682
3	1.33 V vs Fc/Fc^+	156

Table 3.2. H-cell cycling performance comparison

*N_{90} = cycle number at 90% original capacity

3.4.4 Computational Methods

Conformational searches were performed with MacroModel version 11.7[61] and the OPLS3 force field.[62] All conformers within 10 kJ/mol relative to the minimum were optimized with DFT. All structures were optimized in the gas-phase with the B3LYP density functional[63,64] and the 6-31G(d) basis set as implemented in Gaussian09 (revision D.01).[65] Single point energies were performed on these geometries with the M06-2X density functional[66] and the triple-ζ valence quality def2-TZVP basis set of Weigend and Ahlrichs.[67] This energy was used to identify the lowest energy

conformer, which was then re-optimized with IEFPCM(acetonitrile) solvation with the M06-2X density functional and the triple-ζ valence quality def2-TZVP basis set. All of the optimized geometries were verified by frequency computations as minima (zero imaginary frequencies). Gaussian input files were written using a Python script.[68] Oxidation potentials were calculated according to a previously reported method using the free energies obtained from the oxidized and reduced optimized structures.[69]

3.5 References

(1) Rugolo, J.; Aziz, M. J. Electricity Storage for Intermittent Renewable Sources. *Energy Environ. Sci.* **2012**, *5* (5), 7151–7160. https://doi.org/10.1039/C2EE02542F.

(2) Barnhart, C. J.; Dale, M.; Brandt, A. R.; Benson, S. M. The Energetic Implications of Curtailing versus Storing Solar- and Wind-Generated Electricity. *Energy Environ. Sci.* **2013**, *6* (10), 2804–2810. https://doi.org/10.1039/C3EE41973H.

(3) Dunn, B.; Kamath, H.; Tarascon, J.-M. Electrical Energy Storage for the Grid: A Battery of Choices. *Science* **2011**, *334* (6058), 928–935. https://doi.org/10.1126/science.1212741.

(4) Soloveichik, G. L. Flow Batteries: Current Status and Trends. *Chem. Rev.* **2015**, *115* (20), 11533–11558. https://doi.org/10.1021/cr500720t.

(5) Wang, W.; Luo, Q.; Li, B.; Wei, X.; Li, L.; Yang, Z. Recent Progress in Redox Flow Battery Research and Development. *Adv. Funct. Mater.* **2013**, *23* (8), 970–986. https://doi.org/10.1002/adfm.201200694.

(6) Leung, P.; Li, X.; León, C. P. de; Berlouis, L.; Low, C. T. J.; Walsh, F. C. Progress in Redox Flow Batteries, Remaining Challenges and Their Applications in Energy Storage. *RSC Adv.* **2012**, *2* (27), 10125–10156. https://doi.org/10.1039/C2RA21342G.

(7) Noack, J.; Roznyatovskaya, N.; Herr, T.; Fischer, P. The Chemistry of Redox-Flow Batteries. *Angewandte Chemie International Edition* **2015**, *54* (34), 9776–9809. https://doi.org/10.1002/anie.201410823.

(8) Zhao, Y.; Ding, Y.; Li, Y.; Peng, L.; Byon, H. R.; Goodenough, J. B.; Yu, G. A Chemistry and Material Perspective on Lithium Redox Flow Batteries towards High-Density Electrical Energy Storage. *Chem. Soc. Rev.* **2015**, *44* (22), 7968–7996. https://doi.org/10.1039/C5CS00289C.

(9) Brushett, F. R.; Vaughey, J. T.; Jansen, A. N. An All-Organic Non-Aqueous Lithium-Ion Redox Flow Battery. *Advanced Energy Materials* **2012**, *2* (11), 1390–1396. https://doi.org/10.1002/aenm.201200322.

(10) Zhao, Y.; Ding, Y.; Song, J.; Li, G.; Dong, G.; Goodenough, J. B.; Yu, G. Sustainable Electrical Energy Storage through the Ferrocene/Ferrocenium Redox Reaction in Aprotic Electrolyte. *Angewandte Chemie International Edition* **2014**, *53* (41), 11036–11040. https://doi.org/10.1002/anie.201406135.

(11) Park, M.-S.; Lee, N.-J.; Lee, S.-W.; Kim, K. J.; Oh, D.-J.; Kim, Y.-J. High-Energy Redox-Flow Batteries with Hybrid Metal Foam Electrodes. *ACS Appl. Mater. Interfaces* **2014**, *6* (13), 10729–10735. https://doi.org/10.1021/am5025935.

(12) Kwon, G.; Lee, S.; Hwang, J.; Shim, H.-S.; Lee, B.; Lee, M. H.; Ko, Y.; Jung, S.-K.; Ku, K.; Hong, J.; Kang, K. Multi-Redox Molecule for High-Energy Redox Flow Batteries. *Joule* **2018**, *2* (9), 1771–1782. https://doi.org/10.1016/j.joule.2018.05.014.

(13) Wei, X.; Pan, W.; Duan, W.; Hollas, A.; Yang, Z.; Li, B.; Nie, Z.; Liu, J.; Reed, D.; Wang, W.; Sprenkle, V. Materials and Systems for Organic Redox Flow Batteries: Status and Challenges. *ACS Energy Lett.* **2017**, *2* (9), 2187–2204. https://doi.org/10.1021/acsenergylett.7b00650.

(14) Wei, X.; Xu, W.; Vijayakumar, M.; Cosimbescu, L.; Liu, T.; Sprenkle, V.; Wang, W. TEMPO-Based Catholyte for High-Energy Density Nonaqueous Redox Flow Batteries. *Advanced Materials* **2014**, *26* (45), 7649–7653. https://doi.org/10.1002/adma.201403746.

(15) Winsberg, J.; Hagemann, T.; Muench, S.; Friebe, C.; Häupler, B.; Janoschka, T.; Morgenstern, S.; Hager, M. D.; Schubert, U. S. Poly(Boron-Dipyrromethene)—A Redox-Active Polymer Class for Polymer Redox-Flow Batteries. *Chem. Mater.* **2016**, *28* (10), 3401–3405. https://doi.org/10.1021/acs.chemmater.6b00640.

(16) Zhang, C.; Zhang, L.; Ding, Y.; Peng, S.; Guo, X.; Zhao, Y.; He, G.; Yu, G. Progress and Prospects of Next-Generation Redox Flow Batteries. *Energy Storage Materials* **2018**, *15*, 324–350. https://doi.org/10.1016/j.ensm.2018.06.008.

(17) Zhang, J.; Yang, Z.; Shkrob, I. A.; Assary, R. S.; Tung, S. on; Silcox, B.; Duan, W.; Zhang, J.; Su, C. C.; Hu, B.; Pan, B.; Liao, C.; Zhang, Z.; Wang, W.; Curtiss, L. A.; Thompson, L. T.; Wei, X.; Zhang, L. Annulated Dialkoxybenzenes as Catholyte Materials for Non-Aqueous Redox Flow Batteries: Achieving High Chemical Stability through Bicyclic Substitution. *Adv. Energy Mater.* **2017**, *7* (21), 1701272. https://doi.org/10.1002/aenm.201701272.

(18) VanGelder, L. E.; Schreiber, E.; Matson, E. M. Physicochemical Implications of Alkoxide "Mixing" in Polyoxovanadium Clusters for Nonaqueous Energy Storage. *J. Mater. Chem. A* **2019**, *7* (9), 4893–4902. https://doi.org/10.1039/C8TA12306C.

(19) VanGelder, L. E.; Kosswattaarachchi, A. M.; Forrestel, P. L.; Cook, T. R.; Matson, E. M. Polyoxovanadate-Alkoxide Clusters as Multi-Electron Charge Carriers for Symmetric Non-Aqueous Redox Flow Batteries. *Chem. Sci.* **2018**, *9* (6), 1692–1699. https://doi.org/10.1039/C7SC05295B.

(20) A. Kowalski, J.; D. Casselman, M.; Preet Kaur, A.; D. Milshtein, J.; F. Elliott, C.; Modekrutti, S.; Harsha Attanayake, N.; Zhang, N.; R. Parkin, S.; Risko, C.; R. Brushett, F.; A. Odom, S. A Stable Two-Electron-Donating Phenothiazine for Application in Nonaqueous Redox Flow Batteries. *Journal of Materials Chemistry A* **2017**, *5* (46), 24371–24379. https://doi.org/10.1039/C7TA05883G.

(21) Escalante-García, I. L.; Wainright, J. S.; Thompson, L. T.; Savinell, R. F. Performance of a Non-Aqueous Vanadium Acetylacetonate Prototype Redox Flow Battery: Examination of Separators and Capacity Decay. *J. Electrochem. Soc.* **2015**, *162* (3), A363–A372. https://doi.org/10.1149/2.0471503jes.

(22) Carino, E. V.; Staszak-Jirkovsky, J.; Assary, R. S.; Curtiss, L. A.; Markovic, N. M.; Brushett, F. R. Tuning the Stability of Organic Active Materials for Nonaqueous Redox Flow Batteries via Reversible, Electrochemically Mediated Li+ Coordination. *Chem. Mater.* **2016**, *28* (8), 2529–2539. https://doi.org/10.1021/acs.chemmater.5b04053.

(23) Silcox, B.; Zhang, J.; Shkrob, I. A.; Thompson, L.; Zhang, L. On Transferability of Performance Metrics for Redox-Active Molecules. *J. Phys. Chem. C* **2019**, *123* (27), 16516–16524. https://doi.org/10.1021/acs.jpcc.9b02230.

(24) For a summary of properties (potential, solubility, cycling stability) of known catholytes for non-aqueous RFBs, see Table 3.1.

(25) Sevov, C. S.; Samaroo, S. K.; Sanford, M. S. Cyclopropenium Salts as Cyclable, High-Potential Catholytes in Nonaqueous Media. *Advanced Energy Materials* **2017**, *7* (5), 1602027. https://doi.org/10.1002/aenm.201602027.

(26) Bandar, J. S.; Lambert, T. H. Aminocyclopropenium Ions: Synthesis, Properties, and Applications. *Synthesis* **2013**, *45* (18), 2485–2498. https://doi.org/10.1055/s-0033-1338516.

(27) Gerson, F.; Plattner, G.; Yoshida, Z. Tris(Dimethylamino)-Cyclopropenium Radical Dication. *Molecular Physics* **1971**, *21* (6), 1027–1032. https://doi.org/10.1080/00268977100102181.

(28) Yoshida, Z. Heteroatom-Substituted Cyclopropenium Compounds. In *Three-Membered Rings*; Topics in Current Chemistry Fortschritte der Chemischen Forschung; Springer Berlin Heidelberg: Berlin, Heidelberg, 1973; pp 47–72. https://doi.org/10.1007/3-540-06265-3_15.

(29) Weiss, R.; Brenner, T.; Hampel, F.; Wolski, A. The Consequences of an Electrostatic "Forced Marriage" between Two Electron-Rich Particles: Strained Ion Pairs. *Angewandte Chemie International Edition in English* **1995**, *34* (4), 439–441. https://doi.org/10.1002/anie.199504391.

(30) Yoshida, Z.; Tawara, Y. Aminocyclopropenium Ion. *J. Am. Chem. Soc.* **1971**, *93* (10), 2573–2574. https://doi.org/10.1021/ja00739a057.

(31) Weiss, R.; Schloter, K. Stable Radical Dications. *Tetrahedron Letters* **1975**, *16* (40), 3491–3494. https://doi.org/10.1016/S0040-4039(00)91392-3.

(32) Yoshida, Z.; Tawara, Y.; Hirota, S.; Ogoshi, H. Vibrational Spectrum of Trisdimethylaminocyclopropenium Perchlorate. *BCSJ* **1974**, *47* (4), 797–800. https://doi.org/10.1246/bcsj.47.797.

(33) For examples of other highly conjugated molecules being examined as catholytes for RFBs, See: (1) Barton, J. L.; Wixtrom, A. I.; Kowalski, J. A.; Qian, E. A.; Jung, D.; Brushett, F. R.; Spokoyny, A. M. Perfunctionalized Dodecaborate Clusters as Stable Metal-Free Active Materials for Charge Storage. *ACS Appl. Energy Mater*. **2019**, *2 (7)*, 4907–4913. https://doi.org/10.1021/acsaem.9b00610. (2) VanGelder, L. E.; Kosswattaarachchi, A. M.; Forrestel, P. L.; Cook, T. R.; Matson, E. M. Polyoxovanadate-Alkoxide Clusters as Multi-Electron

Charge Carriers for Symmetric Non-Aqueous Redox Flow Batteries. *Chem. Sci.* **2018**, *9 (6)*, 1692–1699. https://doi.org/10.1039/c7sc05295b.

(34) Li, Z.; Li, S.; Liu, S.; Huang, K.; Fang, D.; Wang, F.; Peng, S. Electrochemical Properties of an All-Organic Redox Flow Battery Using 2,2,6,6-Tetramethyl-1-Piperidinyloxy and N-Methylphthalimide. *Electrochem. Solid-State Lett.* **2011**, *14* (12), A171–A173. https://doi.org/10.1149/2.012112esl.

(35) Milshtein, J. D.; Barton, J. L.; Darling, R. M.; Brushett, F. R. 4-Acetamido-2,2,6,6-Tetramethylpiperidine-1-Oxyl as a Model Organic Redox Active Compound for Nonaqueous Flow Batteries. *Journal of Power Sources* **2016**, *327*, 151–159. https://doi.org/10.1016/j.jpowsour.2016.06.125.

(36) Wei, X.; Xu, W.; Huang, J.; Zhang, L.; Walter, E.; Lawrence, C.; Vijayakumar, M.; Henderson, W. A.; Liu, T.; Cosimbescu, L.; Li, B.; Sprenkle, V.; Wang, W. Radical Compatibility with Nonaqueous Electrolytes and Its Impact on an All-Organic Redox Flow Battery. *Angewandte Chemie International Edition* **2015**, *54* (30), 8684–8687. https://doi.org/10.1002/anie.201501443.

(37) Wei, X.; Duan, W.; Huang, J.; Zhang, L.; Li, B.; Reed, D.; Xu, W.; Sprenkle, V.; Wang, W. A High-Current, Stable Nonaqueous Organic Redox Flow Battery. *ACS Energy Lett.* **2016**, *1* (4), 705–711. https://doi.org/10.1021/acsenergylett.6b00255.

(38) Huang, J.; Cheng, L.; Assary, R. S.; Wang, P.; Xue, Z.; Burrell, A. K.; Curtiss, L. A.; Zhang, L. Liquid Catholyte Molecules for Nonaqueous Redox Flow Batteries. *Advanced Energy Materials* **2015**, *5* (6), 1401782. https://doi.org/10.1002/aenm.201401782.

(39) Hansch, Corwin.; Leo, A.; Taft, R. W. A Survey of Hammett Substituent Constants and Resonance and Field Parameters. *Chem. Rev.* **1991**, *91* (2), 165–195. https://doi.org/10.1021/cr00002a004.

(40) Davis, A. P.; Fry, A. J. Experimental and Computed Absolute Redox Potentials of Polycyclic Aromatic Hydrocarbons Are Highly Linearly Correlated Over a Wide Range of Structures and Potentials. *J. Phys. Chem. A* **2010**, *114* (46), 12299–12304. https://doi.org/10.1021/jp106088n.

(41) Freyer, J. L.; Brucks, S. D.; Gobieski, G. S.; Russell, S. T.; Yozwiak, C. E.; Sun, M.; Chen, Z.; Jiang, Y.; Bandar, J. S.; Stockwell, B. R.; Lambert, T. H.; Campos, L. M. Clickable Poly(Ionic Liquids): A Materials Platform for Transfection. *Angewandte Chemie International Edition* **2016**, *55* (40), 12382–12386. https://doi.org/10.1002/anie.201605214.

(42) Furukawa, N.; Glass, R. S.; Nakayama, J.; Sato, S.; Sugihara, Y. *Organosulfur Chemistry II*, Softcover reprint of the original 1st ed. 1999 edition.; Page, P. C. B., Ed.; Springer: Berlin, 2013.

(43) Yoshida, Z.-I.; Konishi, H.; Ogoshi, H. Diaminocyclopropenethiones: Synthesis and Reaction Feature. *Israel Journal of Chemistry* **1981**, *21* (2–3), 139–144. https://doi.org/10.1002/ijch.198100030.

(44) Huang, J.; Su, L.; A. Kowalski, J.; L. Barton, J.; Ferrandon, M.; K. Burrell, A.; R. Brushett, F.; Zhang, L. A Subtractive Approach to Molecular Engineering of Dimethoxybenzene-Based Redox Materials for Non-Aqueous Flow Batteries. *Journal of Materials Chemistry A* **2015**, *3* (29), 14971–14976. https://doi.org/10.1039/C5TA02380G.

(45) Gong, K.; Fang, Q.; Gu, S.; Li, S. F. Y.; Yan, Y. Nonaqueous Redox-Flow Batteries: Organic Solvents, Supporting Electrolytes, and Redox Pairs. *Energy Environ. Sci.* **2015**, *8* (12), 3515–3530. https://doi.org/10.1039/C5EE02341F.

(46) Wei, X.; Cosimbescu, L.; Xu, W.; Hu, J. Z.; Vijayakumar, M.; Feng, J.; Hu, M. Y.; Deng, X.; Xiao, J.; Liu, J.; Sprenkle, V.; Wang, W. Towards High-Performance Nonaqueous Redox Flow

Electrolyte Via Ionic Modification of Active Species. *Advanced Energy Materials* **2015**, *5* (1), 1400678. https://doi.org/10.1002/aenm.201400678.

(47) Nicholson, R. S. Theory and Application of Cyclic Voltammetry for Measurement of Electrode Reaction Kinetics. *Anal. Chem.* **1965**, *37* (11), 1351–1355. https://doi.org/10.1021/ac60230a016.

(48) Hendriks, K. H.; Robinson, S. G.; Braten, M. N.; Sevov, C. S.; Helms, B. A.; Sigman, M. S.; Minteer, S. D.; Sanford, M. S. High-Performance Oligomeric Catholytes for Effective Macromolecular Separation in Nonaqueous Redox Flow Batteries. *ACS Cent. Sci.* **2018**, *4* (2), 189–196. https://doi.org/10.1021/acscentsci.7b00544.

(49) Solubility is another important factor influencing the energy density of flow batteries. Compound **2-Me**$^{+}$ is soluble up to 0.58 M in acetonitrile, while **2-Me**$^{2+}$ has a solubility of >0.2 M in 0.5 M $TBAPF_6$ in MeCN (see SI for complete details on these measurements). Our recent work provides a template for further enhancing this property. Robinson, S. G.; Yan, Y.; Hendriks, K. H.; Sanford, M. S.; Sigman, M. S. Developing a Predictive Solubility Model for Monomeric and Oligomeric Cyclopropenium-Based Flow Battery Catholytes. *J. Am. Chem. Soc.* **2019**, *141 (26)*, 10171–10176. https://doi.org/10.1021/jacs.9b04270.

(50) Leung, P.; Shah, A. A.; Sanz, L.; Flox, C.; Morante, J. R.; Xu, Q.; Mohamed, M. R.; Ponce de León, C.; Walsh, F. C. Recent Developments in Organic Redox Flow Batteries: A Critical Review. *Journal of Power Sources* **2017**, *360*, 243–283. https://doi.org/10.1016/j.jpowsour.2017.05.057.

(51) Xing, X.; Liu, Q.; Xu, W.; Liang, W.; Liu, J.; Wang, B.; Lemmon, J. P. All-Liquid Electroactive Materials for High Energy Density Organic Flow Battery. *ACS Appl. Energy Mater.* **2019**, *2* (4), 2364–2369. https://doi.org/10.1021/acsaem.8b01874.

(52) Shrestha, A., Hendriks, K. H., Carazo, M. B., Ruchti, J., Sigman, M. S., Minteer, S. D., and Sanford, M. S. Molecular Design to Minimize Active Species Crossover and Decomposition Enables an Asymmetric Non-Aqueous Redox Flow Battery. *Manuscript submitted*

(53) Due to the relative instability of **6**, cycling experiments were conducted using 2-Fold redox equivalent Excess of **6** Relative to **2-Me**$^{+}$.

(54) Milshtein, J. D.; Kaur, A. P.; Casselman, M. D.; Kowalski, J. A.; Modekrutti, S.; Zhang, P. L.; Harsha Attanayake, N.; Elliott, C. F.; Parkin, S. R.; Risko, C.; Brushett, F. R.; Odom, S. A. High Current Density, Long Duration Cycling of Soluble Organic Active Species for Non-Aqueous Redox Flow Batteries. *Energy Environ. Sci.* **2016**, *9* (11), 3531–3543. https://doi.org/10.1039/C6EE02027E

(55) Ignasik, M.; Bajda, M.; Guzior, N.; Prinz, M.; Holzgrabe, U.; Malawska, B. Design, Synthesis and Evaluation of Novel 2-(Aminoalkyl)-Isoindoline-1,3-Dione Derivatives as Dual-Binding Site Acetylcholinesterase Inhibitors. *Archiv der Pharmazie* **2012**, *345* (7), 509–516. https://doi.org/10.1002/ardp.201100423.

(56) Hu, B.; Liu, T. L. Two Electron Utilization of Methyl Viologen Anolyte in Nonaqueous Organic Redox Flow Battery. *Journal of Energy Chemistry* **2018**, *27* (5), 1326–1332. https://doi.org/10.1016/j.jechem.2018.02.014.

(57) Shinkle, A. A.; Sleightholme, A. E. S.; Griffith, L. D.; Thompson, L. T.; Monroe, C. W. Degradation Mechanisms in the Non-Aqueous Vanadium Acetylacetonate Redox Flow Battery. *Journal of Power Sources* **2012**, *206*, 490–496. https://doi.org/10.1016/j.jpowsour.2010.12.096.

(58) Nicholson, R. S. Theory and Application of Cyclic Voltammetry for Measurement of Electrode Reaction Kinetics. *Anal. Chem.* **1965**, *37* (11), 1351–1355. https://doi.org/10.1021/ac60230a016.

(59) Sevov, C. S.; Fisher, S. L.; Thompson, L. T.; Sanford, M. S. Mechanism-Based Development of a Low-Potential, Soluble, and Cyclable Multielectron Anolyte for Nonaqueous Redox Flow Batteries. *J. Am. Chem. Soc.* **2016**, *138* (47), 15378–15384. https://doi.org/10.1021/jacs.6b07638.

(60) Hanson, S. S.; Richard, N. A.; Dyker, C. A. Powerful Bispyridinylidene Organic Reducing Agents with Iminophosphorano π-Donor Substituents. *Chemistry – A European Journal* **2015**, *21* (22), 8052–8055. https://doi.org/10.1002/chem.201500809.

(61) *MacroModel*; Schrödinger, LLC: New York, 2017.

(62) Harder, E.; Damm, W.; Maple, J.; Wu, C.; Reboul, M.; Xiang, J. Y.; Wang, L.; Lupyan, D.; Dahlgren, M. K.; Knight, J. L.; Kaus, J. W.; Cerutti, D. S.; Krilov, G.; Jorgensen, W. L.; Abel, R.; Friesner, R. A. OPLS3: A Force Field Providing Broad Coverage of Drug-like Small Molecules and Proteins. *J Chem Theory Comput* **2016**, *12* (1), 281–296. https://doi.org/10.1021/acs.jctc.5b00864.

(63) Becke, A. D. Density-Functional Exchange-Energy Approximation with Correct Asymptotic Behavior. *Phys. Rev. A* **1988**, *38* (6), 3098–3100. https://doi.org/10.1103/PhysRevA.38.3098.

(64) Lee, C.; Yang, W.; Parr, R. G. Development of the Colle-Salvetti Correlation-Energy Formula into a Functional of the Electron Density. *Phys. Rev. B* **1988**, *37* (2), 785–789. https://doi.org/10.1103/PhysRevB.37.785.

(65) Frisch, M. J.; Trucks, G. W.; Schlegel, H. B.; Scuseria, G. E.; Robb, M. A.; Cheeseman, J. R.; Scalmani, G.; Barone, V.; Petersson, G. A.; Nakatsuji, H.; Li, X.; Caricato, M.; Marenich, A. V.; Bloino, J.; Janesko, B. G.; Gomperts, R.; Mennucci, B.; Hratchian, H. P.; Ortiz, J. V.; Izmaylov, A. F.; Sonnenberg, J. L.; Williams; Ding, F.; Lipparini, F.; Egidi, F.; Goings, J.; Peng, B.; Petrone,

A.; Henderson, T.; Ranasinghe, D.; Zakrzewski, V. G.; Gao, J.; Rega, N.; Zheng, G.; Liang, W.; Hada, M.; Ehara, M.; Toyota, K.; Fukuda, R.; Hasegawa, J.; Ishida, M.; Nakajima, T.; Honda, Y.; Kitao, O.; Nakai, H.; Vreven, T.; Throssell, K.; Montgomery Jr., J. A.; Peralta, J. E.; Ogliaro, F.; Bearpark, M. J.; Heyd, J. J.; Brothers, E. N.; Kudin, K. N.; Staroverov, V. N.; Keith, T. A.; Kobayashi, R.; Normand, J.; Raghavachari, K.; Rendell, A. P.; Burant, J. C.; Iyengar, S. S.; Tomasi, J.; Cossi, M.; Millam, J. M.; Klene, M.; Adamo, C.; Cammi, R.; Ochterski, J. W.; Martin, R. L.; Morokuma, K.; Farkas, O.; Foresman, J. B.; Fox, D. J. *Gaussian 16 Rev. B.01*; Wallingford, CT, 2016.

(66) Zhao, Y.; Truhlar, D. G. The M06 Suite of Density Functionals for Main Group Thermochemistry, Thermochemical Kinetics, Noncovalent Interactions, Excited States, and Transition Elements: Two New Functionals and Systematic Testing of Four M06-Class Functionals and 12 Other Functionals. *Theor Chem Account* **2008**, *120* (1), 215–241. https://doi.org/10.1007/s00214-007-0310-x.

(67) Weigend, F.; Ahlrichs, R. Balanced Basis Sets of Split Valence, Triple Zeta Valence and Quadruple Zeta Valence Quality for H to Rn: Design and Assessment of Accuracy. *Phys. Chem. Chem. Phys.* **2005**, *7* (18), 3297–3305. https://doi.org/10.1039/B508541A.

(68) Ermanis, K.; Parkes, K. E. B.; Agback, T.; Goodman, J. M. Expanding DP4: Application to Drug Compounds and Automation. *Org. Biomol. Chem.* **2016**, *14* (16), 3943–3949. https://doi.org/10.1039/C6OB00015K.

(69) Davis, A. P.; Fry, A. J. Experimental and Computed Absolute Redox Potentials of Polycyclic Aromatic Hydrocarbons Are Highly Linearly Correlated Over a Wide Range of Structures and Potentials. *J. Phys. Chem. A* **2010**, *114* (46), 12299–12304. https://doi.org/10.1021/jp106088n.

Chapter 4

Bis(diisopropylamino)cyclopropenium-arene Cations as High Oxidation Potential and High Stability Catholytes for Non-aqueous Redox Flow Batteries

(published as *J. Am. Chem. Soc.* 2020, 142, 41, 17564–17571)

4.1. Introduction

The deployment of wind and solar power as a significant fraction of the energy supplied to the electrical grid will require low-cost energy storage on a very large scale,[1,2] and redox flow batteries represent a promising technology for such inexpensive large-scale stationary storage.[3–5] Current commercial flow batteries employ aqueous electrolyte solutions of inorganic redox-active species such as vanadium salts, iron salts, or zinc-bromine.[6] In contrast to these inorganic redox species, redox-active organic molecules afford opportunities for modification of the molecular structure of the active materials to tune properties such as redox potential, stability, and solubility. A number of organic molecules have been investigated as active species in flow batteries, both in aqueous and organic solvent-based electrolytes.[7–10] Organic solvent electrolytes present some distinct advantages over aqueous ones, particularly their significantly larger electrochemical stability window (4-5 V compared to ~ 1.5 V for aqueous solutions).[11,12] If molecules can be developed that take advantage of this large electrochemical window (while maintaining high solubility and stability), they hold promise for creating flow batteries with significantly higher voltage, and thus higher energy density, than that achievable in aqueous systems (other factors being equal).

A key challenge in this area is identifying organic molecules that undergo oxidation at high potentials or reduction at low potentials while maintaining stability of the oxidized or reduced species toward decomposition or reaction with solvent, supporting electrolyte, electrode, or membrane materials. This challenge is exemplified by our recent efforts in organic catholyte development. Initial work identified tris(dialkylamino)cyclopropenium cations (**1**$^+$) as promising catholytes for nonaqueous flow batteries (Figure 4.1a).[13–16] These undergo stable half-cell charge-discharge cycling (<3% capacity fade over 200 cycles) but at a relatively modest potential of approximately +0.8 V (vs. ferrocene$^{+/0}$ ($Fc^{+/0}$)).[13] Substituting one of the amino substituents with an methylthio group (**2**$^+$, Figure 4.1b) results in a 500 mV increase in oxidation potential (to +1.33 vs. $Fc^{+/0}$), which is the highest reported potential for an organic catholyte to date. However, this is accompanied by a significant decrease in charge-discharge cycling stability due to decomposition of the highly energetic radical dication.[17]

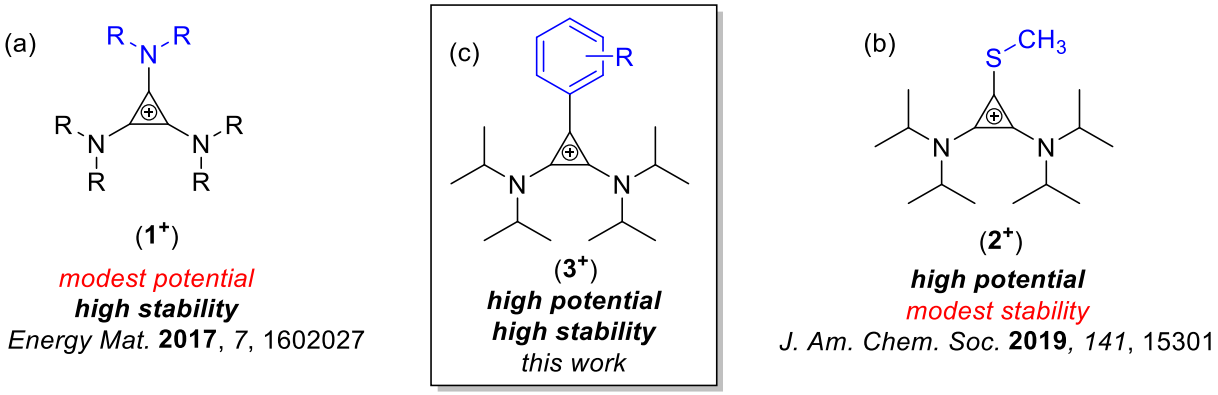

Figure 4.1. Cyclopropenium-based catholytes for non-aqueous redox flow batteries: (a) tris(dialkylamino)cyclopropenium, (b) bis(dialkylamino)alkylthiocyclopropenium, (c) bis(dialkylamino)-arylcyclopropenium

In this report, we develop bis(dialkylamino)-arylcyclopropenium cations ($\mathbf{3}^+$ with aryl = derivatized phenyl group; Figure 4.1c) as novel catholyte candidates for nonaqueous redox flow batteries. We note that a phenyl group is electronically similar to a methylthio substituent (Hammett σ_{para} values of -0.01 and 0.00, respectively),[18] suggesting that $\mathbf{2}^+$ and $\mathbf{3}^+$ should exhibit similar oxidation potentials. However, aryl groups offer the advantage that they are highly electronically and sterically tunable by variation of the substituent pattern on the aromatic ring. Furthermore, phenylcyclopropenium derivatives do not contain a S–C bond, which is the major site of decomposition for the radical dication of $\mathbf{2}^{+\cdot}$.[17] Herein we describe DFT calculations, chemical synthesis, and electrochemical evaluation of a series of 1,2-bis(diisopropylamino)-3-cyclopropenylium-functionalized (DAC-functionalized) benzene derivatives, as well as their performance as catholytes in non-aqueous redox flow batteries.

4.2. Results and Discussions

DFT calculations on DAC-benzenes. We first employed density functional theory (DFT) calculations to predict the $\mathbf{3}^+/\mathbf{3}^{\cdot 2+}$ redox potentials for three DAC-benzene derivatives: DAC-benzene ($\mathbf{3a}^+$), 1-DAC-4-*tert*-butylbenzene ($\mathbf{3b}^+$), and 1-DAC-4-methoxybenzene ($\mathbf{3c}^+$) (see Figure 4.2 for structures). Protocols for the quantum computation of redox potentials are now well developed;[19] we found that a relatively straightforward method[20,21] was quite accurate in its predictions. Using B3LYP/6-31G*/6-311+G** and a conductor-like polarizable continuum model for the solvent acetonitrile, the energy of each cation ($\mathbf{3}^+$) and its radical dication ($\mathbf{3}^{\cdot 2+}$) was calculated, and then the energy of $\mathbf{3}^{\cdot 2+}$ was subtracted from that of $\mathbf{3}^+$ to obtain an ionization energy. An analogous calculation was performed on the tris(diethylamino)cyclopropenium cation, which has an experimental oxidation potential of +0.82 V versus $Fc^{+/0}$ in acetonitrile.[13] The calculated ionization energy of the tris(diethylamino)cyclopropenium cation, 5.39 eV, indicates that

subtraction of 4.57 V from the calculated ionization energies (in eV) of $\mathbf{3}^+$ will yield the solution-phase oxidation potential versus $Fc^{+/0}$ in acetonitrile. Further details of the computational methods are provided in the experimental sections.

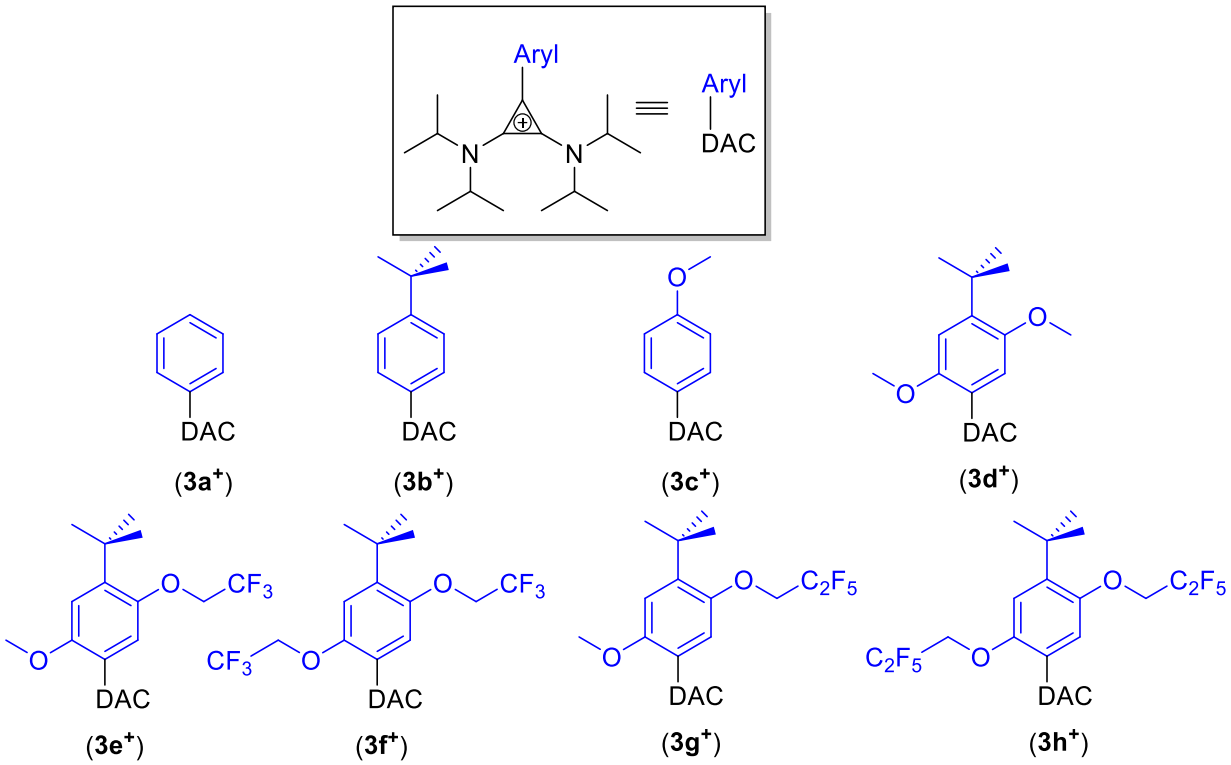

Figure 4.2. Arylcyclopropenium derivatives investigated in this work

The calculated oxidation potentials in acetonitrile versus $Fc^{+/0}$ are +1.64 V for $\mathbf{3a}^+$, +1.51 V for $\mathbf{3b}^+$, and +1.29 V for $\mathbf{3c}^+$. Notably, these values are comparable to or higher than that of $\mathbf{2}^+$ ($E_{1/2}$ = +1.33 V).[17] Furthermore, they suggest that the redox potential can be tuned by at least 350 mV by adding substituents to the aryl ring. Specifically, the electron donating groups *tert*-butyl (on $\mathbf{3b}^+$) and methoxy (on $\mathbf{3c}^+$) result in a lowering of the oxidation potential relative to that of the unsubstituted phenyl analogue ($\mathbf{3a}^+$).

Figure 4.3 shows the calculated SOMO of the radical dications **3a**$^{\cdot 2+}$, **3b**$^{\cdot 2+}$, and **3c**$^{\cdot 2+}$. The unpaired spin density (and likely much of the positive charge density) is delocalized over the cyclopropenium ring, the two nitrogen atoms, the phenyl ring, and, in the case of **3c**$^{\cdot 2+}$, the oxygen atom of the methoxy group. In **3a**$^{\cdot 2+}$, the majority of the spin density on the phenyl ring is localized at the 4-position, with a calculated Mulliken spin density of 0.176 at this carbon. This suggests that **3a**$^{\cdot 2+}$ might be stabilized by the incorporation of substituents at the 4-position, which could sterically block potential dimerization or other decomposition reactions.

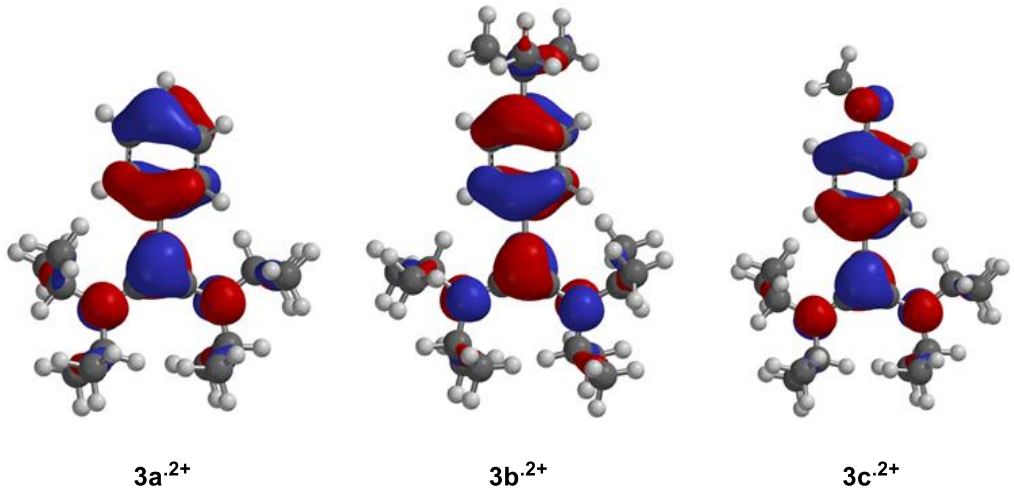

Figure 4.3. Calculated SOMO for the radical dications **3a**$^{\cdot 2+}$, **3b**$^{\cdot 2+}$, and **3c**$^{\cdot 2+}$

*Synthesis of DAC-arenes **3a-h**$^+$*. On the basis of the preliminary DFT calculations, we synthesized [**3a**$^+$][PF_6^-], [**3b**$^+$][PF_6^-], and [**3c**$^+$][PF_6^-] (as well as **3d**$^+$-**3h**$^+$, discussed later) via the sequence shown in Scheme 4.1.[22,23] An initial $AlCl_3$-mediated Friedel-Crafts reaction between the appropriate arene and the *in situ*-generated trichlorocyclopropenium cation was followed by substitution with diisopropylamine to afford the DAC-arene as a chloride salt. Ion exchange with NH_4PF_6 then afforded the DAC-arene hexafluorophosphate salts, which were used for all of the electrochemical studies. Overall yields were 13-47%, and this reaction sequence has been performed on a scale of up to 1.6 g of product (for [**3g**$^+$][PF_6^-]).

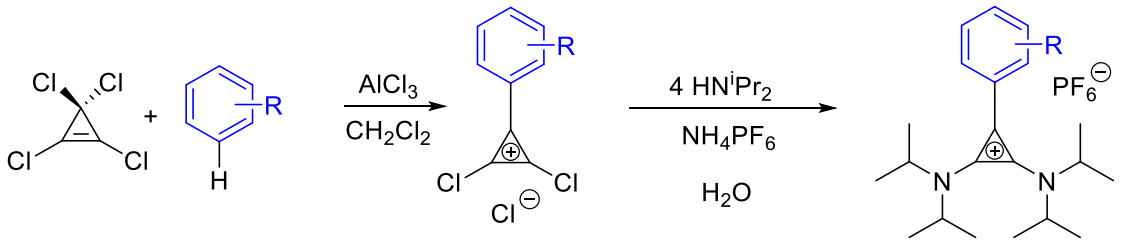

Scheme 4.1. Synthesis of Bis(diisopropylamino)aryl-cyclopropenium Cations

*Characterization of **3a-c**⁺ via cyclic voltammetry.* The cyclic voltammogram (CV) of [**3a**⁺][PF_6^-] (Figure 4; CH_3CN/0.50 M KPF_6, glassy carbon working electrode) shows three anodic peaks at approximately +1.71 V, +1.90 V, and +2.30 V (versus $Fc^{+/0}$), but all of these oxidations are irreversible. The $E_{1/2}$ of an irreversible electrochemical process can be estimated by $E_{p/2}$, the potential at which the current is half of the peak current of the irreversible oxidation or reduction. For **3a**⁺, $E_{p/2}$ of the first irreversible oxidation is +1.60 V, close to the DFT-predicted $E_{1/2}$ value of +1.64 V. However, the irreversibility of the oxidation of **3a**⁺ makes it unsuitable as a catholyte

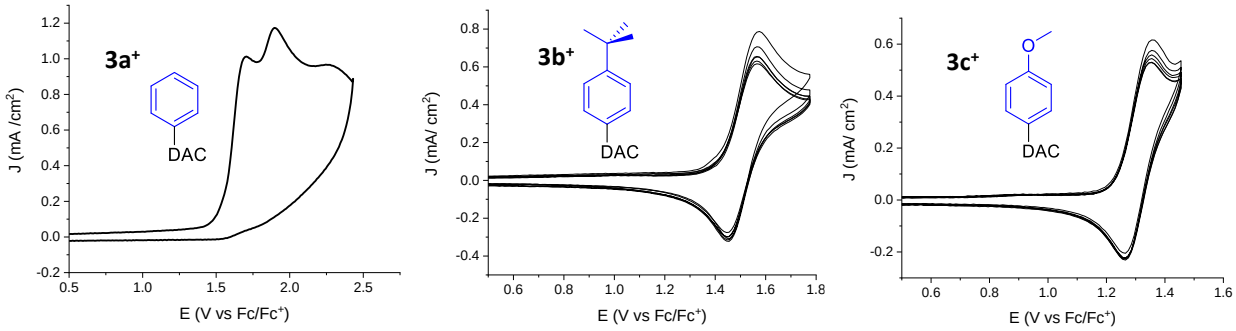

Figure 4.4 Cyclic voltammetry of **3a**⁺ and five cycles (#2-6) of cyclic voltammetry for **3b**⁺ and **3c**⁺ in CH_3CN/0.50 M KPF_6.

In contrast, the *tert*-butyl and methoxy derivatives **3b**⁺ and **3c**⁺ exhibit reversible oxidations at +1.51 and +1.31 V, respectively. These values are within 20 mV of those predicted by DFT (see Table 4.1 for calculated and experimental $E_{1/2}$ values). However, as shown in Figure 4.4,

both **3b**$^+$ and **3c**$^+$ are unstable over multiple CV cycles, exhibiting a decrease in i_{pa} and i_{pc} (peak oxidative and reductive current) over 5 cycles of CV.

catholyte	experimental $E_{1/2}$ (V vs Fc)	calculated $E_{1/2}$ (V vs Fc)
1$^+$	0.82	0.82†
2$^+$	1.33	1.39
3a$^+$	1.60 ($E_{p/2}$)	1.64
3b$^+$	1.51	1.51
3c$^+$	1.31	1.29
3d$^+$	1.00	0.96
3e$^+$	1.18	1.13
3f$^+$	1.34	1.23
3g$^+$	1.19	1.13
3h$^+$	1.37	1.25

Table 4.1. Experimental and Calculated $E_{1/2}$ for Oxidation of 1^+, 2^+, and DAC-Arene Cations in Acetonitrile (†set to the experimental value)

We next evaluated DAC-arenes bearing 2,5-dialkoxy-4-*tert*-butyl substitution on the benzene ring (**3d**$^+$-**3h**$^+$). These were selected based on their similarity to 1,4-dialkoxy-2,5-di-*tert*-butylbenzene derivatives, a well-studied class of molecules that have been applied as redox shuttles for overcharge protection in lithium-ion batteries[24,25] and also as catholytes for nonaqueous flow batteries.[26–30] The calculated oxidation potentials for these DAC-arenes range from +0.96 V for **3d**$^+$ to +1.25 V for **3h**$^+$ (Table 4.1). The presence of three electron-donating substituents (one *tert*-butyl and two alkoxy groups) lowers their calculated potentials relative to those of **3a**$^+$-**3c**$^+$. However, with the fluorinated alkoxy groups in **3e**$^+$-**3h**$^+$, the calculated oxidation potentials still exceed those of the tris(dialkylamino)cyclopropenium cations **1**$^+$ by more than 400 mV and are similar to that of the thioether-substituted derivative **2**$^+$. The DFT calculations indicate that the DAC group is not simply an electron-withdrawing group that increases the oxidation

potential relative to the 2,5-dialkoxy-4-*tert*-butylbenzenes, but also enhances the stability of the molecule overall by delocalizing the charge and unpaired spin density over both ring system. Figure 4.10 shows the SOMO of the radical cation of 1,4-dimethoxy-2,5-di-*tert*-butylbenzene, the SOMO of the tris(diethylamino)-cyclopropenium dication radical, and how they combine in $\mathbf{3g}^{\cdot 2+}$.

Cyclic voltammetry of the 2,5-dimethoxy-4-*tert*-butyl substituted derivative $\mathbf{3d}^{+}$ shows an experimental $E_{1/2}$ of +1.00 V, 40 mV more positive than the calculated value. Minimal change in current was observed over five CV cycles for $\mathbf{3d}^{+}$ (Figure 4.5), indicating that this derivative has significantly enhanced stability relative to $\mathbf{3a}^{+}$-$\mathbf{3c}^{+}$. Replacing the two methoxy groups with two fluoroalkoxy substituents in $\mathbf{3f}^{+}$ and $\mathbf{3h}^{+}$ results in an approximately 350 mV increase in experimental oxidation potential to +1.34 and +1.37 V, respectively.[a] However, both $\mathbf{3f}^{+}$ and $\mathbf{3h}^{+}$ exhibit a decrease in i_{pa} and i_{pc} upon repeated CV cycling (see Figure 4.5). This is accompanied by an increase in the separation of the peak oxidation and reduction potentials (E_{pa} - E_{pc}). These features likely derive from decomposition of the radical dications and deposition/polymerization on the electrode surface, with the increased resistance leading to higher and lower applied potentials for oxidation and reduction, respectively.[31] When the working electrode used for the repeated CV cycles of $\mathbf{3f}^{+}$ was cleaned and replaced in the same solution for another five cycles of CV, the i_{pa} and i_{pc} were partially restored and E_{pa} - E_{pc} returned to that of the initial CVs (see Figure 4.13). This is consistent with the decomposition products of the radical dication $\mathbf{3f}^{\cdot 2+}$ fouling the working electrode during cyclic voltammetry.

[a] Those are higher than their computationally predicted values by more than 100 mV—it is not known why the computations underestimate the oxidation potentials of these fluorinated derivatives.

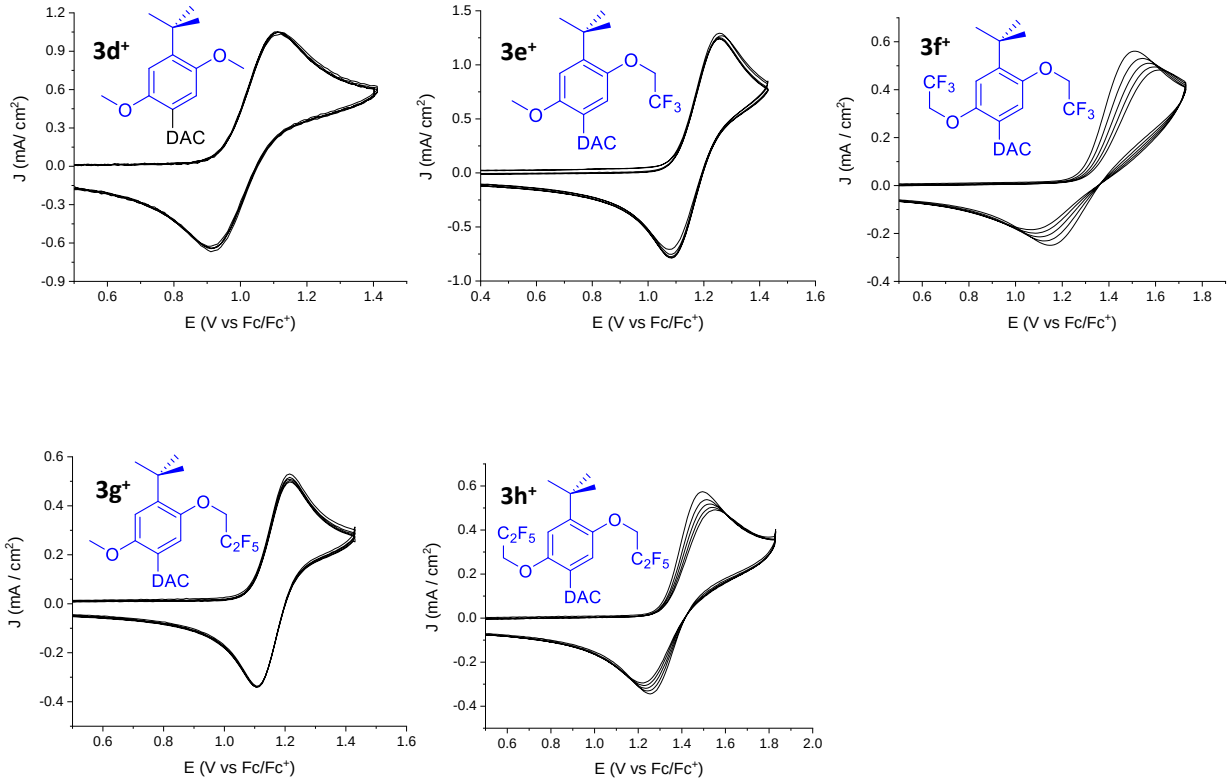

Figure 4.5. Five cycles (#2-6) of cyclic voltammetry for **3d**$^+$-**3h**$^+$ in CH_3CN/0.50 M KPF_6.

The mixed methoxy-fluoroalkoxy derivatives **3e**$^+$ and **3g**$^+$ offer a compromise between the high stability of **3d**$^+$ and the high potentials of **3f**$^+$ and **3h**$^+$. Their CVs show an $E_{1/2}$ of +1.18 V for **3e**$^+$ and +1.19 V for **3g**$^+$. Furthermore, repeated cycles of CV for **3e**$^+$ and **3g**$^+$ show significantly improved stability relative to **3f**$^+$ and **3h**$^+$ (Figure 4.5).

Static H-cell charge-discharge cycling of ***1***$^+$, ***2***$^+$, ***3d***$^+$, ***3e***$^+$, *and* ***3g***$^+$. Based on the CV data, we moved forward with bulk charge-discharge cycling of **3d**$^+$, **3e**$^+$, and **3g**$^+$, along with **1**$^+$ (specifically, tris(di-*n*-propylamino)cyclopropenium) and **2**$^+$ under identical conditions for comparison. Initial cycling experiments were conducted in a static H-cell with an ultrafine fritted glass separator, reticulated vitreous carbon working and counter electrodes, and a Ag/Ag^+ reference electrode on the working electrode side of the cell. The working side of the cell contained 5.0 mL of a 5.0 mM solution of the catholyte of interest (e.g., [**3d**$^+$][PF_6^-]) in CH_3CN/0.50 M KPF_6. The counter-

electrode side contained 5.0 mL of a 5.0 mM solution of methyl viologen hexafluorophosphate in CH_3CN/0.50 M KPF_6. For each cycle, the cell was charged at 5.00 mA to 50% of the theoretical capacity (0.335 mAh) or to a voltage limit of 0.3 V higher than the $E_{1/2}$ of the particular catholyte. The current was then reversed to -5.0 mA and the cell discharged to 0.335 mAh or +0.50 V vs Ag/Ag^+, whichever was reached first. This method has been used to assay the stability of a variety of dialkoxybenzene and cyclopropenium catholytes, enabling straightforward comparison of charge-discharge cycling performance.[17,27,29,30] Note that in this experimental protocol no loss of capacity will be evident until about 50% of the active material has been lost to decomposition or is otherwise inactivated.

The results from these experiments are shown in Figure 4.6. Among the DAC-arene cations, **3d**$^+$ is the most stable, as it does not exhibit any capacity loss through at least cycle 300. The $–OCH_2CF_2CF_3$ analog, **3g**$^+$, shows initial capacity fade at 275 cycles, and maintains 90% of its capacity through 323 cycles. Finally, the $–OCH_2CF_3$ analog, **3e**$^+$, is the least stable of these three DAC-arene cations, beginning to lose capacity after about 145 cycles, and has a discharge capacity of 0.16 mAh (24% of theoretical) after 300 cycles. For comparison, under these conditions **1**$^+$ is highly stable, with no loss of capacity until about cycle 625, far past the data shown in Figure 4.6. In contrast, **2**$^+$ is much less stable than all of the DAC-arene cations, beginning to lose capacity at about cycle 145 and fading to a discharge capacity of 0.11 mAh (16% of theoretical) by cycle 225. The cycling stability of **3g**$^+$ is lower than that of a reported molecule in which the DAC group of **3g**$^+$ is replaced with a *tert*-butyl group. Under analogous cycling conditions, this compound maintained 90% of its capacity to cycle 451.[29] However, the oxidation potential of the *tert*-butyl-substituted derivative is only +0.82 V vs $Fc^{+/0}$, 0.37 V lower than that of **3g**$^+$. Finally, we performed this static H-cell charge-discharge experiment on 2,5-di-*tert*-butyl-1,4-bis(2-methoxyethoxy)-

benzene, the first of this class of molecules employed in a nonaqueous redox flow battery.[26] It was more stable than **3g**$^+$, showing no loss of capacity to cycle 300 (see Figure 4.14), but it has a significantly lower oxidation potential of +0.61 V vs $Fc^{+/0}$.[29]

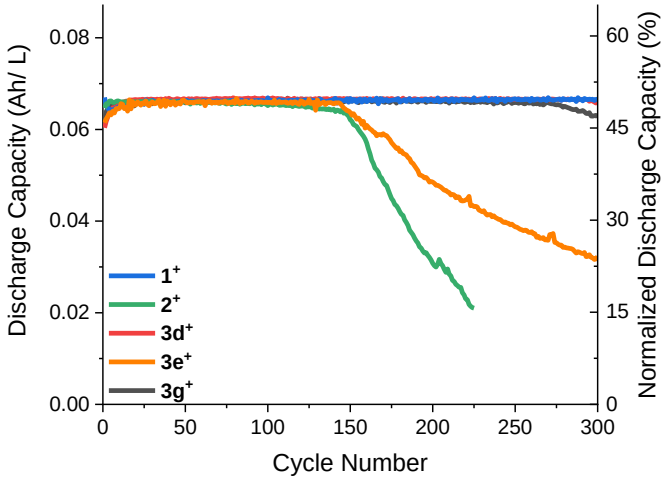

Figure 4.6. H-cell bulk charge-discharge cycling data for **1**$^+$ (all R = *n*-propyl), **2**$^+$, **3d**$^+$, **3e**$^+$, and **3g**$^+$.

Based on these preliminary studies, we conclude that cation **3g**$^+$ offers the best balance of cycling stability and $E_{1/2}$ (which at +1.19 V is ≥0.35 V higher than the first generation tris(dialkylamino)cyclopropenium cations).[13] While **3g**$^+$ sacrifices a small amount of voltage relative to **2**$^+$ ($E_{1/2}$ = +1.19 V vs. +1.33 V), it is much more stable in the H-cell charge-discharge cycling experiments. In addition, [**3g**$^+$][PF_6^-] has high solubility in acetonitrile (1.0 M), an important feature for application in nonaqueous redox flow batteries. The molecule **3g**$^+$ is, to our knowledge, only the second organic catholyte reported with an oxidation potential of greater than +1.0 V vs Fc/Fc^+ (**2**$^+$ is the other).

The heterogeneous electron-transfer kinetics (at the solution-electrode interface) and diffusion constants of the redox-active materials are important for application of those materials

in flow batteries.[32] Both were determined for $\mathbf{3g}^+$ by CVs run at scan rates ranging from 20 to 300 $mV \cdot s^{-1}$.[33,34] Application of the Randles-Sevcik equation (Figure 4.11) to the data from $\mathbf{3g}^+$ yields a diffusion coefficient of 6.2×10^{-6} $cm^2 \cdot s^{-1}$. That is similar to other organic catholytes; for example, a dialkoxy-di-*tert*-butylbenzene has a diffusion coefficient of 5.77×10^{-6} $cm^2 \cdot s^{-1}$.[28] Using the Nicholson method[34] (see Figure 4.12), the heterogeneous electron-transfer constant of $\mathbf{3g}^+$ was found to be 1.6×10^{-3} $cm \cdot s^{-1}$. While this is lower than that of some redox-active organic molecules such as 5,10-dihydro-5,10-dimethylphenazine (2.97×10^{-2} $cm \cdot s^{-1}$) and fluorenone (1.18×10^{-2} $cm \cdot s^{-1}$),[35] it is larger than many metallo-organic complexes proposed for use in flow batteries, such as $V(acac)_3$ (6.5×10^{-4} $cm \cdot s^{-1}$).[36]

Flow cell cycling of $\mathbf{3g}^+$**.** We next examined the charge-discharge cycling of $\mathbf{3g}^+$ in a symmetric flow cell. As detailed below, this experiment better simulates performance in a full flow battery, as it uses the same carbon paper electrodes (in comparison to the RVC electrodes used in the H-cell cycling in Figure 4.6), a polymer-based separator (in comparison to an ultrafine fritted glass separator for the cycling in Figure 4.6), and a much higher concentration of active species (0.3 M versus 5 mM).

In this experiment, the oxidation half reaction $\mathbf{3g}^+ \rightleftarrows \mathbf{3g}^{2+} + e^-$ in one chamber is countered by the reduction half reaction $\mathbf{3g}^{2+} + e^- \rightleftarrows \mathbf{3g}^+$ in the other. One reservoir of the flow cell was loaded with 5.0 mL of a 0.30 M solution of $[\mathbf{3g}^+][PF_6]$ in CH_3CN/0.50 M KPF_6. The other reservoir was loaded with 5.0 mL of a 0.30 M solution of $[\mathbf{3g}^{2+}][PF_6]_2$ (prepared by bulk electrolysis[37]) in CH_3CN/0.50 M KPF_6. A Fumasep® FAP-375-PP anion-exchange membrane was used to separate the two electrodes. Charge and discharge currents of 35 $mA \cdot cm^{-2}$ were used, and the cutoff voltages were 0.8 V and -0.8 V. Complete details of the experimental setup[38] are provided in the experimental sections. Figure 4.7left shows the discharge capacity and coulombic efficiency of the

flow cell over 200 charge-discharge cycles (116 h). Notably, the coulombic efficiency is near 100% for the entire run. The theoretical capacity is 8.04 Ah/L (for one electrolyte chamber), and the initial utilization of that capacity is 6.0 Ah/L, or 75% of the theoretical capacity. After 200 cycles, 92% of the initial capacity is maintained, demonstrating the high stability of $\mathbf{3g}^{+}$ in this symmetrical flow cell at 0.30 M concentration. Furthermore, CVs taken before and after cycling (at the same dilution ratio of the active fluid) show no change in concentration of $\mathbf{3g}^{+/2+}$, nor the formation of any other electrochemically active species during this 116 h cycling experiment (Figure 4.7 right).

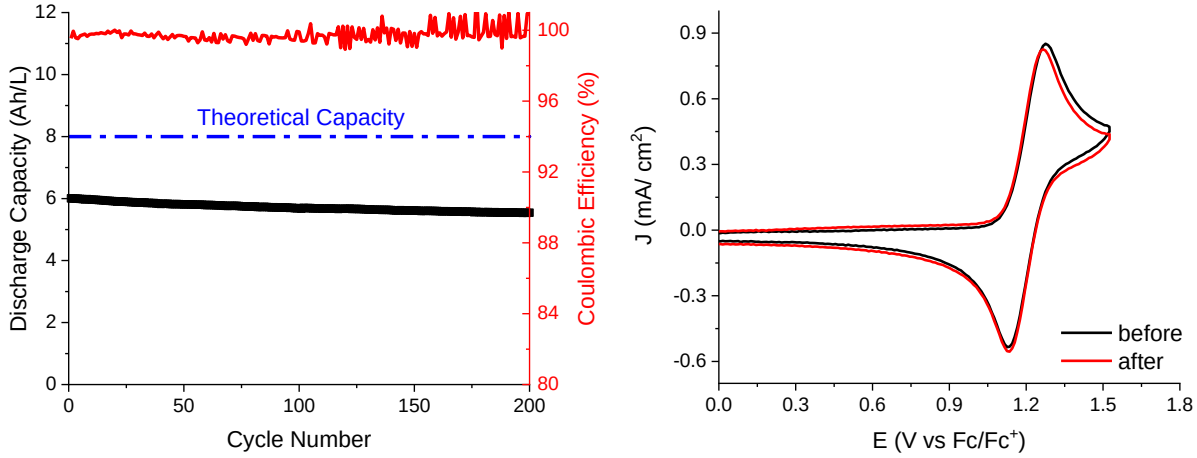

Figure 4.7. Left:Capacity and coulombic efficiency versus cycle number for charge-discharge cycling of a 0.30 M solution of $\mathbf{3g}^{+}/\mathbf{3g}^{2+}$ in CH_3CN/0.50 M KPF_6 in a symmetric flow cell. **Right**: Cyclic voltammograms of the solution of the $\mathbf{3g}^{+}/\mathbf{3g}^{2+}$ symmetric flow cell before and after 200 charge-discharge cycles.

*Flow battery cycling of [**3g**$^{+}$][PF_6^{-}] with butyl viologen hexafluorophosphate.* Finally, we examined the performance of [$\mathbf{3g}^{+}$][PF_6^{-}] as a catholyte in a full flow battery with butyl viologen as the anolyte. The relevant electrochemical reactions for this system are shown in Figure 4.8. Butyl viologen hexafluorophosphate has only moderate solubility in CH3CN/0.50 M KPF_6, so 50

mM solutions of the active materials were used. A mixed solution of 50 mM [**3g**$^+$][PF_6] and 50 mM butyl viologen hexafluorophosphate in 0.50 M CH3CN/0.50 M KPF_6 was placed in both the catholyte and anolyte reservoirs, to limit effects from electrolyte crossover across the two Celgard 2500 membranes. (See Figure 4.15 for the capacity retention curve of a similar battery with a Fumasep anion-exchange membrane.) Cycling was performed with charge and discharge currents of +30 mA/cm^2 and –30 mA/cm^2, respectively, to cutoff voltages of 2.5 V and 0.5 V (battery voltages in a two-electrode system). The nominal battery voltage is 2.00 V (butyl viologen first reduction $E_{1/2}$ = -0.81 V), so charging to 2.5 V represents a charge to full capacity. For comparison, a similar flow battery experiment was conducted using a mixed solution of 50 mM [**2**$^+$][PF_6^-] and 50 mM butyl viologen hexafluorophosphate (with some small differences in the setup; see experimental sections for details)

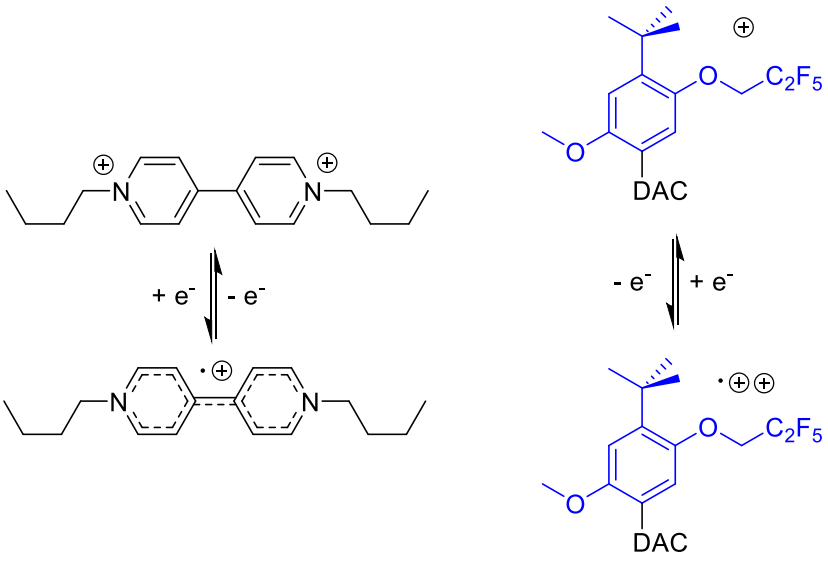

Figure 4.8. Anolyte (left) and catholyte (right) electrochemical reactions in a flow battery of butyl viologen and **3g**$^+$.

A plot of capacity versus cycle number for the **3g**$^+$ and **2**$^+$ batteries is shown in Figure 4.9. The theoretical capacity of both batteries is 1.34 Ah/L, and the initial material utilization is 74% in the

3g^{+} battery and 78% in the **2**$^{+}$ battery. The theoretical energy density of the **3g**$^{+}$ battery is 2.68 Wh/L and that for the **2**$^{+}$ battery is 2.87 Wh/L. The coulombic efficiency (>91%) and energy efficiency (~76%) versus cycle number of the **3g**$^{+}$ battery are given in Figure 4.16 The discharge capacity of the **3g**$^{+}$ battery fades slowly to 74% of its original capacity after 100 cycles (which corresponds to 13 h of run time). This suggests that **3g**$^{+}$ is reasonably stable during flow cell cycling. Indeed, CVs of the anolyte and catholyte chambers before and after cycling the battery show no decomposition products and little change in concentration of the electroactive molecules (Figure 4.9 right). In addition, electrochemical impedance spectroscopy measurements on the battery before and after cycling (Figure 4.17) show no significant increase in resistance of the cell. Thus, the loss in capacity of this battery during cycling is not due to irreversible decomposition of **3g**$^{\cdot 2+}$.[1] In contrast, the battery with the **2**$^{+}$ catholyte showed almost complete capacity loss after 40 cycles (Figure 4.9 left). Thus, while **3g**$^{+}$ sacrifices a small amount of voltage relative to **2**$^{+}$ ($E_{1/2}$ = +1.19 V vs. +1.33 V), it is dramatically more stable during flow cell cycling.

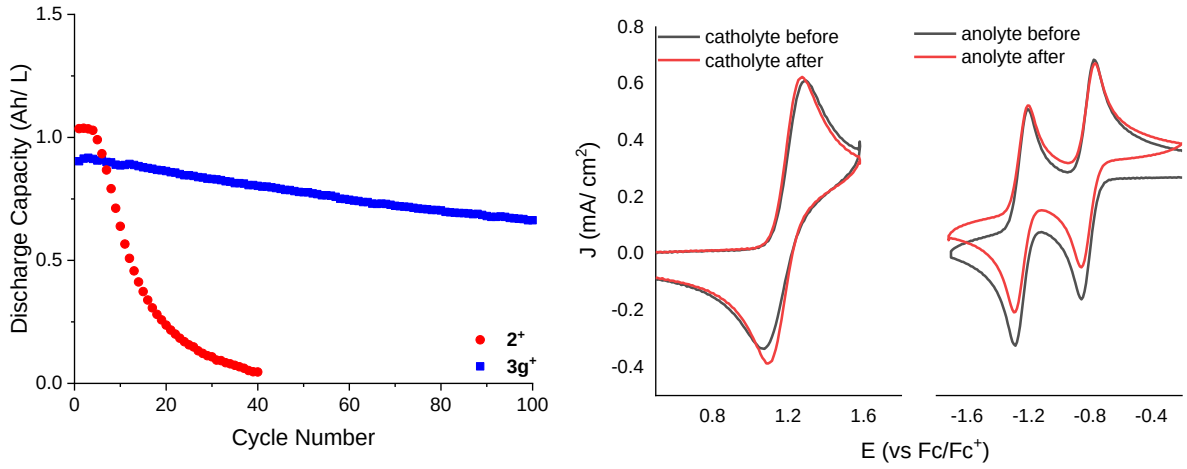

[1] We hypothesize that some competing "self-discharge" of **3g**$^{\cdot 2+}$ to **3g**$^{+}$ (by oxidation of the solvent or supporting electrolyte) leads to a slightly-less-than-complete discharge of the viologen on each individual cycle. Charging on the next cycle is then limited by the (incompletely discharged) viologen, and a small amount of capacity is lost on each cycle. However, neither active material is irreversibly decomposed, and the battery can, in principle, be rebalanced to restore capacity.

Figure 4.9. Left: Discharge capacity versus cycle number of flow cell cycling of 50 mM [**3g**$^+$][PF_6] and 50 mM butyl viologen in 0.50 M KPF_6-MeCN solution (blue) and 50 mM [**2**$^+$][PF_6] and 50 mM butyl viologen in 0.50 M [NBu_4][PF_6]-MeCN solution (red). **Right:** Cyclic voltammograms of the anolyte and catholyte solutions before and after cycling the flow battery of 50 mM [**3g**$^+$][PF_6] and 50 mM butyl viologen in 0.50 M KPF_6-MeCN solution.

4.3. Conclusions

A new class of DAC-functionalized benzene derivatives were examined as catholytes for nonaqueous flow batteries. The oxidation potentials of the molecules vary in a predictable manner depending upon the substituents on the benzene ring (in addition to the DAC group) and were predicted well by DFT calculations. Ultimately, these studies led to the identification of **3g**$^+$, which combines a high oxidation potential ($E_{1/2}$ = +1.19 V vs $Fc^{+/0}$) with good stability during charge-discharge cycling in a flow battery in conjunction with a butyl viologen anolyte. This battery has a theoretical voltage of 2.00 V, larger than what is typically accessible in aqueous systems (where there is a smaller electrochemical stability window). Overall, these studies provide valuable insights into design principles for high-energy and high-stability catholytes for non-aqueous redox flow batteries.

4.4. Experimental Procedures and Characterization of Compounds

4.4.1 Synthetic Procedures

General Information. All commercial chemicals were used as received unless stated otherwise. Anhydrous CH_2Cl_2 was obtained from an Innovative Technology, Inc. (now rebranded to Inert) solvent purification system. Reactions were performed under a nitrogen atmosphere. Dialkoxybenzene derivatives were synthesized according to literature procedures.[39,40] Butyl viologen was synthesized according to literature procedures[41] and then anion exchanged with

NH_4PF_6. The solubility of $[3g^+][PF_6]$ in acetonitrile was determined using a previously reported method.[42] NMR spectra were obtained on Varian VNMRs 700, Varian VNMRs 500, Varian Inova 500, or Varian MR400 spectrometers. ^1H and ^{13}C chemical shifts are reported in parts per million (ppm) relative to TMS, with the residual solvent peak used as an internal reference. ^{19}F chemical shifts are reported relative to the PF_6^- anions at –72.82 ppm, determined from an internal standard of fluorobenzene at –114.81 ppm in CD_3CN.[43] High resolution mass spectroscopy (HRMS) was performed on a Micromass AutoSpec Ultima Magnetic Sector Mass Spectrometer using electrospray ionization (ESI).

General procedure for the synthesis of bis(diisopropylamino)cyclopropenium-arenes. (Based on reported procedures.[44,45]) Tetrachlorocyclopropene (120 mg, 0.67 mmol) and $AlCl_3$ (88 mg, 0.66 mmol) were mixed in 2 mL of CH_2Cl_2 at room temperature for 15 min to form a white suspension. The mixture was cooled to 0 °C and the appropriate benzene derivative (0.66 mmol, dissolved in 2 mL CH_2Cl_2) was added slowly to the reaction mixture. Stirring was continued at 0 °C for 2 h and then diisopropylamine (271 mg, 2.68 mmol) was slowly added. The resulting mixture was stirred at 0 °C for 30 min. The reaction mixture was then filtered, and the filtrate was washed with 10 mL of a 1:1 solution of brine and 2 M HCl. The aqueous layer was extracted with CH_2Cl_2 (2 × 15 mL), and the combined organic fractions were concentrated under vacuum. The resulting residue was dissolved in 5 mL of water, and an aqueous solution of ammonium hexafluorophosphate (NH_4PF_6; 218 mg, 1.34 mmol in 2 mL H_2O) was added with vigorous stirring. A precipitate formed, and this material was extracted into CH_2Cl_2 (3 × 15 mL). The organic extracts were dried over $MgSO_4$ and concentrated under vacuum. The product was then purified by chromatography on silica gel with gradient elution (0–5% acetonitrile in CH_2Cl_2). The main

fractions were then collected and reduced under vacuum to a concentrated solution. Excess diethyl ether was added to precipitate the product, and the resulting white solid was collected via filtration.

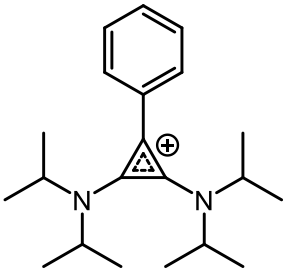

Synthesis of [3a$^+$][PF$_6$]: The general procedure was followed using benzene as the substrate. [**3a**$^+$][PF$_6$] was isolated as a white powder (79 mg, 29%). R_F = 0.24 in 5% acetonitrile/CH_2Cl_2. ^{1}H NMR (401 MHz, CD_3CN) δ 7.63–7.56 (m, 3H), 7.48–7.43 (m, 2H), 4.08 (sept, *J* = 6.9 Hz, 2H), 3.86 (sept, *J* = 6.8 Hz, 2H), 1.37 (d, *J* = 6.8 Hz, 12H), 1.17 (d, *J* = 6.8 Hz, 12H). ^{13}C NMR (126 MHz, CD_3CN) δ 134.81, 131.35, 130.51, 129.52, 127.65, 108.54, 57.90, 48.91, 21.55, 20.75. HRMS (ESI) *m/z* calcd for $C_{21}H_{33}N_2$ (**3a**$^+$): 313.2638, found 313.2636.

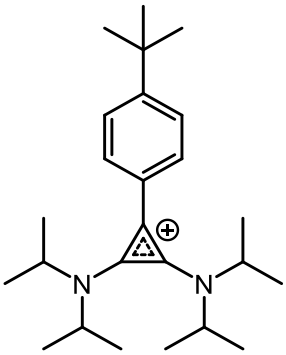

Synthesis of [3b$^+$][PF$_6$]: The general procedure was followed using *tert*-butylbenzene as the substrate. [**3b**$^+$][PF$_6$] was isolated as a white powder (243 mg, 47%). R_F = 0.22 in 5% acetonitrile/CH_2Cl_2. ^{1}H NMR (700 MHz, CD_3CN) δ 7.65 (dd, *J* = 8.3, 2.4 Hz, 2H), 7.42 (dd, *J* = 8.3, 2.4 Hz, 2H), 4.11 (sept, *J* = 7.4 Hz, 2H), 3.89 (sept, *J* = 7.1 Hz, 2H), 1.38 (d, *J* = 6.7 Hz, 12H),

1.37 (s, 9H), 1.21 (d, J = 6.7 Hz, 12H). ^{13}C NMR (176 MHz, CD_3CN) δ 154.86, 134.80, 129.37, 127.50, 124.32, 108.85, 57.68, 49.13, 35.60, 31.29, 21.64, 20.87. HRMS (ESI) *m/z* calcd for $C_{25}H_{41}N_2$ (**3b**$^+$): 369.3264, found 369.3267.

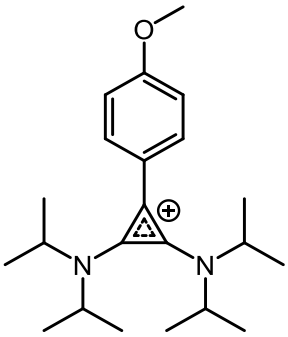

Synthesis of [3c$^+$][PF$_6$]: The general procedure was followed using anisole as the substrate. [**3c**$^+$][PF_6] was isolated as a white powder (112 mg, 35%). R_F = 0.21 in 5% acetonitrile/CH_2Cl_2. ^{1}H NMR (401 MHz, CD_3CN) δ 7.47–7.36 (m, 2H), 7.17–7.08 (m, 2H), 4.07 (sept, J = 6.6 Hz, 2H), 3.89 (sept, 2H), 3.86 (s, 3H), 1.36 (d, J = 6.8 Hz, 12H), 1.20 (d, J = 6.8 Hz, 12H). ^{13}C NMR (176 MHz, CD_3CN) δ 162.15, 134.84, 131.29, 118.78, 115.98, 108.91, 57.62, 56.25, 49.14, 21.68, 20.89. HRMS (ESI) *m/z* calcd for $C_{22}H_{35}N_2O$ (**3c**$^+$): 343.2744, found 343.2741.

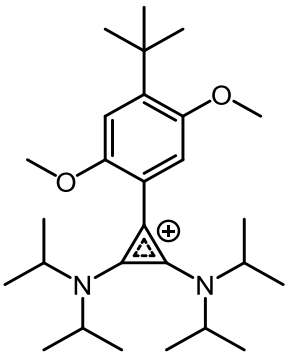

Synthesis of [3d$^+$][PF$_6$]: The general procedure was followed using 1-*tert*-butyl-2,5-dimethoxybenzene as the substrate. [**3d**$^+$][PF_6] was isolated as a white powder (112 mg, 30%). ^{1}H

NMR (401 MHz, CD_3CN) δ 7.06 (s, 1H), 6.88 (s, 1H), 4.10 (sept, *J* = 6.7 Hz, 2H), 3.86 (sept, *J* = 6.7 Hz, 2H), 3.79 (s, 3H), 3.78 (s, 3H), 1.41 (s, 9H), 1.37 (d, *J* = 6.7 Hz, 12H), 1.17 (d, *J* = 6.7 Hz, 12H). ^{13}C NMR (176 MHz, CD_3CN) δ 153.66, 151.55, 143.36, 135.75, 113.72, 112.68, 112.07, 107.07, 57.65, 56.57, 56.54, 49.12, 36.14, 29.67, 21.68, 20.91. HRMS (ESI) *m/z* calcd for $C_{27}H_{45}N_2O_2$ (**3d**$^+$): 429.3476, found 429.3479.

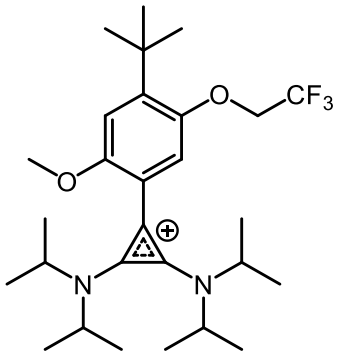

Synthesis of [3e$^+$][PF$_6$]: The general procedure was followed using 1-*tert*-butyl-3-methoxy-6-(2,2,2-trifluoroethoxy)benzene as the substrate. [**3e**$^+$][PF_6] was isolated as a white powder (102 mg, 16%). R_F = 0.30 in 5% acetonitrile/CH_2Cl_2. ^1H NMR (700 MHz, CD_3CN) δ 7.12 (s, 1H), 6.86 (s, 1H), 4.48 (q, *J* = 8.5 Hz 2H), 4.12 (sept, *J* = 6.9 Hz, 2H), 3.87 (sept, *J* = 6.8 Hz, 2H), 3.83 (s, 3H), 1.45 (s, 9H), 1.38 (d, *J* = 6.7 Hz, 12H), 1.17 (d, *J* = 6.7 Hz, 12H). ^{13}C NMR (176 MHz, CD_3CN) δ 152.64, 150.86, 143.74, 135.89, 125.66, 114.42, 113.03, 112.53, 106.53, 66.47 (q, *J* = 35.3 Hz), 57.87, 56.69, 49.14, 36.22, 29.74, 21.76, 20.93. ^{19}F NMR (377 MHz, CD_3CN) δ –72.82 (d, *J* = 706.5 Hz, PF_6), –74.04 (t, 3F, *J* = 8.4 Hz, CF_3). HRMS (ESI) *m/z* calcd for $C_{28}H_{44}F_3N_2O_2$ (**3e**$^+$): 497.3349, found 497.3348.

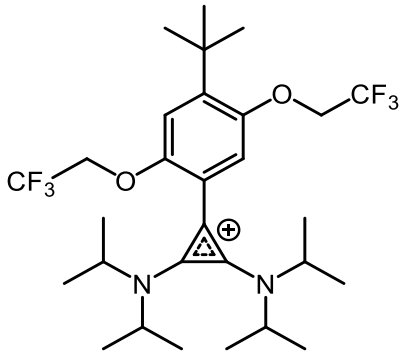

Synthesis of [3f$^+$][PF$_6$]: The general procedure was followed using 1-*tert*-butyl-2,5-bis(2,2,2-trifluoroethoxy)benzene as the substrate. [**3f**$^+$][PF$_6$] was isolated as a white powder (118 mg, 17%). R_F = 0.32 in 5% acetonitrile/CH_2Cl_2. ^{1}H NMR (700 MHz, CD_3CN) δ 7.11 (s, 1H), 6.91 (s, 1H), 4.58 (q, *J* = 8.4, 2H), 4.52 (q, *J* = 8.5, 2H), 4.13 (sept, *J* = 6.7 Hz, 2H), 3.87 (sept, *J* = 6.7 Hz, 2H), 1.44 (s, 9H), 1.38 (d, *J* = 6.8 Hz, 12H), 1.15 (d, *J* = 6.8 Hz, 12H). ^{13}C NMR (176 MHz, CD_3CN) δ 152.06, 149.67, 143.90, 136.05, 125.33, 124.03, 123.76, 114.27, 113.90, 105.60, 66.82 (q, *J* = 35.5 Hz), 66.36 (q, *J* = 35.4 Hz), 58.18, 49.07, 36.27, 29.67, 21.77, 20.89. ^{19}F NMR (377 MHz, CD_3CN) δ –72.82 (d, *J* = 706.4 Hz, PF_6), –73.98 (t, 3F, *J* = 8.4 Hz, CF_3), –74.65 (t, 3F, *J* = 8.3 Hz, CF_3). HRMS (ESI) *m/z* calcd for $C_{29}H_{43}F_6N_2O_2$ (**3f**$^+$): 565.3223, found 565.3226.

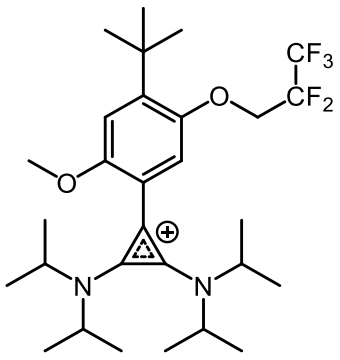

Synthesis of [3g$^+$][PF$_6$]: The general procedure was followed using 1-*tert*-butyl-3-methoxy-6-(2,2,3,3,3-pentafluoropropoxy)benzene as the substrate. [**3g**$^+$][PF$_6$] was isolated as a white powder (202 mg, 29%). R_F = 0.31 in 5% acetonitrile/CH_2Cl_2. ^{1}H NMR (401 MHz, CD_3CN) δ 7.11 (s, 1H),

6.89 (s, 1H), 4.54 (t, J = 13.4 Hz, 2H), 4.10 (sept, J = 6.8 Hz, 2H), 3.86 (sept, J = 6.8 Hz, 2H), 3.81 (s, 3H), 1.42 (s, 9H), 1.37 (d, J = 6.7 Hz, 12H), 1.15 (d, J = 6.7 Hz, 12H). ^{13}C NMR (176 MHz, CD_3CN) δ 152.73, 150.99, 143.92, 135.89, 114.74, 113.08, 112.52, 106.51, 65.81 (t, J = 26.2 Hz), 57.88, 56.69, 49.14, 36.21, 29.72, 21.77, 20.93. The ^{13}C resonances corresponding to the CF_2CF_3 group were poorly resolved due to carbon-fluorine coupling. ^{19}F NMR (377 MHz, CD_3CN) δ –72.82 (d, J = 705.7 Hz, PF_6), –84.02 (m, 3F, CF_3), –123.33 (m, 2F, CF_2). HRMS (ESI) *m/z* calcd for $C_{29}H_{44}F_5N_2O_2$ (**3g**$^+$): 547.3317, found 547.3320.

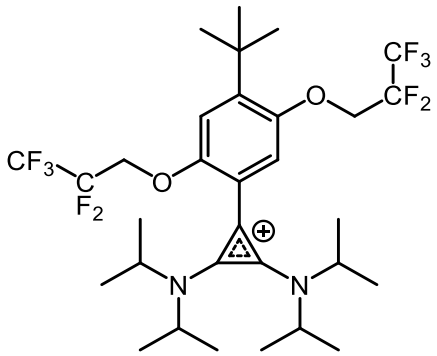

Synthesis of [3h$^+$][PF$_6$]: The general procedure was followed using 1-*tert*-butyl-2,5-bis(2,2,3,3,3-pentafluoropropoxy)benzene as the substrate. [**3h**$^+$][PF_6] was isolated as a white powder (107 mg, 13%). R_F = 0.31 in 5% acetonitrile/CH_2Cl_2. ^{1}H NMR (401 MHz, CD_3CN) δ 7.10 (s, 1H), 6.92 (s, 1H), 4.62 (m, 4H), 4.10 (sept, J = 6.8 Hz, 2H), 3.84 (sept, J = 6.8 Hz, 2H), 1.42 (s, 9H), 1.36 (d, J = 6.7 Hz, 12H), 1.13 (d, J = 6.7 Hz, 12H). ^{13}C NMR (176 MHz, CD_3CN) 152.21, 149.49, 144.04, 135.95, 114.46, 114.04, 113.50, 105.54, 65.90 (t, J = 26.5 Hz), 65.64 (t, J = 26.5 Hz), 58.29, 49.12, 36.30, 29.64, 21.75, 20.86. The ^{13}C resonances corresponding to the CF_2CF_3 groups were poorly resolved due to carbon-fluorine coupling.^{19}F NMR (377 MHz, CD_3CN) δ –72.82 (d, J = 706.4 Hz, PF_6), –83.60 (m, 3F, CF_3), –84.07 (m, 3F, CF_3), –123.31 to –123.41 (m, 4F, CF_2). HRMS (ESI) *m/z* calcd for $C_{31}H_{43}F_{10}N_2O_2$ (**3h**$^+$): 665.3159, found 665.3169.

4.4.2 DFT Calculation Methods and Data

All calculations were done in Spartan (Wavefunction, Inc.). The 6-31G* basis set was used for geometry optimization and 6-311+G** was used for energy and other calculations at the optimized geometry. All were done in "polar solvent," which uses a conductor-like polarizable continuum model for the solvent with a dielectric constant of 37.22, very close to that of acetonitrile. As stated in the main text, to obtain an appropriate constant for this set of molecules to convert to a solution-phase oxidation potential versus $Fc^{+/0}$, a calculation was performed on the tris(diethylamino)cyclopropenium cation, which we have previously reported to have an oxidation potential of +0.82 V versus $Fc^{+/0}$ in acetonitrile. Its calculated ionization energy of 5.39 eV indicates that subtraction of 4.57 eV from the calculated ionization energies will give solution-phase oxidation potentials versus $Fc^{+/0}$ (in V).

The calculated energies of the cations and dication radicals (in hartrees) are given in the following table. The difference between the two gives the ionization energy, which was then converted to an ionization energy in eV. Subtraction of 4.57 V (determined from the tris(diethylamino)cyclopropenium calculation) gives a solution-phase oxidation potential vs $Fc^{+/0}$.

Table 4.2. Calculated Oxidation Potentials

compound number	monocation energy (hartrees)	dication radical energy (hartrees)	IE (hartrees)	IE (eV)	calculated $E_{1/2}$ (V vs Fc)
3a$^+$	929.675093	929.447039	0.228054	6.205668616	1.6357
3b$^+$	1086.972478	1086.749105	0.223373	6.078292052	1.5083
3c$^+$	1044.235448	1044.020077	0.215371	5.860546429	1.2905
3d$^+$	1316.08195	1315.878596	0.203354	5.533547036	0.9635
3e$^+$	1653.233199	1653.023575	0.209624	5.704162514	1.1342
3f$^+$	1990.379359	1990.166302	0.213057	5.79757925	1.2276
3g$^+$	1891.090175	1890.880605	0.20957	5.702693098	1.1327
3h$^+$	2466.093845	2465.880065	0.21378	5.817253092	1.2473

$\mathbf{1}^{+}$	753.933119	753.735044	0.198075	5.389898055	0.8199
$\mathbf{2}^{+}$	1136.10204	1135.882978	0.219062	5.960983707	1.391

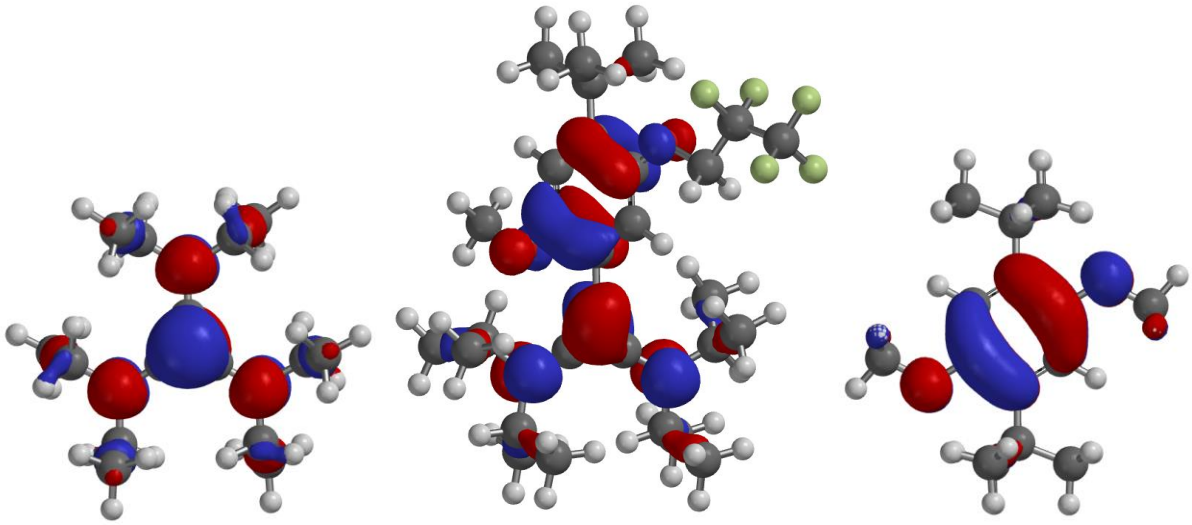

Figure 4.10. The SOMOs of tris(diethylamino)cyclopropenium dication radical (left), 1,4-dimethoxy-2,5-di-*tert*-butylbenzene radical cation (right), and $\mathbf{3g}^{\cdot 2+}$ (middle).

4.4.3 Electrochemistry Experimental Procedures

General methods and materials. Acetonitrile (anhydrous, 99.8%) was obtained from Sigma Aldrich and used as received. Potassium hexafluorophosphate (KPF_6; electrochemical grade) was obtained from Sigma Aldrich and dried under high vacuum for 48 h at 70 °C before being transferred to a N_2-filled glovebox. A 0.50 M stock solution of KPF_6 in acetonitrile was prepared in a N_2-filled glovebox and dried over 3Å molecular sieves for at least two days prior to use. The Celgard 2500 membrane was generously provided by the Celgard company and used as received.

Cyclic voltammetry. Cyclic voltammetry (CV) was performed in a N_2-filled glovebox with a Biologic VSP multichannel potentiostat/galvanostat using a three-electrode electrochemical cell, consisting of a glassy carbon disk working electrode (0.071 cm^2, BASi), a Ag/Ag^+ reference

electrode (BASi) with 0.01 M $AgBF_4$ (Sigma) and 0.5 M KPF_6 in acetonitrile, and a platinum wire counter electrode. All experiments were conducted in a 0.50 M KPF_6 electrolyte stock solution.

Half-cell cycling. Bulk charge/discharge measurements were carried out in a N_2-filled glovebox with a BioLogic VSP galvanostat in a custom glass H-cell with an ultrafine fritted glass separator (P5, Adams and Chittenden). The working and counter electrodes were reticulated vitreous carbon (100 ppi, ~70 cm^2 surface area, Duocel). A Ag/Ag^+ reference electrode was used on the working side of the H-cell. The electrolyte contained 5 mM active species and 0.50 M KPF_6 in acetonitrile. The working chamber of the H-cell was loaded with 5.0 mL of the electrolyte solution, and the counter side was loaded with 5.0 mL of a solution containing methyl viologen hexafluorophosphate. Both chambers were stirred continuously during cycling at a current of 5 mA. Voltage cutoffs of +0.3 V higher than $E_{1/2}$ as the upper limit and +0.5 V as the lower limit were employed.

Flow cell cycling. Cycling under flow conditions was performed with a zero-gap flow cell comprised of graphite charge collecting plates containing an interdigitated flow field in combination with two layers of non-woven carbon felt electrodes (Sigracet 29AA) on each side.[46] PTFE gaskets were used to achieve ~20% compression of the felt. Two Celgard 2500 membranes or separated the two half cells, and the exposed area of the membrane in the gasket window was used as the active area (2.55 cm^2). After assembly, both sides of the cell were loaded with 6.0 mL of a mixed solution containing 0.050 M [**3g**$^+$][PF_6] and 0.050 M butyl viologen hexafluorophosphate in 0.50 M KPF_6/acetonitrile. The cell was pretreated by continuously flowing the solution above at 10 mL/min for 1 h without any charging process using a peristaltic pump (Cole-Parmer) with Solve-Flex and PFA tubing. After this step, using the same flow rate, galvanostatic charge/discharge cycling was performed using a BioLogic VSP galvanostat

employing a charging current of +30 mA/cm^2 and a discharging current of –30 mA/cm^2 with 2.5 V and 0.5 V voltage limits. A flow cell with [**2**$^+$][PF_6^-] catholyte was set up similarly, except that one Fumasep® FAP-375-PP membrane was used, the supporting electrolyte was 0.50 M [NBu_4][PF_6], charge and discharge currents of 10 mA/cm^2 were used, and the cutoff voltages were 2.65 V and 0.50 V.

In the symmetrical flow cell test, one side of the cell was loaded with 5.0 mL of 0.30 M [**3g**$^+$][PF_6] and 0.50 M KPF_6 in CH_3CN and the other side was loaded with 5.0 mL of 0.30 M [**3g**$^{2+}$][PF_6]$_2$ and 0.50 M KPF_6 in CH_3CN. The [**3g**$^{2+}$][PF_6]$_2$ solution was prepared by bulk electrolysis according to a previous method.[47] One Fumasep® FAP-375-PP membrane was used and charge and discharge currents of 35 mA/cm^2 were used, and the cutoff voltages were 0.8 V and -0.8 V.

Determination of the Diffusion Coefficient and Electron Transfer Rate Constant of 3g$^+$.

The diffusion coefficient of **3g**$^+$ was determined by varying the scan rate of cyclic voltammetry measurements between 20 and 300 mV/s, with the data shown in Table S2. Plotting the cathodic and anodic peak currents versus the square root of the scan rate showed a linear relationship, indicating a transport-limited redox process (Figure S1). The slope of this linear relation was used in the Randles-Sevcik equation (eq 1) to determine the diffusion coefficient.[48]

$$i_p = 0.4463\, nFAC\sqrt{\frac{nFvD}{RT}} \qquad (1)$$

The terms of the equation: i_p the peak current in amps, n the number of electrons transferred, F is Faraday's constant, A the area of the electrode in cm^2, C the concentration of redox active species in mol·cm^{-3}, D the diffusion coefficient in cm^2·s^{-1}, v the scan rate in V s^{-1}, R the ideal gas constant (8.314 J·mol^{-1}·K^{-1}), and T the temperature in K.

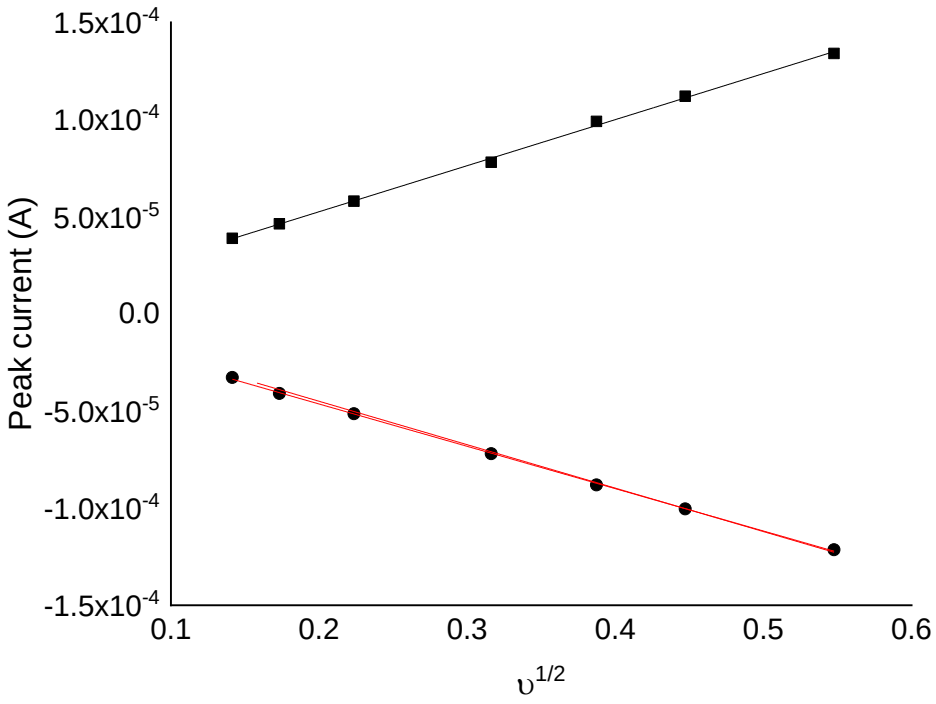

Figure 4.11 Peak current vs square root of the scan rate and linear fits used to determine diffusion coefficients.

The heterogeneous electron transfer rate constant was determined following the Nicholson method.[49] At each scan rate, the separation between the potential of the anodic and cathodic peaks, ΔE_p, can be converted to a dimensionless number Ψ using a "working curve" of the Nicholson paper. The data is given in Table S3. Plotting the resulting values of Ψ versus the inverse square root of the scan rate (Figure S2) gave a relationship from which the slope was used to determine the heterogeneous electron transfer rate constant k_0 according to eq 2,

$$\psi = \frac{\gamma^{\alpha} k_0}{\sqrt{\pi a D_0}} \qquad (2)$$

where Ψ is the Nicolson dimensionless number, $\gamma = D_o/D_r$, where D_o and D_r are the diffusion coefficients ($cm^2 \cdot s^{-1}$) of the oxidized and reduced species, respectively, α is the charge transfer coefficient (assumed to be 0.5), k_0 is the rate constant in $cm \cdot s^{-1}$, $a = nF\nu/RT$, where n is the number of electrons transferred in redox reaction, F is the Faraday constant (96485 C mol^{-1}), ν is the scan

rate in $V \cdot s^{-1}$, R is the ideal gas constant (8.314 J mol^{-1} K^{-1}), T is the temperature in K.

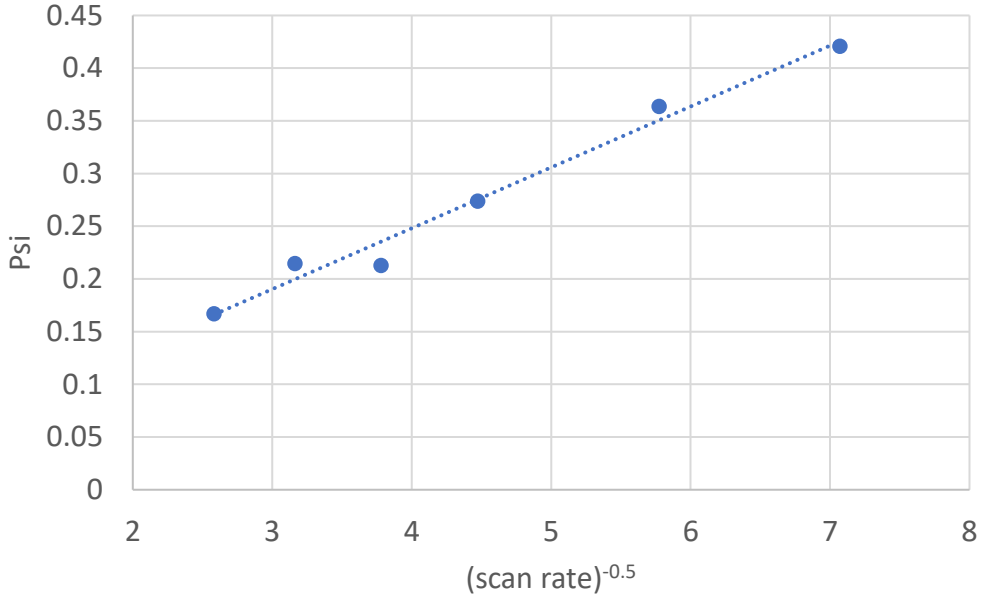

Figure 4.12 Plot of Ψ versus (scan rate)$^{-0.5}$. The slope was used to determine the heterogeneous electron transfer rate constant.

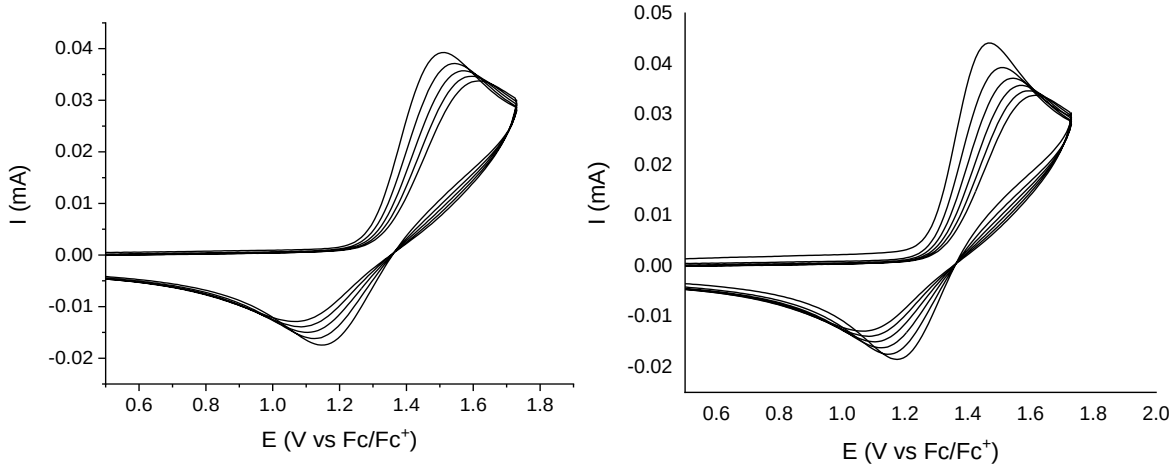

Figure 4.13 Five cycles (#2-6) of cyclic voltammograms of [**3f**$^{+}$][PF_6] (left) and then another six cycles after cleaning the electrode (right) (both in 0.50 M KPF_6 MeCN solution, 100 mV/s scan rate).

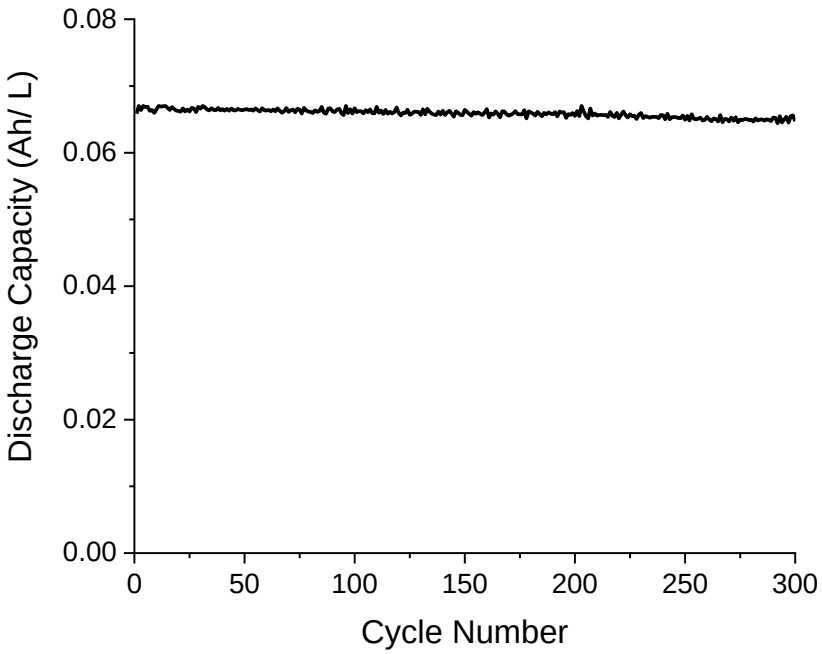

Figure 4.14 H-cell bulk charge-discharge cycling data for 1,4-di-*tert*-butyl-2,5-bis(2-methoxyethoxy)benzene.

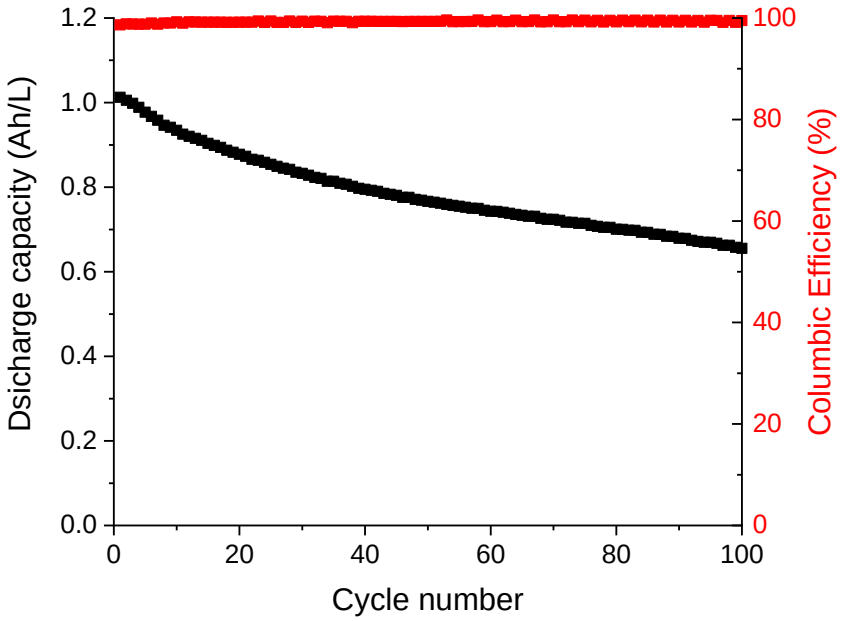

Figure 4.15 Discharge capacity and coulombic efficiency of flow cell cycling of 50 mM [**3g**$^+$][PF_6] and 50 mM butyl viologen in 0.50 M KPF_6-MeCN solution using one Fumasep® FAP-375-PP membrane.

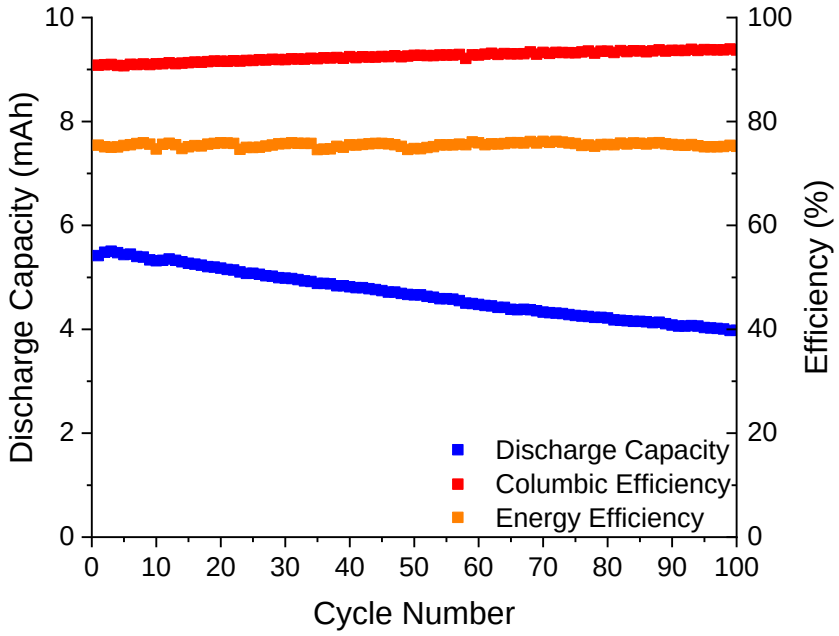

Figure 4.16 Discharge capacity, coulombic efficiency, and energy efficiency of flow cell cycling of 50 mM [**3g**$^+$][PF_6] and 50 mM butyl viologen in 0.50 M KPF_6-MeCN solution using two Celgard 2500 membrane

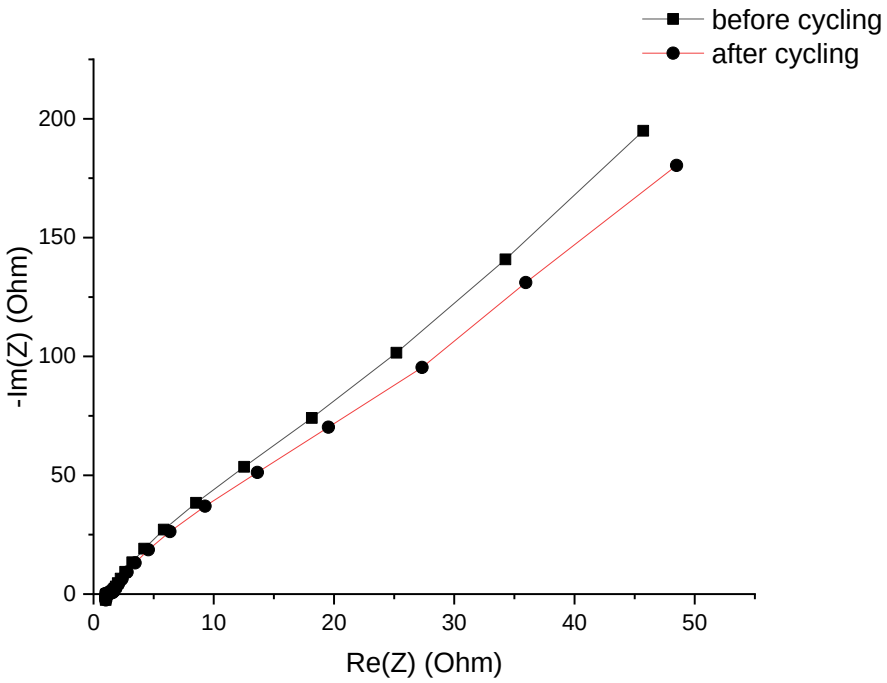

Figure 4.17 Nyquist plot from electrochemical impedance spectroscopy measurements on the **3g**$^{+}$-butyl viologen flow battery before and after cycling

4.5 References

(1) Denholm, P.; Ela, E.; Kirby, B.; Milligan, M. *Role of Energy Storage with Renewable Electricity Generation*; NREL/TP-6A2-47187; National Renewable Energy Lab. (NREL), Golden, CO (United States), 2010. https://doi.org/10.2172/972169.

(2) Hou, Y.; Vidu, R.; Stroeve, P. Solar Energy Storage Methods. *Ind. Eng. Chem. Res.* **2011**, *50* (15), 8954–8964. https://doi.org/10.1021/ie2003413.

(3) Soloveichik, G. L. Flow Batteries: Current Status and Trends. *Chem. Rev.* **2015**, *115* (20), 11533–11558. https://doi.org/10.1021/cr500720t.

(4) Winsberg, J.; Hagemann, T.; Janoschka, T.; Hager, M. D.; Schubert, U. S. Redox-Flow Batteries: From Metals to Organic Redox-Active Materials. *Angew. Chem. Int. Ed.* **2017**, *56* (3), 686–711. https://doi.org/10.1002/anie.201604925.

(5) Noack, J.; Roznyatovskaya, N.; Herr, T.; Fischer, P. The Chemistry of Redox-Flow Batteries. *Angew. Chem. Int. Ed.* **2015**, *54* (34), 9776–9809. https://doi.org/10.1002/anie.201410823.

(6) Service, R. F. Advances in Flow Batteries Promise Cheap Backup Power. *Science* **2018**, *362* (6414), 508. https://doi.org/10.1126/science.362.6414.508.

(7) Leung, P.; Shah, A. A.; Sanz, L.; Flox, C.; Morante, J. R.; Xu, Q.; Mohamed, M. R.; Ponce de León, C.; Walsh, F. C. Recent Developments in Organic Redox Flow Batteries: A Critical Review. *J. Power Sources* **2017**, *360*, 243–283. https://doi.org/10.1016/j.jpowsour.2017.05.057.

(8) Kowalski, J. A.; Su, L.; Milshtein, J. D.; Brushett, F. R. Recent Advances in Molecular Engineering of Redox Active Organic Molecules for Nonaqueous Flow Batteries. *Curr. Opin. Chem. Eng.* **2016**, *13*, 45–52. https://doi.org/10.1016/j.coche.2016.08.002.

(9) Wei, X.; Pan, W.; Duan, W.; Hollas, A.; Yang, Z.; Li, B.; Nie, Z.; Liu, J.; Reed, D.; Wang, W.; Sprenkle, V. Materials and Systems for Organic Redox Flow Batteries: Status and Challenges. *ACS Energy Lett.* **2017**, *2* (9), 2187–2204. https://doi.org/10.1021/acsenergylett.7b00650.

(10) Luo, J.; Hu, B.; Hu, M.; Zhao, Y.; Liu, T. L. Status and Prospects of Organic Redox Flow Batteries toward Sustainable Energy Storage. *ACS Energy Lett.* **2019**, *4* (9), 2220–2240. https://doi.org/10.1021/acsenergylett.9b01332.

(11) Bard, A. J.; Faulkner, L. R. *Electrochemical Methods : Fundamentals and Applications*, 2nd ed.; Wiley: New York :, 2001.

(12) Darling, R. M.; Gallagher, K. G.; Kowalski, J. A.; Ha, S.; Brushett, F. R. Pathways to Low-Cost Electrochemical Energy Storage: A Comparison of Aqueous and Nonaqueous Flow Batteries. *Energy Environ. Sci.* **2014**, *7* (11), 3459–3477. https://doi.org/10.1039/C4EE02158D.

(13) Sevov, C. S.; Samaroo, S. K.; Sanford, M. S. Cyclopropenium Salts as Cyclable, High-Potential Catholytes in Nonaqueous Media. *Adv. Energy Mater.* **2017**, *7* (5), 1602027. https://doi.org/10.1002/aenm.201602027.

(14) Hendriks, K. H.; Robinson, S. G.; Braten, M. N.; Sevov, C. S.; Helms, B. A.; Sigman, M. S.; Minteer, S. D.; Sanford, M. S. High-Performance Oligomeric Catholytes for Effective Macromolecular Separation in Nonaqueous Redox Flow Batteries. *ACS Cent. Sci.* **2018**, *4* (2), 189–196. https://doi.org/10.1021/acscentsci.7b00544.

(15) Bandar, J. S.; Lambert, T. H. Aminocyclopropenium Ions: Synthesis, Properties, and Applications. *Synthesis* **2013**, *45* (18), 2485–2498. https://doi.org/10.1055/s-0033-1338516.

(16) Robinson, S. G.; Yan, Y.; Hendriks, K. H.; Sanford, M. S.; Sigman, M. S. Developing a Predictive Solubility Model for Monomeric and Oligomeric Cyclopropenium-Based Flow Battery Catholytes. *J. Am. Chem. Soc.* **2019**, *141* (26), 10171–10176. https://doi.org/10.1021/jacs.9b04270.

(17) Yan, Y.; Robinson, S. G.; Sigman, M. S.; Sanford, M. S. Mechanism-Based Design of a High-Potential Catholyte Enables a 3.2 V All-Organic Nonaqueous Redox Flow Battery. *J. Am. Chem. Soc.* **2019**, *141* (38), 15301–15306. https://doi.org/10.1021/jacs.9b07345.

(18) Hansch, Corwin.; Leo, A.; Taft, R. W. A Survey of Hammett Substituent Constants and Resonance and Field Parameters. *Chem. Rev.* **1991**, *91* (2), 165–195. https://doi.org/10.1021/cr00002a004.

(19) Marenich, A. V.; Ho, J.; Coote, M. L.; Cramer, C. J.; Truhlar, D. G. Computational Electrochemistry: Prediction of Liquid-Phase Reduction Potentials. *Phys. Chem. Chem. Phys.* **2014**, *16* (29), 15068–15106. https://doi.org/10.1039/C4CP01572J.

(20) Speelman, A. L.; Gillmore, J. G. Efficient Computational Methods for Accurately Predicting Reduction Potentials of Organic Molecules. *J. Phys. Chem. A* **2008**, *112* (25), 5684–5690. https://doi.org/10.1021/jp800782e.

(21) Lynch, E. J.; Speelman, A. L.; Curry, B. A.; Murillo, C. S.; Gillmore, J. G. Expanding and Testing a Computational Method for Predicting the Ground State Reduction Potentials of Organic Molecules on the Basis of Empirical Correlation to Experiment. *J. Org. Chem.* **2012**, *77* (15), 6423–6430. https://doi.org/10.1021/jo300853k.

(22) Chickos, J. S.; Patton, E.; West, R. Aryltrichlorocyclopropenes and Arylhydroxycyclopropenones. *J. Org. Chem.* **1974**, *39* (12), 1647–1650. https://doi.org/10.1021/jo00925a009.

(23) Wu, M. T.; Taub, D.; Patchett, A. A. Preparation and Hydrolysis of Phenylbisdialkylaminocyclopropenium Cations. *Tetrahedron Lett.* **1976**, *17* (28), 2405–2408. https://doi.org/10.1016/0040-4039(76)90004-6.

(24) Moshurchak, L. M.; Lamanna, W. M.; Bulinski, M.; Wang, R. L.; Garsuch, R. R.; Jiang, J.; Magnuson, D.; Triemert, M.; Dahn, J. R. High-Potential Redox Shuttle for Use in Lithium-Ion Batteries. *J. Electrochem. Soc.* **2009**, *156* (4), A309–A312. https://doi.org/10.1149/1.3077578.

(25) Zhang, L.; Zhang, Z.; Redfern, P. C.; Curtiss, L. A.; Amine, K. Molecular Engineering towards Safer Lithium-Ion Batteries: A Highly Stable and Compatible Redox Shuttle for Overcharge Protection. *Energy Environ. Sci.* **2012**, *5* (8), 8204–8207. https://doi.org/10.1039/C2EE21977H.

(26) Brushett, F. R.; Vaughey, J. T.; Jansen, A. N. An All-Organic Non-Aqueous Lithium-Ion Redox Flow Battery. *Adv. Energy Mater.* **2012**, *2* (11), 1390–1396. https://doi.org/10.1002/aenm.201200322.

(27) Huang, J.; Cheng, L.; Assary, R. S.; Wang, P.; Xue, Z.; Burrell, A. K.; Curtiss, L. A.; Zhang, L. Liquid Catholyte Molecules for Nonaqueous Redox Flow Batteries. *Adv. Energy Mater.* **2015**, *5* (6), 1401782. https://doi.org/10.1002/aenm.201401782.

(28) Wei, X.; Duan, W.; Huang, J.; Zhang, L.; Li, B.; Reed, D.; Xu, W.; Sprenkle, V.; Wang, W. A High-Current, Stable Nonaqueous Organic Redox Flow Battery. *ACS Energy Lett.* **2016**, *1* (4), 705–711. https://doi.org/10.1021/acsenergylett.6b00255.

(29) Silcox, B.; Zhang, J.; Shkrob, I. A.; Thompson, L.; Zhang, L. On Transferability of Performance Metrics for Redox-Active Molecules. *J. Phys. Chem. C* **2019**, *123* (27), 16516–16524. https://doi.org/10.1021/acs.jpcc.9b02230.

(30) Huang, J.; Su, L.; A. Kowalski, J.; L. Barton, J.; Ferrandon, M.; K. Burrell, A.; R. Brushett, F.; Zhang, L. A Subtractive Approach to Molecular Engineering of Dimethoxybenzene-Based Redox Materials for Non-Aqueous Flow Batteries. *Journal of Materials Chemistry A* **2015**, *3* (29), 14971–14976. https://doi.org/10.1039/C5TA02380G.

(31) Yang, X.; Kirsch, J.; Fergus, J.; Simonian, A. Modeling Analysis of Electrode Fouling during Electrolysis of Phenolic Compounds. *Electrochimica Acta* **2013**, *94*, 259–268. https://doi.org/10.1016/j.electacta.2013.01.019.

(32) Gong, K.; Fang, Q.; Gu, S.; Li, S. F. Y.; Yan, Y. Nonaqueous Redox-Flow Batteries: Organic Solvents, Supporting Electrolytes, and Redox Pairs. *Energy Environ. Sci.* **2015**, *8* (12), 3515–3530. https://doi.org/10.1039/C5EE02341F.

(33) Elgrishi, N.; Rountree, K. J.; McCarthy, B. D.; Rountree, E. S.; Eisenhart, T. T.; Dempsey, J. L. A Practical Beginner's Guide to Cyclic Voltammetry. *J. Chem. Educ.* **2018**, *95* (2), 197–206. https://doi.org/10.1021/acs.jchemed.7b00361.

(34) Nicholson, R. S. Theory and Application of Cyclic Voltammetry for Measurement of Electrode Reaction Kinetics. *Anal. Chem.* **1965**, *37* (11), 1351–1355. https://doi.org/10.1021/ac60230a016.

(35) Kwon, G.; Lee, S.; Hwang, J.; Shim, H.-S.; Lee, B.; Lee, M. H.; Ko, Y.; Jung, S.-K.; Ku, K.; Hong, J.; Kang, K. Multi-Redox Molecule for High-Energy Redox Flow Batteries. *Joule* **2018**, *2* (9), 1771–1782. https://doi.org/10.1016/j.joule.2018.05.014.

(36) Herr, T.; Noack, J.; Fischer, P.; Tübke, J. 1,3-Dioxolane, Tetrahydrofuran, Acetylacetone and Dimethyl Sulfoxide as Solvents for Non-Aqueous Vanadium Acetylacetonate Redox-Flow-Batteries. *Electrochim. Acta* **2013**, *113*, 127–133. https://doi.org/10.1016/j.electacta.2013.09.055.

(37) Sevov, C. S.; Samaroo, S. K.; Sanford, M. S. Cyclopropenium Salts as Cyclable, High-Potential Catholytes in Nonaqueous Media. *Advanced Energy Materials* **2017**, *7* (5), 1602027. https://doi.org/10.1002/aenm.201602027.

(38) Milshtein, J. D.; Kaur, A. P.; Casselman, M. D.; Kowalski, J. A.; Modekrutti, S.; Zhang, P. L.; Attanayake, N. H.; Elliott, C. F.; Parkin, S. R.; Risko, C.; Brushett, F. R.; Odom, S. A. High Current Density, Long Duration Cycling of Soluble Organic Active Species for Non-Aqueous Redox Flow Batteries. *Energy Environ. Sci.* **2016**, *9* (11), 3531–3543. https://doi.org/10.1039/C6EE02027E.

(39) Weng, W.; Tao, Y.; Zhang, Z.; Redfern, P. C.; Curtiss, L. A.; Amine, K. Asymmetric Form of Redox Shuttle Based on 1,4-Di-Tert-Butyl-2,5-Dimethoxybenzene. *J. Electrochem. Soc.* **2013**, *160* (10), A1711–A1715. https://doi.org/10.1149/2.044310jes.

(40) Silcox, B.; Zhang, J.; Shkrob, I. A.; Thompson, L.; Zhang, L. On Transferability of Performance Metrics for Redox-Active Molecules. *J. Phys. Chem. C* **2019**, *123* (27), 16516–16524. https://doi.org/10.1021/acs.jpcc.9b02230.

(41) Moon, K.; Kaifer, A. E. Modes of Binding Interaction between Viologen Guests and the Cucurbit[7]Uril Host. *Org. Lett.* **2004**, *6* (2), 185–188. https://doi.org/10.1021/ol035967x.

(42) Robinson, S. G.; Yan, Y.; Hendriks, K. H.; Sanford, M. S.; Sigman, M. S. Developing a Predictive Solubility Model for Monomeric and Oligomeric Cyclopropenium-Based Flow Battery Catholytes. *J. Am. Chem. Soc.* **2019**, *141* (26), 10171–10176. https://doi.org/10.1021/jacs.9b04270.

(43) Rosenau, C. P.; Jelier, B. J.; Gossert, A. D.; Togni, A. Exposing the Origins of Irreproducibility in Fluorine NMR Spectroscopy. *Angewandte Chemie International Edition* **2018**, *57* (30), 9528–9533. https://doi.org/10.1002/anie.201802620.

(44) Chickos, J. S.; Patton, E.; West, R. Aryltrichlorocyclopropenes and Arylhydroxycyclopropenones. *J. Org. Chem.* **1974**, *39* (12), 1647–1650. https://doi.org/10.1021/jo00925a009.

(45) Wu, M. T.; Taub, D.; Patchett, A. A. Preparation and Hydrolysis of Phenylbisdialkylaminocyclopropenium Cations. *Tetrahedron Letters* **1976**, *17* (28), 2405–2408. https://doi.org/10.1016/0040-4039(76)90004-6.

(46) Milshtein, J. D.; Kaur, A. P.; Casselman, M. D.; Kowalski, J. A.; Modekrutti, S.; Zhang, P. L.; Harsha Attanayake, N.; Elliott, C. F.; Parkin, S. R.; Risko, C.; Brushett, F. R.; Odom, S. A. High Current Density, Long Duration Cycling of Soluble Organic Active Species for Non-Aqueous Redox Flow Batteries. *Energy Environ. Sci.* **2016**, *9* (11), 3531–3543. https://doi.org/10.1039/C6EE02027E.

(47) Sevov, C. S.; Samaroo, S. K.; Sanford, M. S. Cyclopropenium Salts as Cyclable, High-Potential Catholytes in Nonaqueous Media. *Advanced Energy Materials* **2017**, *7* (5), 1602027. https://doi.org/10.1002/aenm.201602027.

(48) Elgrishi, N.; Rountree, K. J.; McCarthy, B. D.; Rountree, E. S.; Eisenhart, T. T.; Dempsey, J. L. A Practical Beginner's Guide to Cyclic Voltammetry. *J. Chem. Educ.* **2018**, *95* (2), 197–206. https://doi.org/10.1021/acs.jchemed.7b00361.

(49) Nicholson, R. S. Theory and Application of Cyclic Voltammetry for Measurement of Electrode Reaction Kinetics. *Anal. Chem.* **1965**, *37* (11), 1351–1355. https://doi.org/10.1021/ac60230a016.

Chapter 5

Simultaneously Enhancing the Redox Potential and Stability of Multi-Redox Organic Catholytes by Incorporating Cyclopropenium Substituents

(published as *J. Am. Chem. Soc.* 2021, 143, 33, 13450–13459)

5.1. Introduction

Redox flow batteries (RFBs) store energy in solutions of redox-active molecules, termed catholytes and anolytes, that undergo oxidation and reduction, respectively, on opposite sides of the cell during battery charging.[1-18] The energy density of an RFB is dictated by three key properties: (1) the potential difference between the paired oxidative and reductive redox events (V_{cell}), (2) the number of electrons transferred on each side of the cell (n), and (3) the concentration of the solution.[19-22] Over the past several decades, a variety of single electron (n = 1) organic catholytes have been developed.[2,12,17,18,23,24] Manipulation of their structures has uncovered derivatives that undergo stable electrochemical cycling at high potentials,[12,25-28] thus enabling a large V_{cell} in redox flow batteries. An attractive strategy to further enhance energy density in these systems would be to translate these insights to multi-electron (n > 1) catholytes. However, to date, the design of high potential, multi-electron catholytes has proven extremely challenging, as the molecular architectures and substituents required to access multiple reversible oxidations typically result in concomitant decreases in their redox potentials.[9,29]

This tradeoff between n and redox potential is exemplified by phenazine and phenothiazine (Figure 5.1), which are rare examples of organic catholytes that undergo two reversible oxidations.[5,9,13,23,29,30] However, both oxidations of the parent phenazine and phenothiazine cores

occur at modest potentials [less than 0.7 V vs ferrocene/ferrocenium (Fc/Fc^+)], thereby limiting V_{cell} for RFBs employing these molecules.[13,29] In addition, the second oxidation of phenothiazine is unstable to electrochemical cycling, which precludes its deployment in an RFB with n = 2.[9] Recent work by Odom and coworkers demonstrated that the introduction of electron-donating methoxy substituents at the 3- and 7-positions of phenothiazine stabilizes the second oxidation, thus enabling two-electron cycling.[9,29] However, the tradeoff for accessing a derivative with two reversible oxidations is that this system has an ~300 mV lower potential for both couples.[9,29]

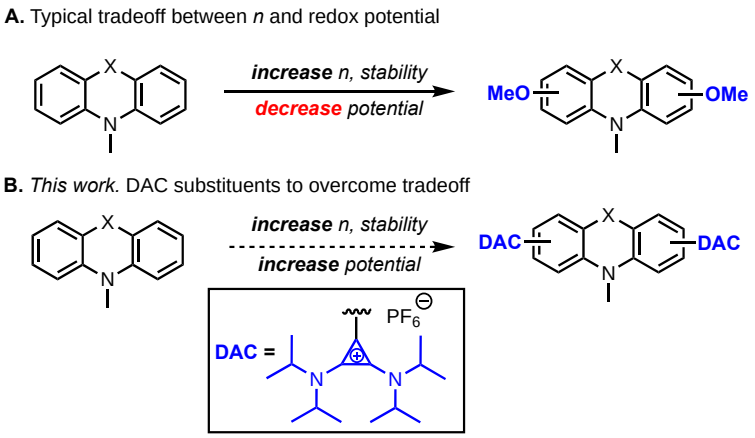

Figure 5.1. Evolution of two-electron catholytes. Phenothiazine, X = S; phenazine, X = NR.

Herein, we demonstrate that the incorporation of diaminocyclopropenium (DAC) substituents onto phenazine and phenothiazine cores can be used to override the stability/potential tradeoff in multi-electron organic catholytes. This idea was predicated on our recent study showing that appending a DAC group to single-electron dialkoxybenzene catholytes results in an ~400 mV increase in redox potential *while maintaining high stability to oxidative cycling*.[26] This led us to hypothesize that the inductive electron-withdrawing but resonance-stabilizing properties of DACs could transform the phenazine and phenothiazine cores into stable, high potential, two-electron catholytes. We report the realization of this concept via the synthesis and electrochemical

evaluation of DAC-substituted phenazine and phenothiazine derivatives. The optimal derivatives are deployed in unsymmetrical, two-electron, non-aqueous RFBs, in which they are paired with a viologen derivative as the anolyte.

5.2. Results and Discussion

DAC substituents on phenazine. Our initial studies probed the impact of DAC substituents on the two-electron catholyte 5,10-dihydro-5,10-dimethylphenazine (**1**, Figure 5.2a)[5,13]. As described above, we hypothesized that the inductive and resonance electron-withdrawing properties of DAC would increase the undesirably low potentials for the two oxidations of **1** (–0.29 V and 0.50 V vs Fc/Fc^+),[5] while resonance delocalization imparted by the DAC groups would maintain the stability of the oxidized species. The target molecule **1-DAC** was synthesized in two steps via an $AlCl_3$-mediated Friedel–Crafts reaction between **1** and tetrachlorocyclopropene followed by reaction of the in situ-generated intermediate with diisopropylamine.[31] Compound **1-DAC** was characterized by NMR spectroscopy, mass spectrometry, and X-ray crystallography (see Supporting Information for complete details).

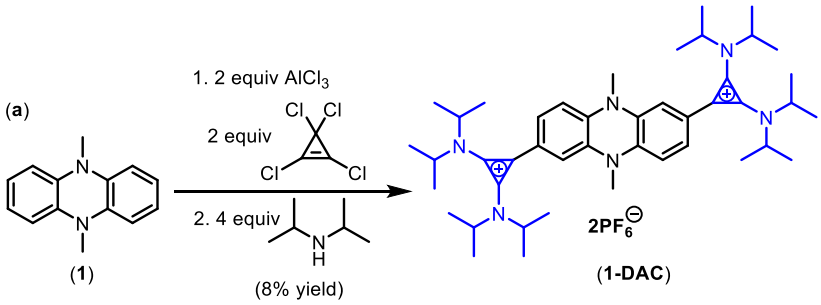

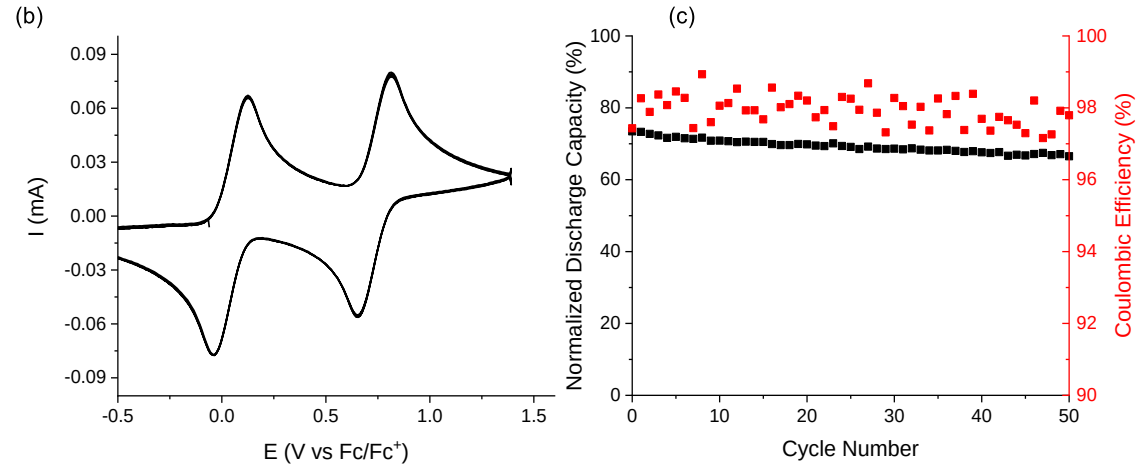

Figure 5.2. (a) Synthesis of **1-DAC**. (b) Five cycles of CV for **1-DAC** (5 mM in 0.5 M $TBAPF_6$/acetonitrile with a glassy carbon working electrode, 100 mV/s). (c) Discharge capacity versus cycle number and coulombic efficiency for two-electron cycling of **1-DAC** (2.5 mM in 0.5 M $TBAPF_6$/acetonitrile) in a static H-cell.

The electrochemical properties of **1-DAC** were initially evaluated using cyclic voltammetry (CV). CV experiments were conducted using a 5 mM solution in 0.5 M NBu_4PF_6/acetonitrile, with a glassy carbon disk working electrode (0.071 cm^2, BASi) and a scan rate of 100 mV/s. Acetonitrile was chosen as the solvent due to its high dielectric constant and its large anodic potential window compared to that of other possible solvents (e.g., water, DMSO, or TEGDME).[32,33,34] Nbu_4PF_6 was selected as the supporting electrolyte as the weakly coordinating anion and cation are expected to minimize interactions of the salt with redox active molecules in solution,[35] while maintaining high conductivity.[36,37] The first oxidation of **1-DAC** occurs at 0.08 V vs Fc/Fc^+, while the second is at 0.78 V vs Fc/Fc^+ under these conditions. Each of these potentials is ~300 mV higher than that of the parent phenazine **1**.[5,13] The ratio of the diffusion-limited peak heights of the cathodic (i_{pc}) and anodic (i_{pa}) peaks for the two oxidations is close to 1, with i_{pc}/i_{pa} = 1.05 (0.08 V) and 0.90 (0.78 V)

at a scan rate of 100 mV/s. In addition, negligible loss of signal is observed after five continuous CVs at the 100 mV/s scan rate (Figure 5.2b).

The experiments above establish that **1-DAC** is stable on the (relatively short) CV timescale. However, for successful deployment in a redox flow battery, a catholyte must display long-term stability in all oxidation states. This can be assessed by two types of experiments: (1) shelf stability tests, where a solution of the charged form of the molecule is monitored for decomposition over time, and (2) electrochemical cycling experiments, where capacity retention is monitored during extended bulk charge-discharge cycling. To evaluate the shelf stability of the doubly oxidized form, **1-DAC**$^{2+}$, a 2.5 mM sample of **1-DAC**$^{2+}$ in 0.5 M Nbu_4PF_6/acetonitrile was generated via bulk electrolysis. This purple brown solution was then stored at room temperature in a N_2-filled glovebox and was analyzed by CV every 2 days to test for decomposition. Over 7 days at room temperature, no decomposition was detected, indicating high shelf stability of **1-DAC**$^{2+}$.

Galvanostatic charge-discharge experiments were next performed in a three-electrode H-cell to interrogate the stability of **1-DAC** towards two-electron electrochemical cycling. The H-cell was separated with an ultrafine glass frit and contained reticulated vitreous carbon (RVC) working and counter electrodes. The working side of the cell was loaded with 5.0 mL of a 2.5 mM solution of **1-DAC** in 0.5 M $TBAPF_6$/acetonitrile, while the counter electrode side contained 5.0 mL of a 5 mM solution of methyl viologen (a commonly used anolyte)[34-38] in 0.5 M $TBAPF_6$/acetonitrile. The cell was charged at a rate of 5 mA (7.5 C) using voltaic cutoffs to maximize the state-of-charge. The discharge capacity was then monitored versus cycle number. Approximately 70% material utilization was attained during two-electron cycling of **1-DAC**. The redox potential was simultaneously monitored to ensure that all the cycling involves **1-DAC** and not its decomposition products.

As shown in Figure 5.2c, **1-DAC** shows 91% capacity retention over 50 cycles. In addition, cycling occurs with ~98% coulombic efficiency throughout the experiment. These data can be compared to those for the parent phenazine **1**, which cycles at 300 mV lower potential than **1-DAC**. Under otherwise similar conditions, **1** shows comparable capacity retention: ~95% over 50 cycles.[5] Overall, these studies demonstrate that the incorporation of DAC substituents on **1** results in the predicted increase in potential of both redox couples without sacrificing electrochemical cycling stability.

DAC substituents on phenothiazine. We next applied an analogous approach to 10-methylphenothiazine (**2**), a catholyte with modest redox potential and poor cycling stability for the second oxidation.[9] We hypothesized that the DAC substituents would increase the redox potential while stabilizing the second oxidation. As described in Figure 5.1, this would be counter to most other literature reports (e.g., Odom's methoxy-substituted phenothiazines)[9,12,25] where a tradeoff is typically observed between stability and potential. The target compound **2-DAC** was prepared by an analogous electrophilic aromatic substitution/amine substitution sequence (Figure 5.3a), and the product was characterized via NMR spectroscopy, mass spectrometry, and X-ray crystallography.

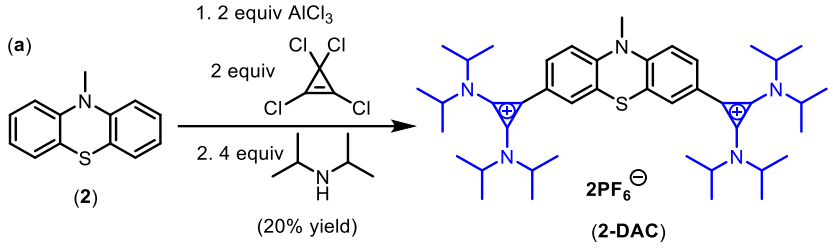

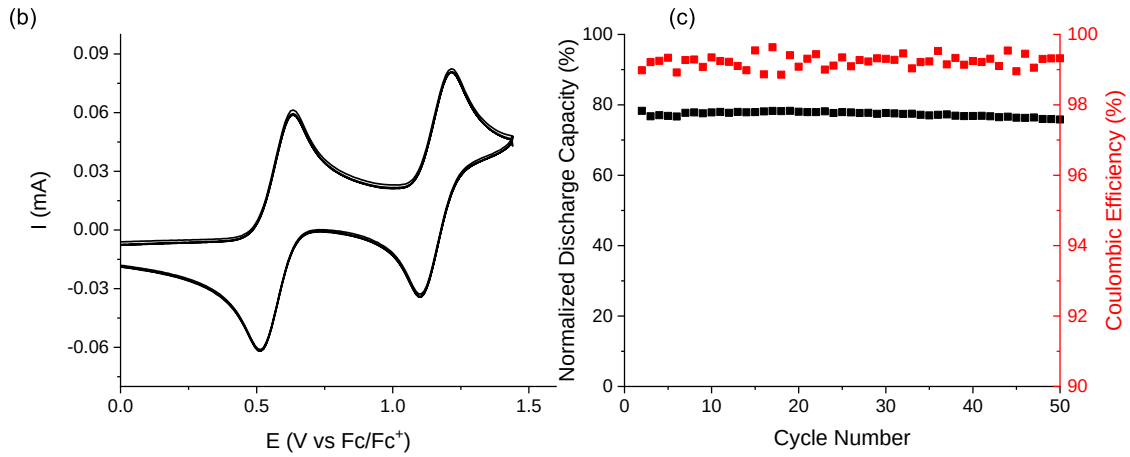

Figure 5.3. (a) Synthesis of **2-DAC**. (b) Five cycles of CV for **2-DAC** (5 mM in 0.5 M $TBAPF_6$/acetonitrile with a glassy carbon working electrode, 100 mV/s). (c) Discharge capacity versus cycle number and coulombic efficiency for two-electron cycling of **2-DAC** (2.5 mM in 0.5 M $TBAPF_6$/acetonitrile) in an H-cell.

Compound **2-DAC** was assessed using a similar set of experiments as those employed for **1-DAC** above. The CV of **2-DAC** shows two oxidations at +0.63 V and +1.20 V vs Fc/Fc^+ (Figure 5.3b). These are ~300 mV higher than those for the parent 10-methylphenothiazine and more than 600 mV higher than those of the stable two-electron catholyte, 3,7-OMe-substituted derivative, **2-OMe**. The i_{pc}/i_{pa} values for each couple at 100 mV/s scan rate are 0.93 (0.63 V) and 0.87 (1.2 V), and minimal loss of CV signal was observed over five CV cycles (Figure 5.3b).

A shelf stability test was conducted for a 2.5 mM solution of the doubly oxidized compound **2-DAC**$^{2+}$. Analysis by CV over 1 week at room temperature in N_2-filled glovebox showed no observable decomposition. H-cell cycling experiments show that **2-DAC** exhibits comparable or even higher electrochemical cycling stability than **2-OMe**[9] for two-electron cycling, despite the 600 mV increase in redox potential. As shown in Figure 3c, only 3% capacity loss is observed over

50 cycles while cycling at 80% of the theoretical capacity and with 99% coulombic efficiency. In summary, these experiments demonstrate that DAC substituents effectively defy the tradeoff between stability and potential in two-electron organic catholytes.

Mass transport and electrokinetics. The mass transport and electrokinetics of **1-DAC** and **2-DAC** were next evaluated. These properties are imperative for effective flow battery applications because fast diffusional and electron-transfer processes are required to achieve high current densities and low overpotentials.[43] The increased size/molecular weight of **1-DAC** and **2-DAC** relative to the parent heterocycles raises the possibility that these processes could be prohibitively slow. Diffusion coefficients were determined by varying the CV scan rate from 20 to 700 mV/s and then applying the Randles–Sevcik equation (Figure 5.8). The observed values for **1-DAC** (first couple: 5.29×10^{-6} cm^2/s; second couple: 4.99×10^{-6} cm^2/s) and **2-DAC** (first couple: 5.40×10^{-6} cm^2/s; second couple: 3.56×10^{-6} cm^2/s) are in the range of those of the parent molecules tris(dialkylamino)cyclopropenium (7.0×10^{-6} cm^2/s),[44] 10-methylphenothiazine (2.3×10^{-6} cm^2/s),[29] and 5,10-dihydro-5,10-dimethylphenazine (8.82×10^{-6} cm^2/s).[5]

Heterogeneous electron-transfer rates were determined for **1-DAC** (first couple: 3.65×10^{-3} cm/s; second couple: 3.54×10^{-3} cm/s) and **2-DAC** (first couple: 2.53×10^{-3} cm/s; second couple: 3.47×10^{-3} cm/s) using the Nicholson method[45] (Figure 5.9). Again, these are comparable to that of tris(dialkylamino)cyclopropenium (2.2×10^{-3} cm/s) and 5,10-dihydro-5,10-dimethylphenazine (5.53×10^{-3} cm/s).[5] Furthermore, the observed values for **1-DAC** and **2-DAC** are also similar to those of other catholyte materials such as ferrocene derivatives, dialkoxybenzene derivatives, and $V(acac)_3$.[43,46,47]

Deployment in asymmetric flow cells. Both catholyte candidates **1-DAC** and **2-DAC** were next deployed in prototype redox flow batteries. In comparison to change-discharge cycling in a static

H-cell, full battery cycling presents a variety of additional challenges, including: (1) the presence of multiple interfaces (e.g., tubing, electrode, and membrane) that interact with the redox active molecule; (2) a higher concentration of redox active molecules (2.5 vs 15 mM in this case); (3) the presence of a second change carrier (the anolyte, which undergoes reduction during battery charging); and (4) the possibility for cross-over of catholyte and anolyte through the separator between the two sides of the cell during cycling. All of these factors open the possibility of new decomposition pathways that can significantly decrease capacity retention during flow cell cycling compared to that observed in a static H-cell.[23,48–51]

We note that a key advantage of the DAC substituents, in addition to imparting high potential and stability, is that they serve as permanent cations attached to the phenazine/phenothiazine core. Recent work has demonstrated that such cationic substituents can effectively impede crossover in non-aqueous redox flow batteries separated by the anion exchange membrane Fumasep FAPQ-375-PP.[52] Therefore, we pursued asymmetric RFBs in which **1-DAC** or **2-DAC** were paired with the viologen dimer **3** (used as a two-electron tetracationic anolyte) in order to limit challenges associated with cross-over during cycling. These molecules were cycled in a two-electron battery accessing both oxidation states of the monomeric catholyte and one oxidation state (at –0.80 V vs Fc/Fc^{+})[38] of the dimeric anolyte.[53] This constitutes a V_{cell} of up to 1.6 V for **1-DAC** and up to 2.0 V for **2-DAC**.[54]

Charge-discharge cycling was conducted in a Fumasep FAPQ-375-PP-separated asymmetric flow cell containing a 15 mM solution of **3** (anolyte) and a 15 mM solution of **1-DAC** or **2-DAC** (catholyte) in 0.5 M $TBAPF_6$/acetonitrile. The flow cell contains graphite charge collecting plates with an interdigitated flow field in combination with 400 μm thick carbon-felt electrodes. These Sigracet 29 AA electrodes have a porosity of 80% and electrical resistivity of < 5 mΩ· cm², and

their surface chemistry has been analyzed as detailed in the literature.[55,56] The electrolyte solutions were flowed through the cell at 10 mL/min and were subjected to galvanostatic cycling at 10 mA/cm^2. For the **1-DAC**/**3** battery, the cell potential was 1.6 V, and the initial material utilization was approximately 74%. The energy efficiency was ~50%, and the coulombic efficiency was 100% (Figure 5.4b). Minimal (<5%) crossover from either side was detected, as measured by CV at the completion of cycling (Figure 5.4c). After 250 cycles (77 h), this battery retained 93% of its original capacity.

For the **2-DAC**/**3** battery, the initial material utilization was ~72%, the coulombic efficiency was >99%, and the energy efficiency was ~62% (Figure 5.4d).[57–67] This battery shows 80% retention of the initial capacity after 250 cycles.[68,69] This flow cell provides one of the highest molar energy densities (~92 W h/mol) reported for an RFB, even with the modest reduction potential anolyte (see Supporting Information section V for detailed comparison).[5,70,71] The CVs after cycling (Figure 5.4e) demonstrate that there is <5% crossover over the ~63 h of this experiment, consistent with the cationic DAC substituents limiting crossover through the anion exchange membrane.

We note that the solubilities of **1-DAC** (**~**100 mM) and **2-DAC** (~90 mM) in acetonitrile are not sufficient for a high concentration battery.[72] Therefore, ongoing efforts are focused on developing more soluble versions through rational molecular design. Previous reports have demonstrated that solubility can be enhanced by altering the amino groups on the DAC or by attaching glycol chains to the nitrogen in related structures.[13,29,73,74]

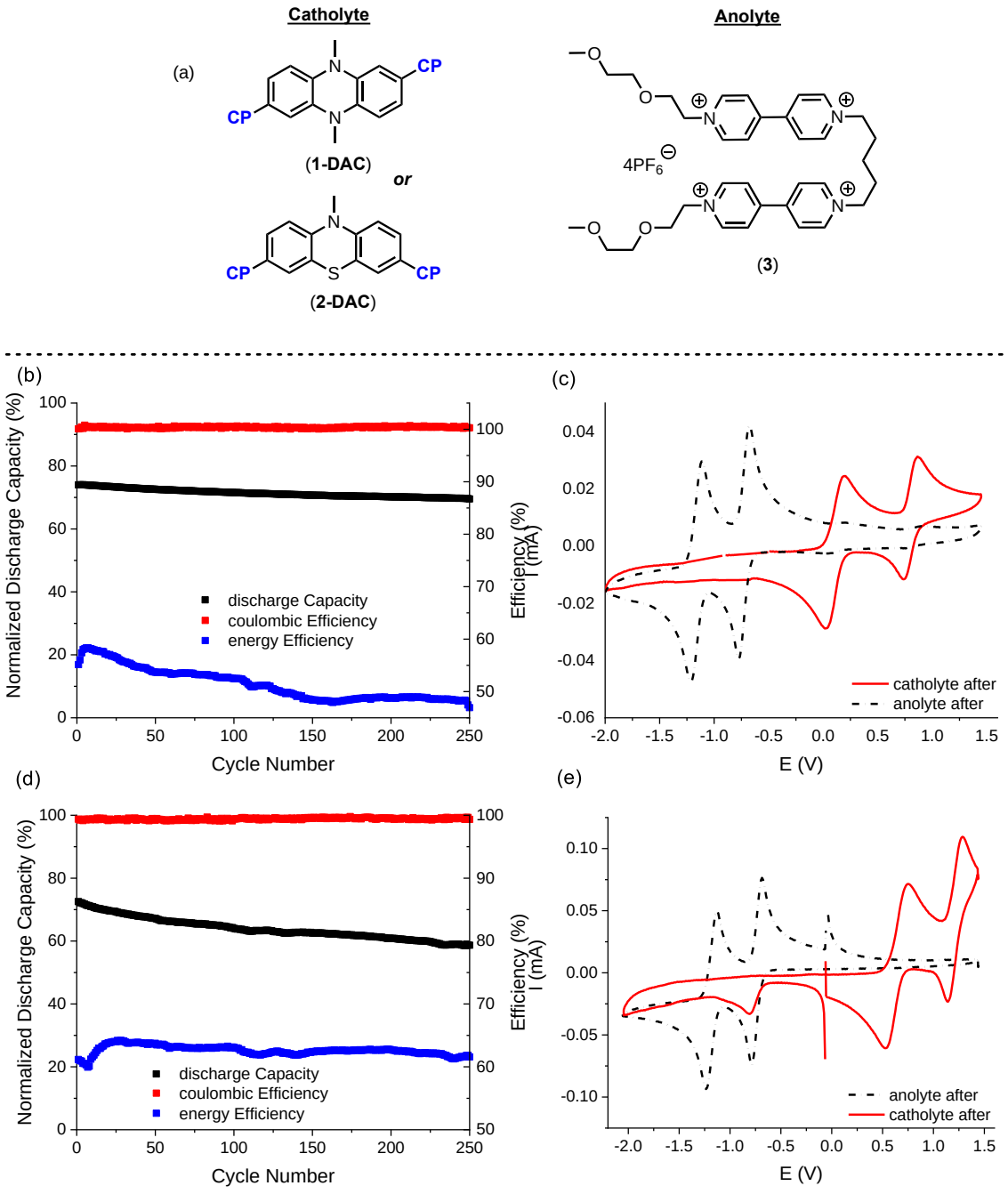

Figure 5.4. (a) Anolyte/catholytes for asymmetric flow cell cycling. (b) Discharge capacity, energy efficiency, and coulombic efficiency versus cycle number for asymmetric flow cell cycling of **1-DAC** and **3**. (c) CV of material from each side of flow cell after cycle 250 for **1-DAC** and **3**. (d) Discharge capacity, energy efficiency, and coulombic efficiency versus cycle number for

asymmetric flow cell cycling of **2-DAC** and **3**. I CV of material from each side of flow cell after cycle 250 for **2-DAC** and **3**.

Computational studies. To obtain further insight into the dual impact of the DAC substituents on the redox potential and cycling stability of phenothiazine, we conducted density-functional theory (DFT) calculations. Computations were carried out at the B3LYP/6-31G(d) level of theory[75,76] on **2-DAC** in the three battery-relevant oxidation states (**2-DAC**, **2-DAC**$^{\bullet+}$, and **2-DAC**$^{2+}$). These structures were then compared to those of the parent *N*-methyl phenothiazine (**2**) as well as to those of Odom's dimethoxy-substituted derivative **2-OMe**. To validate the DFT method, redox potentials were predicted using the computed ionization energies for these structures.[77] The calculated oxidation potentials for **2-DAC** in acetonitrile versus $Fc^{+/0}$ are 0.69 V and 1.2 V, which is in excellent agreement with the experimentally measured values of 0.63 V and 1.2 V. Furthermore, the general trend in oxidation potentials for **2**, **2-OMe**, and **2-DAC** aligns with the experimentally measured values.

The relevant highest occupied molecular orbital (HOMO) or singly occupied molecular orbital (SOMO) for each redox state of the three catholytes is shown in Figure 5.5. A first key observation is that the incorporation of both OMe and DAC substituents results in significantly enhanced delocalization of electron density in all oxidation states. In particular, in the highest energy doubly oxidized state, for **2-OMe**$^{2+}$ and **2-DAC**$^{2+}$, electron density is dispersed away from the phenothiazine core to the periphery of the molecule.

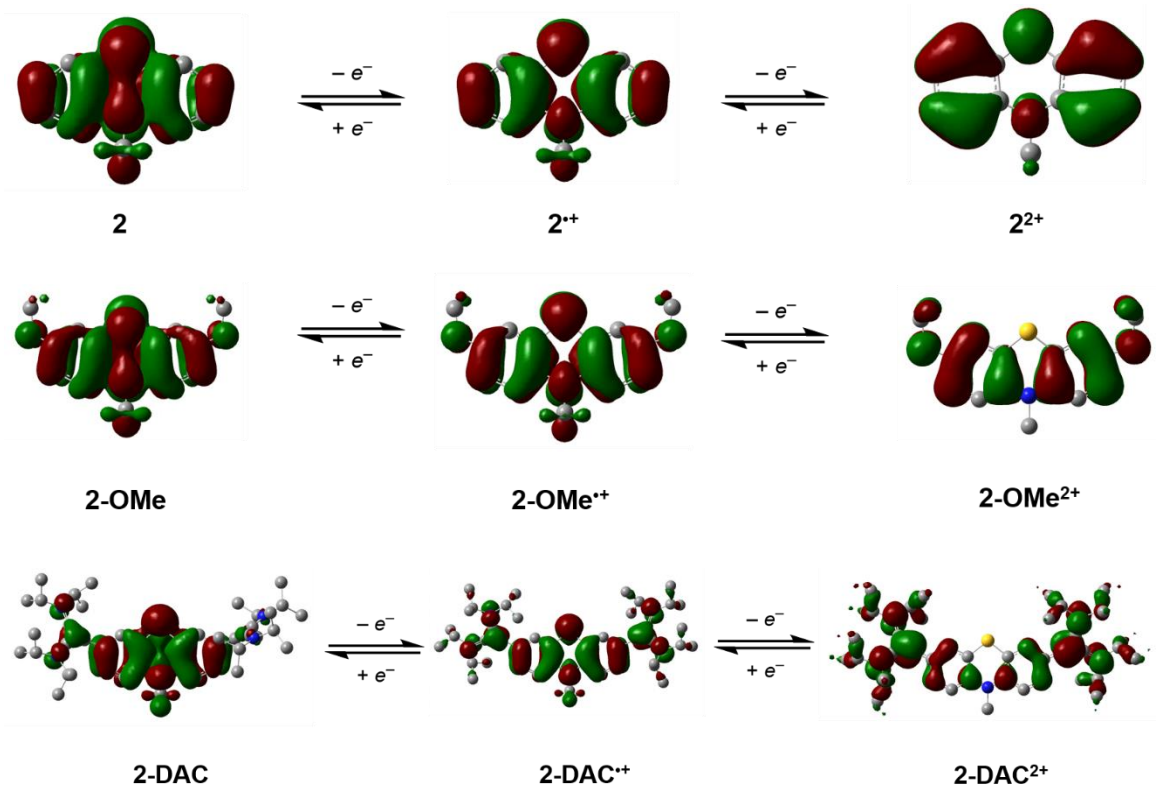

Figure 5.5. HOMO and SOMO visualization of **2**, **2-OMe**, and **2-DAC** (isovalue = 0.02).

The divergent impact of the DAC and OMe substituents on the redox potential can be understood by comparing the computed spin densities in $\mathbf{2}^{\bullet+}$, $\mathbf{2\text{-}OMe}^{\bullet+}$, and $\mathbf{2\text{-}DAC}^{\bullet+}$ (Table 5.1). The difference in OMe and DAC as resonance electron-donating and -withdrawing substituents, respectively, is reflected in the spin densities at nitrogen, the ring heteroatom that is *para*- to the OMe or DAC substituent. Specifically, the spin density at nitrogen in $\mathbf{2\text{-}OMe}^{\bullet+}$ is significantly larger than that in $\mathbf{2}^{\bullet+}$ (0.349 and 0.300, respectively). In contrast, the spin density at nitrogen is significantly reduced in $\mathbf{2\text{-}DAC}^{\bullet+}$ versus in $\mathbf{2}^{\bullet+}$ (0.281 and 0.300, respectively). These data reflect both inductive and resonance electron-withdrawing properties of the DAC substituents.

	Spin density at S (radical cation)	Spin density at N (radical cation)	NBO charge at S (radical cation)	NBO charge at N (radical cation)	NBO charge at S (dication)	NBO charge at N (dication)
2	0.254	0.300	0.401	–0.555	0.644	–0.549
2-OMe	0.117	0.349	0.343	–0.557	0.533	–0.553
2-DAC	0.232	0.281	0.416	–0.564	0.565	–0.562

Table 5.1. NBO charges and spin density of **2**, **2-OMe**, and **2-DAC**

To quantify the inductive electronic effect of the DAC substituent, a Hammett σ-value was estimated for *para*-DAC on a benzoic acid.[78] This analysis involved calculating the C=O stretching frequency for a series of *para*-substituted benzoic acids with reported Hammett values. Extrapolation of the fit of this correlation provided a Hammett σ value of +2.27 for DAC. This value is remarkably large when considered in the context of more commonly utilized electron-withdrawing groups, such as *para*-NO_2 ($\sigma = 0.78$) and *para*-Nme_3^+ ($\sigma = 0.82$). Notably, DAC has a similar σ Hammett value to that predicted for 4-N-methylpyridinium ($\sigma = 2.31$), which was recently demonstrated as an effective substituent for tuning molecular electrocatalyst overpotential through a combination of conjugation, electron-withdrawing ability, and electrostatic effects.[79] As such, we anticipate that the incorporation of DAC substituents on an aromatic core could prove much more broadly useful in contexts where cationic and/or strongly electron withdrawing groups are desired to tune the electronic, electrostatic, and/or solubility properties of molecules, polymers, and/or catalysts.[80–86]

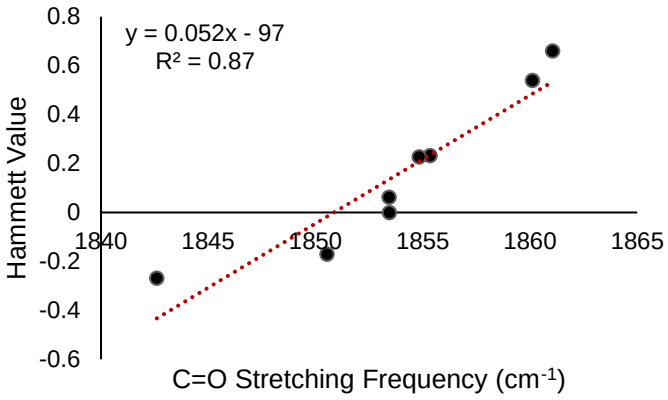

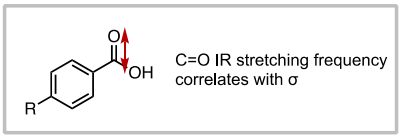

R Para Substituent	σ	C=O stretching frequency (cm^{-1})
OMe	-0.268	1842.6
Me	-0.170	1850.5
H	0.00	1853.4
F	0.062	1853.4
Cl	0.227	1854.8
Br	0.232	1855.3
CF_3	0.54	1860.1
CN	0.66	1861.1
DAC	$2.27_{predicted}$	1894.5

Scheme 5.1. Quantification of electronic effect of DAC substituent

The cycling stability of **2-DAC**, particularly for the **2-DAC**$^{\bullet+}$/**2-DAC**$^{2+}$ redox couple, can be rationalized by examination of the natural bond orbital (NBO) charges in these two oxidation states. The radical cation **2-DAC**$^{\bullet+}$ has significantly more electron density at S and N than in the analogous species **2**$^{\bullet+}$ or **2-OMe**$^{\bullet+}$. However, upon oxidation to the dication, **2**$^{2+}$ has the greatest electron density at S. Comparison of the NBO charges at S in the radical cation and dication redox states demonstrates a more substantial change in the electron density at S for **2**$^{2+}$ (ΔNBO = 0.243) than for either **2-OMe**$^{2+}$ (ΔNBO = 0.190) or **2-DAC**$^{2+}$ (ΔNBO = 0.149). The resonance effects afforded by the substituents [either OMe (donating) or DAC (withdrawing)] enables a greater degree of electron delocalization, which is likely a key factor in the enhanced stability of these species in the doubly oxidized state.

Overall, the electron-withdrawing nature of the DAC unit coincides with an increase in redox potential while stabilizing all redox states through significant delocalization. In addition to these electronic considerations, there is also likely a substantial steric effect of the 3,7-substituents suppressing dimerization decomposition pathways of the oxidized species[87] since previous studies on the decomposition of phenothiazine showed oligomer and polymer could form at the positions *para* to the phenothiazine nitrogen atoms.[30]

5.3 Conclusion

In summary, this report introduces diaminocyclopropenium (DAC) as an inductive electron-withdrawing but resonance-stabilizing substituent for multi-electron RFB catholytes. We demonstrate that the introduction of DAC substituents at appropriate sites transforms the phenazine and phenothiazine cores into stable, high potential two-electron catholytes. The DAC groups significantly increase the oxidation potential relative to the parent heterocycles while concomitantly imparting enhanced stability to the second oxidation. As such, these systems deviate from the typical paradigm in which increasing the redox potential results in decreased stability, particularly in systems with $n > 1$. These new DAC-substituted two-electron catholytes were deployed in prototype flow batteries, where they showed long-duration stable cycling and the added advantage of negligible crossover through an anion-exchange membrane. Overall, we anticipate that DACs and related substituents could prove broadly useful in the design of next-generation multi-electron catholytes for non-aqueous RFBs. More broadly, the unusual properties of DAC substituents, which include being positively charged, strongly inductively electron withdrawing, and capable of resonance delocalizing positive charge and spin density, could prove generally useful in the tailoring the electronic properties of organic molecules, polymers, and catalysts.

5.4. Experimental Procedures and Characterization of Compounds

5.4.1 Synthetic Procedures

General Information. All commercial chemicals were used as received unless stated otherwise. Anhydrous CH_2Cl_2 was obtained from an Innovative Technology, Inc. (now rebranded to Inert) solvent purification system. Reactions were performed under a nitrogen atmosphere. The solubilities of **1-DAC** and **2-DAC** in acetonitrile were determined using a previously reported

method.[73] 2-(2-Methoxyethoxy)ethyl tosylate was prepared by a reported procedure.[88] NMR spectra were obtained on Varian VNMRs 700, Varian VNMRs 500, Varian Inova 500, or Varian MR400 spectrometers. ^{1}H and ^{13}C NMR chemical shifts are reported in parts per million (ppm) relative to TMS, with the residual solvent peak used as an internal reference. High-resolution mass spectroscopy (HRMS) was performed on a Micromass AutoSpec Ultima Magnetic Sector Mass Spectrometer using electrospray ionization (ESI).

General procedure for the synthesis of 1-DAC, 2-DAC, and 2-DAC-2.[89, 90]Tetrachlorocyclopropene (120 mg, 0.67 mmol) and $AlCl_3$ (88 mg, 0.66 mmol) were dissolved in 1,2-dichloroethane (3 mL) at room temperature. This mixture was stirred for 15 min at room temperature to form a white suspension. The reaction mixture was cooled to 0 °C, and 10-methylphenothiazine or 5,10-dihydro-5,10-dimethylphenazine (0.30 mmol, dissolved in 3 mL of 1,2-dichloroethane) was slowly added. The reaction mixture was warmed to room temperature and then heated at reflux overnight. The mixture was then cooled to 0 °C, and diisopropylamine (271 mg, 2.68 mmol) was slowly added. The resulting mixture was stirred at 0 °C for 30 min. It was then filtered, and the filtrate was washed with 10 mL of a 1:1 solution of brine and 2 M HCl. The organic extracts were collected, and the aqueous layer was extracted with CH_2Cl_2 (2 × 15 mL). The combined organic extracts were concentrated under vacuum. The resulting residue was dissolved in water (5 mL), and an aqueous solution of ammonium hexafluorophosphate (NH_4PF_6; 218 mg, 1.34 mmol in 2 mL H_2O) was added with vigorous stirring. A precipitate formed, and this material was extracted into CH_2Cl_2 (3 × 15 mL). The organic extracts were dried over $MgSO_4$ and concentrated under vacuum. The product was then purified by chromatography on silica gel with gradient elution (0 to 8% acetonitrile in CH_2Cl_2). The product-containing fractions were collected

and concentrated under vacuum to a volume of ~1 mL. Diethyl ether (~10 mL) was added to precipitate the product, and the resulting white solid was collected and dried under vacuum.

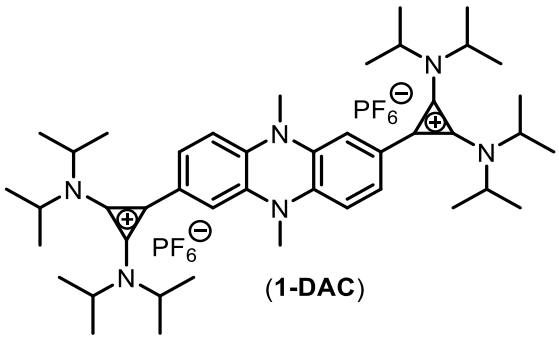

(**1-DAC**)

Synthesis of 1-DAC: The general procedure was followed using 10-methylphenothiazine as the substrate. Compound **1-DAC** was isolated as a yellow powder (20 mg, 8% yield). R_F = 0.28 in 10% acetonitrile/CH_2Cl_2. ^{1}H NMR (700 MHz, acetonitrile-d_3): δ 6.87 (dd, J = 8.1, 1.9 Hz, 2H), 6.60 (d, J = 8.1 Hz, 2H), 6.47 (d, J = 1.8 Hz, 2H), 4.07 (m, 4H), 3.92 (m, 4H), 3.02 (s, 6H), 1.35 (d, J = 6.7 Hz, 24H), 1.24 (d, J = 6.7 Hz, 24H). ^{13}C NMR (176 MHz, acetonitrile-d_3): δ 140.0, 138.5, 133.4, 123.2, 118.6, 111.7, 111.0, 108.2, 56.4, 48.4, 31.9, 20.8, 20.0. HRMS (ESI) *m/z* calcd for $C_{44}H_{68}N_6^{2+}$, [**1-DAC**]$^{2+}$: 340.2747, found: 340.2748.

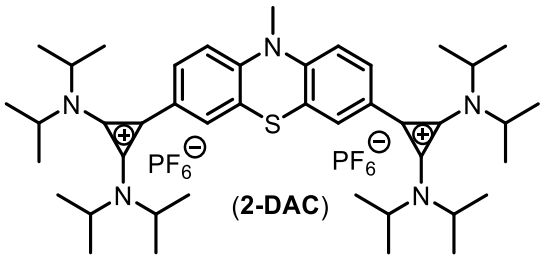

(**2-DAC**)

Synthesis of 2-DAC: The general procedure was followed using 10-methylphenothiazine as the substrate. Compound **2-DAC** was isolated as a yellowish-green powder (57 mg, 20% yield). R_F = 0.30 in 10% acetonitrile/CH_2Cl_2. ^{1}H NMR (700 MHz, acetonitrile-d_3): δ 7.31 (dd, J = 8.4, 2.0 Hz, 2H), 7.18 (d, J = 2.0 Hz, 2H), 7.11 (d, J = 8.5 Hz, 2H), 4.08 (m, 4H), 3.87 (m, 4H), 3.44 (s, 3H),

1.36 (d, J = 6.7 Hz, 24H), 1.18 (d, J = 6.8 Hz, 24H). ^{13}C NMR (176 MHz, acetonitrile-d_3): δ 147.6, 134.9, 129.8, 127.5, 124.5, 121.7, 116.7, 107.7, 57.8, 49.2, 36.3, 21.8, 20.9. HRMS (ESI) *m/z* calcd for $C_{43}H_{65}N_5S^{2+}$, [**2-DAC**]$^{2+}$: 341.7475, found: 341.7480.

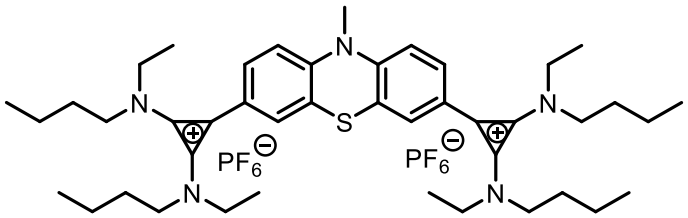

(**2-DAC-2**)

Synthesis of 2-DAC-2: The general procedure was followed using ethylbutylaminotrimethylsilane[90, 91] as the substrate. Compound **2-DAC-2** was isolated as a yellow-green oil (66 mg, 23% yield). R_F = 0.30 in 10% acetonitrile/CH_2Cl_2. ^{1}H NMR (700 MHz, acetonitrile-d_3): δ 7.50-7.43 (m, 2H), 7.31-7.25 (m, 2H), 7.10-7.04 (m, 2H), 3.72-3.66 (m, 4H), 3.65-3.60 (m, 4H), 3.58-3.51 (m, 4H), 3.51-3.46 (m, 4H), 3.45 (s, 3H), 1.73-1.66 (m, 8H), 1.44-1.35 (m, 8H), 1.34-1.29 (m, 12H), 0.99-0.92 (m, 12H).^{13}C NMR (176 MHz, acetonitrile-d_3):δ 147.94, 133.01, 131.20, 128.65, 124.18, 117.40, 116.78, 106.90, 54.30, 53.76, 49.82, 49.41, 36.51, 31.58, 20.33, 14.45, 14.05. HRMS (ESI) *m/z* calcd for $C_{43}H_{65}N_5S^{2+}$, [**2-DAC**]$^{2+}$: 341.7475, found: 341.7475.

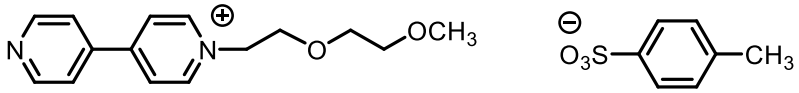

[R-bipy][TsO] (with 0.04 equiv [R-bipy-R][TsO]$_2$). A solution of 4,4′-bipyridine (9.37 g, 60.0 mmol) and 2-(2-methoxyethoxy)ethyl tosylate (4.12 g, 15.0 mmol) in acetonitrile (50 mL) was heated at reflux under N_2 for 48 h. The resulting yellow solution was allowed to cool to room temperature and then transferred to a 500 mL round-bottomed flask (tared with its magnetic stir bar). To the stirred solution was slowly added diethyl ether (400 mL), causing the product to

separate as an oil. The mixture was stirred gently for 2 h during which time the supernatant went from cloudy to clear, and the clear, colorless supernatant was then decanted into a 1 L round-bottomed flask. The product oil was then washed with diethyl ether (2 × 50 mL), stirring for 15 min each time, and these extracts were combined with the original supernatant in the 1 L flask. The solvent was then removed from the combined extracts by rotary evaporation to yield 6.60 g (42.3 mmol) of 4,4′-bipyridine contaminated only with a trace of [R-bipy][TsO]; this 4,4′-bipyridine can be used in subsequent runs of this reaction. The viscous oil product was then stirred with 150 mL of diethyl ether for 16 h, which caused it to solidify to a pale yellow solid. The ether was removed by decantation, and the solid residue was dissolved in acetonitrile (20 mL). A total of 200 mL of diethyl ether was added slowly, causing the product to separate as an oil. After 20 min of stirring, the product had solidified, and the cloudiness of the supernatant had cleared. The supernatant was removed by decantation, and the solid product was placed under vacuum to yield 6.14 g of a pale yellowish solid. ^{1}H NMR spectroscopic analysis showed a 25:1 molar ratio of [R-bipy][TsO] to [R-bipy-R][TsO]$_2$, corresponding to a yield of 13.4 mmol (89% yield) of [R-bipy][TsO], which was used in its entirety for the next step. ^{1}H NMR (500 MHz, DMSO-d_6): δ 9.16 (d, J = 6.7 Hz, 2H), 8.87 (d, J = 6.2 Hz, 2H), 8.64 (d, J = 6.8 Hz, 2H), 8.05 (d, J = 6.3 Hz, 2H), 7.48 (d, J = 8.0 Hz, 2H), 7.10 (d, J = 7.8 Hz, 2H), 4.83 (t, J = 4.9 Hz, 2H), 3.94 (t, J = 4.9 Hz, 2H), 3.56 (m, 2H), 3.37 (m, 2H), 3.16 (s, 3H), 2.27 (s, 3H). [Attributed to R-bipy-R^{2+}: 9.30 (d, J = 6.8 Hz), 8.79 (d, J = 6.7 Hz), 4.89 (t, J = 4.9 Hz).] ^{13}C NMR (126 MHz, DMSO-d_6): δ 152.5, 151.0, 145.8, 140.9, 137.6, 128.1, 126.3, 125.5, 125.0, 122.0, 71.1, 69.5, 68.6, 60.0, 58.1, 20.8. HRMS (ESI) *m/z* calcd for $C_{15}H_{19}N_2O_2^+$, [**R-bipy**]$^+$: 259.1441, found: 259.1432.

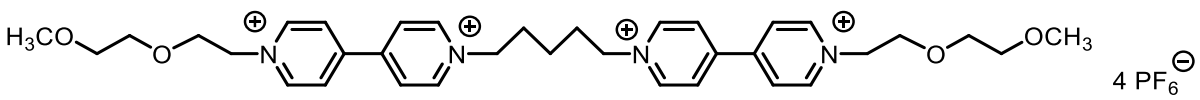

Synthesis of [R-bipy-$(CH_2)_5$-bipy-R][PF_6]$_4$ (3). The product of the previous reaction is a 25:1 mixture of [R-bipy][TsO] and [R-bipy-R][TsO], so that 6.14 g corresponds to 13.4 mmol of [R-bipy][TsO]. A portion of 1,5-dibromopentane (1.54 g, 6.70 mmol) was weighed into a vial. A 30 mL portion of acetonitrile was used to wash both [R-bipy][TsO] and 1,5-dibromopentane into a 100 mL round-bottomed flask, and the resulting homogeneous solution was placed in a 100 °C oil bath to reflux under nitrogen for 70 h, during which time a yellow precipitate formed. The reaction mixture was then allowed to cool to room temperature. A solution of [Nbu_4][Br] (6.45 g, 20.0 mmol) in acetonitrile (20 mL) was prepared and then added slowly to the stirring reaction mixture, resulting in the formation of more yellow precipitate. The yellow solid was isolated by filtration, and the filter flask was subsequently switched out for a new one. Water (25 mL) was added to redissolve the yellow solid and to wash the yellow solution through the filter into the clean flask. Separately, a solution of [NH_4][PF_6] (9.78 g, 60.0 mmol) in water (40 mL) was prepared. The yellow product solution was slowly added to the stirring [NH_4][PF_6] solution, resulting in the formation of a white precipitate. An additional 10 mL of water was used to wash the yellow solution into the [NH_4][PF_6] solution. The white solid was isolated by filtration and washed with water (10 mL). The off-white, pasty solid was dried under vacuum for 2 h. The solid was dissolved in acetonitrile (20 mL) to give a light brown solution. A 150 mL portion of ethanol was very slowly added to the stirred solution. This caused the separation of an oil partway through the ethanol addition, which quickly solidified. The resulting off-white powder was isolated by filtration, washed with ethanol and then diethyl ether, and was then allowed to air-dry. Yield: 6.23 g (80% yield). ^{1}H NMR (500 MHz, DMSO-d_6): δ 9.37 (d, J = 6.3 Hz, 4H), 9.31 (d, J = 6.3 Hz, 4H), 8.80 (d, J = 6.3 Hz, 4H), 8.78 (d, J = 6.3 Hz, 4H), 4.89 (t, J = 5.0 Hz, 4H), 4.70 (t, J = 7.7 Hz, 4H), 3.98 (t, J = 4.9 Hz, 4H), 3.58 (dd, J = 5.6, 3.6 Hz, 4H), 3.39 (dd, J = 5.6, 3.6 Hz, 4H), 3.17 (s, 6H), 2.07

(p, *J* = 7.5 Hz, 4H), 1.44 (p, *J* = 7.8 Hz, 2H). ^{13}C NMR (126 MHz, DMSO-d_6): δ 148.9, 148.7, 146.3, 145.8, 126.7, 126.2, 71.0, 69.5, 68.6, 60.5, 58.1, 30.1, 22.11 (one linking CH_2 is missing, possibly obscured by DMSO). HRMS (ESI) *m/z* calcd for $C_{35}H_{48}F_{18}N_4O_4P_3^+$: 1023.2595, found 1023.2579; *m/z* calcd for $C_{35}H_{48}F_{12}N_4O_4P_2^{2+}$: 439.1474, found 439.1463.

5.4.2 X-ray Crystallographic Data for 1-DAC and 2-DAC

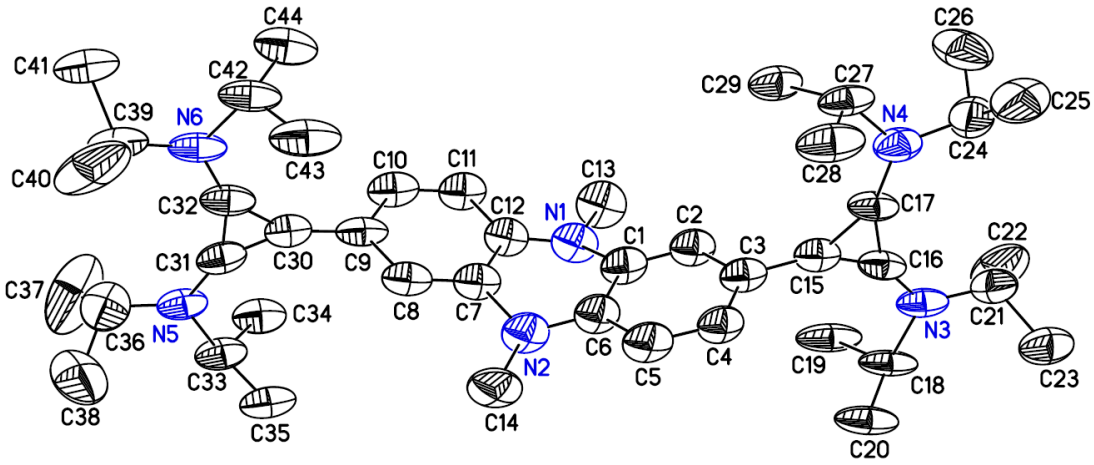

Figure 5.6 PLUTO representation **1-DAC**. The PF_6 anions are omitted for clarity.

Structure Determination.

Colorless needles of **1-DAC** were grown from a tetrahydrofuran solution of the compound at 22 °C. A crystal of dimensions 0.14 × 0.03 × 0.03 mm was mounted on a Rigaku AFC10K Saturn 944+ CCD-based X-ray diffractometer equipped with a low-temperature device and Micromax-007HF Cu-target micro-focus rotating anode (l = 1.54187 Å) operated at 1.2 kW power (40 kV, 30 mA). The X-ray intensities were measured at 85(1) K with the detector placed at a distance 42.00 mm from the crystal. A total of 2028 images were collected with an oscillation width of 1.0° in w. The exposure times were 5 s for the low-angle images, 30 s for high angle. Rigaku d*trek images were exported to CrysAlisPro for processing and corrected for absorption.

The integration of the data yielded a total of 141388 reflections to a maximum 2q value of 117.86° of which 8146 were independent, and 5795 were greater than 2s(I). The final cell constants (Table S1) were based on the xyz centroids of 13155 reflections above 10s(I). Analysis of the data showed negligible decay during data collection. The structure was solved and refined with the Bruker SHELXTL (version 2018/3) software package, using the space group Pbca with Z = 8 for the formula $C_{52}H_{84}N_6O_2F_{12}P_2$. All non-hydrogen atoms were refined anisotropically with the hydrogen atoms placed in idealized positions. Full matrix least-squares refinement based on F^2 converged at R1 = 0.1207 and wR2 = 0.3122 [based on I > 2sigma(I)], R1 = 0.1468 and wR2 = 0.3371 for all data. Additional details are presented in Table S1 and are given as Supporting Information in a CIF file. Acknowledgment is made for funding from NSF grant CHE-0840456 for X-ray instrumentation.

Table 5.2 Crystal data and structure refinement for **1-DAC**

Empirical formula	$C_{52}H_{84}F_{12}N_6O_2P_2$
Formula weight	1115.19
Temperature	85(2) K
Wavelength	1.54184 Å
Crystal system, space group	Orthorhombic, Pbca
Unit cell dimensions	a = 17.7900(5) Å alpha = 90°
	b = 16.7530(7) Å beta = 90°
	c = 38.066(3) Å gamma = 90°
Volume	11344.9(10) $Å^3$
Z, Calculated density	8, 1.306 Mg/m^3
Absorption coefficient	1.418 mm^{-1}
F(000)	4736
Crystal size	0.140 × 0.030 × 0.030 mm
Theta range for data collection	3.401 to 58.931°

Limiting indices	–19<=h<=19, –18<=k<=18, –42<=l<=42
Reflections collected / unique	141388 / 8146 [R(int) = 0.1715]
Completeness to theta = 58.931	100.0 %
Absorption correction	Semi-empirical from equivalents
Max. and min. transmission	1.00000 and 0.66284
Refinement method	Full-matrix least-squares on F^2
Data / restraints / parameters	8146 / 229 / 721
Goodness-of-fit on F^2	1.040
Final R indices [I>2sigma(I)]	R1 = 0.1207, wR2 = 0.3122
R indices (all data)	R1 = 0.1468, wR2 = 0.3371
Extinction coefficient	n/a
Largest diff. peak and hole	0.622 and –0.595 eÅ^{-3}

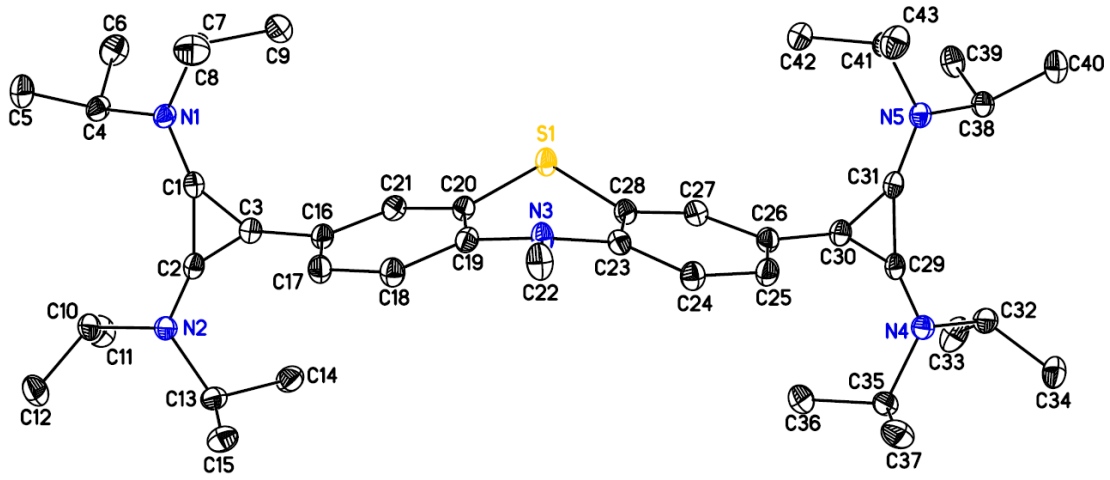

Figure 5.7 PLUTO representation of **2-DAC**. The PF_6 anions are omitted for clarity.

Structure Determination.

Pale green blocks of **2-DAC** were grown from an acetonitrile solution of the compound at 22 °C. A crystal of dimensions 0.18 × 0.14 × 0.10 mm was mounted on a Rigaku AFC10K Saturn 944+ CCD-based X-ray diffractometer equipped with a low-temperature device and Micromax-

007HF Cu-target micro-focus rotating anode (l = 1.54187 Å) operated at 1.2 kW power (40 kV, 30 mA). The X-ray intensities were measured at 85(1) K with the detector placed at a distance 42.00 mm from the crystal. A total of 2028 images were collected with an oscillation width of 1.0° in w. The exposure times were 1 s for the low-angle images, 4 s for high angle. Rigaku d*trek images were exported to CrysAlisPro for processing and corrected for absorption. The integration of the data yielded a total of 156095 reflections to a maximum 2q value of 139.39° of which 9781 were independent, and 9210 were greater than 2s(I). The final cell constants (Table S2) were based on the xyz centroids of 50877 reflections above 10s(I). Analysis of the data showed negligible decay during data collection. The structure was solved and refined with the Bruker SHELXTL (version 2018/3) software package, using the space group Pbca with Z = 8 for the formula $C_{45}H_{68}N_6F_{12}P_2S$. All non-hydrogen atoms were refined anisotropically with the hydrogen atoms placed in idealized positions. One PF_6 anion is disordered 50/50 over two closely related sites. Full matrix least-squares refinement based on F2 converged at R1 = 0.0406 and wR2 = 0.1091 [based on I > 2sigma(I)], R1 = 0.0426 and wR2 = 0.1111 for all data. Additional details are presented in Table S2 and are given as Supporting Information in a CIF file. Acknowledgment is made for funding from NSF grant CHE-0840456 for X-ray instrumentation.

Table 5.3. Crystal data and structure refinement for **2-DAC**.

Empirical formula	$C_{45}H_{68}F_{12}N_6P_2S$
Formula weight	1015.05
Temperature	85(2) K
Wavelength	1.54184 A
Crystal system, space group	Orthorhombic, Pbca
Unit cell dimensions	a = 24.91583(16) Å alpha = 90°
	b = 14.96037(9) Å beta = 90°
	c = 28.14342(17) Å gamma = 90°

Volume	10490.46(11) $Å^3$
Z, Calculated density	8, 1.285 Mg/m^3
Absorption coefficient	1.818 mm^{-1}
F(000)	4272
Crystal size	0.180 × 0.140 × 0.100 mm
Theta range for data collection	3.141 to 69.696°
Limiting indices	–29<=h<=30, –18<=k<=17, –34<=l<=34
Reflections collected / unique	156095 / 9781 [R(int) = 0.0675]
Completeness to theta = 67.684	100.0 %
Absorption correction	Semi-empirical from equivalents
Max. and min. transmission	1.00000 and 0.77553
Refinement method	Full-matrix least-squares on F^2
Data / restraints / parameters	9781 / 189 / 677
Goodness-of-fit on F^2	1.002
Final R indices [I>2sigma(I)]	R1 = 0.0406, wR2 = 0.1091
R indices (all data)	R1 = 0.0426, wR2 = 0.1111
Extinction coefficient	0.000073(12)
Largest diff. peak and hole	0.658 and –0.303 $eÅ^{–3}$

5.4.2 Electrochemistry Experimental Procedures

General methods and materials. Acetonitrile (anhydrous, 99.8%) was obtained from Sigma-Aldrich and used as received. Tetrabutylammonium hexafluorophosphate ($TBAPF_6$; electrochemical grade) was obtained from Sigma-Aldrich and dried under high vacuum for 48 h at 70 °C before being transferred to a N_2-filled glovebox. A 0.50 M stock solution of $TBAPF_6$ in acetonitrile was prepared in a N_2-filled glovebox and dried over 3Å molecular sieves for at least two days prior to use. A Fumasep FAP-375-PP membrane was obtained from Fumatech and ion-exchanged in saturated KPF_6[6] and then dried under high vacuum overnight before use.

Cyclic voltammetry. Cyclic voltammetry (CV) was performed in a N_2-filled glovebox with a Biologic VSP multichannel potentiostat/galvanostat using a three-electrode electrochemical cell,

consisting of a glassy carbon disk working electrode (0.071 cm^2, BASi), a Ag/Ag^+ reference electrode (BASi) with 0.01 M $AgBF_4$ (Sigma) and 0.5 M $TBAPF_6$ in acetonitrile, and a platinum wire counter electrode. All experiments were conducted in a 0.50 M $TBAPF_6$/acetonitrile electrolyte stock solution.

H-cell cycling. Bulk charge-discharge measurements were carried out in a N_2-filled glovebox with a BioLogic VSP galvanostat in a custom glass H-cell with an ultrafine fritted glass separator (P5, Adams and Chittenden). The working and counter electrodes were reticulated vitreous carbon (100 ppi, ~70 cm^2 surface area, Duocel). A Ag/Ag^+ reference electrode was used on the working side of the H-cell. The electrolyte contained 2.5 mM active species and 0.50 M $TBAPF_6$ in acetonitrile. The working chamber of the H-cell was loaded with 5.0 mL of the electrolyte solution, and the counter side was loaded with 5.0 mL of a solution containing methyl viologen hexafluorophosphate. Both chambers were stirred continuously during cycling at a current of 5 mA. Voltage cutoffs of +0.3 V higher than $E_{1/2}$ as the upper limit and +0.5 V as the lower limit were employed.

Shelf stability test. 2.5 mM of **1-DAC** or **2-DAC** in 0.5 M $TBAPF_6$ was charged to 100% SOC in an H-cell and the solution was stored in a Teflon vial; active species concentration was monitored by CV every two days over a week.

Flow cell cycling. Cycling under flow conditions was performed with a zero-gap flow cell comprised of graphite charge collecting plates containing an interdigitated flow field in combination with two layers of non-woven carbon felt electrodes (Sigracet 29AA) on each side. PTFE gaskets were used to achieve ~20% compression of the felt. One Fumasep FAP-375-PP membrane (pretreated in saturated KPF_6 aqueous solution) separated the two half cells, and the exposed area of the membrane in the gasket window was used as the active area (2.55 cm^2). After

assembly, the catholyte side of the cell was loaded with 6.0 mL of a solution containing 0.015 M **1-DAC** or **2-DAC** in 0.50 M $TBAPF_6$/acetonitrile, and the anolyte side was filled with 6.0 mL (0.015 M) of **3** in 0.50 M $TBAPF_6$/acetonitrile. The cell was pretreated by continuously flowing the solution above at 10 mL/min for 1 h, without any charging process, using a peristaltic pump (Cole-Parmer) with Solve-Flex and PFA tubing. After this step, using the same flow rate, galvanostatic charge-discharge cycling was performed using a BioLogic VSP galvanostat employing a charging current of +10 mA/cm^2 and a discharging current of –10 mA/cm^2 with 1.9 V and 0.3 V limits for the battery containing **1-DAC** and **3** or 2.3 V and 1.0 V voltage limits for the battery containing **2-DAC** and **3**.

Determination of the Diffusion Coefficient and Electron Transfer Rate Constant of 1-DAC and 2-DAC.

The diffusion coefficient was determined by varying the scan rate of CV measurements between 20 and 700 mV/s (Figure S3, left). Plotting the cathodic and anodic peak height currents versus the square root of the scan rate showed a linear relationship, indicating a transport-limited redox process (Figure S3, right). The slope of this linear relation was used in the Randles–Sevcik equation (eq 1) to determine the diffusion coefficient.[92]

$$i_p = 0.4463\, nFAC\sqrt{\frac{nFvD}{RT}} \qquad (1)$$

The terms of the equation: i_p is the peak current in amps, n is the number of electrons transferred, F is Faraday's constant, A is the area of the electrode in cm^2, C *is* the concentration of redox-active species in mol/cm^3, D is the diffusion coefficient in cm^2/s, v is the scan rate in V/s, R is the gas constant in JK^{-1}mol^{-1}, and T is the temperature in K.

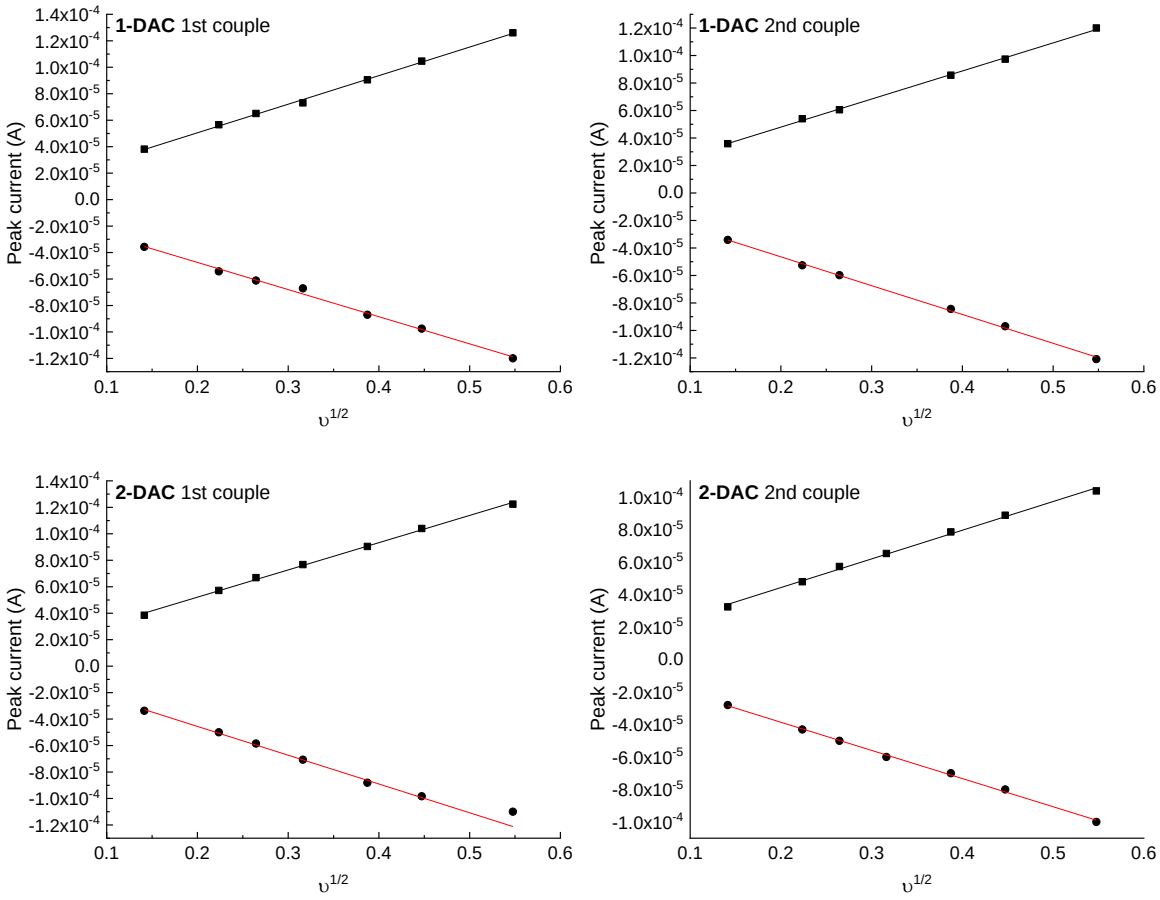

Figure 5.8. Peak current (A) versus square root of the scan rate ($v^{½}$) and linear fits used to determine diffusion coefficients.

The heterogeneous electron transfer rate constant was determined following the Nicholson method.[93] The peak separations between the cathodic and anodic peaks at various scan rates were fit to a working curve. Plotting the resulting values of Nicholson dimensionless number Ψ versus the inverse square root of the scan rate (Figure S4) gave a relationship from which the slope was used to determine k_0 according to eq 2,

$$\psi = \frac{\gamma k_0}{\sqrt{\pi a D_0}} \qquad (2)$$

where k_0 is the standard rate constant in cm s^{-1}; Ψ is the Nicholson dimensionless number, which is a function of the peak potential separation (ΔE_p) from CV curve. D_0 is the diffusion coefficient

in cm^2/s. α is the dimensionless charge transfer coefficient. $\gamma = \sqrt{\frac{RT}{nF}}$, where n is the number of electrons transferred in the redox reaction, F is Faraday's constant (96485 C/mol), R is the ideal gas constant (8.314 J mol/K), T is the absolute temperature in K.

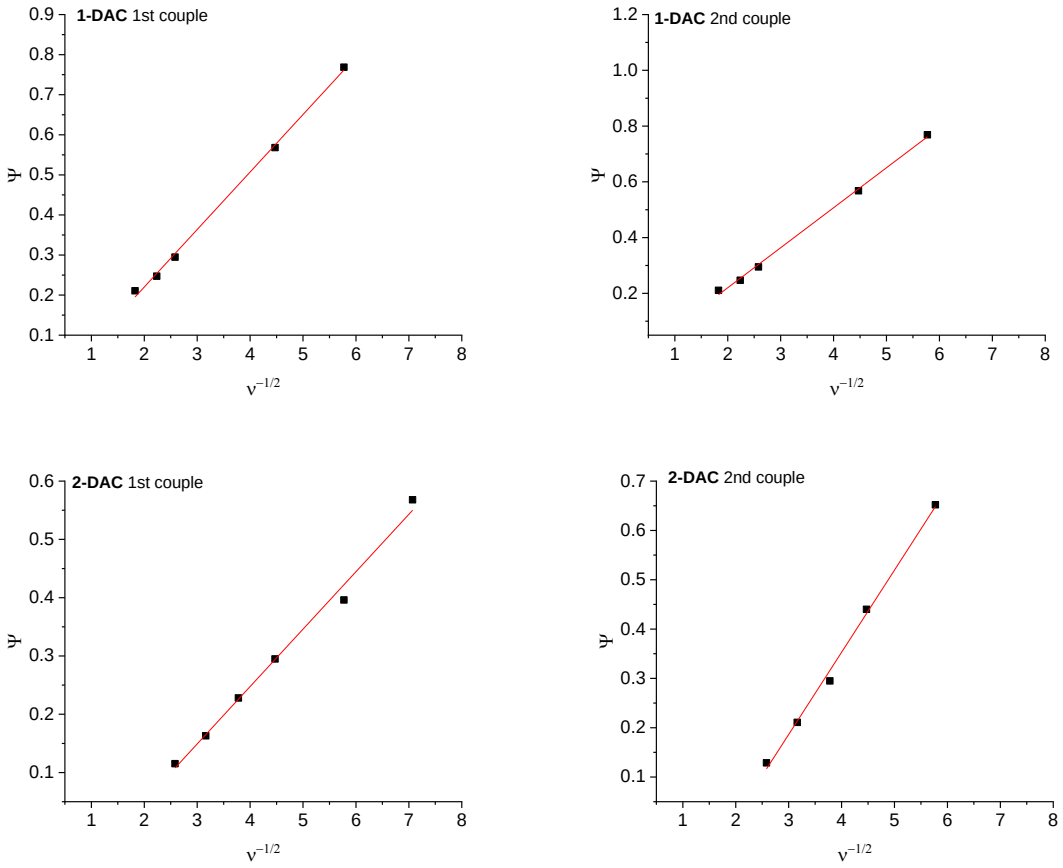

Figure 5.9. Plots of the Nicholson dimensionless number (Ψ) versus inverse of the scan rate ($v^{-½}$). A linear fit was used to determine heterogeneous electron transfer rates.

5.4.3 Computational Methods

Conformational searches were performed with MacroModel version 11.7[94] and the OPLS3 force field.[95] All conformers within 10 kJ/mol relative to the minimum were optimized with DFT. All relevant redox states for **2**, **2-OMe**, and **2-DAC** were optimized with IEFPCM (acetonitrile) solvation with the B3LYP density functional[96, 97] and the 6-31G(d) basis set as implemented in

Gaussian09 (revision D.01).[98] All of the optimized geometries were verified by frequency computations as minima (zero imaginary frequencies). Gaussian input files were written using a Python script.[99] Oxidation potentials were calculated according to a previously reported method using the free energies obtained from the optimized oxidized and reduced structures (Table S4).[100]

5.5 References

(1) Wei, X.; Pan, W.; Duan, W.; Hollas, A.; Yang, Z.; Li, B.; Nie, Z.; Liu, J.; Reed, D.; Wang, W.; Sprenkle, V. Materials and Systems for Organic Redox Flow Batteries: Status and Challenges. *ACS Energy Lett.* **2017**, *2* (9), 2187–2204. https://doi.org/10.1021/acsenergylett.7b00650.

(2) Wei, X.; Xu, W.; Vijayakumar, M.; Cosimbescu, L.; Liu, T.; Sprenkle, V.; Wang, W. TEMPO-Based Catholyte for High-Energy Density Nonaqueous Redox Flow Batteries. *Advanced Materials* **2014**, *26* (45), 7649–7653. https://doi.org/10.1002/adma.201403746.

(3) Winsberg, J.; Hagemann, T.; Muench, S.; Friebe, C.; Häupler, B.; Janoschka, T.; Morgenstern, S.; Hager, M. D.; Schubert, U. S. Poly(Boron-Dipyrromethene)—A Redox-Active Polymer Class for Polymer Redox-Flow Batteries. *Chem. Mater.* **2016**, *28* (10), 3401–3405. https://doi.org/10.1021/acs.chemmater.6b00640.

(4) Zhang, C.; Zhang, L.; Ding, Y.; Peng, S.; Guo, X.; Zhao, Y.; He, G.; Yu, G. Progress and Prospects of Next-Generation Redox Flow Batteries. *Energy Storage Materials* **2018**, *15*, 324–350. https://doi.org/10.1016/j.ensm.2018.06.008.

(5) Kwon, G.; Lee, S.; Hwang, J.; Shim, H.-S.; Lee, B.; Lee, M. H.; Ko, Y.; Jung, S.-K.; Ku, K.; Hong, J.; Kang, K. Multi-Redox Molecule for High-Energy Redox Flow Batteries. *Joule* **2018**, *2* (9), 1771–1782. https://doi.org/10.1016/j.joule.2018.05.014.

(6) Zhang, J.; Yang, Z.; Shkrob, I. A.; Assary, R. S.; Tung, S. on; Silcox, B.; Duan, W.; Zhang, J.; Su, C. C.; Hu, B.; Pan, B.; Liao, C.; Zhang, Z.; Wang, W.; Curtiss, L. A.; Thompson, L. T.;

Wei, X.; Zhang, L. Annulated Dialkoxybenzenes as Catholyte Materials for Non-Aqueous Redox Flow Batteries: Achieving High Chemical Stability through Bicyclic Substitution. *Adv. Energy Mater.* **2017**, *7* (21), 1701272. https://doi.org/10.1002/aenm.201701272.

(7) VanGelder, L. E.; Schreiber, E.; Matson, E. M. Physicochemical Implications of Alkoxide "Mixing" in Polyoxovanadium Clusters for Nonaqueous Energy Storage. *J. Mater. Chem. A* **2019**, *7* (9), 4893–4902. https://doi.org/10.1039/C8TA12306C.

(8) VanGelder, L. E.; Kosswattaarachchi, A. M.; Forrestel, P. L.; Cook, T. R.; Matson, E. M. Polyoxovanadate-Alkoxide Clusters as Multi-Electron Charge Carriers for Symmetric Non-Aqueous Redox Flow Batteries. *Chem. Sci.* **2018**, *9* (6), 1692–1699. https://doi.org/10.1039/C7SC05295B.

(9) A. Kowalski, J.; D. Casselman, M.; Preet Kaur, A.; D. Milshtein, J.; F. Elliott, C.; Modekrutti, S.; Harsha Attanayake, N.; Zhang, N.; R. Parkin, S.; Risko, C.; R. Brushett, F.; A. Odom, S. A Stable Two-Electron-Donating Phenothiazine for Application in Nonaqueous Redox Flow Batteries. *Journal of Materials Chemistry A* **2017**, *5* (46), 24371–24379. https://doi.org/10.1039/C7TA05883G.

(10) Escalante-García, I. L.; Wainright, J. S.; Thompson, L. T.; Savinell, R. F. Performance of a Non-Aqueous Vanadium Acetylacetonate Prototype Redox Flow Battery: Examination of Separators and Capacity Decay. *J. Electrochem. Soc.* **2015**, *162* (3), A363–A372. https://doi.org/10.1149/2.0471503jes.

(11) Carino, E. V.; Staszak-Jirkovsky, J.; Assary, R. S.; Curtiss, L. A.; Markovic, N. M.; Brushett, F. R. Tuning the Stability of Organic Active Materials for Nonaqueous Redox Flow Batteries via Reversible, Electrochemically Mediated Li+ Coordination. *Chem. Mater.* **2016**, *28* (8), 2529–2539. https://doi.org/10.1021/acs.chemmater.5b04053.

(12) Silcox, B.; Zhang, J.; Shkrob, I. A.; Thompson, L.; Zhang, L. On Transferability of Performance Metrics for Redox-Active Molecules. *J. Phys. Chem. C* **2019**, *123* (27), 16516–16524. https://doi.org/10.1021/acs.jpcc.9b02230.

(13) Kwon, G.; Lee, K.; Lee, M. H.; Lee, B.; Lee, S.; Jung, S.-K.; Ku, K.; Kim, J.; Park, S. Y.; Kwon, J. E.; Kang, K. Bio-Inspired Molecular Redesign of a Multi-Redox Catholyte for High-Energy Non-Aqueous Organic Redox Flow Batteries. *Chem* **2019**, *5* (10), 2642–2656. https://doi.org/10.1016/j.chempr.2019.07.006.

(14) Sevov, C. S.; Fisher, S. L.; Thompson, L. T.; Sanford, M. S. Mechanism-Based Development of a Low-Potential, Soluble, and Cyclable Multielectron Anolyte for Nonaqueous Redox Flow Batteries. *J. Am. Chem. Soc.* **2016**, *138* (47), 15378–15384. https://doi.org/10.1021/jacs.6b07638.

(15) Duan, W.; Huang, J.; Kowalski, J. A.; Shkrob, I. A.; Vijayakumar, M.; Walter, E.; Pan, B.; Yang, Z.; Milshtein, J. D.; Li, B.; Liao, C.; Zhang, Z.; Wang, W.; Liu, J.; Moore, J. S.; Brushett, F. R.; Zhang, L.; Wei, X. "Wine-Dark Sea" in an Organic Flow Battery: Storing Negative Charge in 2,1,3-Benzothiadiazole Radicals Leads to Improved Cyclability. *ACS Energy Lett.* **2017**, *2* (5), 1156–1161. https://doi.org/10.1021/acsenergylett.7b00261.

(16) Huang, J.; Cheng, L.; Assary, R. S.; Wang, P.; Xue, Z.; Burrell, A. K.; Curtiss, L. A.; Zhang, L. Liquid Catholyte Molecules for Nonaqueous Redox Flow Batteries. *Advanced Energy Materials* **2015**, *5* (6), 1401782. https://doi.org/10.1002/aenm.201401782.

(17) Zhang, C.; Qian, Y.; Ding, Y.; Zhang, L.; Guo, X.; Zhao, Y.; Yu, G. Biredox Eutectic Electrolytes Derived from Organic Redox-Active Molecules: High-Energy Storage Systems. *Angewandte Chemie International Edition* **2019**, *58* (21), 7045–7050. https://doi.org/10.1002/anie.201902433.

(18) Zhang, C.; Niu, Z.; Ding, Y.; Zhang, L.; Zhou, Y.; Guo, X.; Zhang, X.; Zhao, Y.; Yu, G. Highly Concentrated Phthalimide-Based Anolytes for Organic Redox Flow Batteries with Enhanced Reversibility. *Chem* **2018**, *4* (12), 2814–2825. https://doi.org/10.1016/j.chempr.2018.08.024.

(19) Wang, W.; Luo, Q.; Li, B.; Wei, X.; Li, L.; Yang, Z. Recent Progress in Redox Flow Battery Research and Development. *Advanced Functional Materials* **2013**, *23* (8), 970–986. https://doi.org/10.1002/adfm.201200694.

(20) Leung, P.; Li, X.; León, C. P. de; Berlouis, L.; Low, C. T. J.; Walsh, F. C. Progress in Redox Flow Batteries, Remaining Challenges and Their Applications in Energy Storage. *RSC Adv.* **2012**, *2* (27), 10125–10156. https://doi.org/10.1039/C2RA21342G.

(21) Noack, J.; Roznyatovskaya, N.; Herr, T.; Fischer, P. The Chemistry of Redox-Flow Batteries. *Angewandte Chemie International Edition* **2015**, *54* (34), 9776–9809. https://doi.org/10.1002/anie.201410823.

(22) Zhao, Y.; Ding, Y.; Li, Y.; Peng, L.; Byon, H. R.; Goodenough, J. B.; Yu, G. A Chemistry and Material Perspective on Lithium Redox Flow Batteries towards High-Density Electrical Energy Storage. *Chem. Soc. Rev.* **2015**, *44* (22), 7968–7996. https://doi.org/10.1039/C5CS00289C.

(23) Milshtein, J. D.; Kaur, A. P.; Casselman, M. D.; Kowalski, J. A.; Modekrutti, S.; Zhang, P. L.; Harsha Attanayake, N.; Elliott, C. F.; Parkin, S. R.; Risko, C.; Brushett, F. R.; Odom, S. A. High Current Density, Long Duration Cycling of Soluble Organic Active Species for Non-Aqueous Redox Flow Batteries. *Energy Environ. Sci.* **2016**, *9* (11), 3531–3543. https://doi.org/10.1039/C6EE02027E.

(24) Takechi, K.; Kato, Y.; Hase, Y. A Highly Concentrated Catholyte Based on a Solvate Ionic Liquid for Rechargeable Flow Batteries. *Advanced Materials* **2015**, *27* (15), 2501–2506. https://doi.org/10.1002/adma.201405840.

(25) Yan, Y.; Robinson, S. G.; Sigman, M. S.; Sanford, M. S. Mechanism-Based Design of a High-Potential Catholyte Enables a 3.2 V All-Organic Nonaqueous Redox Flow Battery. *J. Am. Chem. Soc.* **2019**, *141* (38), 15301–15306. https://doi.org/10.1021/jacs.9b07345.

(26) Yan, Y.; Vaid, T. P.; Sanford, M. S. Bis(Diisopropylamino)Cyclopropenium-Arene Cations as High Oxidation Potential and High Stability Catholytes for Non-Aqueous Redox Flow Batteries. *J. Am. Chem. Soc.* **2020**, *142* (41), 17564–17571. https://doi.org/10.1021/jacs.0c07464.

(27) Harsha Attanayake, N.; Preet Kaur, A.; Malsha Suduwella, T.; F. Elliott, C.; R. Parkin, S.; A. Odom, S. A Stable, Highly Oxidizing Radical Cation. *New Journal of Chemistry* **2020**, *44* (42), 18138–18148. https://doi.org/10.1039/D0NJ04434B.

(28) Ergun, S.; Casselman, M. D.; Kaur, A. P.; Attanayake, N. H.; Parkin, S. R.; Odom, S. A. Improved Synthesis of N-Ethyl-3,7-Bis(Trifluoromethyl)Phenothiazine. *New J. Chem.* **2020**, *44* (26), 11349–11355. https://doi.org/10.1039/D0NJ00184H.

(29) Attanayake, N. H.; Kowalski, J. A.; Greco, K. V.; Casselman, M. D.; Milshtein, J. D.; Chapman, S. J.; Parkin, S. R.; Brushett, F. R.; Odom, S. A. Tailoring Two-Electron-Donating Phenothiazines To Enable High-Concentration Redox Electrolytes for Use in Nonaqueous Redox Flow Batteries. *Chem. Mater.* **2019**, *31* (12), 4353–4363. https://doi.org/10.1021/acs.chemmater.8b04770.

(30) Kaur, A. P.; Harris, O. C.; Attanayake, N. H.; Liang, Z.; Parkin, S. R.; Tang, M. H.; Odom, S. A. Quantifying Environmental Effects on the Solution and Solid-State Stability of a

Phenothiazine Radical Cation. *Chem. Mater.* **2020**, *32* (7), 3007–3017. https://doi.org/10.1021/acs.chemmater.9b05345.

(31) Strater, Z. M.; Rauch, M.; Jockusch, S.; Lambert, T. H. Oxidizable Ketones: Persistent Radical Cations from the Single-Electron Oxidation of 2,3-Diaminocyclopropenones. *Angewandte Chemie International Edition* **2019**, *58* (24), 8049–8052. https://doi.org/10.1002/anie.201902265.

(32) Xu, D.; Wang, Z.; Xu, J.; Zhang, L.; Wang, L.; Zhang, X. A Stable Sulfone Based Electrolyte for High Performance Rechargeable Li–O2 Batteries. *Chem. Commun.* **2012**, *48* (95), 11674–11676. https://doi.org/10.1039/C2CC36815C.

(33) It is important to note that acetonitrile has some disadvantages for commercialization, including relatively high cost, flammability, and toxicity.

(34) Xie, Z.; Liu, Q.; Chang, Z.; Zhang, X. The Developments and Challenges of Cerium Half-Cell in Zinc–Cerium Redox Flow Battery for Energy Storage. *Electrochimica Acta* **2013**, *90*, 695–704. https://doi.org/10.1016/j.electacta.2012.12.066.

(35) Sun Tao; Li Zong-Jun; Yang Xu; Wang Sai; Zhu Yun-Hai; Zhang Xin-Bo. Imine-Rich Poly(o-Phenylenediamine) as High-Capacity Trifunctional Organic Electrode for Alkali-Ion Batteries. *CCS Chemistry 1* (4), 365–372. https://doi.org/10.31635/ccschem.019.20190003.

(36) Goldfarb, D. L.; Longinotti, M. P.; Corti, H. R. Electrical Conductances of Tetrabutylammonium and Decamethylferrocenium Hexafluorophosphate in Organic Solvents. *Journal of Solution Chemistry* **2001**, *30* (4), 307–322. https://doi.org/10.1023/A:1010334021934.

(37) Zhong, C.; Deng, Y.; Hu, W.; Qiao, J.; Zhang, L.; Zhang, J. A Review of Electrolyte Materials and Compositions for Electrochemical Supercapacitors. *Chem. Soc. Rev.* **2015**, *44* (21), 7484–7539. https://doi.org/10.1039/C5CS00303B.

(38) Hu, B.; Liu, T. L. Two Electron Utilization of Methyl Viologen Anolyte in Nonaqueous Organic Redox Flow Battery. *Journal of Energy Chemistry* **2018**, *27* (5), 1326–1332. https://doi.org/10.1016/j.jechem.2018.02.014.

(39) Hu, B.; DeBruler, C.; Rhodes, Z.; Liu, T. L. Long-Cycling Aqueous Organic Redox Flow Battery (AORFB) toward Sustainable and Safe Energy Storage. *J. Am. Chem. Soc.* **2017**, *139* (3), 1207–1214. https://doi.org/10.1021/jacs.6b10984.

(40) Liu, T.; Wei, X.; Nie, Z.; Sprenkle, V.; Wang, W. A Total Organic Aqueous Redox Flow Battery Employing a Low Cost and Sustainable Methyl Viologen Anolyte and 4-HO-TEMPO Catholyte. *Advanced Energy Materials* **2016**, *6* (3), 1501449. https://doi.org/10.1002/aenm.201501449.

(41) DeBruler, C.; Hu, B.; Moss, J.; Liu, X.; Luo, J.; Sun, Y.; Liu, T. L. Designer Two-Electron Storage Viologen Anolyte Materials for Neutral Aqueous Organic Redox Flow Batteries. *Chem* **2017**, *3* (6), 961–978. https://doi.org/10.1016/j.chempr.2017.11.001.

(42) Hu, B.; Tang, Y.; Luo, J.; Grove, G.; Guo, Y.; Liu, T. L. Improved Radical Stability of Viologen Anolytes in Aqueous Organic Redox Flow Batteries. *Chem. Commun.* **2018**, *54* (50), 6871–6874. https://doi.org/10.1039/C8CC02336K.

(43) Gong, K.; Fang, Q.; Gu, S.; Li, S. F. Y.; Yan, Y. Nonaqueous Redox-Flow Batteries: Organic Solvents, Supporting Electrolytes, and Redox Pairs. *Energy Environ. Sci.* **2015**, *8* (12), 3515–3530. https://doi.org/10.1039/C5EE02341F.

(44) Hendriks, K. H.; Robinson, S. G.; Braten, M. N.; Sevov, C. S.; Helms, B. A.; Sigman, M. S.; Minteer, S. D.; Sanford, M. S. High-Performance Oligomeric Catholytes for Effective Macromolecular Separation in Nonaqueous Redox Flow Batteries. *ACS Cent. Sci.* **2018**, *4* (2), 189–196. https://doi.org/10.1021/acscentsci.7b00544.

(45) Nicholson, R. S. Theory and Application of Cyclic Voltammetry for Measurement of Electrode Reaction Kinetics. *Anal. Chem.* **1965**, *37* (11), 1351–1355. https://doi.org/10.1021/ac60230a016.

(46) Wei, X.; Cosimbescu, L.; Xu, W.; Hu, J. Z.; Vijayakumar, M.; Feng, J.; Hu, M. Y.; Deng, X.; Xiao, J.; Liu, J.; Sprenkle, V.; Wang, W. Towards High-Performance Nonaqueous Redox Flow Electrolyte Via Ionic Modification of Active Species. *Advanced Energy Materials* **2015**, *5* (1), 1400678. https://doi.org/10.1002/aenm.201400678.

(47) Wei, X.; Duan, W.; Huang, J.; Zhang, L.; Li, B.; Reed, D.; Xu, W.; Sprenkle, V.; Wang, W. A High-Current, Stable Nonaqueous Organic Redox Flow Battery. *ACS Energy Lett.* **2016**, *1* (4), 705–711. https://doi.org/10.1021/acsenergylett.6b00255.

(48) Kowalski, J. A.; Neyhouse, B. J.; Brushett, F. R. The Impact of Bulk Electrolysis Cycling Conditions on the Perceived Stability of Redox Active Materials. *Electrochemistry Communications* **2020**, *111*, 106625. https://doi.org/10.1016/j.elecom.2019.106625.

(49) Forner-Cuenca, A.; Penn, E. E.; Oliveira, A. M.; Brushett, F. R. Exploring the Role of Electrode Microstructure on the Performance of Non-Aqueous Redox Flow Batteries. *J. Electrochem. Soc.* **2019**, *166* (10), A2230. https://doi.org/10.1149/2.0611910jes.

(50) Zhao, Y.; Yu, Z.; A. Robertson, L.; Zhang, J.; Shi, Z.; R. Bheemireddy, S.; A. Shkrob, I.; Z, Y.; Li, T.; Zhang, Z.; Cheng, L.; Zhang, L. Unexpected Electrochemical Behavior of an Anolyte Redoxmer in Flow Battery Electrolytes: Solvating Cations Help to Fight against the Thermodynamic–Kinetic Dilemma. *Journal of Materials Chemistry A* **2020**, *8* (27), 13470–13479. https://doi.org/10.1039/D0TA02214D.

(51) S. Watkins, T.; Sarbapalli, D.; J. Counihan, M.; S. Danis, A.; Zhang, J.; Zhang, L.; R. Zavadil, K.; Rodríguez-López, J. A Combined SECM and Electrochemical AFM Approach to

Probe Interfacial Processes Affecting Molecular Reactivity at Redox Flow Battery Electrodes. *Journal of Materials Chemistry A* **2020**, *8* (31), 15734–15745. https://doi.org/10.1039/D0TA00836B.

(52) Shrestha, A.; Hendriks, K. H.; Sigman, M. S.; Minteer, S. D.; Sanford, M. S. Realization of an Asymmetric Non-Aqueous Redox Flow Battery through Molecular Design to Minimize Active Species Crossover and Decomposition. *Chemistry – A European Journal* **2020**, *26* (24), 5369–5373. https://doi.org/10.1002/chem.202000749.

(53) This is to maintain dicationic charge and thus impede cross-over with the selected anion-exchange membrane.

(54) This potential is based on the difference between the highest oxidation potential of the catholyte and the first reduction potential of the anolyte.

(55) Greco, K. V.; Forner-Cuenca, A.; Mularczyk, A.; Eller, J.; Brushett, F. R. Elucidating the Nuanced Effects of Thermal Pretreatment on Carbon Paper Electrodes for Vanadium Redox Flow Batteries. *ACS Appl. Mater. Interfaces* **2018**, *10* (51), 44430–44442. https://doi.org/10.1021/acsami.8b15793.

(56) Wang, Z.-L.; Xu, D.; Xu, J.-J.; Zhang, L.-L.; Zhang, X.-B. Graphene Oxide Gel-Derived, Free-Standing, Hierarchically Porous Carbon for High-Capacity and High-Rate Rechargeable Li-O2 Batteries. *Advanced Functional Materials* **2012**, *22* (17), 3699–3705. https://doi.org/10.1002/adfm.201200403.

(57) Xiong, Q.; Huang, G.; Zhang, X.-B. High-Capacity and Stable Li-O2 Batteries Enabled by a Trifunctional Soluble Redox Mediator. *Angewandte Chemie International Edition* **2020**, *59* (43), 19311–19319. https://doi.org/10.1002/anie.202009064.

(58) Chen, Y.; Freunberger, S. A.; Peng, Z.; Fontaine, O.; Bruce, P. G. Charging a Li–O 2 Battery Using a Redox Mediator. *Nature Chem* **2013**, *5* (6), 489–494. https://doi.org/10.1038/nchem.1646.

(59) Sun, D.; Shen, Y.; Zhang, W.; Yu, L.; Yi, Z.; Yin, W.; Wang, D.; Huang, Y.; Wang, J.; Wang, D.; Goodenough, J. B. A Solution-Phase Bifunctional Catalyst for Lithium–Oxygen Batteries. *J. Am. Chem. Soc.* **2014**, *136* (25), 8941–8946. https://doi.org/10.1021/ja501877e.

(60) Bergner, B. J.; Schürmann, A.; Peppler, K.; Garsuch, A.; Janek, J. TEMPO: A Mobile Catalyst for Rechargeable Li-O2 Batteries. *J. Am. Chem. Soc.* **2014**, *136* (42), 15054–15064. https://doi.org/10.1021/ja508400m.

(61) Zhao, Q.; Katyal, N.; Seymour, I. D.; Henkelman, G.; Ma, T. Vanadium(III) Acetylacetonate as an Efficient Soluble Catalyst for Lithium–Oxygen Batteries. *Angewandte Chemie International Edition* **2019**, *58* (36), 12553–12557. https://doi.org/10.1002/anie.201907477.

(62) Kundu, D.; Black, R.; Adams, B.; Nazar, L. F. A Highly Active Low Voltage Redox Mediator for Enhanced Rechargeability of Lithium–Oxygen Batteries. *ACS Cent. Sci.* **2015**, *1* (9), 510–515. https://doi.org/10.1021/acscentsci.5b00267.

(63) Liang, Z.; Lu, Y.-C. Critical Role of Redox Mediator in Suppressing Charging Instabilities of Lithium–Oxygen Batteries. *J. Am. Chem. Soc.* **2016**, *138* (24), 7574–7583. https://doi.org/10.1021/jacs.6b01821.

(64) Kwak, W.-J.; Hirshberg, D.; Sharon, D.; Afri, M.; Frimer, A. A.; Jung, H.-G.; Aurbach, D.; Sun, Y.-K. Li–O2 Cells with LiBr as an Electrolyte and a Redox Mediator. *Energy Environ. Sci.* **2016**, *9* (7), 2334–2345. https://doi.org/10.1039/C6EE00700G.

(65) Ko, Y.; Park, H.; Lee, K.; Kim, S. J.; Park, H.; Bae, Y.; Kim, J.; Park, S. Y.; Kwon, J. E.; Kang, K. Anchored Mediator Enabling Shuttle-Free Redox Mediation in Lithium-Oxygen Batteries. *Angewandte Chemie International Edition* **2020**, *59* (13), 5376–5380. https://doi.org/10.1002/anie.201916682.

(66) Wang, J.; Huang, G.; Zhang, X.-B. Interface between Lithium Metal and Garnet Electrolyte: Recent Progress and Perspective. *Batteries & Supercaps* **2020**, *3* (10), 1006–1015. https://doi.org/10.1002/batt.202000082.

(67) The energy efficiency in this system is modest due to the high resistance of the anion-exchange membrane as well as the two-electron transfer of the catholytes. Future improvements in the battery performance will require new separators that limit cross-over of active species while maintaining high ion conductivity. In addition, redox mediators and catalysts could potentially be used to enhance the electrochemical kinetics.

(68) We note that there is an initial period of relatively fast capacity fade in this system. We hypothesize that this may originate from a side reaction of **2-CP** with residual water, as a new peak appears in the CV of catholyte side of the cell (Figure 4e).

(69) Sun, T.; Li, Z.-J.; Zhang, X.-B. Achieving of High Density/Utilization of Active Groups via Synergic Integration of C=N and C=O Bonds for Ultra-Stable and High-Rate Lithium-Ion Batteries. *Research* **2018**, *2018*, 1–10. https://doi.org/10.1155/2018/1936735.

(70) Wei, X.; Xu, W.; Huang, J.; Zhang, L.; Walter, E.; Lawrence, C.; Vijayakumar, M.; Henderson, W. A.; Liu, T.; Cosimbescu, L.; Li, B.; Sprenkle, V.; Wang, W. Radical Compatibility with Nonaqueous Electrolytes and Its Impact on an All-Organic Redox Flow Battery. *Angewandte Chemie International Edition* **2015**, *54* (30), 8684–8687. https://doi.org/10.1002/anie.201501443.

(71) Notably, molar energy density is a useful metric to highlight the intrinsic multi-electron redox activity of the molecules independent of solubility.

(72) Cong, G.; Zhou, Y.; Li, Z.; Lu, Y.-C. A Highly Concentrated Catholyte Enabled by a Low-Melting-Point Ferrocene Derivative. *ACS Energy Lett.* **2017**, *2* (4), 869–875. https://doi.org/10.1021/acsenergylett.7b00115.

(73) Robinson, S. G.; Yan, Y.; Hendriks, K. H.; Sanford, M. S.; Sigman, M. S. Developing a Predictive Solubility Model for Monomeric and Oligomeric Cyclopropenium-Based Flow Battery Catholytes. *J. Am. Chem. Soc.* **2019**, *141* (26), 10171–10176. https://doi.org/10.1021/jacs.9b04270.

(74) Changing the DAC substituents from isopropyl to ethylbutyl results in a catholyte (**2-DAC-2**) with greatly improved solubility (miscible in acetonitrile at room temperature vs 0.09 M maximum solubility for **2-DAC**). However, **2-DAC-2** is significantly less stable to electrochemical cycling (74% capacity retention after 50 cycles compared to 97% for **2-DAC** under analogous conditions). See Supporting Information for complete details. Ongoing work is focused on identifying the decomposition mechanism in this system.

(75) Becke, A. D. Density-Functional Exchange-Energy Approximation with Correct Asymptotic Behavior. *Phys. Rev. A* **1988**, *38* (6), 3098–3100. https://doi.org/10.1103/PhysRevA.38.3098.

(76) Lee, C.; Yang, W.; Parr, R. G. Development of the Colle-Salvetti Correlation-Energy Formula into a Functional of the Electron Density. *Phys. Rev. B* **1988**, *37* (2), 785–789. https://doi.org/10.1103/PhysRevB.37.785.

(77) Davis, A. P.; Fry, A. J. Experimental and Computed Absolute Redox Potentials of Polycyclic Aromatic Hydrocarbons Are Highly Linearly Correlated Over a Wide Range of

Structures and Potentials. *J. Phys. Chem. A* **2010**, *114* (46), 12299–12304. https://doi.org/10.1021/jp106088n.

(78) Santiago, C. B.; Milo, A.; Sigman, M. S. Developing a Modern Approach To Account for Steric Effects in Hammett-Type Correlations. *J. Am. Chem. Soc.* **2016**, *138* (40), 13424–13430. https://doi.org/10.1021/jacs.6b08799.

(79) Nie, W.; Tarnopol, D. E.; McCrory, C. C. L. Enhancing a Molecular Electrocatalyst's Activity for CO2 Reduction by Simultaneously Modulating Three Substituent Effects. *J. Am. Chem. Soc.* **2021**, *143* (10), 3764–3778. https://doi.org/10.1021/jacs.0c09357.

(80) Wang, M.; Torbensen, K.; Salvatore, D.; Ren, S.; Joulié, D.; Dumoulin, F.; Mendoza, D.; Lassalle-Kaiser, B.; Işci, U.; Berlinguette, C. P.; Robert, M. CO 2 Electrochemical Catalytic Reduction with a Highly Active Cobalt Phthalocyanine. *Nat Commun* **2019**, *10* (1), 3602. https://doi.org/10.1038/s41467-019-11542-w.

(81) Rao, H.; Schmidt, L. C.; Bonin, J.; Robert, M. Visible-Light-Driven Methane Formation from CO 2 with a Molecular Iron Catalyst. *Nature* **2017**, *548* (7665), 74–77. https://doi.org/10.1038/nature23016.

(82) Azcarate, I.; Costentin, C.; Robert, M.; Savéant, J.-M. Through-Space Charge Interaction Substituent Effects in Molecular Catalysis Leading to the Design of the Most Efficient Catalyst of CO2-to-CO Electrochemical Conversion. *J. Am. Chem. Soc.* **2016**, *138* (51), 16639–16644. https://doi.org/10.1021/jacs.6b07014.

(83) Zhu, M.; Yang, D.-T.; Ye, R.; Zeng, J.; Corbin, N.; Manthiram, K. Inductive and Electrostatic Effects on Cobalt Porphyrins for Heterogeneous Electrocatalytic Carbon Dioxide Reduction. *Catal. Sci. Technol.* **2019**, *9* (4), 974–980. https://doi.org/10.1039/C9CY00102F.

(84) Sahu, S.; Cheung, P. L.; Machan, C. W.; Chabolla, S. A.; Kubiak, C. P.; Gianneschi, N. C. Charged Macromolecular Rhenium Bipyridine Catalysts with Tunable CO2 Reduction Potentials. *Chemistry – A European Journal* **2017**, *23* (36), 8619–8622. https://doi.org/10.1002/chem.201701901.

(85) Sung, S.; Li, X.; Wolf, L. M.; Meeder, J. R.; Bhuvanesh, N. S.; Grice, K. A.; Panetier, J. A.; Nippe, M. Synergistic Effects of Imidazolium-Functionalization on Fac-Mn(CO)3 Bipyridine Catalyst Platforms for Electrocatalytic Carbon Dioxide Reduction. *J. Am. Chem. Soc.* **2019**, *141* (16), 6569–6582. https://doi.org/10.1021/jacs.8b13657.

(86) Sung, S.; Kumar, D.; Gil-Sepulcre, M.; Nippe, M. Electrocatalytic CO2 Reduction by Imidazolium-Functionalized Molecular Catalysts. *J. Am. Chem. Soc.* **2017**, *139* (40), 13993–13996. https://doi.org/10.1021/jacs.7b07709.

(87) Sevov, C. S.; Hickey, D. P.; Cook, M. E.; Robinson, S. G.; Barnett, S.; Minteer, S. D.; Sigman, M. S.; Sanford, M. S. Physical Organic Approach to Persistent, Cyclable, Low-Potential Electrolytes for Flow Battery Applications. *J. Am. Chem. Soc.* **2017**, *139* (8), 2924–2927. https://doi.org/10.1021/jacs.7b00147.

(88) Kota, R.; Samudrala, R.; Mattern, D. L. Synthesis of Donor-σ-Perylenebisimide-Acceptor Molecules Having PEG Swallowtails and Sulfur Anchors. *J. Org. Chem.* **2012**, *77* (21), 9641–9651. https://doi.org/10.1021/jo301701a.

(89) Chickos, J. S.; Patton, E.; West, R. Aryltrichlorocyclopropenes and Arylhydroxycyclopropenones. *J. Org. Chem.* **1974**, *39* (12), 1647–1650. https://doi.org/10.1021/jo00925a009.

(90) Wu, M. T.; Taub, D.; Patchett, A. A. Preparation and Hydrolysis of Phenylbisdialkylaminocyclopropenium Cations. *Tetrahedron Letters* **1976**, *17* (28), 2405–2408. https://doi.org/10.1016/0040-4039(76)90004-6.

(91) Yoshida, H.; Morishita, T.; Fukushima, H.; Ohshita, J.; Kunai, A. Three-Component Coupling of Arynes, Aminosilanes, and Aldehydes. *Org. Lett.* **2007**, *9* (17), 3367–3370. https://doi.org/10.1021/ol071347a.

(92) Aljabali, A. A. A.; Barclay, J. E.; Butt, J. N.; Lomonossoff, G. P.; Evans, D. J. Redox-Active Ferrocene-Modified Cowpea Mosaic Virus Nanoparticles. *Dalton Trans.* **2010**, *39* (32), 7569–7574. https://doi.org/10.1039/C0DT00495B.

(93) Nicholson, R. S. Theory and Application of Cyclic Voltammetry for Measurement of Electrode Reaction Kinetics. *Anal. Chem.* **1965**, *37* (11), 1351–1355. https://doi.org/10.1021/ac60230a016.

(94) *MacroModel*; Schrödinger, LLC: New York, 2017.

(95) Harder, E.; Damm, W.; Maple, J.; Wu, C.; Reboul, M.; Xiang, J. Y.; Wang, L.; Lupyan, D.; Dahlgren, M. K.; Knight, J. L.; Kaus, J. W.; Cerutti, D. S.; Krilov, G.; Jorgensen, W. L.; Abel, R.; Friesner, R. A. OPLS3: A Force Field Providing Broad Coverage of Drug-like Small Molecules and Proteins. *J Chem Theory Comput* **2016**, *12* (1), 281–296. https://doi.org/10.1021/acs.jctc.5b00864.

(96) Becke, A. D. Density-Functional Exchange-Energy Approximation with Correct Asymptotic Behavior. *Phys. Rev. A* **1988**, *38* (6), 3098–3100. https://doi.org/10.1103/PhysRevA.38.3098.

(97) Lee, C.; Yang, W.; Parr, R. G. Development of the Colle-Salvetti Correlation-Energy Formula into a Functional of the Electron Density. *Phys. Rev. B* **1988**, *37* (2), 785–789. https://doi.org/10.1103/PhysRevB.37.785.

(98) Frisch, M. J.; Trucks, G. W.; Schlegel, H. B.; Scuseria, G. E.; Robb, M. A.; Cheeseman, J. R.; Scalmani, G.; Barone, V.; Petersson, G. A.; Nakatsuji, H.; Li, X.; Caricato, M.; Marenich, A. V.; Bloino, J.; Janesko, B. G.; Gomperts, R.; Mennucci, B.; Hratchian, H. P.; Ortiz, J. V.; Izmaylov, A. F.; Sonnenberg, J. L.; Williams; Ding, F.; Lipparini, F.; Egidi, F.; Goings, J.; Peng, B.; Petrone, A.; Henderson, T.; Ranasinghe, D.; Zakrzewski, V. G.; Gao, J.; Rega, N.; Zheng, G.; Liang, W.; Hada, M.; Ehara, M.; Toyota, K.; Fukuda, R.; Hasegawa, J.; Ishida, M.; Nakajima, T.; Honda, Y.; Kitao, O.; Nakai, H.; Vreven, T.; Throssell, K.; Montgomery Jr., J. A.; Peralta, J. E.; Ogliaro, F.; Bearpark, M. J.; Heyd, J. J.; Brothers, E. N.; Kudin, K. N.; Staroverov, V. N.; Keith, T. A.; Kobayashi, R.; Normand, J.; Raghavachari, K.; Rendell, A. P.; Burant, J. C.; Iyengar, S. S.; Tomasi, J.; Cossi, M.; Millam, J. M.; Klene, M.; Adamo, C.; Cammi, R.; Ochterski, J. W.; Martin, R. L.; Morokuma, K.; Farkas, O.; Foresman, J. B.; Fox, D. J. *Gaussian 16 Rev. B.01*; Wallingford, CT, 2016.

(99) Ermanis, K.; Parkes, K. E. B.; Agback, T.; Goodman, J. M. Expanding DP4: Application to Drug Compounds and Automation. *Org. Biomol. Chem.* **2016**, *14* (16), 3943–3949. https://doi.org/10.1039/C6OB00015K.

(100) Davis, A. P.; Fry, A. J. Experimental and Computed Absolute Redox Potentials of Polycyclic Aromatic Hydrocarbons Are Highly Linearly Correlated Over a Wide Range of Structures and Potentials. *J. Phys. Chem. A* **2010**, *114* (46), 12299–12304. https://doi.org/10.1021/jp106088n.

Chapter 6

Development of High Energy Density Diaminoyclopropenium-Phenothiazine Hybrid Catholytes for Non-Aqueous Redox Flow Batteries

6.1 Introduction

Nonaqueous redox flow batteries (RFBs) offer opportunities for achieving high energy density storage due to the large electrochemical potential window of organic solvents.[1,2] To take complete advantage of this large potential window, it is critical to develop storage materials (catholytes and anolytes) that undergo multiple reversible redox reactions at extreme potentials, exhibit high solubility in all oxidation states, and possess high calendar and cycling stability.[3–20] Over the past decade, a variety of anolytes that fit these criteria have been identified.[16,21–25] In marked contrast, their multi-electron catholyte counterparts remain extremely limited.[3–20] Phenothiazine is a rare example of a catholyte that undergoes two electron transfers in organic solvents.[7,11,15,26–28] However, as depicted in Figure 6.1, existing phenothiazine derivatives suffer from some combination of modest solubility, modest oxidation potential, and/or poor electrochemical stability for the second couple.[7,11,15,28]

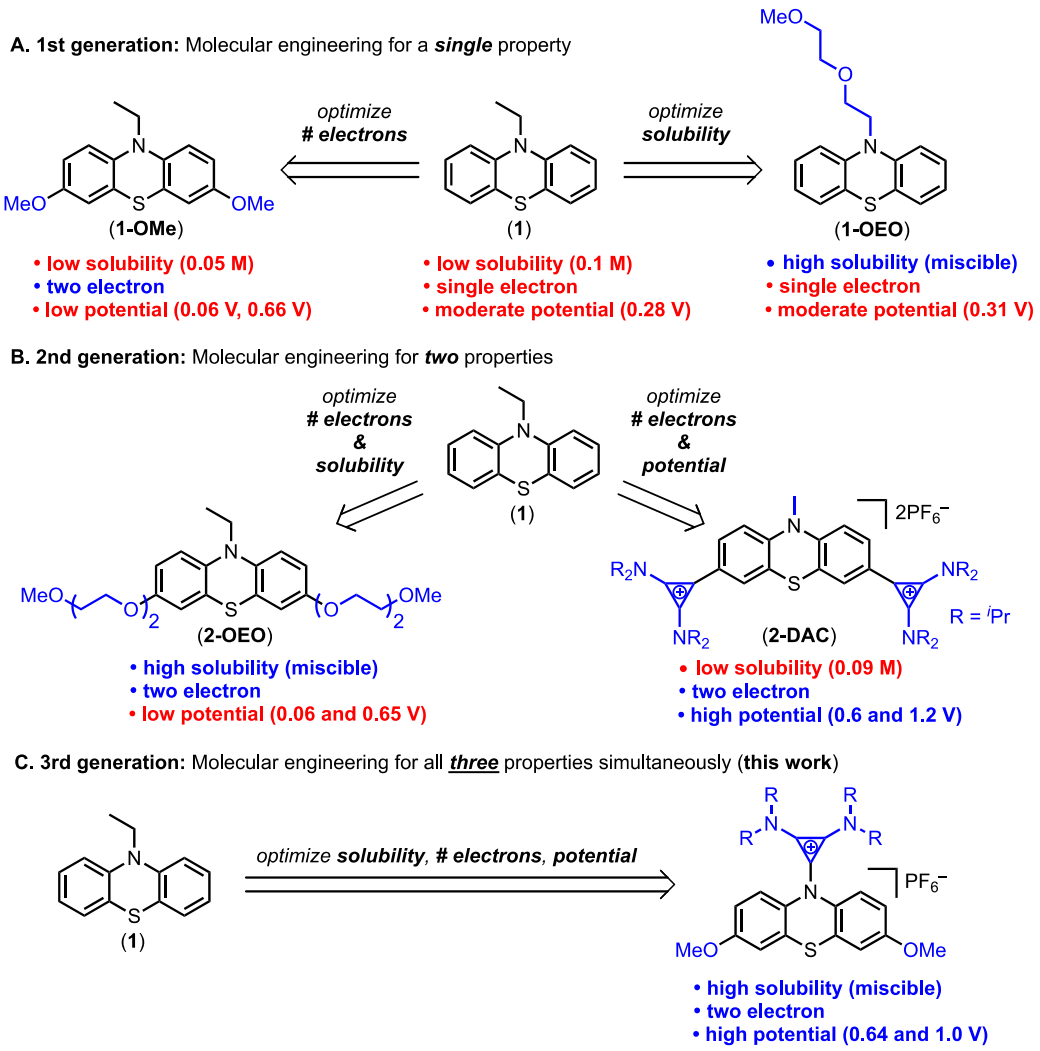

Figure 6.1. Evolution of phenothiazine-based catholytes

Several research teams have made progress in the molecular engineering of next-generation phenothiazine derivatives (Figure 6.1).[11,26,28–32] Odom and coworkers conducted early investigations of the parent *N*-ethyl phenothiazine (**1**) and disclosed that it suffers from low solubility (0.1 M for the neutral molecule and 0.1 M for the radical cation in $TEABF_4$/MeCN) and an unstable second oxidation.[26] As shown in Figure 1A, their team initially used molecular engineering to address each of these individual properties. For instance, they showed that replacing the *N*-ethyl substituent with an *N*-oligoethylene oxide (OEO) chain (**1-OEO**) resulted in dramatically enhanced solubility for both the neutral (miscible) and radical cation (0.5 M) in

$TEABF_4$/MeCN. However, the second oxidative couple of **1-OEO** remained unstable, so only single-electron cycling was achieved.[26] In a separate study, Odom and coworkers demonstrated that stable two-electron cycling could be realized by installing electron-donating methoxy (MeO-) substituents at the 3- and 7- sites of the phenothiazine core (**1-OMe**). However, this resulted in a significant (~300 mV) decrease in the redox potential for each couple.[11,28] In addition, the solubility of **1-OMe** is poor (0.05 M in 0.5 M TEATFSI/MeCN).

Second-generation approaches have leveraged these early insights to simultaneously optimize two properties of phenothiazines (Figure 6.1B). For instance, Odom and coworkers demonstrated that integrating oligoethylene oxide groups at the 3- and 7-sites (**2-OEO**) results in enhanced solubility (miscible) as well as stable two-electron cycling, albeit at low potentials (0.06 and 0.65 V vs Fc/Fc^+).[28] Additionally, our group recently showed that installing resonance electron-withdrawing diaminocyclopropenium substituents at the 3- and 7- positions (**2-DAC**) results in both stabilization of the second redox couple and an ~600 mV increase in redox potential relative to **1-OMe** (to 0.6 and 1.2 V).[33] However, **2-DAC** remains limited by extremely poor solubility in the electrolyte solution (0.09 M in MeCN). Additionally, **2-DAC** derivatives bearing different substituents are not readily accessible due to challenges associated with the C–C bond-forming step that couples the DAC to the phenothiazine core.

In this report, we identify next generation diaminocyclopropenium-phenothiazine hybrid catholytes of the general structure **3** that are accessible in a rapid and modular fashion, thus expediting molecular engineering of all three key properties simultaneously (Figure 6.1C). We demonstrate that attaching the DAC to phenothiazine via a C–N bond (rather than a C–C bond) circumvents the synthetic challenges associated with **2-DAC**. Combining this modular C–N coupling protocol with computation and structure-property analysis enabled the identification of a

derivative that displays stable two-electron cycling at high potentials (0.64 and 1.00 V vs Fc/Fc^+) as well as high solubility (≥0.45 M in $TBAPF_6$/MeCN in all relevant redox states). This catholyte was deployed in a two-electron RFB, exhibiting > 90 % capacity retention over 266 hours of flow cell cycling at > 0.5 M electron concentration.

6.2 Results and Discussion

We previously reported that appending resonance-electron-withdrawing diaminocyclopropenium substituents to the phenothiazine core (**2-DAC**) results in dramatic increases in redox potential as well as stabilization of two-electron cycling compared to the parent catholyte **1**.[33] However, a key limitation of **2-DAC** is its poor solubility (0.09 M in MeCN). In addition, this molecule has an undesirably high molecular weight (~1000 g/mol), which limits the maximum achievable concentration in an RFB.[34] Literature precedent suggests that modifying the R substituents on the DAC could be effective for enhancing solubility across all redox states.[35,36] However, analogues of **2-DAC** bearing different R groups were not readily accessible due to synthetic limitations. Specifically, the carbon-carbon bond forming reaction required to access **2-DAC** does not proceed cleanly without bulky diisopropylamino groups on the cyclopropenium. Additionally, this sequence does not accommodate diverse substituents on the phenothiazine core.

We reasoned that these challenges could be addressed by changing the attachment linkage between the two components. Specifically, we hypothesized that diverse DAC and phenothiazine derivatives could be coupled in a single synthetic step via a carbon–nitrogen bond-forming reaction between the parent phenothiazine and 1-chloro-2,3-bis(dialkylamino)cyclopropenium chlorides.[37,38] Diverse substitution can be incorporated on both reaction partners, enabling the one-step synthesis of 10 derivatives (**Scheme 6.1**, series **3** and **4**). All products were characterized via ^1H and ^{13}C NMR spectroscopy as well as high resolution mass spectrometry.

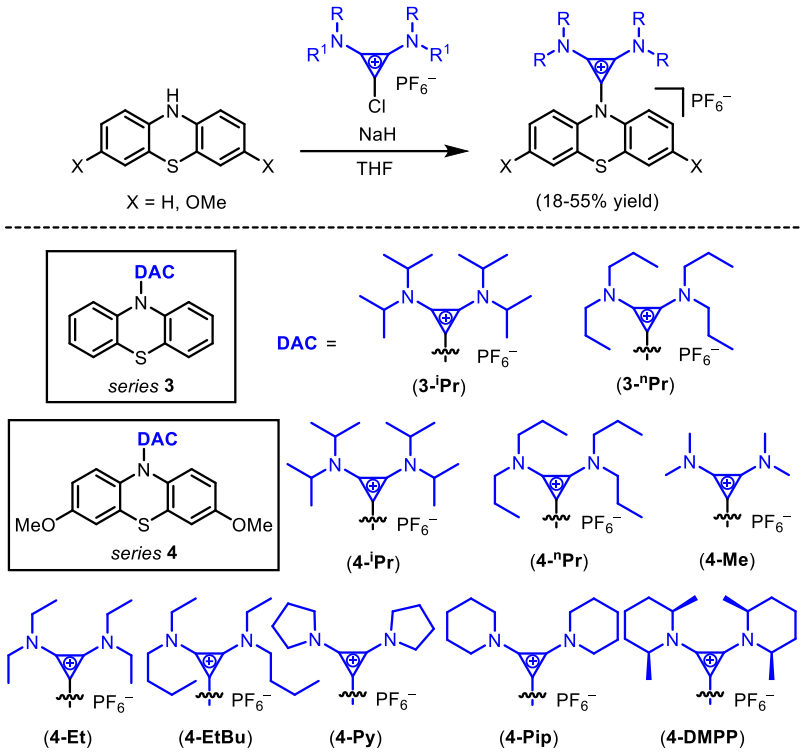

Scheme 6.1. Synthesis of **3** and **4**

The redox properties of the catholyte candidates in series **3** and **4** were initially interrogated using cyclic voltammetry (CV). CV experiments were conducted using 5 mM solutions of the redox active molecules in 0.5 M $TBAPF_6$/MeCN with a glassy carbon working electrode (0.071 cm^2, BASi) and a scan rate of 100 mV/s. Representative CVs are shown in Figure 6.2, and the redox potential (vs Fc/Fc^+) and peak height ratio for each couple are summarized in Table 6.1.

The phenothiazine-derived compound **3-^{i}Pr** undergoes two single-electron oxidations at 0.70 and ~1.40 V vs Fc/Fc^+. Notably, these oxidation potentials are 100-200 mV higher than those of **2-DAC** (0.60 and 1.20 V vs Fc/Fc^+), despite the presence of a single DAC moiety on **3-^{i}Pr**. However, unlike **2-DAC**, the second oxidation is not reversible, as indicated by the lack of a significant return wave for this peak (Figure 6.2a). In addition, **3-^{i}Pr** exhibits only modest (0.15 M) solubility in 0.5 M $TBAPF_6$/MeCN. The *n*-propyl derivative **3-^{n}Pr** undergoes oxidation at slightly higher

potentials (0.72 and 1.30 V vs Fc/Fc^+) but also exhibits low stability in the second redox couple (i_{pc2}/i_{pa2} = 0.83, see Figure S2 for multiple CV scans of **3-^{n}Pr**). However, the solubility of **3-^{n}Pr** is more than five-fold higher than that of **3-^{i}Pr** (0.86 in 0.5 M $TBAPF_6$/MeCN), indicating that modification of the DAC substituents is an effective approach to tuning solubility in these systems.

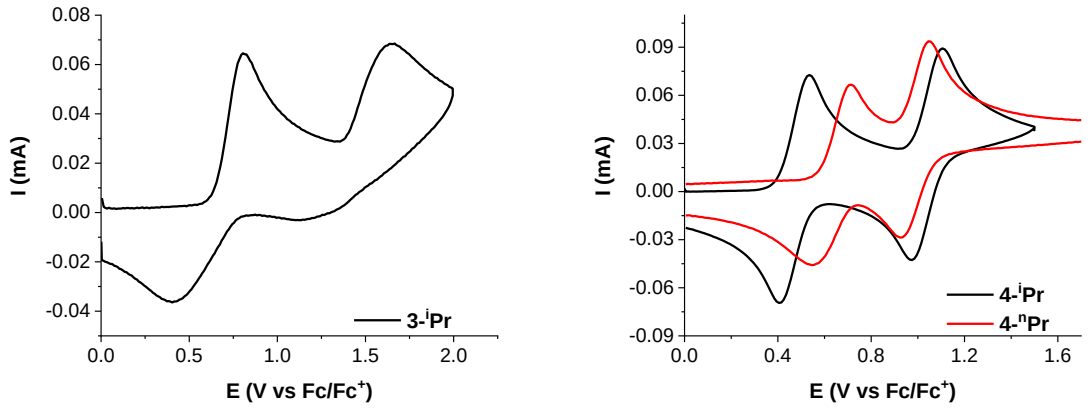

Figure 6.2. (a) CV of **3-^{i}Pr**. (b) CVs of **4-^{i}Pr** (black) and **4-^{n}Pr** (red). CVs conducted with 5 mM solutions of the redox active molecules in 0.5 M $TBAPF_6$ in MeCN at 100 mV/s scan rate.

Table 6.1. CV data of all compounds

compound	1st $E_{1/2}$[a]	i_{pc1}/i_{pa1}[b]	2nd $E_{1/2}$[a]	i_{pc2}/i_{pa2}[b]
3-^{i}Pr	0.70 V	0.93	1.40 V	irreversible
3-^{n}Pr	0.72 V	0.90	1.30 V	0.83
4-^{i}Pr	0.47 V	1.00	1.04 V	0.97
4-^{n}Pr	0.67 V	0.99	1.00 V	1.02
4-Me	0.65 V	0.97	1.01 V	1.02
4-Et	0.65 V	0.92	1.00 V	1.01
4-EtBu	0.65 V	0.92	1.00 V	1.07
4-Py	0.65 V	0.96	0.95 V	1.07
4-Pip	0.63 V	0.97	1.00 V	1.03
4-DMPP	0.64 V	0.93	1.00 V	1.05

[a]2.5 mM substrate in 0.5 M $TBAPF_6$/MeCN and referenced to Fc/Fc^+. [b]Calculated at a scan rate of 20 mV/s.

On the basis of Odom's previous work,[27] we reasoned that the reversibility of the second redox couple could be enhanced by introducing methoxy (MeO-) substituents at the 3- and 7-positions of the phenothiazine core. To tets this hypothesis, we synthesized and evaluated **4-^{i}Pr**. As illustrated in Figure 6.2b, the CV of **4-^{i}Pr** displays two single-electron oxidations at 0.47 V and 1.04 vs Fc/Fc^+. While these potentials are 200-400 mV lower than those of **3-^{i}Pr**, the second oxidation exhibits significantly enhanced reversibility versus that of **3-^{i}Pr** (i_{pc2}/i_{pa2} = 0.97 at a scan rate of 100 mV/s for the oxidation at 1.04 V in **4-^{i}Pr**).

We next changed the amine substituent from isopropyl to *n*-propyl with the goal of improving the solubility of **4-^{i}Pr** (which is just 0.08 M in 0.5 M $TBAPF_6$/MeCN). Indeed, **4-^{n}Pr** exhibits >15-fold higher solubility than **4-^{i}Pr** (1.42 M in 0.5 M $TBAPF_6$/MeCN). Unexpectedly, the oxidation potential also changes significantly between the *iso*-propyl and *n*-propyl derivatives. While the second oxidation occurs at comparable potential ($E_{1/2}$ = 1.00 V for **4-^{n}Pr** and 1.06 V for **4-^{i}Pr**), the first oxidation for **4-^{n}Pr** is almost 200 mV higher ($E_{1/2}$ = 0.65 V versus 0.47 V, respectively).[36]

To identify trends in this first oxidation potential as a function of DAC nitrogen substituent, we explored a series of derivatives bearing methyl (**4-Me**), ethyl (**4-Et**), ethyl butyl (**4-EtBu**), pyrrolidine (**4-Py**), piperidine (**4-Pip**), and 2,6-dimethylpiperidine (**4-DMPP**) substituents. As summarized in Table 1 and Figure 2, these derivatives all show two reversible oxidations with peak height ratios close to 1. Furthermore, their oxidation potentials are all nearly identical to those of **4-^{n}Pr**. Thus, rather than a trend of potential as a function of nitrogen substituent, we see that **4-^{i}Pr** is the only molecule with a lower first redox potential.

To investigate the origin of this outcome, we turned to computational analysis via density-functional theory (DFT; see Supporting Information for complete details). We hypothesized that oxidation potential in these systems is influenced by overlap between the electron-poor cyclopropenium and electron-rich phenothiazine orbitals, which affects the overall charge distribution in the molecule. To evaluate this proposal, we collected Boltzmann-averaged data from a conformational ensemble of each molecule in series **4** (Table 6.1). We collected these data for both the unoxidized molecule (+1 charge, **4**) and the two oxidation products [+2 charge ($\mathbf{4}^{\bullet+}$) and +3 charge ($\mathbf{4}^{++}$)].

Thees studies reveal that the steric bulk of **4-*i*Pr** imposes a drastic geometric change that accompanies removal of the first electron (ΔCp^{+} $twist_{(ox1)}$ = 71°, **Figure 3A**) and ultimately results in nearly perpendicular (Cp^{+} twist = 87°), and thus unconjugated, ring systems in the first oxidation product $\mathbf{4}$-$^{i}\mathbf{Pr}^{\bullet+}$. In contrast, this geometric change is much less pronounced in the other series **4** electrolytes (average ΔCp^{+} $twist_{(ox1)}$ = 29 ± 0.6° for all series 4 compounds excluding **4-*i*Pr**, Figure 3A, **4-Me** shown as representative example), thus yielding a more conjugated first oxidation product (Cp^{+} twist = 46° for $\mathbf{4}$-$\mathbf{Me}^{\bullet+}$). This effect can also be seen in Figure 3B when comparing the singly occupied molecular orbital (SOMO) of the first oxidation products, $\mathbf{4}$-$^{i}\mathbf{Pr}^{\bullet+}$ and $\mathbf{4}$-$\mathbf{Me}^{\bullet+}$.

Overall, this analysis indicates that the first oxidation of **4-*i*Pr** is effectively isolated to the dimethoxyphenothiazine core, with the DAC substituent serving as an inductive electron withdrawing group. This results in a positive shift in potential relative to that of the parent **1-OMe** (from 0.06 V to 0.47 V vs Fc/Fc^{+}). In contrast, the first oxidation of **4-Me** occurs across both rings, and thus can be viewed as a mixture of the two component redox potentials, resulting in a significantly more positive first oxidation potential (at 0.65 V vs Fc/Fc^{+}).

While the first oxidation of **4-^{i}Pr** occurs at lower potential than that of the other series **4** derivatives in Table 1, the second oxidation is at nearly the same potential (~1.0 V) for all eight compounds. We evaluated the geometries and frontier molecular orbitals of the second oxidation products (**4**$^{++}$) and found a uniformly insignificant amount of geometric reorganization accompanying the removal of the second electron (average ΔCp^{+} $twist_{(ox2)}$ = 12 ± 8° for all series 4 compounds). Additionally, for both **4-^{i}Pr**$^{\bullet+}$ and **4-Me**$^{\bullet+}$, the majority of SOMO electron density is concentrated on the phenothiazine portion of the molecule despite **4-^{i}Pr** having less conjugation between the rings (Figure 3B, **4-^{i}Pr**$^{\bullet+}$ and **4-Me**$^{\bullet+}$ SOMO). This suggests that conjugation between the two rings plays a minimal role in the second oxidation. Thus, the large difference in Cp^{+} twist angle between the two structures (which is maintained in **4-^{i}Pr**$^{++}$ and **4-Me**$^{++}$, see Supporting information for complete details) does not manifest in significantly different potentials for this second oxidation.

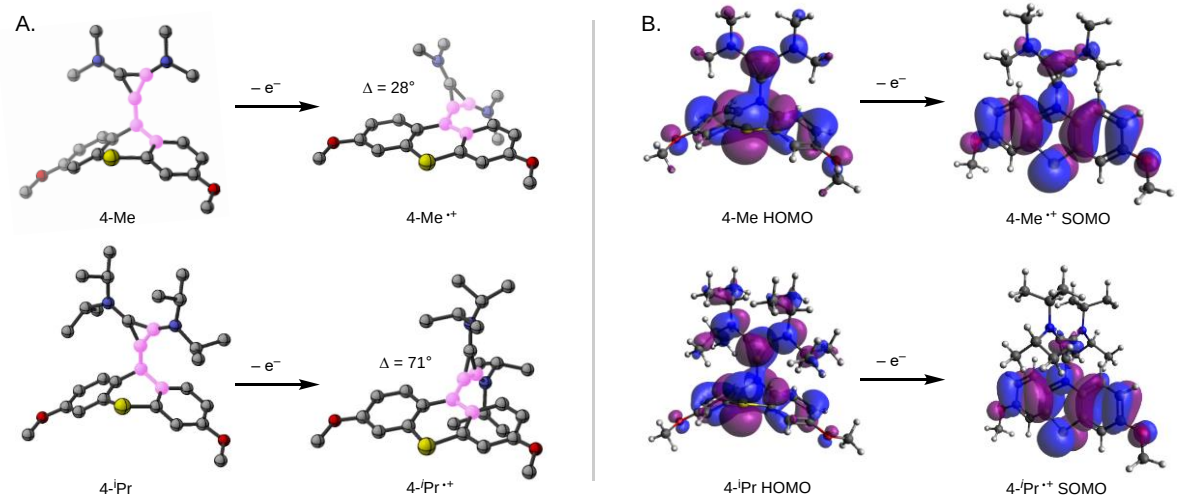

Figure 6.3. (A) Geometry changes accompanying the first oxidation of **4-Me** (used as a representative example of the series **4** compounds; data for the other series **4** molecules is in SI) and **4-^{i}Pr**. "Cp^{+} twist" is visualized by the dihedral angle highlighted in pink. (B) HOMO and SOMO of **4-Me** and **4-^{i}Pr** before (+1 charge) and after the first oxidation (+2 charge).

Table 6.2. Capacity retention data for the two-electron cycling of **4** in an H-cell

compound	accessed capacity[a] (%)	coulombic efficiency (%)	capacity fade in 100 cycles (%)
4-Me	77.7	>98	28.7
4-Et	80.0	>98	21.2
4-^{n}Pr	81.7	>98	31.7
4-^{i}Pr	78.3	>99	14.9
4-EtBu	84.8	>99	13.8
4-Py	86.5	>99	17.5
4-Pip	85.8	>99	15.2
4-DMPP	81.9	>99	14.5

[a]2.5 mM substrate in 0.5 M $TBAPF_6$/MeCN

We next compared capacity retention in series **4** derivatives during charge-discharge cycling in a static H-cell. These experiments were conducted in a three-electrode H-cell separated with an ultrafine glass frit, using reticulated vitreous carbon (RVC) working and counter electrodes.[35] Two-electron cycling was conducted with a 2.5 mM solution of **4** in 0.5 M $TBAPF_6$/acetonitrile on both the working and counter electrode sides of the cell. After the initial charge, the solution on the counter electrode side was exchanged for a fresh solution of **4** in 0.5 M $TBAPF_6$/acetonitrile to enable symmetrical two-electron cycling. The solution on the working side of the cell was charged at a rate of 2.5 C using voltaic cutoffs to achieve the maximum state-of-charge (SOC). The discharged capacity was then monitored versus cycle number to assess capacity retention. As summarized in Table 6.2, over 100 cycles all eight of these derivatives show comparable capacity fade (14-31%) and coulombic efficiency (98-99%) while charging similar amounts of catholyte during cycling (achieving 78-87% of theoretical capacity).

Based on the similar charge-discharge cycling data for the compounds in series **4**, we moved forward with the most soluble of these derivatives for flow cell cycling. While **4-Me**, **4-Et**, **4-^{n}Pr**, **4-^{i}Pr**, **4-pip**, and **4-py** are solids at room temperature, **4-EtBu** and **4-DMPP** are viscous oils that are fully miscible in 0.5 M $TBAPF_6$/MeCN. Thus, each of these two-electron catholytes was next cycled in a flow cell, using viologen **5** (see Figure 6.4) as a two-electron anolyte.[22,23,39,40] The flow cell contains graphite charge collecting plates with an interdigitated flow field in combination with 400 µm thick carbon-felt electrodes. The electrolyte solutions were flowed through the cell at 10 mL/min and were subjected to galvanostatic cycling at 40 mA/cm^2. The cell was separated by a Celgard 4560 membrane. For initial cycling studies, the catholyte and anolyte reservoirs were loaded with 50 mM solutions of **4-EtBu** or **4-DMPP** and **5** in 0.50 M MeCN/$TBAPF_6$. In these systems, the electron concentration is 0.1 M, with a battery potential up to 2.2 V, and a theoretical capacity of 2.68 Ah/L.

Figure 4 shows the capacity retention data (panel a), pre- and post-cycling CVs (panels b and c), and pre- and post-cycling electrochemical impedance spectroscopy (EIS) measurements for the two flow cell experiments. The flow cells with **4-EtBu/5** and **4-DMPP/5** exhibit dramatically different performances, despite similar levels of material utilization (78% and 82%, respectively) and coulombic efficiency (91% and 92%, respectively) during cycling. The **4-EtBu/5** flow cell shows much lower capacity retention over 100 cycles (20% versus 86% for **4-DMPP/5**). The post-cycling CV from the catholyte side of the **4-EtBu/5** cell (Figure 6.4b, red) shows that the reduction of **5** is no longer reversible. In addition, the post-cycling electrochemical impedance spectroscopy (EIS) of the **4-EtBu/5** cell shows an approximately 20-fold increase in the impedance. Collectively, these data suggest that decomposition of the redox-active molecule(s) is occurring during flow cell cycling, likely depositing insoluble material on the electrodes and/or the membrane. The post-run

CVs indicate that this is particularly problematic for the catholyte solution, suggesting a key contribution from decomposition/side reactions between either **4-EtBu**$^{\bullet+}$ or **4-EtBu**$^{++}$ and the anolyte **5**.

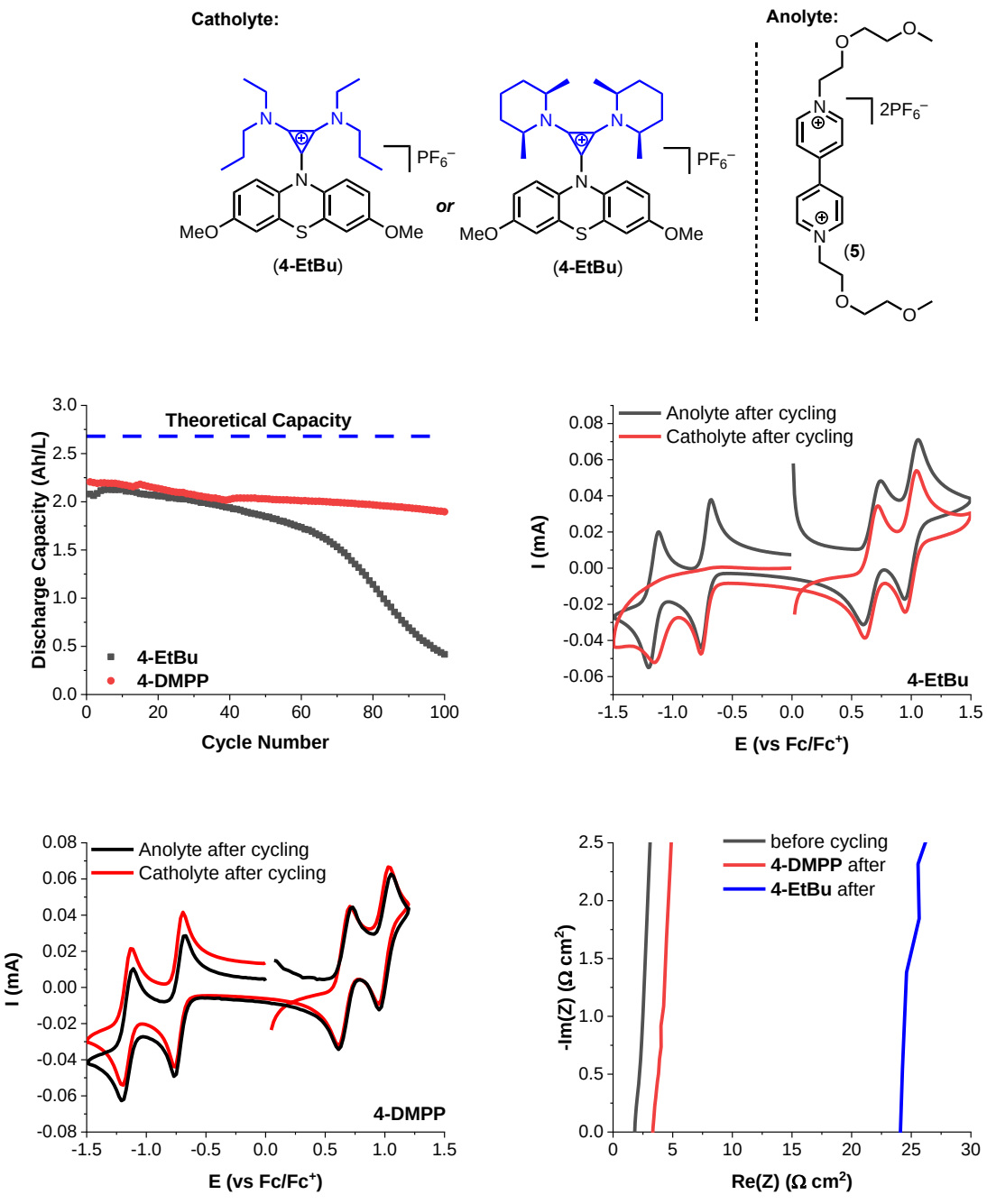

Figure 6.4. (a) Flow cell cycling of 50 mM **4-DMPP** or **4-EtBu** as catholyte and 50 mM **5** as anolyte. (b) CVs after flow cell cycling of **4-EtBu** (black = anolyte side of cell; red = catholyte

side of cell). (c) CVs after flow cell cycling of **4-DMPP** (black = anolyte side of cell; red = catholyte side of cell); (d) Electrochemical impedance spectroscopy (EIS) on cells for before and after 100 cycles.

Based on the initial flow cell results, the **4-DMPP/5** system was selected for high concentration cycling. To assess the maximum feasible concentration for this battery, we evaluated solubility in the two limiting oxidation states: **4-DMPP** and **4-DMPP**$^{++}$ (the product of two-electron oxidation). **4-DMPP**$^{++}$ was prepared by bulk electrolysis (see experimental section for complete details).[35,38] The maximum solubilities of **4-DMPP** and **4-DMPP**$^{++}$ were then determined to be miscible and 0.45 M, respectively, in 0.5 M $TBAPF_6$/MeCN. Importantly, because **4-DMPP** undergoes two electron transfers, the limiting 0.45 M concentration of **4-DMPP**$^{++}$ corresponds to a 0.90 M electron concentration.

The mass transport and electrokinetics of **4-DMPP** were also evaluated. These properties are important for flow battery applications because fast diffusional and electron-transfer processes are critical for achieving high current densities and low overpotentials.[41] The diffusion coefficient was determined by varying the CV scan rate from 20 to 300 mV/s and then applying the Randles-Sevcik equation (Figure 6.9). The observed values for **4-DMPP** (first couple: 5.77×10^{-6} cm^2 s^{-1}; second couple: 4.51×10^{-6} cm^2 s^{-1}) are comparable to those for other organic catholyte materials, including ferrocene derivative Fc1N112-TFSI (4.25×10^{-7} cm^2 s^{-1})[42] and dialkoxybenzene derivative DBMMB (5.77×10^{-6} cm^2 s^{-1}),[43] as well as the related pheonthiazine derivatives **2-OEO** (0.8×10^{-6} cm^2 s^{-1})[28] and **2-DAC** (first couple: 5.29×10^{-6} cm^2 s^{-1}; second couple: 4.99×10^{-6} cm^2 s^{-1}).[33] The heterogeneous electron-transfer rates were determined to be 4.84×10^{-3} cm s^{-1} (first couple) and 4.62×10^{-3} cm s^{-1} (second couple) using the Nicholson method (Figure 6.10).[44]

Again, these are comparable to those for other catholyte materials, including 5,10-dihydro-5,10-dimethylphenazine (5.53×10^{-3} cm s^{-1}),[7] $V(acac)_3$ (6.5×10^{-4} cm s^{-1}),[41] and **2-DAC** (first couple: 2.53×10^{-3} cm^2 s^{-1}; second couple: 3.47×10^{-3} cm^2 s^{-1}).[33]

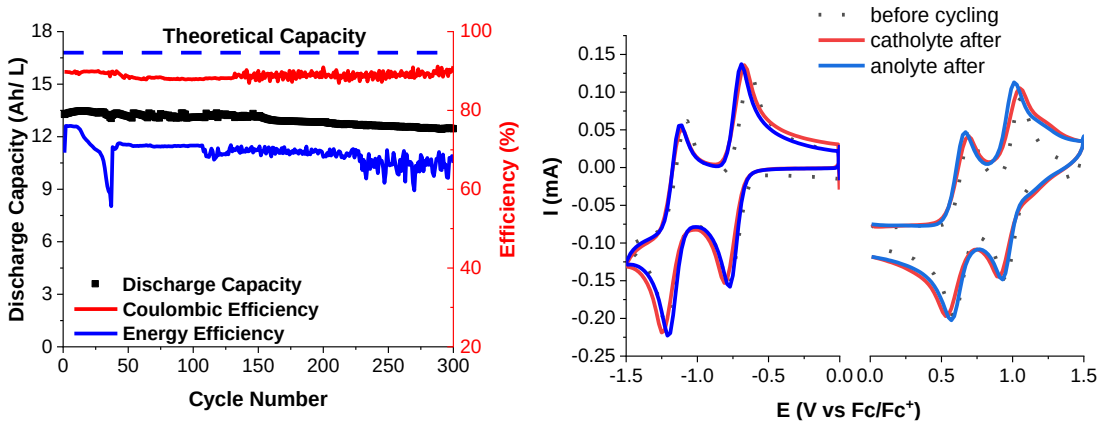

Figure 6.5. (a) Flow cell cycling of 0.3 M of **4-DMPP** as catholyte and 0.6 M of **5** as anolyte. (b) CV after cycling on both sides

A high concentration flow cell was assembled using **4-DMPP** (0.30 M in 0.50 M MeCN/$TBAPF_6$) and **5** (0.60 M in 0.50 M MeCN/$TBAPF_6$) as the catholyte and anolyte, respectively. For this experiment only the first reduction of **5** was accessed due to the modest solubility and stability of the doubly reduced viologen at high concentration. As such, the maximum cell potential in this system is 1.8 V. The charging and discharging rates were set to 60 mA/cm^2. These relatively fast rates are possible despite the high concentration due to the low resistance of the Daramic-175 membrane. The theoretical capacity of this system is 16.08 Ah/L, and the initial material utilization is 84%. As shown in Figure 6.5a, over 300 cycles (266 hours) 92.5% capacity retention was achieved with 89% coulombic efficiency and ~70% energy efficiency, demonstrating the long-term cycling stability of **4-DMPP**. Moreover, CVs of the diluted solution after cycling show no change in concentration of active species (Figure 6.5b). Instead, the observed capacity fade appears to be due to pressure/viscosity differences that result

in preferential diffusion of the electrolyte solution to create a volume discrepancy in the reservoirs at the end of the experiment.

6.3 Conclusion

In summary, a novel soluble, high potential two-electron catholyte for non-aqueous RFBs has been developed. The discovery was enabled by linking phenothiazine to diaminocyclopropenium scaffolds via a C–N bond. The formation of this C–N bond is synthetically straightforward, thus facilitating the rapid, one-step synthesis of diverse derivatives and evaluation of the relationship between chemical structure and electrochemical and solubility properties. This enabled the simultaneous optimization of three key properties (solubility, two electron redox, and redox potential), resulting in a catholyte, **4-DMPP**, with one of the best combination of properties reported to date for this application. Furthermore, we anticipate that this approach could prove generalizable to other catholyte candidates bearing amine and/or N-heterocyclic cores.

6.4 Experimental Procedures and Characterization of Compounds

6.4.1 Synthetic Procedures

General Information. All commercial chemicals were used as received unless stated otherwise. Anhydrous CH_2Cl_2 was obtained from an Innovative Technology (now rebranded to Inert) solvent purification system. Reactions were performed under a nitrogen atmosphere. 3,7-Dimethoxy-10H-phenothiazine was prepared according to a reported method.[45] Compound **5** was prepared as the tosylate salt using a published method[46] and was then subjected to anion-exchange with NH_4PF_6. 1-Chloro-2,3-bis(dialkylamino)cyclopropenium chloride was prepared according to a literature procedure.[47,38] NMR spectra were obtained on Varian VNMRs 700, Varian VNMRs 500, Varian Inova 500, or Varian MR400 spectrometers. ^{1}H and ^{13}C chemical shifts are reported in parts per million (ppm) relative to TMS, with the residual

solvent peak used as an internal reference. High resolution mass spectroscopy (HRMS) was performed on a Micromass AutoSpec Ultima Magnetic Sector Mass Spectrometer using electrospray ionization (ESI).

General procedure for the synthesis of 3 and 4. Under a N_2 atmosphere, the appropriate phenothiazine derivative (0.18 mmol, 1 equiv) was dissolved in dry THF (2 mL). Sodium hydride (0.22 mmol, 1.2 equiv) was added at room temperature. After stirring for 1 h, 1-chloro-2,3-bis(dialkylamino)cyclopropenium chloride (0.18 mmol, 1 equiv) was added. The mixture was then heated at 50 °C for overnight. The reaction was quenched with 1 M HCl (10 mL), and the resulting solution was extracted with dichloromethane (3 x 20 mL). The organic extracted were collected and concentrated under reduced pressure. The resulting residue was dissolved in water (5 mL), and ammonium hexafluorophosphate (2 equiv) was added with vigorous stirring. A precipitate formed, and this material was extracted into CH_2Cl_2 (3 × 15 mL). The combined organic extractys were dried over Na_2SO_4 and concentrated under reduced pressure. Column chromatography on silica gel afforded **3** and **4**.

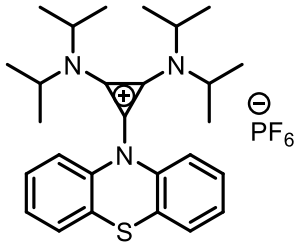

Synthesis of 3-^{i}Pr: The general procedure was followed using 1-chloro-2,3-bis(diisopropylamino)cyclopropenium chloride[47,48] as the substrate. Compound **3-^{i}Pr** was isolated as a white powder (11 mg, 18% yield) using 5% ethyl acetate in DCM as the eluent. R_F = 0.26 in 5% ethyl acetate/ DCM. ^{1}H NMR (500 MHz, CD_3CN) δ 7.19-7.08 (multiple peaks, 4H), 7.08-6.97 (m, 2H), 6.83-6.70 (m, 2H), 4.03 (hept, *J* = 6.8 Hz, 4H), 1.30 (d, *J* = 6.8 Hz,

24H).[13]C NMR (126 MHz, CD_3CN) δ 138.55, 136.16, 128.49, 128.18, 125.94, 120.92, 117.45, 102.89, 53.98, 21.80. HRMS (ESI) *m/z* calcd for $C_{27}H_{36}N_3S^+$ (**3-^{i}Pr$^+$**): 434.2624, found: 434.2619.

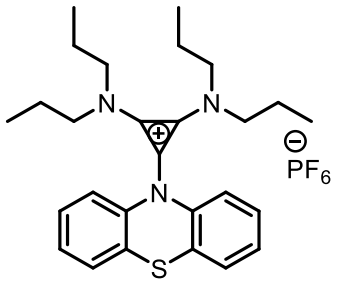

Synthesis of 3-^{n}Pr: The general procedure was followed using 1-chloro-2,3-bis(di-*n*-propylamino)cyclopropenium chloride[47,48] as the substrate. Compound **3-^{n}Pr** was isolated as a white powder (25 mg, 41% yield) using 5% ethyl acetate in DCM as the eluent. R_F = 0.30 in 5% ethyl acetate/DCM. [1]H NMR (700 MHz, CD_3CN) δ 7.67 (d, *J* = 7.9 Hz, 2H), 7.58 (d, *J* = 7.8 Hz, 2H), 7.47 (t, *J* = 7.7 Hz, 2H), 7.40 (t, *J* = 7.6 Hz, 2H), 3.07 (t, *J* = 7.6 Hz, 8H), 1.48 (h, *J* = 7.9 Hz, 8H), 0.74 (t, *J* = 7.4 Hz, 12H). [13]C NMR (176 MHz, CD_3CN) δ 140.75, 134.25, 129.70, 129.67, 129.39, 125.31, 119.87, 112.50, 55.06, 22.38, 10.75. HRMS (ESI) *m/z* calcd for $C_{27}H_{36}N_3S^+$ (**3-^{n}Pr$^+$**): 434.2624, found: 434.2615.

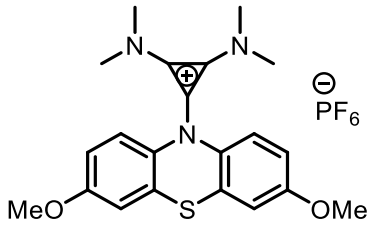

Synthesis of 4-Me: The general procedure was followed using 1-chloro-2,3-bis(dimethylamino)cyclopropenium chloride[47,48] as the substrate. Compound **4-Me** was isolated as a white powder (38 mg, 41%) using 8% ethyl acetate in DCM as the eluent. R_F =

0.21 in 8% ethyl acetate/DCM. ^{1}H NMR (400 MHz, CD_3CN) δ 7.51 (d, *J* = 8.8 Hz, 2H), 7.10 (d, *J* = 2.8 Hz, 2H), 6.95 (dd, *J* = 8.8, 2.8 Hz, 2H), 3.80 (s, 6H), 2.92 (s, 12H). ^{13}C NMR (126 MHz, CD_3CN) δ 159.97, 134.32, 133.52, 126.00, 120.36, 114.91, 114.16, 112.81, 56.60, 43.09. HRMS (ESI) *m/z* calcd for $C_{21}H_{24}N_3O_2S^+$ (**4-Me**$^+$): 382.1584, found: 382.1575.

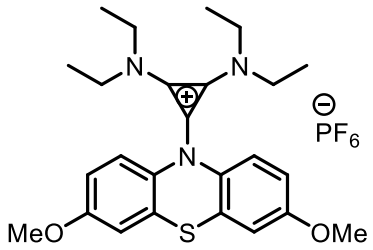

Synthesis of 4-Et: The general procedure was followed using 1-chloro-2,3-bis(diethylamino)cyclopropenium chloride[47,48] as the substrate. Compound **4-Et** was isolated as a white powder (40 mg, 39% yield) using 8% ethyl acetate in DCM as the eluent. R_F = 0.25 in 8% ethyl acetate/DCM. ^{1}H NMR (700 MHz, CD_3CN) δ 7.54 (d, *J* = 8.7 Hz, 2H), 7.12 (d, *J* = 2.8 Hz, 2H), 6.97 (dd, *J* = 8.7, 2.8 Hz, 2H), 3.81 (s, 6H), 3.14 (q, *J* = 7.2 Hz, 8H), 1.03 (t, *J* = 7.2 Hz, 12H). ^{13}C NMR (176 MHz, CD_3CN) δ 160.18, 135.71, 133.87, 126.43, 119.46, 114.94, 114.24, 113.95, 56.65, 48.02, 14.12. HRMS (ESI) *m/z* calcd for $C_{25}H_{32}N_3O_2S^+$ (**4-Et**$^+$): 438.2210, found: 438.2195.

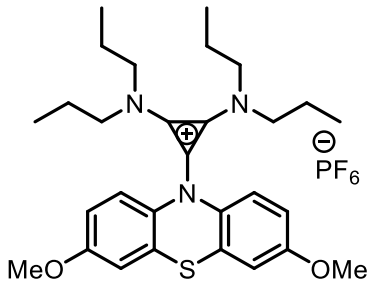

Synthesis of 4-^{n}Pr: The general procedure was followed using 1-chloro-2,3-bis(di-*n*-propylamino)cyclopropenium chloride[47,48] as the substrate. Compound **4-^{n}Pr** was isolated as a

white powder (45 mg, 40% yield) using 8% ethyl acetate in DCM as the eluent. R_F = 0.27 in 8% ethyl acetate/DCM. ^{1}H NMR (500 MHz, CD_3CN) δ 7.55 (d, *J* = 8.7 Hz, 2H), 7.14 (d, *J* = 2.8 Hz, 2H), 6.97 (dd, *J* = 8.8, 2.8 Hz, 2H), 3.81 (s, 6H), 3.12-2.95 (m, 8H), 1.57-1.34 (m, 8H), 0.82-0.66 (m, 12H). ^{13}C NMR (126 MHz, CD_3CN) δ 160.16, 136.13, 133.98, 126.55, 119.72, 115.25, 114.39, 113.73, 56.68, 54.98, 22.31, 10.77. HRMS (ESI) *m/z* calcd for $C_{29}H_{40}N_3O_2S^+$ (**4-*n*Pr**$^+$): 494.2836, found: 494.2838.

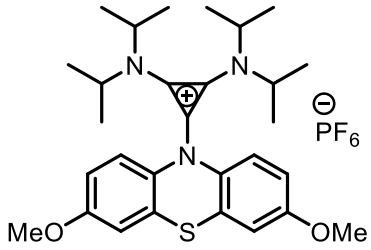

Synthesis of 4-*i*Pr: The general procedure was followed using 1-chloro-2,3-bis(di-iso propylamino)cyclopropenium chloride[47,48] as the substrate. Compound **4-*i*Pr** was isolated as a white powder (22 mg, 20% yield) using 8% ethyl acetate in DCM as the eluent. R_F = 0.24 in 8% ethyl acetate/DCM. ^{1}H NMR (400 MHz, CD_3CN) δ 6.87-6.81 (m, 4H), 6.72 (dd, *J* = 8.9, 2.9 Hz, 2H), 3.93 (hept, *J* = 6.9 Hz, 5H), 3.75 (s, 6H), 2.14 (s, 8H), 1.26 (d, *J* = 6.7 Hz, 26H). ^{13}C NMR (176 MHz, CD_3CN) δ 157.10, 132.34, 131.70, 123.89, 119.21, 112.81, 112.67, 104.99, 55.47, 52.76, 20.84. HRMS (ESI) *m/z* calcd for $C_{29}H_{40}N_3O_2S^+$ (**4-*i*Pr**$^+$): 494.2836, found: 494.2832.

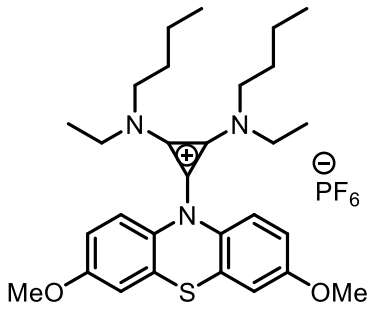

Synthesis of 4-EtBu: The general procedure was followed using 1-chloro-2,3-bis(ethylbutylamino)cyclopropenium chloride[47,48] as the substrate. Compound **4-EtBu** was isolated as a light-yellow viscous oil (50 mg, 45% yield) using 8% ethyl acetate in DCM as the eluent. R_F = 0.25 in 8% ethyl acetate/DCM. ^{1}H NMR (401 MHz, CD_3CN) δ 7.54 (d, *J* = 8.8 Hz, 2H), 7.13 (d, *J* = 2.8 Hz, 2H), 6.97 (dd, *J* = 8.7, 2.8 Hz, 2H), 3.81 (s, 6H), 3.16 (q, *J* = 7.2 Hz, 4H), 3.06 (t, *J* = 7.9 Hz, 4H), 1.44-1.29 (m, 4H), 1.15-0.98 (m, 10H), 0.84 (t, J = 7.3 Hz, 6H). ^{13}C NMR (176 MHz, CD_3CN) δ 160.16, 135.95, 133.93, 126.47, 119.60, 115.11, 114.29, 113.91, 56.66, 52.94, 48.53, 31.26, 20.19, 14.04, 13.98. HRMS (ESI) *m/z* calcd for $C_{29}H_{40}N_3O_2S^+$ (**4-EtBu**$^+$): 494.2836, found: 494.2829.

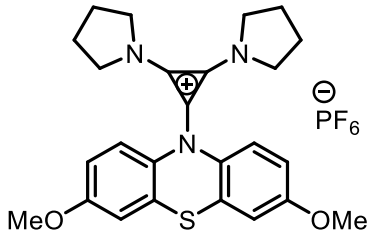

Synthesis of 4-Py: The general procedure was followed using 1-chloro-2,3-bis(pyrrolidino)cyclopropenium chloride[47,48] as the substrate. Compound **4-Py** was isolated as a white powder (52 mg, 52% yield) using 8% ethyl acetate in DCM as the eluent. R_F = 0.22 in 8% ethyl acetate/DCM. ^{1}H NMR (700 MHz, CD_3CN) δ 7.47 (d, *J* = 8.7 Hz, 2H), 7.05 (d, *J* = 2.8 Hz, 2H), 6.95 (dd, *J* = 8.8, 2.8 Hz, 2H), 3.81 (s, 6H), 3.53-3.25 (m, 8H), 1.93-1.86 (m, 8H). ^{13}C NMR (176 MHz, CD_3CN) δ 159.70, 132.95, 132.39, 124.70, 116.71, 114.76, 113.82, 110.81, 56.56, 52.58, 26.35. HRMS (ESI) *m/z* calcd for $C_{19}H_{22}N_3O^+$ (**4-Py**$^+$): 434.1897, found: 434.1889.

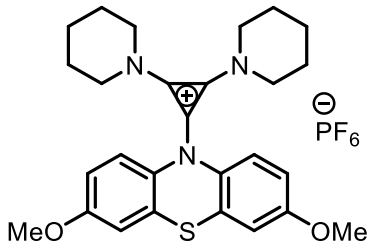

Synthesis of 4-Pip: The general procedure was followed using 1-chloro-2,3-bis(piperdino)cyclopropenium chloride[47,48] as the substrate. Compound **4-Pip** was isolated as a white powder (58 mg, 55% yield) using 8% ethyl acetate in DCM as the eluent. R_F = 0.24 in 8% ethyl acetate/DCM. ^{1}H NMR (500 MHz, CD_3CN) δ 7.47 (d, *J* = 8.7 Hz, 2H), 7.10 (d, *J* = 2.8 Hz, 2H), 6.96 (dd, *J* = 8.8, 2.8 Hz, 2H), 3.80 (s, 6H), 3.29-3.15 (m, 8H), 1.67-1.49 (multiple peaks, 12H). ^{13}C NMR (126 MHz, CD_3CN) δ 160.00, 134.53, 133.60, 125.68, 119.00, 114.81, 114.20, 112.89, 56.63, 52.68, 26.05, 23.60. HRMS (ESI) *m/z* calcd for $C_{27}H_{32}N_3O_2S^+$ (**4-Pip**$^+$): 462.2210, found: 462.2200.

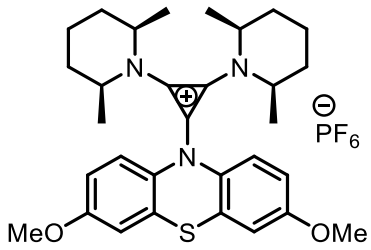

Synthesis of 4-DMPP: The general procedure was followed using 1-chloro-2,3-bis(cis-dimethylpiperdino)cyclopropenium chloride[47,48] as the substrate (2.4 mmol). Compound **4-DMPP** was isolated as a white powder (811 mg, 51% yield) using 8% ethyl acetate in DCM as the eluent. R_F = 0.25 in 8% ethyl acetate/DCM. ^{1}H NMR (700 MHz, CD_3CN) δ 7.54 (d, *J* = 8.7 Hz, 2H), 7.14 (d, *J* = 2.3 Hz, 2H), 6.97 (dd, *J* = 8.8, 2.8 Hz, 2H), 3.81 (s, 6H), 3.60-3.38 (m, 4H), 1.76-1.68 (m, 2H), 1.68-1.60 (m, 4H), 1.53-1.41 (m, 6H), 1.13 (d, J = 7.0 Hz, 12H). ^{13}C NMR (176 MHz, CD_3CN) δ 160.26, 136.79, 134.32, 127.29, 120.11, 115.03, 114.93,

114.34, 56.69, 54.78, 29.99, 21.53, 13.02. HRMS (ESI) *m/z* calcd for $C_{31}H_{40}N_3O_2S^+$ (**4-DMPP**$^+$): 518.2836, found: 518.2826.

6.4.2 X-ray Crystallographic Data for 4-DMPP

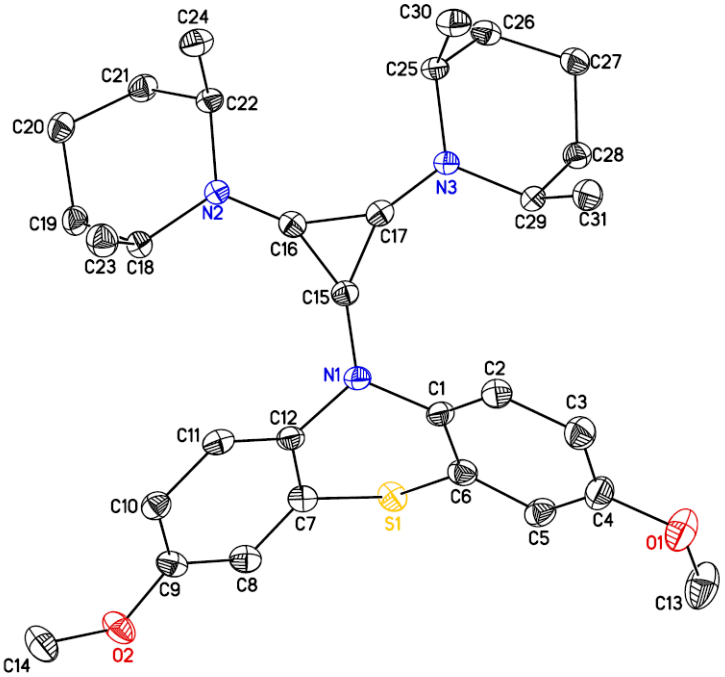

Figure 6.6. PLUTO representation of **4-DMPP**. The PF_6 anions are omitted for clarity.

Structure Determination.

Colorless blocks of **4-DMPP** were grown from an ethyl acetate/diethyl ether solution of the compound at -30 deg. C. A crystal of dimensions 0.18 x 0.11 x 0.08 mm was mounted on a Rigaku AFC10K Saturn 944+ CCD-based X-ray diffractometer equipped with a low temperature device and Micromax-007HF Cu-target micro-focus rotating anode (λ = 1.54187 A) operated at 1.2 kW power (40 kV, 30 mA). The X-ray intensities were measured at 85(1) K with the detector placed at a distance 42.00 mm from the crystal. A total of 2028 images were collected with an oscillation width of 1.0° in ω. The exposure times were 1 sec. for the low angle images, 5 sec. for high angle. Rigaku d*trek images were exported to CrysAlisPro for processing and corrected for

absorption. The crystal was determined to be a two component, non-merohedral twin. The twin domains are related by a -179.97 deg. Rotation about the direct space 91 0 0) vector and a refined twin ratio of 0.515(1). Reflections from both components as well as overlaps were used as the basis of an HKLF% format reflection file for refinement. The integration of the data yielded a total of 84874 reflections to a maximum 2θ value of 139.37° of which 13148 were independent and 9701 were greater than 2σ(I). The final cell constants (Table 6.3) were based on the xyz centroids of 14463 reflections above 10σ(I). Analysis of the data showed negligible decay during data collection. The structure was solved and refined with the Bruker SHELXTL (version 2018/3) software package, using the space group P2(1)/c with Z = 4 for the formula $C_{35}H_{50}N_3O_3F_6PS$. All non-hydrogen atoms were refined anisotropically with the hydrogen atoms placed in idealized positions. Full matrix least-squares refinement based on F^2 converged at R1 = 0.0524 and wR2 = 0.1391 [based on I > 2sigma(I)], R1 = 0.0670 and wR2 = 0.1440 for all data. Additional details are presented in Table 1 and are given as Supporting Information in a CIF file. Acknowledgement is made for funding from NSF grant CHE-0840456 for X-ray instrumentation.

Table 6.3. Crystal data and structure refinement for **4-DMPP**.

Empirical formula	$C_{35}H_{50}F_6N_3O_3PS$
Formula weight	737.81
Temperature	85(2) K
Wavelength	1.54184 A
Crystal system, space group	Monoclinic, P2(1)/c
Unit cell dimensions	a = 15.4786(5) Å alpha = 90°
	b = 27.7901(8) Å beta = 92.250(3)°
	c = 8.4187(2) Å gamma = 90°
Volume	3618.51(19) $Å^3$
Z, Calculated density	4, 1.354 Mg/m^3

Absorption coefficient	1.818 mm^{-1}
F(000)	1560
Crystal size	0.180 x 0.110 x 0.080 mm
Theta range for data collection	2.857 to 69.684°
Limiting indices	–17<=h<=18, –33<=k<=33, –10<=l<=10
Reflections collected / unique	84874 / 13148 [R(int) = 0.0951]
Completeness to theta = 67.684	100.0 %
Absorption correction	Semi-empirical from equivalents
Max. and min. transmission	1.00000 and 0.70179
Refinement method	Full-matrix least-squares on F^2
Data / restraints / parameters	13148 / 0 / 451
Goodness-of-fit on F^2	1.004
Final R indices [I>2sigma(I)]	R1 = 0.0524, wR2 = 0.1391
R indices (all data)	R1 = 0.0670, wR2 = 0.1440
Extinction coefficient	n/a
Largest diff. peak and hole	0.732 and –0.466 $eÅ^{-3}$

6.4.3 Electrochemistry Experimental Procedures

General methods and materials. Acetonitrile (anhydrous, 99.8%) was obtained from Sigma Aldrich and used as received. Tetrabutylammonium hexafluorophosphate ($TBAPF_6$; electrochemical grade) was obtained from Sigma Aldrich and dried under high vacuum for 48 h at 80 °C before being transferred to a N_2-filled glovebox. A 0.50 M stock solution of $TBAPF_6$ in acetonitrile was prepared in a N_2-filled glovebox and dried over 3Å molecular sieves for at least two days prior to use. Celgard-4560 membrane was provided by Celgard company and Daramic-175 membrane was provided by Daramic company. Both were used as received. The solubility of **4-DMPP^{2+}** in 0.5 M $TBAPF_6$/MeCN was determined using a previously reported method.[36]

Cyclic voltammetry. Cyclic voltammetry (CV) was performed in a N_2-filled glovebox with a Biologic VSP multichannel potentiostat/galvanostat using a three-electrode electrochemical cell, consisting of a glassy carbon disk working electrode (0.071 cm^2, BASi), a Ag/Ag^+ reference electrode (BASi) with 0.01 M $AgBF_4$ (Sigma) and 0.5 M $TBAPF_6$ in acetonitrile, and a platinum wire counter electrode. All experiments were conducted in a 0.50 M $TBAPF_6$/acetonitrile electrolyte stock solution.

H-cell cycling. Bulk charge/discharge measurements were carried out in a N_2-filled glovebox with a BioLogic VSP galvanostat in a custom glass H-cell with an ultrafine fritted glass separator (P5, Adams and Chittenden). The working and counter electrodes were reticulated vitreous carbon (100 ppi, ~70 cm^2 surface area, Duocel). A Ag/Ag^+ reference electrode was used on the working side of the H-cell. The electrolyte contained 2.5 mM active species and 0.50 M $TBAPF_6$ in acetonitrile. Both chambers of the H-cell were loaded with 5 mL of electrolyte solution and were stirred continuously during cycling at a current of 5 mA. Voltage cutoffs of +0.5 V higher than $E_{1/2}$ as the upper limit and -0.5 V lower than $E_{1/2}$ as the lower limit were employed.

Flow cell cycling. Cycling under flow conditions was performed with a zero-gap flow cell comprised of graphite charge collecting plates containing an interdigitated flow field in combination with two layers of non-woven carbon felt electrodes (Sigracet 29AA) on each side.[26] PTFE gaskets were used to achieve ~20% compression of the felt. One Celgard 4560 or Daramic 175 membrane separated the two half cells, and the exposed area of the membrane in the gasket window was used as the active area (2.55 cm^2). After assembly, both sides are filled with a 50 mM solution of the catholyte and a 50 mM solution of the anolyte in 0.5 M $TBAPF_6$ (Figure 4a) or 0.3 M catholyte and 0.6 M anolyte in 0.5 M $TBAPF_6$ (Figure 5a). The cell was pretreated by continuously flowing the solutions above at 10 mL/min for 1 h without any charging process using

a peristaltic pump (Cole-Parmer) with Solve-Flex and PFA tubing. After this step, using the same flow rate, galvanostatic charge/discharge cycling was performed using a BioLogic VSP galvanostat employing a certain charging/discharging current. Electrochemical impedance spectroscopy (EIS) was performed before and after cycling from 500 kHz to 1 Hz at OCV using a 10-mV sine perturbation.

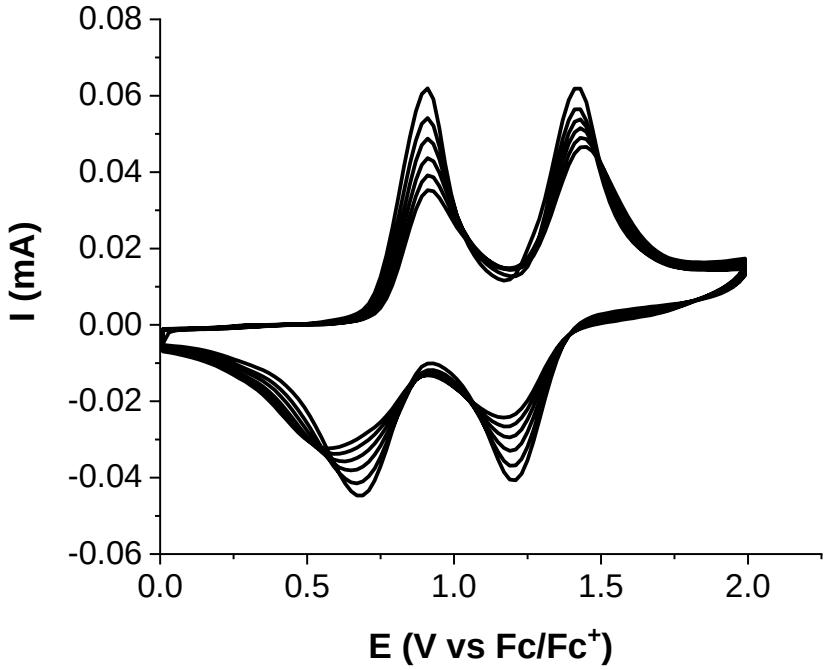

Figure 6.7. CV of **3-^{n}Pr** (5 cycles) CVs conducted with a 5 mM solution in 0.5 M NBu_4PF_6/MeCN at 100 mV/s scan rate.

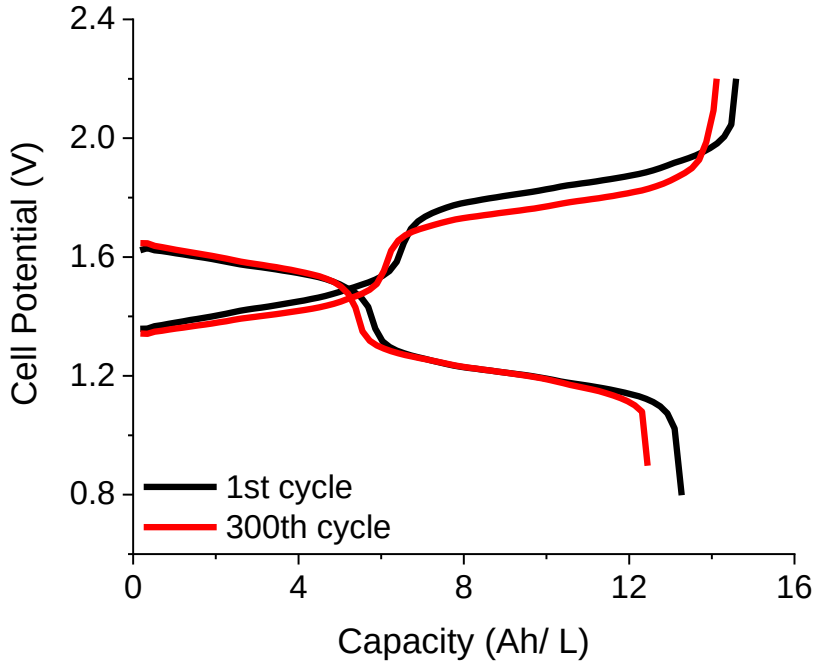

Figure 6.8. Charge and Discharge curves of the high concentration cycling using **4-DMPP** and **4**.

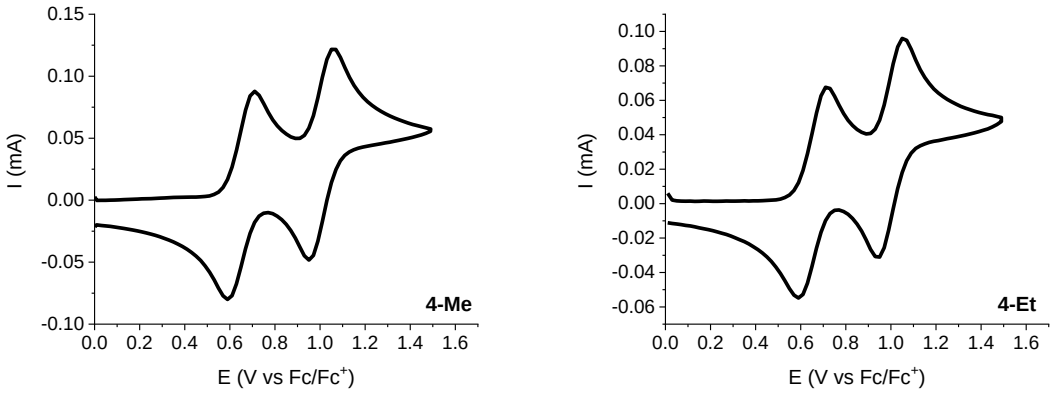

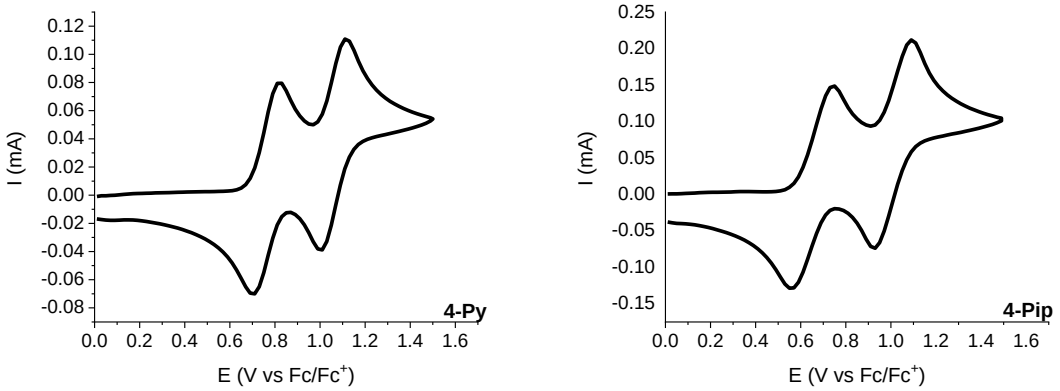

Figure 6.9. CV for series **4** compounds not showing in the main article (5 mM active materials in 0.5 M $TBAPF_6$)

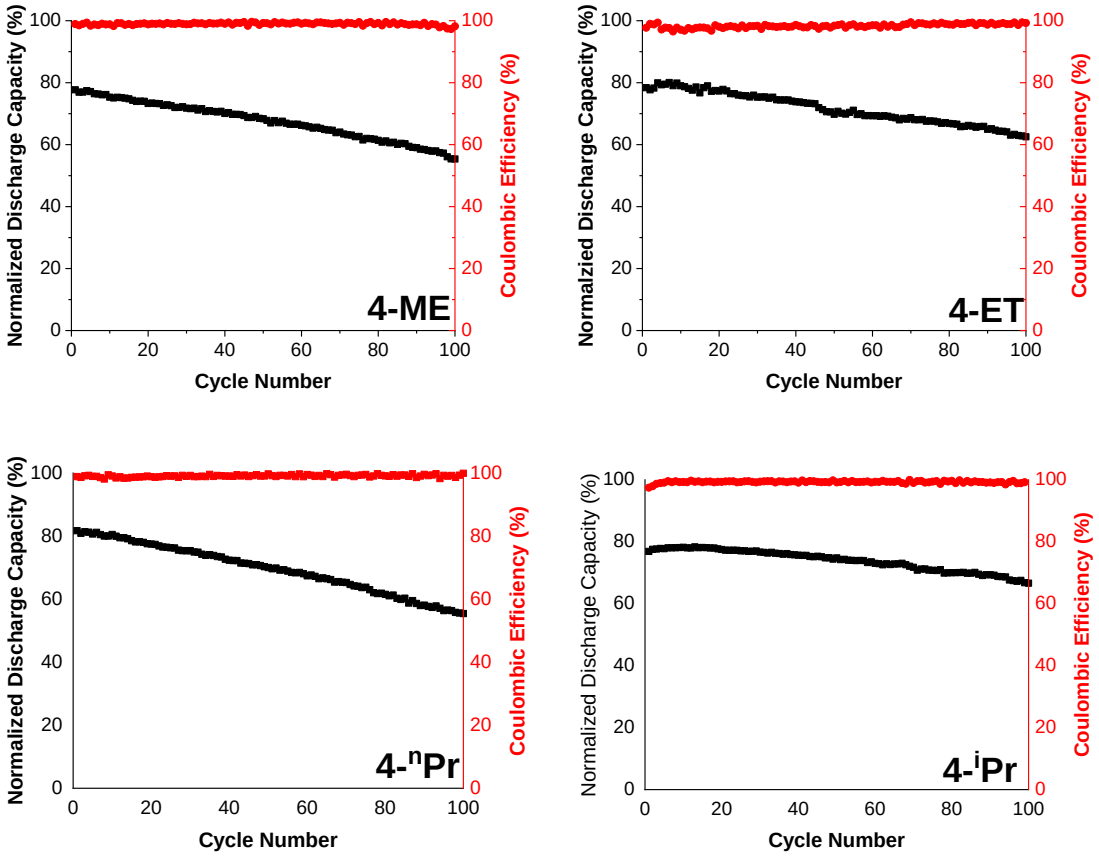

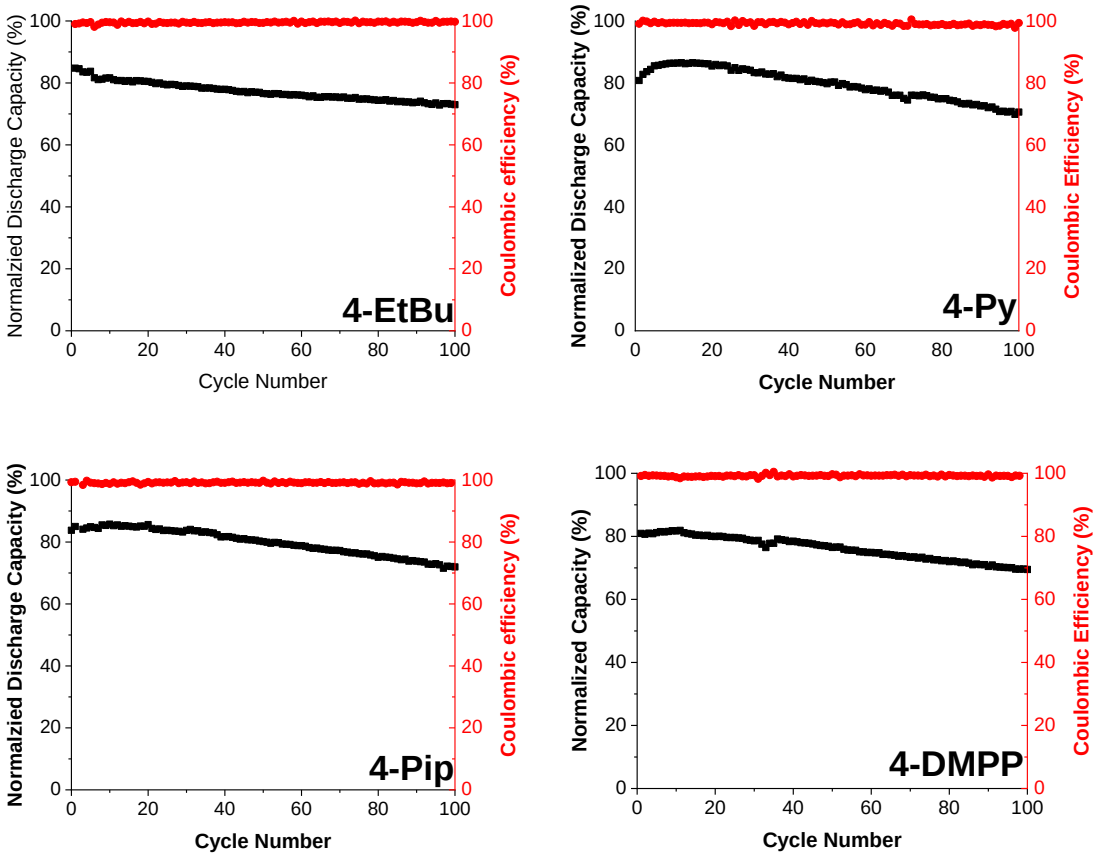

Figure 6.10. Bulk electrolysis data for series **4** compounds (2.5 mM active materials in 0.5 M $TBAPF_6$)

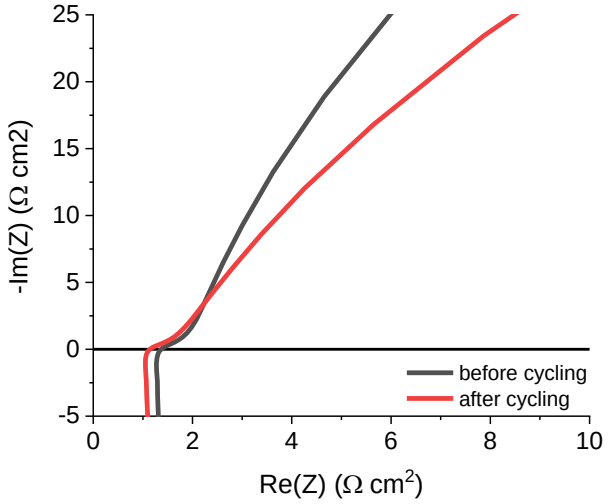

Figure 6.11. Electrochemical impedance spectroscopy (EIS) on cells for before and after for Figure 6.5

Determination of the Diffusion Coefficient and Electron Transfer Rate Constant of 4-DMPP.

The diffusion coefficient was determined by varying the scan rate of CV measurements between 20 and 700 mV/s (Figure 6.12, left). Plotting the cathodic and anodic peak height currents versus the square root of the scan rate showed a linear relationship, indicating a transport-limited redox process (Figure 6.12, right). The slope of this linear relation was used in the Randles-Sevcik equation (eq 1) to determine the diffusion coefficient.[49]

$$i_p = 0.4463\, nFAC\sqrt{\frac{nF\upsilon D}{RT}} \qquad (1)$$

The terms of the equation: i_p is the peak current in amps, n is the number of electrons transferred, F is Faraday's constant, A is the area of the electrode in cm^2, C *is* the concentration of redox active species in mol cm^{-3}, D is the diffusion coefficient in $cm^2\ s^{-1}$, v is the scan rate in $V\ s^{-1}$, R is the gas constant in $JK^{-1}mol^{-1}$, and T is the temperature in K.

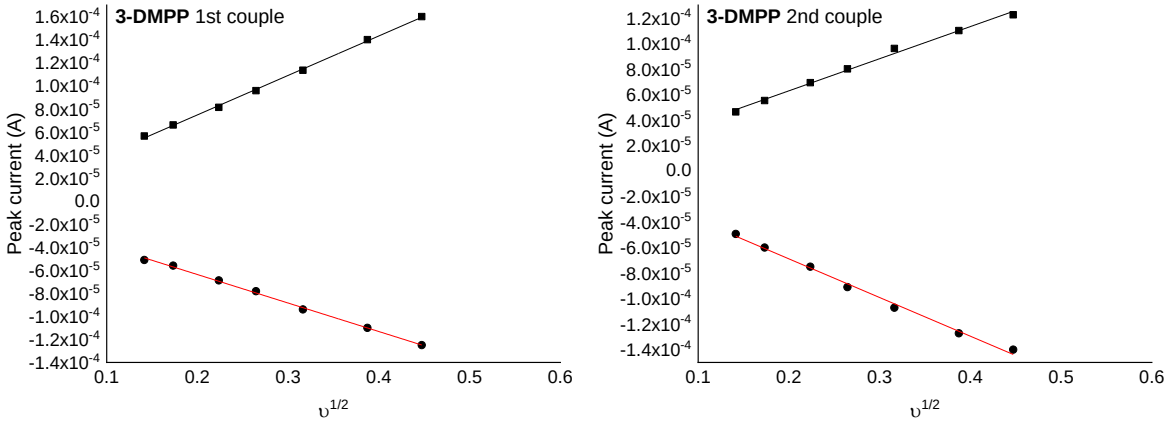

Figure 6.12. Peak current (A) vs square root of the scan rate ($v^{½}$) and linear fits used to determine diffusion coefficients.

The heterogeneous electron transfer rate constant was determined following the Nicholson method.[44] The peak separations between the cathodic and anodic peaks at various scan rates were fit to a working curve. Plotting the resulting values of Nicholson dimensionless number Ψ versus the inverse square root of the scan rate (Figure 6.13) gave a relationship from which the slope was used to determine k_0 according to eq 2,

$$\psi = \frac{\gamma k_0}{\sqrt{\pi a D_0}} \qquad (2)$$

where k_0 is the standard rate constant in cm s^{-1}; Ψ is the Nicholson dimensionless number, which is a function of the peak potential separation (ΔE_p) from CV curve. D_0 is the diffusion coefficient in cm^2 s^{-1}. α is the charge transfer coefficient, dimensionless. $\gamma = \sqrt{\frac{RT}{nF}}$, where n is the number of electrons transferred in the redox reaction, F is Faraday's constant (96485 C mol^{-1}), R is the ideal gas constant (8.314 J mol K^{-1}), T is the absolute temperature in K.

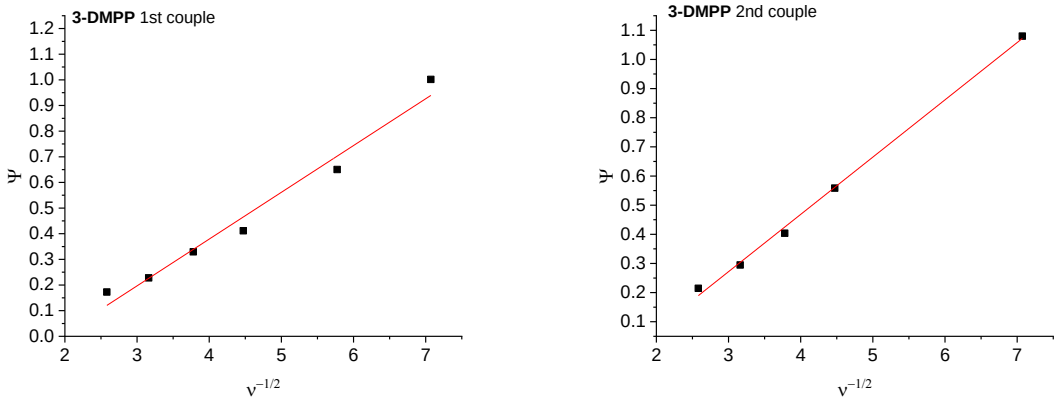

Figure 6.13 Plots of the Nicholson dimensionless number (Ψ) versus inverse of the scan rate ($\nu^{-½}$). A linear fit was used to determine heterogeneous electron transfer rates.

6.4.4 Computational Methods

Conformational Analysis

Conformational searches were performed on the substrates using Macromodel version 11.7 with the OPLS3 force field.[50,51] Conformers within 2.5 kcal/mol of the lowest energy conformer were taken forward for DFT optimization.

DFT Properties

DFT calculations were undertaken using Gaussian 16 (Revision A.03).[52] Geometry optimization was carried out at the B3LYP/6-31+G(d,p)[53] and utilizing the GD3BJ empirical dispersion correction, as implemented in Gaussian 16 (Revision A.03). All ground states (zero imaginary frequencies) were verified as stationary points by frequency analysis. Optimized structures were visualized using CYLview.[54] NBO calculations were performed on the optimized geometry of most stable conformers at the uM06/def2tzvp level of theory using NBO 3.1. [55] HOMOs were visualized with Avogadro 1.2.0 using an isosurface value of 0.02. [56]

Parameter Collection

Parameters were then collected using Python scripts, similarly to previous reports from the Sigman lab.[57] Boltzmann-weighting of the properties was carried out using all of the computed conformers within 2.5 kcal/mol of the most stable conformer.

Geometry Data

The following data are Boltzmann averaged values from a conformational ensemble as described above. **SNCp$^+$ angle** refers to the angle created by the phenothiazine sulfur (10), phenothiazine nitrogen (5), and the connecting carbon (11). **Cp$^+$ twist** refers to the dihedral angle created by carbon 13, nitrogen 5, carbon 11, and carbon 12. Though consistent atom selection was used to define these angles, depending on conformation, **Cp$^+$ twist** was either acute or obtuse. To normalize for comparison, when an obtuse value was obtained (>90°), the supplementary angle (180° – obtuse angle) was used as the corrected value of **Cp$^+$ twist**. These parameters are visualized on a +1 charged species of **4-Me** as an example below.

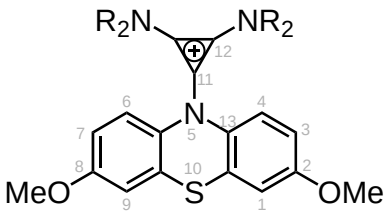

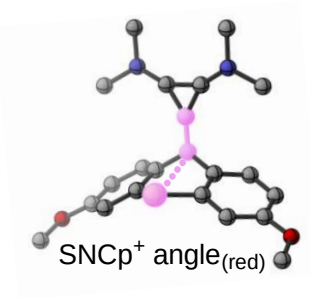

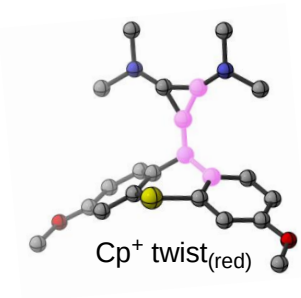

Table 6.4. Selected Geometric Properties of Electrolytes in +1, +2, and +3 Oxidation State

	+1 Charge (Starting Material)		**+2 Charge (First Oxidation)**		**+3 Charge (Second Oxidation)**	
Compound	**SNCp Angle**	**Cp Twist**	**SNCp Angle**	**Cp Twist**	**SNCp Angle**	**Cp Twist**
4-Me	107.2	17.7	174.3	45.8	179.9	59.3
4-Et	104.5	18.5	170.1	47.5	179.5	59.0
4-nPr	104.5	16.7	167.4	45.8	179.4	59.7
4-iPr	98.5	16.7	175.0	87.2	179.1	81.9

4-EtBu	102.7	17.9	167.3	46.8	179.9	64.6
4-Py	112.3	14.5	170.4	42.7	179.6	56.5
4-PIP	101.8	17.9	175.0	46.8	179.9	54.3
4-DMPP	143.2	27.2	179.9	54.7	179.4	75.7

Table 6.5. Change in Selected Geometric Properties of Electrolytes from +1 to +2, and +2 to +3 Oxidation State

	+1 to +2 Charge (First Oxidation)		**+2 to +3 Charge (Second Oxidation)**	
Compound	**ΔSNCp Angle**	**ΔCp Twist**	**ΔSNCp Angle**	**ΔCp Twist**
4-Me	67.1	28.2	5.6	13.5
4-Et	65.6	29.0	9.3	11.6
4-nPr	62.9	29.2	12.0	13.9
4-iPr	76.5	70.5	4.1	-5.3
4-EtBu	64.6	28.9	12.6	17.8
4-Py	58.0	28.2	9.3	13.8
4-PIP	73.3	28.9	4.8	7.5
4-DMPP	34.3	27.5	1.9	21.0

6.5 References

(1) Rugolo, J.; Aziz, M. J. Electricity Storage for Intermittent Renewable Sources. *Energy Environ. Sci.* **2012**, *5* (5), 7151–7160. https://doi.org/10.1039/C2EE02542F.

(2) Barnhart, C. J.; Dale, M.; Brandt, A. R.; Benson, S. M. The Energetic Implications of Curtailing versus Storing Solar- and Wind-Generated Electricity. *Energy Environ. Sci.* **2013**, *6* (10), 2804–2810. https://doi.org/10.1039/C3EE41973H.

(3) Wei, X.; Pan, W.; Duan, W.; Hollas, A.; Yang, Z.; Li, B.; Nie, Z.; Liu, J.; Reed, D.; Wang, W.; Sprenkle, V. Materials and Systems for Organic Redox Flow Batteries: Status and Challenges. *ACS Energy Lett.* **2017**, *2* (9), 2187–2204. https://doi.org/10.1021/acsenergylett.7b00650.

(4) Wei, X.; Xu, W.; Vijayakumar, M.; Cosimbescu, L.; Liu, T.; Sprenkle, V.; Wang, W. TEMPO-Based Catholyte for High-Energy Density Nonaqueous Redox Flow Batteries. *Advanced Materials* **2014**, *26* (45), 7649–7653. https://doi.org/10.1002/adma.201403746.

(5) Winsberg, J.; Hagemann, T.; Muench, S.; Friebe, C.; Häupler, B.; Janoschka, T.; Morgenstern, S.; Hager, M. D.; Schubert, U. S. Poly(Boron-Dipyrromethene)—A Redox-Active Polymer Class for Polymer Redox-Flow Batteries. *Chem. Mater.* **2016**, *28* (10), 3401–3405. https://doi.org/10.1021/acs.chemmater.6b00640.

(6) Zhang, C.; Zhang, L.; Ding, Y.; Peng, S.; Guo, X.; Zhao, Y.; He, G.; Yu, G. Progress and Prospects of Next-Generation Redox Flow Batteries. *Energy Storage Materials* **2018**, *15*, 324–350. https://doi.org/10.1016/j.ensm.2018.06.008.

(7) Kwon, G.; Lee, S.; Hwang, J.; Shim, H.-S.; Lee, B.; Lee, M. H.; Ko, Y.; Jung, S.-K.; Ku, K.; Hong, J.; Kang, K. Multi-Redox Molecule for High-Energy Redox Flow Batteries. *Joule* **2018**, *2* (9), 1771–1782. https://doi.org/10.1016/j.joule.2018.05.014.

(8) Zhang, J.; Yang, Z.; Shkrob, I. A.; Assary, R. S.; Tung, S. on; Silcox, B.; Duan, W.; Zhang, J.; Su, C. C.; Hu, B.; Pan, B.; Liao, C.; Zhang, Z.; Wang, W.; Curtiss, L. A.; Thompson, L. T.; Wei, X.; Zhang, L. Annulated Dialkoxybenzenes as Catholyte Materials for Non-Aqueous

Redox Flow Batteries: Achieving High Chemical Stability through Bicyclic Substitution. *Adv. Energy Mater.* **2017**, *7* (21), 1701272. https://doi.org/10.1002/aenm.201701272.

(9) VanGelder, L. E.; Schreiber, E.; Matson, E. M. Physicochemical Implications of Alkoxide "Mixing" in Polyoxovanadium Clusters for Nonaqueous Energy Storage. *J. Mater. Chem. A* **2019**, *7* (9), 4893–4902. https://doi.org/10.1039/C8TA12306C.

(10) VanGelder, L. E.; Kosswattaarachchi, A. M.; Forrestel, P. L.; Cook, T. R.; Matson, E. M. Polyoxovanadate-Alkoxide Clusters as Multi-Electron Charge Carriers for Symmetric Non-Aqueous Redox Flow Batteries. *Chem. Sci.* **2018**, *9* (6), 1692–1699. https://doi.org/10.1039/C7SC05295B.

(11) A. Kowalski, J.; D. Casselman, M.; Preet Kaur, A.; D. Milshtein, J.; F. Elliott, C.; Modekrutti, S.; Harsha Attanayake, N.; Zhang, N.; R. Parkin, S.; Risko, C.; R. Brushett, F.; A. Odom, S. A Stable Two-Electron-Donating Phenothiazine for Application in Nonaqueous Redox Flow Batteries. *Journal of Materials Chemistry A* **2017**, *5* (46), 24371–24379. https://doi.org/10.1039/C7TA05883G.

(12) Escalante-García, I. L.; Wainright, J. S.; Thompson, L. T.; Savinell, R. F. Performance of a Non-Aqueous Vanadium Acetylacetonate Prototype Redox Flow Battery: Examination of Separators and Capacity Decay. *J. Electrochem. Soc.* **2015**, *162* (3), A363–A372. https://doi.org/10.1149/2.0471503jes.

(13) Carino, E. V.; Staszak-Jirkovsky, J.; Assary, R. S.; Curtiss, L. A.; Markovic, N. M.; Brushett, F. R. Tuning the Stability of Organic Active Materials for Nonaqueous Redox Flow Batteries via Reversible, Electrochemically Mediated Li+ Coordination. *Chem. Mater.* **2016**, *28* (8), 2529–2539. https://doi.org/10.1021/acs.chemmater.5b04053.

(14) Silcox, B.; Zhang, J.; Shkrob, I. A.; Thompson, L.; Zhang, L. On Transferability of Performance Metrics for Redox-Active Molecules. *J. Phys. Chem. C* **2019**, *123* (27), 16516–16524. https://doi.org/10.1021/acs.jpcc.9b02230.

(15) Kwon, G.; Lee, K.; Lee, M. H.; Lee, B.; Lee, S.; Jung, S.-K.; Ku, K.; Kim, J.; Park, S. Y.; Kwon, J. E.; Kang, K. Bio-Inspired Molecular Redesign of a Multi-Redox Catholyte for High-Energy Non-Aqueous Organic Redox Flow Batteries. *Chem* **2019**, *5* (10), 2642–2656. https://doi.org/10.1016/j.chempr.2019.07.006.

(16) Sevov, C. S.; Fisher, S. L.; Thompson, L. T.; Sanford, M. S. Mechanism-Based Development of a Low-Potential, Soluble, and Cyclable Multielectron Anolyte for Nonaqueous Redox Flow Batteries. *J. Am. Chem. Soc.* **2016**, *138* (47), 15378–15384. https://doi.org/10.1021/jacs.6b07638.

(17) Duan, W.; Huang, J.; Kowalski, J. A.; Shkrob, I. A.; Vijayakumar, M.; Walter, E.; Pan, B.; Yang, Z.; Milshtein, J. D.; Li, B.; Liao, C.; Zhang, Z.; Wang, W.; Liu, J.; Moore, J. S.; Brushett, F. R.; Zhang, L.; Wei, X. "Wine-Dark Sea" in an Organic Flow Battery: Storing Negative Charge in 2,1,3-Benzothiadiazole Radicals Leads to Improved Cyclability. *ACS Energy Lett.* **2017**, *2* (5), 1156–1161. https://doi.org/10.1021/acsenergylett.7b00261.

(18) Huang, J.; Cheng, L.; Assary, R. S.; Wang, P.; Xue, Z.; Burrell, A. K.; Curtiss, L. A.; Zhang, L. Liquid Catholyte Molecules for Nonaqueous Redox Flow Batteries. *Advanced Energy Materials* **2015**, *5* (6), 1401782. https://doi.org/10.1002/aenm.201401782.

(19) Zhang, C.; Qian, Y.; Ding, Y.; Zhang, L.; Guo, X.; Zhao, Y.; Yu, G. Biredox Eutectic Electrolytes Derived from Organic Redox-Active Molecules: High-Energy Storage Systems. *Angewandte Chemie International Edition* **2019**, *58* (21), 7045–7050. https://doi.org/10.1002/anie.201902433.

(20) Zhang, C.; Niu, Z.; Ding, Y.; Zhang, L.; Zhou, Y.; Guo, X.; Zhang, X.; Zhao, Y.; Yu, G. Highly Concentrated Phthalimide-Based Anolytes for Organic Redox Flow Batteries with Enhanced Reversibility. *Chem* **2018**, *4* (12), 2814–2825. https://doi.org/10.1016/j.chempr.2018.08.024.

(21) Hendriks, K. H.; Sevov, C. S.; Cook, M. E.; Sanford, M. S. Multielectron Cycling of a Low-Potential Anolyte in Alkali Metal Electrolytes for Nonaqueous Redox Flow Batteries. *ACS Energy Lett.* **2017**, *2* (10), 2430–2435. https://doi.org/10.1021/acsenergylett.7b00559.

(22) Hu, B.; Liu, T. L. Two Electron Utilization of Methyl Viologen Anolyte in Nonaqueous Organic Redox Flow Battery. *Journal of Energy Chemistry* **2018**, *27* (5), 1326–1332. https://doi.org/10.1016/j.jechem.2018.02.014.

(23) Chai, J.; Lashgari, A.; Wang, X.; Williams, C. K.; Jiang, J. "Jimmy." All-PEGylated Redox-Active Metal-Free Organic Molecules in Non-Aqueous Redox Flow Battery. *J. Mater. Chem. A* **2020**, *8* (31), 15715–15724. https://doi.org/10.1039/D0TA02303E.

(24) P. Vaid, T.; S. Sanford, M. An Organic Super-Electron-Donor as a High Energy Density Negative Electrolyte for Nonaqueous Flow Batteries. *Chemical Communications* **2019**, *55* (74), 11037–11040. https://doi.org/10.1039/C9CC06080D.

(25) Zhang, L.; Qian, Y.; Feng, R.; Ding, Y.; Zu, X.; Zhang, C.; Guo, X.; Wang, W.; Yu, G. Reversible Redox Chemistry in Azobenzene-Based Organic Molecules for High-Capacity and Long-Life Nonaqueous Redox Flow Batteries. *Nature Communications* **2020**, *11* (1), 3843. https://doi.org/10.1038/s41467-020-17662-y.

(26) Milshtein, J. D.; Kaur, A. P.; Casselman, M. D.; Kowalski, J. A.; Modekrutti, S.; Zhang, P. L.; Harsha Attanayake, N.; Elliott, C. F.; Parkin, S. R.; Risko, C.; Brushett, F. R.; Odom, S. A. High Current Density, Long Duration Cycling of Soluble Organic Active Species for Non-

Aqueous Redox Flow Batteries. *Energy Environ. Sci.* **2016**, *9* (11), 3531–3543. https://doi.org/10.1039/C6EE02027E.

(27) Kaur, A. P.; Harris, O. C.; Attanayake, N. H.; Liang, Z.; Parkin, S. R.; Tang, M. H.; Odom, S. A. Quantifying Environmental Effects on the Solution and Solid-State Stability of a Phenothiazine Radical Cation. *Chem. Mater.* **2020**, *32* (7), 3007–3017. https://doi.org/10.1021/acs.chemmater.9b05345.

(28) Attanayake, N. H.; Kowalski, J. A.; Greco, K. V.; Casselman, M. D.; Milshtein, J. D.; Chapman, S. J.; Parkin, S. R.; Brushett, F. R.; Odom, S. A. Tailoring Two-Electron-Donating Phenothiazines To Enable High-Concentration Redox Electrolytes for Use in Nonaqueous Redox Flow Batteries. *Chem. Mater.* **2019**, *31* (12), 4353–4363. https://doi.org/10.1021/acs.chemmater.8b04770.

(29) Ergun, S.; F. Elliott, C.; Preet Kaur, A.; R. Parkin, S.; A. Odom, S. Overcharge Performance of 3,7-Disubstituted N -Ethylphenothiazine Derivatives in Lithium-Ion Batteries. *Chemical Communications* **2014**, *50* (40), 5339–5341. https://doi.org/10.1039/C3CC47503D.

(30) Preet Kaur, A.; Ergun, S.; F. Elliott, C.; A. Odom, S. 3,7-Bis(Trifluoromethyl)- N -Ethylphenothiazine: A Redox Shuttle with Extensive Overcharge Protection in Lithium-Ion Batteries. *Journal of Materials Chemistry A* **2014**, *2* (43), 18190–18193. https://doi.org/10.1039/C4TA04463K.

(31) Elliott, C. F.; Fraser, K. E.; Odom, S. A.; Risko, C. Steric Manipulation as a Mechanism for Tuning the Reduction and Oxidation Potentials of Phenothiazines. *J. Phys. Chem. A* **2021**, *125* (1), 272–278. https://doi.org/10.1021/acs.jpca.0c09801.

(32) Harsha Attanayake, N.; Liang, Z.; Wang, Y.; Preet Kaur, A.; R. Parkin, S.; K. Mobley, J.; H. Ewoldt, R.; Landon, J.; A. Odom, S. Dual Function Organic Active Materials for Nonaqueous

Redox Flow Batteries. *Materials Advances* **2021**, *2* (4), 1390–1401. https://doi.org/10.1039/D0MA00881H.

(33) Yan, Y.; Robinson, S. G.; Vaid, T. P.; Sigman, M. S.; Sanford, M. S. Simultaneously Enhancing the Redox Potential and Stability of Multi-Redox Organic Catholytes by Incorporating Cyclopropenium Substituents. *J. Am. Chem. Soc.* **2021**. https://doi.org/10.1021/jacs.1c07237.

(34) Park, M.; Ryu, J.; Wang, W.; Cho, J. Material Design and Engineering of Next-Generation Flow-Battery Technologies. *Nature Reviews Materials* **2016**, *2* (1), 1–18. https://doi.org/10.1038/natrevmats.2016.80.

(35) Sevov, C. S.; Samaroo, S. K.; Sanford, M. S. Cyclopropenium Salts as Cyclable, High-Potential Catholytes in Nonaqueous Media. *Advanced Energy Materials* **2017**, *7* (5), 1602027. https://doi.org/10.1002/aenm.201602027.

(36) Robinson, S. G.; Yan, Y.; Hendriks, K. H.; Sanford, M. S.; Sigman, M. S. Developing a Predictive Solubility Model for Monomeric and Oligomeric Cyclopropenium-Based Flow Battery Catholytes. *J. Am. Chem. Soc.* **2019**, *141* (26), 10171–10176. https://doi.org/10.1021/jacs.9b04270.

(37) Yan, Y.; Robinson, S. G.; Sigman, M. S.; Sanford, M. S. Mechanism-Based Design of a High-Potential Catholyte Enables a 3.2 V All-Organic Nonaqueous Redox Flow Battery. *J. Am. Chem. Soc.* **2019**, *141* (38), 15301–15306. https://doi.org/10.1021/jacs.9b07345.

(38) Hendriks, K. H.; Robinson, S. G.; Braten, M. N.; Sevov, C. S.; Helms, B. A.; Sigman, M. S.; Minteer, S. D.; Sanford, M. S. High-Performance Oligomeric Catholytes for Effective Macromolecular Separation in Nonaqueous Redox Flow Batteries. *ACS Cent. Sci.* **2018**, *4* (2), 189–196. https://doi.org/10.1021/acscentsci.7b00544.

(39) Kuroboshi, M.; Yamamoto, T.; Tanaka, H. Amphiphilic Viologen: Electrochemical Generation of Organic Reductant and Pd-Catalyzed Reductive Coupling of Aryl Halides in Water. *Synlett* **2013**, *24* (2), 197–200. https://doi.org/10.1055/s-0032-1317857.

(40) Chai, J.; Lashgari, A.; Cao, Z.; Williams, C. K.; Wang, X.; Dong, J.; Jiang, J. "Jimmy." PEGylation-Enabled Extended Cyclability of a Non-Aqueous Redox Flow Battery. *ACS Appl. Mater. Interfaces* **2020**, *12* (13), 15262–15270. https://doi.org/10.1021/acsami.0c01045.

(41) Gong, K.; Fang, Q.; Gu, S.; Li, S. F. Y.; Yan, Y. Nonaqueous Redox-Flow Batteries: Organic Solvents, Supporting Electrolytes, and Redox Pairs. *Energy Environ. Sci.* **2015**, *8* (12), 3515–3530. https://doi.org/10.1039/C5EE02341F.

(42) Wei, X.; Cosimbescu, L.; Xu, W.; Hu, J. Z.; Vijayakumar, M.; Feng, J.; Hu, M. Y.; Deng, X.; Xiao, J.; Liu, J.; Sprenkle, V.; Wang, W. Towards High-Performance Nonaqueous Redox Flow Electrolyte Via Ionic Modification of Active Species. *Advanced Energy Materials* **2015**, *5* (1), 1400678. https://doi.org/10.1002/aenm.201400678.

(43) Wei, X.; Duan, W.; Huang, J.; Zhang, L.; Li, B.; Reed, D.; Xu, W.; Sprenkle, V.; Wang, W. A High-Current, Stable Nonaqueous Organic Redox Flow Battery. *ACS Energy Lett.* **2016**, *1* (4), 705–711. https://doi.org/10.1021/acsenergylett.6b00255.

(44) Nicholson, R. S. Theory and Application of Cyclic Voltammetry for Measurement of Electrode Reaction Kinetics. *Anal. Chem.* **1965**, *37* (11), 1351–1355. https://doi.org/10.1021/ac60230a016.

(45) Chiykowski, V. A.; Lam, B.; Du, C.; Berlinguette, C. P. Comparative Analysis of Triarylamine and Phenothiazine Sensitizer Donor Units in Dye-Sensitized Solar Cells. *Chem. Commun.* **2017**, *53* (15), 2367–2370. https://doi.org/10.1039/C6CC09178D.

(46) Kuroboshi, M.; Yamamoto, T.; Tanaka, H. Amphiphilic Viologen: Electrochemical Generation of Organic Reductant and Pd-Catalyzed Reductive Coupling of Aryl Halides in Water. *Synlett* **2013**, *24* (2), 197–200. https://doi.org/10.1055/s-0032-1317857.

(47) Jiang, Y.; Freyer, J. L.; Cotanda, P.; Brucks, S. D.; Killops, K. L.; Bandar, J. S.; Torsitano, C.; Balsara, N. P.; Lambert, T. H.; Campos, L. M. The Evolution of Cyclopropenium Ions into Functional Polyelectrolytes. *Nature Communications* **2015**, *6* (1), 5950. https://doi.org/10.1038/ncomms6950.

(48) Strater, Z. M.; Rauch, M.; Jockusch, S.; Lambert, T. H. Oxidizable Ketones: Persistent Radical Cations from the Single-Electron Oxidation of 2,3-Diaminocyclopropenones. *Angewandte Chemie International Edition* **2019**, *58* (24), 8049–8052. https://doi.org/10.1002/anie.201902265.

(49) Aljabali, A. A. A.; Barclay, J. E.; Butt, J. N.; Lomonossoff, G. P.; Evans, D. J. Redox-Active Ferrocene-Modified Cowpea Mosaic Virus Nanoparticles. *Dalton Trans.* **2010**, *39* (32), 7569–7574. https://doi.org/10.1039/C0DT00495B.

(50) Harder, E.; Damm, W.; Maple, J.; Wu, C.; Reboul, M.; Xiang, J. Y.; Wang, L.; Lupyan, D.; Dahlgren, M. K.; Knight, J. L.; Kaus, J. W.; Cerutti, D. S.; Krilov, G.; Jorgensen, W. L.; Abel, R.; Friesner, R. A. OPLS3: A Force Field Providing Broad Coverage of Drug-like Small Molecules and Proteins. *J Chem Theory Comput* **2016**, *12* (1), 281–296. https://doi.org/10.1021/acs.jctc.5b00864.

(51) Roos, K.; Wu, C.; Damm, W.; Reboul, M.; Stevenson, J. M.; Lu, C.; Dahlgren, M. K.; Mondal, S.; Chen, W.; Wang, L.; Abel, R.; Friesner, R. A.; Harder, E. D. OPLS3e: Extending Force Field Coverage for Drug-Like Small Molecules. *J. Chem. Theory Comput.* **2019**, *15* (3), 1863–1874. https://doi.org/10.1021/acs.jctc.8b01026.

(52) Frisch, M. J.; Trucks, G. W.; Schlegel, H. B.; Scuseria, G. E.; Robb, M. A.; Cheeseman, J. R.; Scalmani, G.; Barone, V.; Petersson, G. A.; Nakatsuji, H.; Li, X.; Caricato, M.; Marenich, A. V.; Bloino, J.; Janesko, B. G.; Gomperts, R.; Mennucci, B.; Hratchian, H. P.; Ortiz, J. V.; Izmaylov, A. F.; Sonnenberg, J. L.; Williams; Ding, F.; Lipparini, F.; Egidi, F.; Goings, J.; Peng, B.; Petrone, A.; Henderson, T.; Ranasinghe, D.; Zakrzewski, V. G.; Gao, J.; Rega, N.; Zheng, G.; Liang, W.; Hada, M.; Ehara, M.; Toyota, K.; Fukuda, R.; Hasegawa, J.; Ishida, M.; Nakajima, T.; Honda, Y.; Kitao, O.; Nakai, H.; Vreven, T.; Throssell, K.; Montgomery Jr., J. A.; Peralta, J. E.; Ogliaro, F.; Bearpark, M. J.; Heyd, J. J.; Brothers, E. N.; Kudin, K. N.; Staroverov, V. N.; Keith, T. A.; Kobayashi, R.; Normand, J.; Raghavachari, K.; Rendell, A. P.; Burant, J. C.; Iyengar, S. S.; Tomasi, J.; Cossi, M.; Millam, J. M.; Klene, M.; Adamo, C.; Cammi, R.; Ochterski, J. W.; Martin, R. L.; Morokuma, K.; Farkas, O.; Foresman, J. B.; Fox, D. J. *Gaussian 16 Rev. B.01*; Wallingford, CT, 2016.

(53) McLean, A. D.; Chandler, G. S. Contracted Gaussian Basis Sets for Molecular Calculations. I. Second Row Atoms, Z=11–18. *J. Chem. Phys.* **1980**, *72* (10), 5639–5648. https://doi.org/10.1063/1.438980.

(54) Legault, C. *CYLview 1.0b*; Université de Sherbrooke, 2009.

(55) Glendening, E.; Reed, A.; Carpenter, F. *NBO Version 3.1*.

(56) Hanwell, M. D.; Curtis, D. E.; Lonie, D. C.; Vandermeersch, T.; Zurek, E.; Hutchison, G. R. Avogadro: An Advanced Semantic Chemical Editor, Visualization, and Analysis Platform. *Journal of Cheminformatics* **2012**, *4* (1), 17. https://doi.org/10.1186/1758-2946-4-17.

(57) Zhao, S.; Gensch, T.; Murray, B.; Niemeyer, Z. L.; Sigman, M. S.; Biscoe, M. R. Enantiodivergent Pd-Catalyzed C–C Bond Formation Enabled through Ligand Parameterization. *Science* **2018**, *362* (6415), 670–674. https://doi.org/10.1126/science.aat2299.

Chapter 7

Targeted Optimization of Phenoxazine Redox Center for Non-Aqueous Redox Flow Batteries

7.1 Introduction

Redox active organic molecules (ROMs) have attracted significant attention as electrolytes for redox flow batteries (RFBs).[1–18] Compared to more conventional inorganic RFB electrolytes,[19–22] ROMs offer the advantages that they derive from inexpensive raw materials and that their key properties (solubility, redox potential, electrochemical cycling stability) can be tuned by incorporating substituents onto a redox active core.[1–18] However, the incorporation of these substituents often requires multi-step syntheses; furthermore, the integration of multiple substituents at different sites on a redox active core is typically required to impart the desired properties. As such, it is highly desirable to identify systems in which modifications at a single site are effective for efficiently iterating molecular properties.

In this report, we describe the development of N-substituted phenoxazines as catholytes for non-aqueous RFBs. Despite their widespread use in other electrochemical systems[23,24] (for example, as cathode materials for metal-ion batteries[25,26] and as redox mediators for electrocatalysis),[27,28] to date substituted phenoxazines have not been explored as catholytes for redox flow batteries outside of the patent literature.[29] We show herein that variation of the N-substituent, which is accomplished via straightforward and modular single-step modification of commercially available phenoxazine, can dramatically enhance the solubility, redox potential, and electrochemical cycling stability of these molecules. We note that N-methyl phenoxazine is a liquid at room temperature

and is miscible with acetonitrile. Switching the N-methyl group with an isopropyl leads to the further increase of solubility of all oxidation states to >0.3 M in supporting electrolyte solution while not being attached with any expensive polyethylene oxide (PEO) chains. Another modification of the N-substituted group with a diaminocyclopropenium (DAC) unit results in a new type of derivatives with about 0.5 V enhanced redox potential. Further tuning of the amino groups on the DAC unit improves both the cycling stability and solubility of the catholyte material. Although a few catholyte molecules with potential >0.6 V vs Fc/Fc^+ have been reported for this application, most of them suffer from low chemical or cycling stability, making them unsuitable for practical use.[11,12,16,30–32] With a comparative flow cell cycling study with two other well-studied catholyte materials, N-DAC substituted phenoxazine exhibits significantly enhanced battery performance, removing barriers for possibility in a real world application.

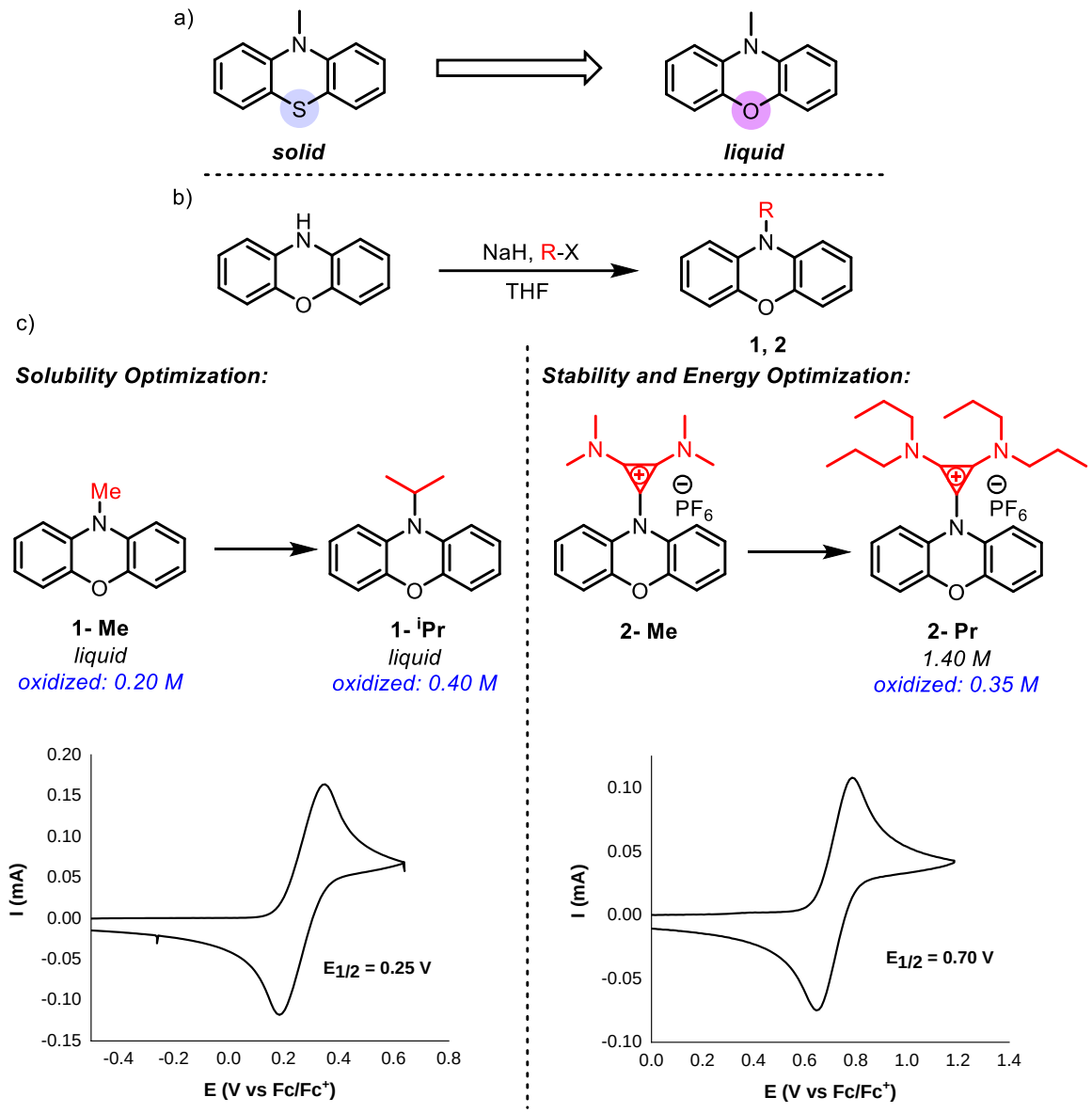

Figure 7.1. (a) Evolution from phenothiazine to phenoxazine; (b) General synthesis of N-substituted phenoxazine derivatives; (c) two new pairs of derivatives and their CVs

7.2 Results and discussion

Solubility Optimization

Our initial investigations focused on N-methylphenoxazine (**1-Me**), which is readily synthesized via the reaction of phenoxazine with methyl iodide (Figure 7.1a). While the sulfur analogue *N*-

methylphenathiazine and nitrogen analogue *N, N*- dimethylphenazine are solids, **1-Me** is a liquid at room temperature and is fully miscible with 0.5 M LiTFSI in MeCN.

The redox chemistry of **1-Me** was first characterized by cyclic voltammetry (CV). CV experiments were conducted using 5 mM solutions of **1-Me** in 0.5 M NBu_4PF_6/MeCN using a glassy carbon working electrode (0.07 cm^2, BASi). At a scan rate of 100 mV/s, **1-Me** shows a reversible oxidation at 0.25 V vs Fc/Fc^+ with a peak height ratio of 0.94.[25] This is comparable to the potential of the first oxidation of N-methylphenathiazine (0.21 vs Fc/Fc^+)[33] and is ~500 mV higher than that of N, N-dimethylphenazine (-0.29 V vs Fc/Fc^+).[5,13]

Galvanostatic charge-discharge cycling of **1-Me** (5 mM in 0.5 M $TBAPF_6$/ acetonitrile) was evaluated in a three-electrode H-cell separated with a fine glass frit. Reticulated vitreous carbon (RVC) was used as the working and counter electrodes.[31] The cycling experiments were conducted as symmetric batteries with same solution on both working and counter side. After the first charge, the counter chamber of the cell was emptied and refilled with fresh electrolyte solution and a new RVC electrode after which cycling was resumed. The working side was charged at a rate of 2.5 C with voltaic cutoffs in order to achieve the maximum accessible state of charge (SOC). Discharge capacity on the working side was then monitored versus cycle number (Figure 7.2a). These data show that **1-Me** initially charges to 85% of theoretical capacity and then cycles with 91% capacity retention over 50 cycles. The coulombic efficiency is >99% throughout this experiment. This result shows comparable or even better stability than that of its phenothiazine analog.[34]

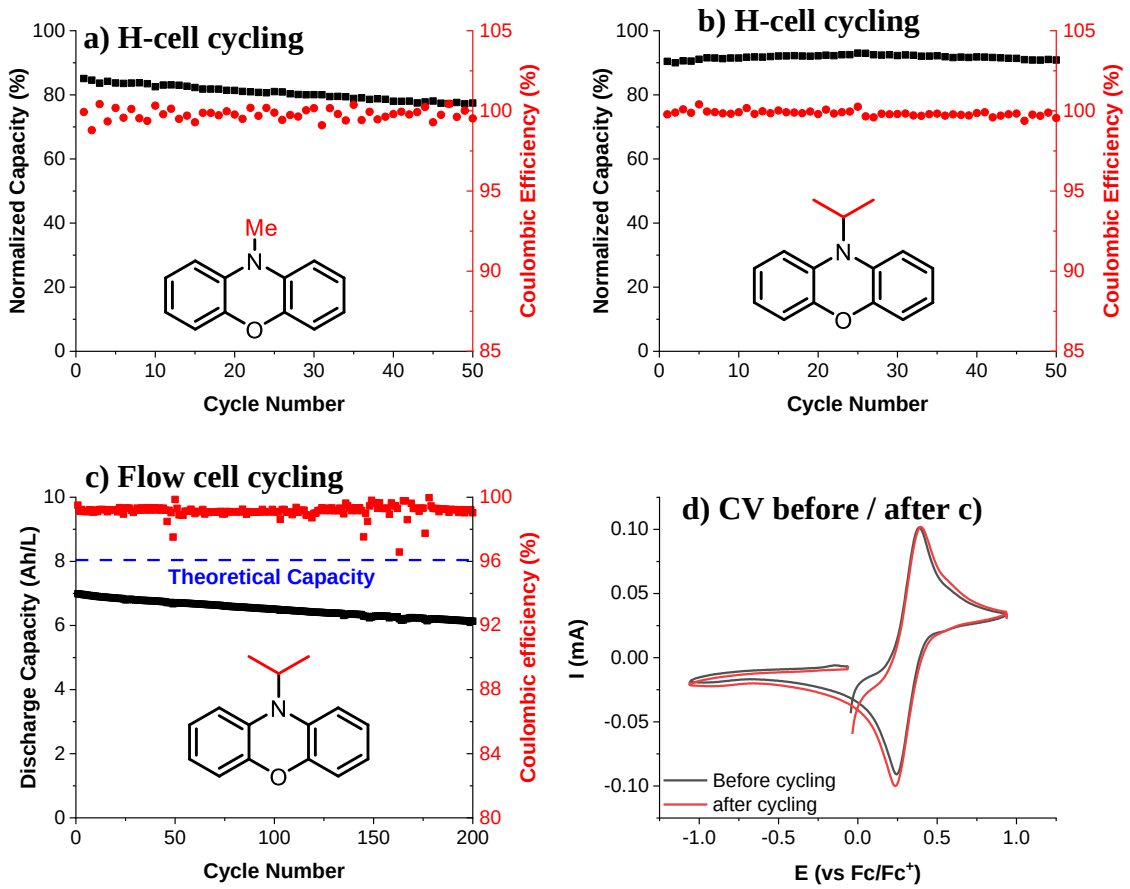

Figure 7.2. Discharge capacity (normalized to theoretical capacity) and coulombic efficiency versus cycle number for H-cell cycling of (5 mM in 0.5 M $TBAPF_6$/ MeCN) a) 1- Me; b) 1- ^{i}Pr; c) Symmetrical flow cell cycling of 0.3 M 1- ^{i}Pr in 0.5 M LiTFSI / MeCN; d) CV before and after symmetrical cycling.

To achieve a high energy density battery, the solubility of all redox states of the compound needs to be sufficiently high. Compound **1-Me** was thus chemically oxidized to **1-Me**$^{+\bullet}$ using $NOPF_6$ and isolated as violet powder.[35] The solubility of the radical cation **1-Me**$^{+\bullet}$ was then measured in 0.5 M LiTFSI/MeCN to be 0.2 M. Although it is double that of the N-methyl phenothiazine radical cation (0.1 M)[34], it is still significantly lower than that of its unoxidized state (miscible with 0.5 M

LiTFSI/MeCN). This drastic decrease of solubility before and after oxidation is mainly due to the pi-stacking of the charged molecule.[36]

We hypothesized that the introduction of an N-isopropyl group could disrupt this pi-stacking interaction and thus enhance solubility. The N-isopropyl analogue **1-^{i}Pr** was synthesized using isopropyl iodide, and its radical cation **1-^{i}Pr$^{+\bullet}$** was accessed by oxidation of **1-^{i}Pr** with $NOPF_6$. As predicted the solubility of **1-^{i}Pr$^{+\bullet}$** was significantly higher than that of the methyl analogue (0.4 M in 0.5 M LiTFSI/MeCN), while the neutral **1-^{i}Pr** remains miscible in 0.5 M LiTFSI/MeCN. Notably, this solubility is similar to the radical cation of the phenothiazine (0.4 M) attached with a PEO chain in 0.5 M TEATFSI/MeCN.[37] CV analysis of **1-^{i}Pr** shows a redox potential nearly identical to that of **1-Me**. Galvanostatic charge-discharge cycling of **1-^{i}Pr** shows even better stability with 97% capacity retention for over 50 cycles and was able to achieve 93% theoretical capacity and > 99% columbic efficiency. (Figure 7.2b) Therefore, **1-^{i}Pr** became a good candidate to be tested in a protype flow cell at relatively high concentration.

The cycling performance of **1-^{i}Pr** was evaluated in a symmetric flow cell, in which each reservoir contained the same compound in different redox states. This cycling experiment has been widely used to evaluate the cycling stability of a single active species as it provides isolated testing of the cycling stability of the catholyte.[32,34,35,37] Solutions of **1-^{i}Pr** and [**1-^{i}Pr^{+}**][**PF_6^-**] (0.3 M in 0.5 M LiTFSI/MeCN) were loaded into reservoirs on opposite sides of the flow cell and a Daramic 175 membrane was used to limit crossover of active species. Cycling was performed with charge and discharge currents of +60 mA/cm^2 and –60 mA/cm^2, respectively, to cutoff voltages of 0.5 V and -0.5 V. The high current cycling is made possible because of the low resistance of the selected membrane as indicated by the impedance spectrum. The theoretical capacity is 8.04 Ah/L, the material utilization of this cycling is 86% and the coulombic efficiency is about 99%. After 200

cycles (81 h), 88% of its original capacity was contained, indicating the high cycling stability of **1-^{i}Pr** at a relatively high concentration. (Figure 7.2c) Moreover, the CVs of the diluted solution before and after show no change in concentration of active species (Figure 7.2d). The capacity fade is likely from solution slowly diffusing to one side due to pressure differences, as small solvent volume discrepancy in reservoirs was observed after cycling.[38]

Stability and Energy Optimization

With this stable but with moderate redox potential compound in hand, our next objective is to further improve the energy capacity of the phenoxazine redox center to achieve higher energy density devices. With regards to this purpose, two directions are usually explored: one is to increase the number of electrons transfer[2] and another is to enhance the redox potential. We next prepared **2** in the similar way as **1**. We recently showed DAC as an outstanding substitution group that not only strongly withdraws electrons to increase the potential but provides extra stability through more delocalized conjugation as well. This dual effect helps the generation of a stable and energetic catholytes. **2-Me** was first prepared and characterized by CV. With the incorporation of DAC group, **2-Me** has a redox potential of 0.70 V vs Fc/Fc^{+}, about 3 times increase in redox potential (> 400 mV) than those of **1**. Notably, this potential is higher than those of most known catholyte platforms such as dimethoxy-di-tert-butyl-benzene[16], TEMPO[2,39,40], phenothiazine[9,34,37] and phenazine[5,13]. However, galvanostatic charging and discharging experiment of **2-Me** in H-cell using the same set up in Figure 7.2a, b shows quick capacity fade with 54 % capacity lost in 50

[2] We first prepared scaffolds that have previously shown success in helping stabilize the second redox couple of phenothiazine derivative (methoxy, DAC on the 3, 7 positions of the aromatic ring). However, none of them exhibit sufficient stability for further application.

cycles. (Figure 7.3a). This fast capacity fade could come from decomposition pathways involving deprotonation of the acidic hydrogen alpha to nitrogen. To impede such pathways, we introduced secondary alkyl substituents to slow down this potential decomposition. Also, with experience acquired from previous solubility study on cyclopropenium derivatives, **2-Pr** was prepared in order to improve its solubility by longer alkyl chains for high energy density battery. It turns out to be not only highly soluble at both oxidation states (1.40 M before oxidation and 0.35 M after oxidation in 0.5 M $TBAPF_6$/acetonitrile) but also highly stable in H-cell cycling with 96% capacity retention after 50 cycles. (Figure 7.3a)

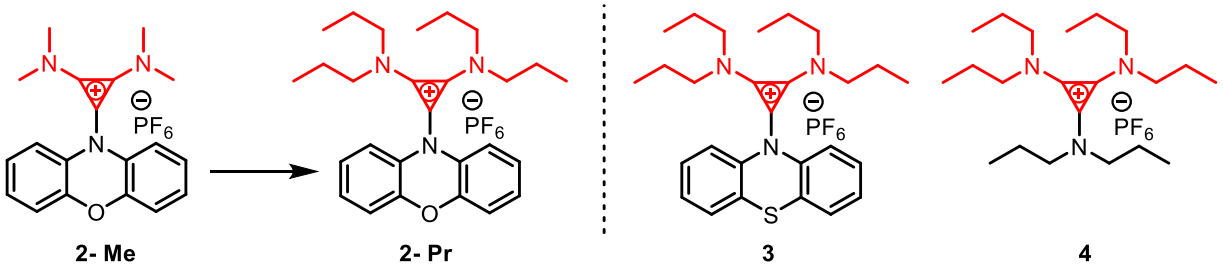

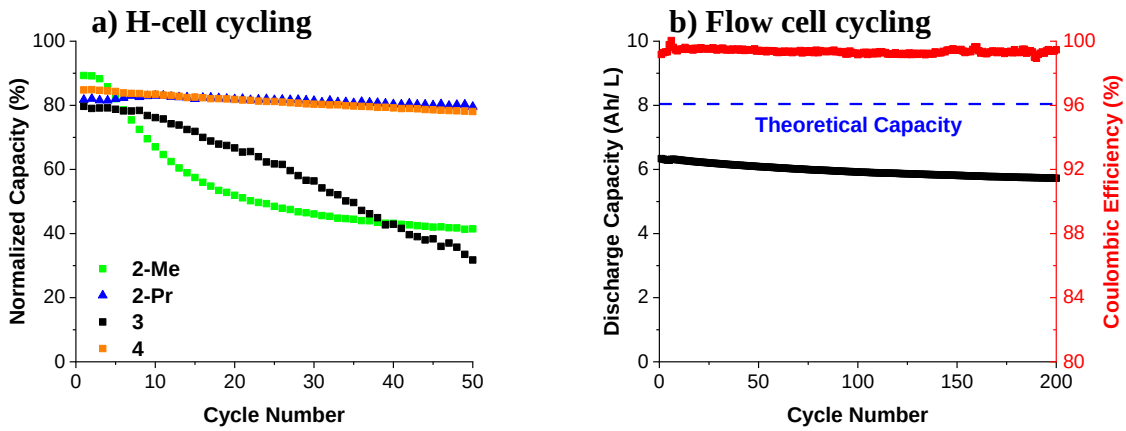

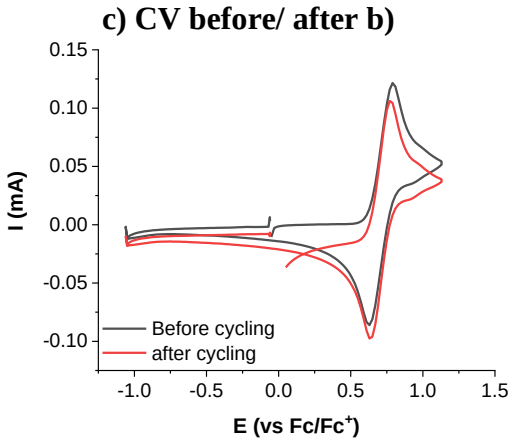

Figure 7.3. (a) H-cell bulk charge-discharge cycling date for 2-Me, 2-Pr (5 mM in 0.5 M $TBAPF_6$/ MeCN); (b) Symmetrical cycling of 0.3 M 2-Pr in MeCN without supporting electrolyte added; (c) CV before and after symmetrical cycling.

Compared with its sulfur analog **3** reported before, **2-Pr** shows much better cycling stability (Figure 7.3a) with lower molecular weight and increased solubility (1.40 vs 0.86 M). Compared with the tris(n-propyl)amino cyclopropenium **4**,[31,35] **2-Pr** has slighter lower redox potential (0.81 V vs 0.70 V) and solubility (1.84 vs 1.40 M) while with slightly better cycling stability potentially due to the extra resonance stabilization from the phenoxazine core. Notably, although containing an aromatic amine, **2-Pr** exhibits much better cycling stability than that of tris(anilino) cyclopropenium reported before.

To evaluate the long-term stability of **2-Pr** in a more relevant environment, the same symmetrical flow cell cycling experiment was conducted. Cycling was performed using a 0.3 M MeCN solution of **2-Pr** without an added supporting electrolyte. Such strategy, shown in our previous work,[35] could potentially decrease the viscosity of the solution and the cost of these systems. This is possible as this compound is at ionic states at both redox states, thus making the solution of it conductive without adding supporting salts. An anion-exchange membrane Fumasep FAP-375-PP

was selected as the separator to reduce crossover of cationic species and due to its relatively high resistance, the charging and discharging current were adjusted to ±35 mA. The theoretical capacity is 8.04 Ah/L, the material utilization of this cycling is 79% and the coulombic efficiency is about 99.5 %. After 200 cycles (131 h), 91% of its original capacity was contained, indicating the high cycling stability of **2-Pr** at a relatively high concentration (Figure 7.3b). Again, the CVs of the diluted solution before and after shows no change in concentration of active species, indicating no capacity loss from irreversible chemical decomposition (Figure 7.3c).[32,35]

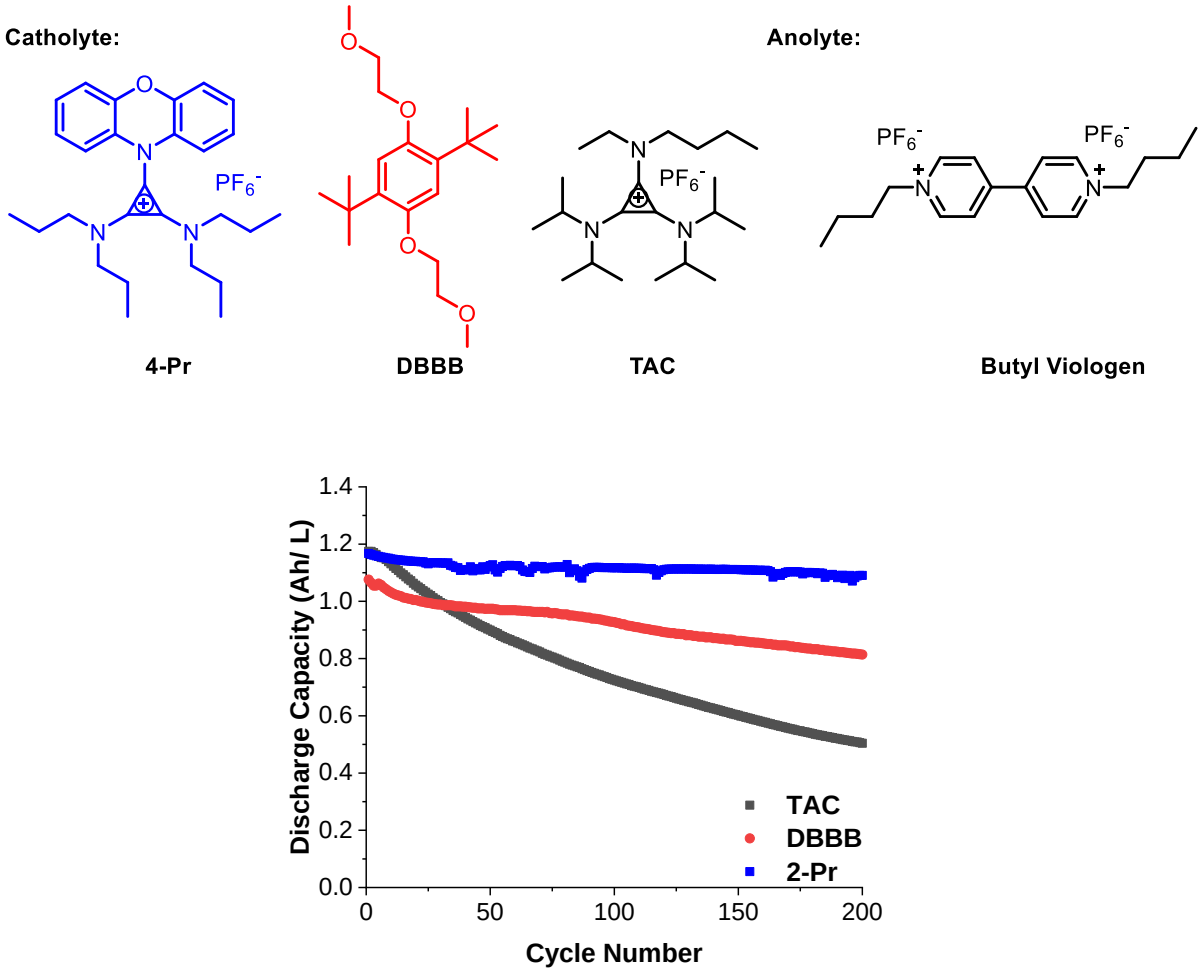

Figure 7.4. Comparative study of three full flow batteries with 50 mM butyl viologen as anolyte and 50 mM TAC, DBBB and 2-Pr as catholytes in 0.5 M TBAPF6 /MeCN.

Knowing **2-Pr** is very stable by itself in a flow cell environment, we designed a comparative study that using a full flow battery setup with butyl viologen as anolyte to study the more practical cycling performances of different catholytes. Two other well-studied catholyte, 2, 5-di-*tert*-butyl-1,4-bis(2-methoxyethoxy) benzene (DBBB) and trisaminocyclopropenium (TAC) cation were selected due to their similar potentials and known good chemical and cycling stability. As discussed in our previous studies on cyclopropenium-based extremely high potential catholytes (>1 V vs Fc/Fc^+),[30,32] high stability can be observed in symmetric cycling but can suffer from fast self-discharge and other detrimental interactions when anolyte molecules are present in the same solution leading to poor cycling performance of a high potential battery. Such disadvantages make those extremely high potential hard to be competitive with commercial flow batteries. To achieve practical energy storage devices, the cycling stability and efficient performance are vital requirements. Thus, these experiments are important for evaluation of catholytes' stability in more complex environment. A very stable anolyte was chosen in order to exclude the influence on cycling performance from chemical decomposition of the anolyte. To keep experimental conditions consistent, a mixed solution of 50 mM specific catholyte and 50 mM butyl viologen hexafluorophosphate in 0.50 M MeCN/ $TBAPF_6$ was placed in both the catholyte and anolyte reservoirs, to limit effects from electrolyte cross over across the Daramic-175 membrane. All cycling experiments were performed using a ± 20 mA charging/discharging currents. The theoretical capacity of all three batteries is 1.34 Ah/L, and the initial material utilization is 87% in the **2-Pr** battery, 88% in the TAC battery and 80% in the DBBB battery. The coulombic efficiency is about 93% for **2-Pr** and about 92% for DBBB and TAC. The cycling time is around 1-2 days for three experiments. As Figure x shows, **2-Pr** outperforms the other two materials in the same

setup with 93% capacity retention after 200 cycles while DBBB has 75% left and TAC has 43% left. Overall, these experiments reassure the outstanding chemical and cycling stability of **2-Pr**, making it a possible candidate for application in commercial devices.

7.3 Conclusion

Two new classes of phenoxazine-based derivatives were examined as catholytes for non-aqueous flow batteries. Molecules with simple short alkyl chain substitutions on nitrogen shows unexpected liquid feature, making them possible for application in high energy density battery. After rational molecular design, a promising candidate with high solubility at all redox states and cycling stability are generated at a much cheaper cost compared with its precedent literature counterparts. The optimal compound of another class of molecules incorporates DAC with phenoxazine, leading to a much higher redox potential while still with outstanding stability. This compound outperforms current state-of-arts catholytes in both potential and stability.

7.4 Experimental Procedures and Characterization of Compounds

7.4.1 Synthetic Procedures

General Information. All commercial chemicals were used as received unless stated otherwise. Anhydrous CH_2Cl_2 was obtained from an Innovative Technology, Inc. (now rebranded to Inert) solvent purification system. Reactions were performed under a nitrogen atmosphere. The solubility of **1-Me**$^+$, **1-**^{i}**Pr**$^+$, **2-Pr** and **2-Pr**$^+$ in acetonitrile with 0.5 M supporting electrolytes was determined using a previously reported method.[35] **1-Me** was prepared according to a published report.[41] **TAC** was prepared according to previous reports.[31,35] Butyl viologen was synthesized according to literature procedures[4] and then anion exchanged with NH_4PF_6. NMR spectra were obtained on Varian VNMRs 700, Varian VNMRs 500, Varian Inova 500, or Varian MR400 spectrometers. ^{1}H and ^{13}C chemical shifts are reported in parts per million (ppm) relative to TMS, with the residual

solvent peak used as an internal reference. High resolution mass spectroscopy (HRMS) was performed on a Micromass AutoSpec Ultima Magnetic Sector Mass Spectrometer using electrospray ionization (ESI).

General procedure for the synthesis of 1 and 2. Under inert atmosphere, a solution of phenoxazine (500 mg, 2.73 mmol) in dry THF (10 mL) was added with NaH (80 mg, 3.33mmol) at room temperature. After stirring for 1h, alkyl iodide or 1-chloro-2,3-bis(dialkylamino)cyclopropenium chloride (1 equiv) was added to the solution. The mixture was then heat to 50 °C for overnight. The reaction was quenched with 1 M HCl (10 mL), and the resulting mixture was extracted with DCM (3 x 20 mL). For Structure **2**, the organic layers were evaporated under reduced pressure and the residue was dissolved in 5 mL of water, and an aqueous solution of ammonium hexafluorophosphate (NH_4PF_6; 890 mg, 5.46 mmol in 10 mL H_2O) was added with vigorous stirring. A precipitate formed, and this material was extracted into CH_2Cl_2 (3 × 15 mL). The combined organic layers were dried over Na_2SO_4, filtered and evaporated under reduced pressure. Column chromatography afforded **1** and **2**.

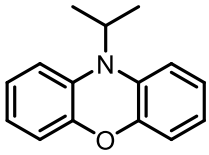

Synthesis of 1-^{i}Pr: The general procedure was followed using isopropyl iodide as the substrate. Compound **1-^{i}Pr** was isolated as a colorless liquid using 10% ethyl acetate in hexane (485 mg, 79%). R_F = 0.25 in 10% ethyl acetate/ hexane. ^{1}H NMR (500 MHz, DMSO-d6) δ 6.97 – 6.83 (m, 4H), 6.83 – 6.69 (m, 4H), 4.16 (hept, J = 7.0 Hz, 1H), 1.44 (d, J = 6.9 Hz, 6H). ^{13}C NMR (126 MHz, DMSO-d6) δ 147.16, 134.43, 123.88, 121.34, 115.43, 115.35, 50.20, 40.02, 39.85, 39.69,

39.52, 39.35, 39.19, 39.02, 19.34. HRMS (ESI) *m/z* calcd for $C_{15}H_{15}NO$ (**1-** ^{i}**Pr**): 225.1154, found: 225.1144.

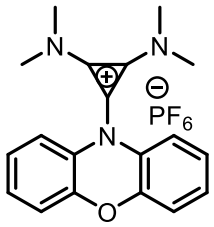

Synthesis of 2-Me: The general procedure was followed using 1-chloro-2,3-bis(dimethylamino)cyclopropenium chloride[42, 43] as the substrate. Compound **2-Me** was isolated as a white powder using 10% ethyl acetate in DCM. (311 mg, 45%) R_F = 0.23 in 10% ethyl acetate/ DCM. ^{1}H NMR (500 MHz, Acetonitrile-d3) δ 7.11 – 7.01 (m, 4H), 6.99 – 6.91 (m, 2H), 6.90 – 6.81 (m, 2H), 3.22 (s, 12H). ^{13}C NMR (126 MHz, Acetonitrile-d3) δ 145.09, 129.82, 128.82, 126.44, 125.14, 117.67, 116.20, 101.95, 43.02. HRMS (ESI) *m/z* calcd for $C_{19}H_{22}N_3O^+$ (**2-Me**$^+$): 306.1601, found: 306.1598.

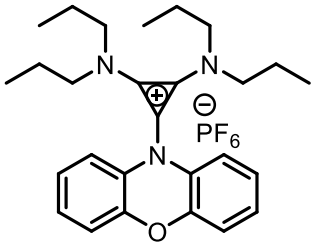

Synthesis of 2-Pr: The general procedure was followed using 1-chloro-2,3-bis(di-n-propyl)cyclopropenium chloride[42, 43] as the substrate. Compound **2-Me** was isolated as a white powder using 10% ethyl acetate in DCM. R_F = 0.31 in 10% ethyl acetate/ DCM (814mg, 58%). ^{1}H NMR (400 MHz, Acetonitrile-d3) δ 7.12 – 6.98 (m, 6H), 6.98 – 6.88 (m, 3H), 6.84 – 6.69 (m, 3H), 3.39 (t, J = 7.5 Hz, 12H), 1.70 (h, J = 7.3 Hz, 12H), 0.88 (t, J = 7.3 Hz, 18H). ^{13}C NMR (176

MHz, Acetonitrile-d3) δ 145.55, 130.18, 129.17, 126.57, 125.15, 118.64, 117.76, 116.30, 55.11, 22.09, 10.97. HRMS (ESI) *m/z* calcd for $C_{27}H_{38}N_3O^+$ (**2-Pr**$^+$): 418.2853, found: 418.2844.

7.4.2 Electrochemistry Experimental Procedures

General methods and materials. Acetonitrile (anhydrous, 99.8%) was obtained from Sigma Aldrich and used as received. Tetrabutylammonium hexafluorophosphate ($TBAPF_6$; electrochemical grade) was obtained from Sigma Aldrich and dried under high vacuum for 48 h at 70 °C before being transferred to a N_2-filled glovebox. A 0.50 M stock solution of $TBAPF_6$ in acetonitrile was prepared in a N_2-filled glovebox and dried over 3Å molecular sieves for at least two days prior to use. A Fumasep® FAP-375-PP membrane was obtained from Fumatech and ion-exchanged in saturated KPF_6 and then dried under high vacuum overnight before use. Daramic-175 membrane was generously provided by Daramic company and used as received.

Cyclic voltammetry. Cyclic voltammetry (CV) was performed in a N_2-filled glovebox with a Biologic VSP multichannel potentiostat/galvanostat using a three-electrode electrochemical cell, consisting of a glassy carbon disk working electrode (0.071 cm^2, BASi), a Ag/Ag^+ reference electrode (BASi) with 0.01 M $AgBF_4$ (Sigma) and 0.5 M $TBAPF_6$ in acetonitrile, and a platinum wire counter electrode. All experiments were conducted in a 0.50 M $TBAPF_6$/acetonitrile electrolyte stock solution.

H-cell cycling. Bulk charge/discharge measurements were carried out in a N_2-filled glovebox with a BioLogic VSP galvanostat in a custom glass H-cell with an ultrafine fritted glass separator (P5, Adams and Chittenden). The working and counter electrodes were reticulated vitreous carbon (100 ppi, ~70 cm^2 surface area, Duocel). A Ag/Ag^+ reference electrode was used on the working side of the H-cell. The electrolyte contained 5 mM active species and 0.50 M $TBAPF_6$ in acetonitrile. Both chambers of the H-cell were loaded with 5 mL electrolyte solution and were stirred

continuously during cycling at a current of 5 mA. Voltage cutoffs of +0.5 V higher than $E_{1/2}$ as the upper limit and -0.5 V lower than $E_{1/2}$ as the lower limit were employed.

Flow cell cycling. Cycling under flow conditions was performed with a zero-gap flow cell comprised of graphite charge collecting plates containing an interdigitated flow field in combination with two layers of non-woven carbon felt electrodes (Sigracet 29AA) on each side.[34] PTFE gaskets were used to achieve ~20% compression of the felt. One Fumasep® FAP-375-PP or Daramic 175 membrane separated the two half cells, and the exposed area of the membrane in the gasket window was used as the active area (2.55 cm^2). After assembly, both sides are filled with 50mM or 0.3 M compounds of interest. The cell was pretreated by continuously flowing the solution above at 10 mL/min for 1 h without any charging process using a peristaltic pump (Cole-Parmer) with Solve-Flex and PFA tubing. After this step, using the same flow rate, galvanostatic charge/discharge cycling was performed using a BioLogic VSP galvanostat employing a certain charging/ discharging current.

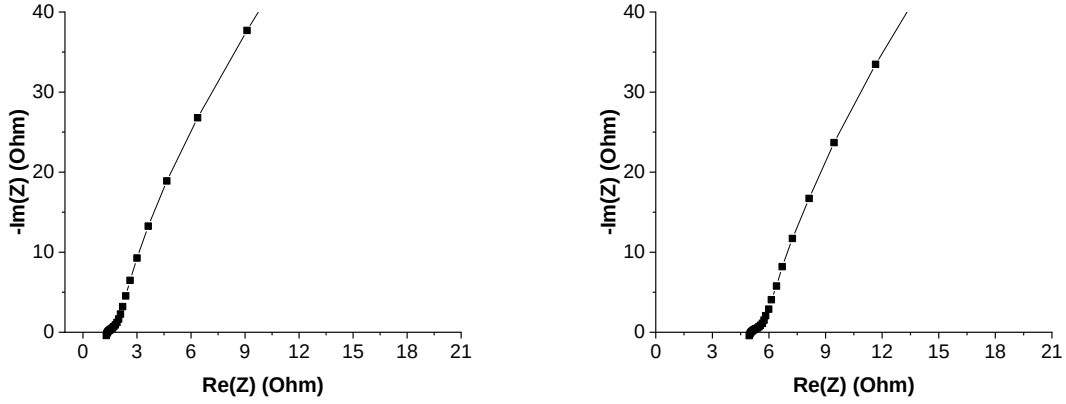

Figure 7.5 Nyquist plot from electrochemical impedance spectroscopy measurements for flow cell with Daramic-175 membrane (left) and Fumasep® FAP-375-PP (right)

7.5 Reference

(1) Wei, X.; Pan, W.; Duan, W.; Hollas, A.; Yang, Z.; Li, B.; Nie, Z.; Liu, J.; Reed, D.; Wang, W.; Sprenkle, V. Materials and Systems for Organic Redox Flow Batteries: Status and Challenges. *ACS Energy Lett.* **2017**, *2* (9), 2187–2204. https://doi.org/10.1021/acsenergylett.7b00650.

(2) Wei, X.; Xu, W.; Vijayakumar, M.; Cosimbescu, L.; Liu, T.; Sprenkle, V.; Wang, W. TEMPO-Based Catholyte for High-Energy Density Nonaqueous Redox Flow Batteries. *Advanced Materials* **2014**, *26* (45), 7649–7653. https://doi.org/10.1002/adma.201403746.

(3) Winsberg, J.; Hagemann, T.; Muench, S.; Friebe, C.; Häupler, B.; Janoschka, T.; Morgenstern, S.; Hager, M. D.; Schubert, U. S. Poly(Boron-Dipyrromethene)—A Redox-Active Polymer Class for Polymer Redox-Flow Batteries. *Chem. Mater.* **2016**, *28* (10), 3401–3405. https://doi.org/10.1021/acs.chemmater.6b00640.

(4) Zhang, C.; Zhang, L.; Ding, Y.; Peng, S.; Guo, X.; Zhao, Y.; He, G.; Yu, G. Progress and Prospects of Next-Generation Redox Flow Batteries. *Energy Storage Materials* **2018**, *15*, 324–350. https://doi.org/10.1016/j.ensm.2018.06.008.

(5) Kwon, G.; Lee, S.; Hwang, J.; Shim, H.-S.; Lee, B.; Lee, M. H.; Ko, Y.; Jung, S.-K.; Ku, K.; Hong, J.; Kang, K. Multi-Redox Molecule for High-Energy Redox Flow Batteries. *Joule* **2018**, *2* (9), 1771–1782. https://doi.org/10.1016/j.joule.2018.05.014.

(6) Zhang, J.; Yang, Z.; Shkrob, I. A.; Assary, R. S.; Tung, S. on; Silcox, B.; Duan, W.; Zhang, J.; Su, C. C.; Hu, B.; Pan, B.; Liao, C.; Zhang, Z.; Wang, W.; Curtiss, L. A.; Thompson, L. T.; Wei, X.; Zhang, L. Annulated Dialkoxybenzenes as Catholyte Materials for Non-Aqueous Redox Flow Batteries: Achieving High Chemical Stability through Bicyclic Substitution. *Adv. Energy Mater.* **2017**, *7* (21), 1701272. https://doi.org/10.1002/aenm.201701272.

(7) VanGelder, L. E.; Schreiber, E.; Matson, E. M. Physicochemical Implications of Alkoxide “Mixing” in Polyoxovanadium Clusters for Nonaqueous Energy Storage. *J. Mater. Chem. A* **2019**, *7* (9), 4893–4902. https://doi.org/10.1039/C8TA12306C.

(8) VanGelder, L. E.; Kosswattaarachchi, A. M.; Forrestel, P. L.; Cook, T. R.; Matson, E. M. Polyoxovanadate-Alkoxide Clusters as Multi-Electron Charge Carriers for Symmetric Non-Aqueous Redox Flow Batteries. *Chem. Sci.* **2018**, *9* (6), 1692–1699. https://doi.org/10.1039/C7SC05295B.

(9) A. Kowalski, J.; D. Casselman, M.; Preet Kaur, A.; D. Milshtein, J.; F. Elliott, C.; Modekrutti, S.; Harsha Attanayake, N.; Zhang, N.; R. Parkin, S.; Risko, C.; R. Brushett, F.; A. Odom, S. A Stable Two-Electron-Donating Phenothiazine for Application in Nonaqueous Redox Flow Batteries. *Journal of Materials Chemistry A* **2017**, *5* (46), 24371–24379. https://doi.org/10.1039/C7TA05883G.

(10) Escalante-García, I. L.; Wainright, J. S.; Thompson, L. T.; Savinell, R. F. Performance of a Non-Aqueous Vanadium Acetylacetonate Prototype Redox Flow Battery: Examination of Separators and Capacity Decay. *J. Electrochem. Soc.* **2015**, *162* (3), A363–A372. https://doi.org/10.1149/2.0471503jes.

(11) Carino, E. V.; Staszak-Jirkovsky, J.; Assary, R. S.; Curtiss, L. A.; Markovic, N. M.; Brushett, F. R. Tuning the Stability of Organic Active Materials for Nonaqueous Redox Flow Batteries via Reversible, Electrochemically Mediated Li+ Coordination. *Chem. Mater.* **2016**, *28* (8), 2529–2539. https://doi.org/10.1021/acs.chemmater.5b04053.

(12) Silcox, B.; Zhang, J.; Shkrob, I. A.; Thompson, L.; Zhang, L. On Transferability of Performance Metrics for Redox-Active Molecules. *J. Phys. Chem. C* **2019**, *123* (27), 16516–16524. https://doi.org/10.1021/acs.jpcc.9b02230.

(13) Kwon, G.; Lee, K.; Lee, M. H.; Lee, B.; Lee, S.; Jung, S.-K.; Ku, K.; Kim, J.; Park, S. Y.; Kwon, J. E.; Kang, K. Bio-Inspired Molecular Redesign of a Multi-Redox Catholyte for High-Energy Non-Aqueous Organic Redox Flow Batteries. *Chem* **2019**, *5* (10), 2642–2656. https://doi.org/10.1016/j.chempr.2019.07.006.

(14) Sevov, C. S.; Fisher, S. L.; Thompson, L. T.; Sanford, M. S. Mechanism-Based Development of a Low-Potential, Soluble, and Cyclable Multielectron Anolyte for Nonaqueous Redox Flow Batteries. *J. Am. Chem. Soc.* **2016**, *138* (47), 15378–15384. https://doi.org/10.1021/jacs.6b07638.

(15) Duan, W.; Huang, J.; Kowalski, J. A.; Shkrob, I. A.; Vijayakumar, M.; Walter, E.; Pan, B.; Yang, Z.; Milshtein, J. D.; Li, B.; Liao, C.; Zhang, Z.; Wang, W.; Liu, J.; Moore, J. S.; Brushett, F. R.; Zhang, L.; Wei, X. "Wine-Dark Sea" in an Organic Flow Battery: Storing Negative Charge in 2,1,3-Benzothiadiazole Radicals Leads to Improved Cyclability. *ACS Energy Lett.* **2017**, *2* (5), 1156–1161. https://doi.org/10.1021/acsenergylett.7b00261.

(16) Huang, J.; Cheng, L.; Assary, R. S.; Wang, P.; Xue, Z.; Burrell, A. K.; Curtiss, L. A.; Zhang, L. Liquid Catholyte Molecules for Nonaqueous Redox Flow Batteries. *Advanced Energy Materials* **2015**, *5* (6), 1401782. https://doi.org/10.1002/aenm.201401782.

(17) Zhang, C.; Qian, Y.; Ding, Y.; Zhang, L.; Guo, X.; Zhao, Y.; Yu, G. Biredox Eutectic Electrolytes Derived from Organic Redox-Active Molecules: High-Energy Storage Systems. *Angewandte Chemie International Edition* **2019**, *58* (21), 7045–7050. https://doi.org/10.1002/anie.201902433.

(18) Zhang, C.; Niu, Z.; Ding, Y.; Zhang, L.; Zhou, Y.; Guo, X.; Zhang, X.; Zhao, Y.; Yu, G. Highly Concentrated Phthalimide-Based Anolytes for Organic Redox Flow Batteries with

Enhanced Reversibility. *Chem* **2018**, *4* (12), 2814–2825. https://doi.org/10.1016/j.chempr.2018.08.024.

(19) Wang, W.; Luo, Q.; Li, B.; Wei, X.; Li, L.; Yang, Z. Recent Progress in Redox Flow Battery Research and Development. *Advanced Functional Materials* **2013**, *23* (8), 970–986. https://doi.org/10.1002/adfm.201200694.

(20) Leung, P.; Li, X.; León, C. P. de; Berlouis, L.; Low, C. T. J.; Walsh, F. C. Progress in Redox Flow Batteries, Remaining Challenges and Their Applications in Energy Storage. *RSC Adv.* **2012**, *2* (27), 10125–10156. https://doi.org/10.1039/C2RA21342G.

(21) Noack, J.; Roznyatovskaya, N.; Herr, T.; Fischer, P. The Chemistry of Redox-Flow Batteries. *Angewandte Chemie International Edition* **2015**, *54* (34), 9776–9809. https://doi.org/10.1002/anie.201410823.

(22) Zhao, Y.; Ding, Y.; Li, Y.; Peng, L.; Byon, H. R.; Goodenough, J. B.; Yu, G. A Chemistry and Material Perspective on Lithium Redox Flow Batteries towards High-Density Electrical Energy Storage. *Chem. Soc. Rev.* **2015**, *44* (22), 7968–7996. https://doi.org/10.1039/C5CS00289C.

(23) Wu, Y.; Liu, W.; Liu, T.; Li, F.; Xiao, T.; Wu, Q.; He, Y. Sustainable Electron Shuttling Processes Mediated by In Situ-Deposited Phenoxazine. *ChemElectroChem* **2018**, *5* (16), 2171–2175. https://doi.org/10.1002/celc.201800470.

(24) O'Loughlin, E. J. Effects of Electron Transfer Mediators on the Bioreduction of Lepidocrocite (γ-FeOOH) by Shewanella Putrefaciens CN32. *Environ. Sci. Technol.* **2008**, *42* (18), 6876–6882. https://doi.org/10.1021/es800686d.

(25) Otteny, F.; Perner, V.; Wassy, D.; Kolek, M.; Bieker, P.; Winter, M.; Esser, B. Poly(Vinylphenoxazine) as Fast-Charging Cathode Material for Organic Batteries. *ACS Sustainable Chem. Eng.* **2020**, *8* (1), 238–247. https://doi.org/10.1021/acssuschemeng.9b05253.

(26) Lee, K.; E. Serdiuk, I.; Kwon, G.; Joo Min, D.; Kang, K.; Young Park, S.; Eon Kwon, J. Phenoxazine as a High-Voltage p-Type Redox Center for Organic Battery Cathode Materials: Small Structural Reorganization for Faster Charging and Narrow Operating Voltage. *Energy & Environmental Science* **2020**, *13* (11), 4142–4156. https://doi.org/10.1039/D0EE01003K.

(27) Treat, N. J.; Sprafke, H.; Kramer, J. W.; Clark, P. G.; Barton, B. E.; Read de Alaniz, J.; Fors, B. P.; Hawker, C. J. Metal-Free Atom Transfer Radical Polymerization. *J. Am. Chem. Soc.* **2014**, *136* (45), 16096–16101. https://doi.org/10.1021/ja510389m.

(28) McCarthy, B. G.; Pearson, R. M.; Lim, C.-H.; Sartor, S. M.; Damrauer, N. H.; Miyake, G. M. Structure–Property Relationships for Tailoring Phenoxazines as Reducing Photoredox Catalysts. *J. Am. Chem. Soc.* **2018**, *140* (15), 5088–5101. https://doi.org/10.1021/jacs.7b12074.

(29) Wang, Q.; Huang, Q. Redox Flow Battery System. US20140178735A1, June 26, 2014.

(30) Yan, Y.; Robinson, S. G.; Sigman, M. S.; Sanford, M. S. Mechanism-Based Design of a High-Potential Catholyte Enables a 3.2 V All-Organic Nonaqueous Redox Flow Battery. *J. Am. Chem. Soc.* **2019**, *141* (38), 15301–15306. https://doi.org/10.1021/jacs.9b07345.

(31) Sevov, C. S.; Samaroo, S. K.; Sanford, M. S. Cyclopropenium Salts as Cyclable, High-Potential Catholytes in Nonaqueous Media. *Advanced Energy Materials* **2017**, *7* (5), 1602027. https://doi.org/10.1002/aenm.201602027.

(32) Yan, Y.; Vaid, T. P.; Sanford, M. S. Bis(Diisopropylamino)Cyclopropenium-Arene Cations as High Oxidation Potential and High Stability Catholytes for Non-Aqueous Redox Flow Batteries. *J. Am. Chem. Soc.* **2020**, *142* (41), 17564–17571. https://doi.org/10.1021/jacs.0c07464.

(33) Kolek, M.; Otteny, F.; Schmidt, P.; Mück-Lichtenfeld, C.; Einholz, C.; Becking, J.; Schleicher, E.; Winter, M.; Bieker, P.; Esser, B. Ultra-High Cycling Stability of Poly(Vinylphenothiazine) as a Battery Cathode Material Resulting from π–π Interactions. *Energy Environ. Sci.* **2017**, *10* (11), 2334–2341. https://doi.org/10.1039/C7EE01473B.

(34) Milshtein, J. D.; Kaur, A. P.; Casselman, M. D.; Kowalski, J. A.; Modekrutti, S.; Zhang, P. L.; Harsha Attanayake, N.; Elliott, C. F.; Parkin, S. R.; Risko, C.; Brushett, F. R.; Odom, S. A. High Current Density, Long Duration Cycling of Soluble Organic Active Species for Non-Aqueous Redox Flow Batteries. *Energy Environ. Sci.* **2016**, *9* (11), 3531–3543. https://doi.org/10.1039/C6EE02027E.

(35) Robinson, S. G.; Yan, Y.; Hendriks, K. H.; Sanford, M. S.; Sigman, M. S. Developing a Predictive Solubility Model for Monomeric and Oligomeric Cyclopropenium-Based Flow Battery Catholytes. *J. Am. Chem. Soc.* **2019**, *141* (26), 10171–10176. https://doi.org/10.1021/jacs.9b04270.

(36) Tang, M.; Zhu, S.; Liu, Z.; Jiang, C.; Wu, Y.; Li, H.; Wang, B.; Wang, E.; Ma, J.; Wang, C. Tailoring π-Conjugated Systems: From π-π Stacking to High-Rate-Performance Organic Cathodes. *Chem* **2018**, *4* (11), 2600–2614. https://doi.org/10.1016/j.chempr.2018.08.014.

(37) Attanayake, N. H.; Kowalski, J. A.; Greco, K. V.; Casselman, M. D.; Milshtein, J. D.; Chapman, S. J.; Parkin, S. R.; Brushett, F. R.; Odom, S. A. Tailoring Two-Electron-Donating Phenothiazines To Enable High-Concentration Redox Electrolytes for Use in Nonaqueous Redox Flow Batteries. *Chem. Mater.* **2019**, *31* (12), 4353–4363. https://doi.org/10.1021/acs.chemmater.8b04770.

(38) Barton, J. L.; Wixtrom, A. I.; Kowalski, J. A.; Qian, E. A.; Jung, D.; Brushett, F. R.; Spokoyny, A. M. Perfunctionalized Dodecaborate Clusters as Stable Metal-Free Active

Materials for Charge Storage. *ACS Appl. Energy Mater.* **2019**, *2* (7), 4907–4913. https://doi.org/10.1021/acsaem.9b00610.

(39) Liu, Y.; Goulet, M.-A.; Tong, L.; Liu, Y.; Ji, Y.; Wu, L.; Gordon, R. G.; Aziz, M. J.; Yang, Z.; Xu, T. A Long-Lifetime All-Organic Aqueous Flow Battery Utilizing TMAP-TEMPO Radical. *Chem* **2019**, *5* (7), 1861–1870. https://doi.org/10.1016/j.chempr.2019.04.021.

(40) Liu, T.; Wei, X.; Nie, Z.; Sprenkle, V.; Wang, W. A Total Organic Aqueous Redox Flow Battery Employing a Low Cost and Sustainable Methyl Viologen Anolyte and 4-HO-TEMPO Catholyte. *Advanced Energy Materials* **2016**, *6* (3), 1501449. https://doi.org/10.1002/aenm.201501449.

(41) Otteny, F.; Perner, V.; Wassy, D.; Kolek, M.; Bieker, P.; Winter, M.; Esser, B. Poly(Vinylphenoxazine) as Fast-Charging Cathode Material for Organic Batteries. *ACS Sustainable Chem. Eng.* **2020**, *8* (1), 238–247. https://doi.org/10.1021/acssuschemeng.9b05253.

Chapter 8

Development of Benzotriazoles as Low Potential Anolytes for Non-aqueous Redox Flow Batteries

8.1 Introduction

Redox flow batteries (RFBs) are energy storage devices designed to facilitate the integration of renewable energy resources into the electrical grid.[1,2] In these systems, energy is stored in solutions of redox active molecules that are charged and discharged by flowing through an electrochemical cell. The energy density of an RFB is directly proportional to the potential difference between the redox reactions occurring on each side of the cell. As such, a key goal for the field is to identify molecules that undergo reversible reduction (on the anolyte side of cell) and oxidation (on the catholyte side of cell) at extreme potentials in order to maximize the overall cell potential. These low potential anolytes and high potential catholytes are typically deployed in organic solvents, due their large potential windows relative to that of water.[3–6]

A major challenge for the field of non-aqueous RFB anolyte development is identifying stable redox active molecules that more fully leverage the cathodic potential limit of non-aqueous solvents (approximately -3.0 V versus ferrocene/ferrocenium (Fc/Fc^+) for acetonitrile and N,N-dimethylformamide).[7–24] While a variety organic and organometallic compounds have been successfully deployed as anolytes,[20,21,25–29] to date none of them have reduction potentials below -2.0 V versus Fc/Fc^+. This limitation stems primarily from the poor chemical and electrochemical cycling stability of the highly energetic radical anions formed upon one electron reduction.

2, 1, 3-Benzothiadiazole (**BzNSN**)[21,30,31] is among the lowest potential anolytes to be developed to date, with a reduction potential of -1.8 V versus Fc/Fc^+ in 0.5 M TEATFSI/ MeCN.[30] Over the past 5 years, a variety of **BzNSN** derivatives have been prepared by substitution at the 5-position of the redox active core (R in Figure 8.1).[31] While these modifications have led to the improvement of some key properties (e.g., cycling performance[31]and radical anion stability[30,31]), their redox potentials can be pushed by only 100-200 mV.

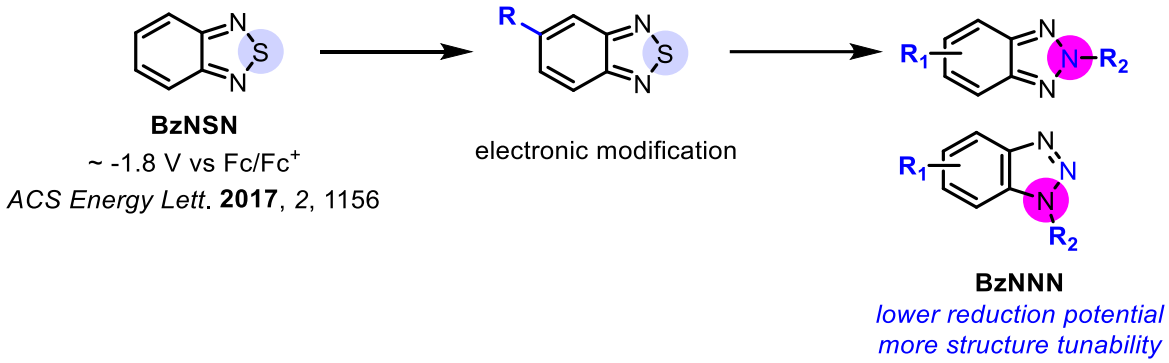

Figure 8.1. Development of extremely low potential anolytes

We hypothesized that dramatically lower potential anolytes could be accessed by moving to the structurally related benzotriazole (**BzNNN**) derivatives. The **BzNNN** molecules offer two key advantages compared to their **BzNSN** counterparts. First, replacing a sulfur with a nitrogen on the aromatic core is expected to increase the pi-electron density of the system, thus lowering the redox potential.[32,33] Second, moving from divalent sulfur to trivalent nitrogen necessitates the incorporation of a N-substituent (R_2 in Figure 8.1), which can be used to further tune the redox potential and other properties of the **BzNNN**-based anolytes. In this report, we use a combination of iterative molecular design, organic synthesis, and electrochemical evaluation to rapidly optimize **BzNNN**-based anolytes. Ultimately, we identify 2-aryl benzotriazole derivative **4** as an optimal

candidate with a redox potential of -2.3 V vs Fc/Fc^+, >0.3 M solubility in all redox states, and stable electrochemical cycling in a flow cell.

8.2. Results and Discussion

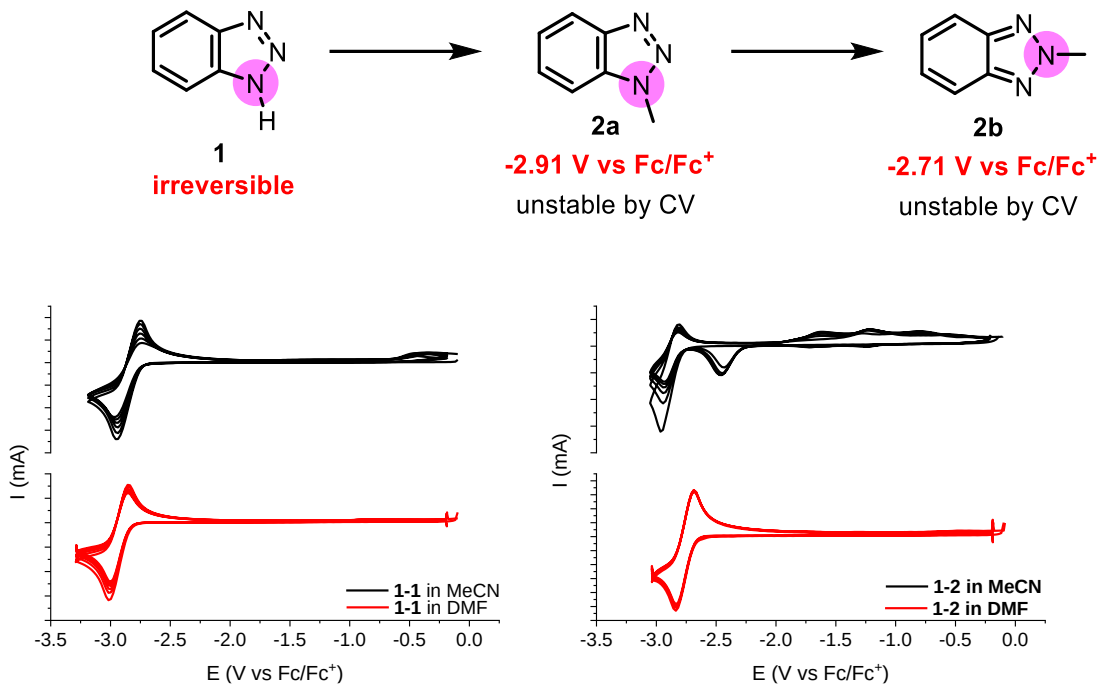

Figure 8.2. 5 continuous CV scans conducted with 5 mM solutions of **2a** in 0.5 M $TEABF_4$ in MeCN or DMF for **2a** (left) and **2b** (right)

Commercially available **1** was first studied via cyclic voltammetry (CV) under flow battery relevant conditions. The CV experiments were conducted using 5 mM solutions of **1** with 0.5 M $TEABF_4$ as supporting electrolyte in DMF or MeCN, a glassy carbon working electrode (0.07 cm^2, BASi), and a scan rate of 100 mV/s. The results showed irreversible reduction (E_{pc} ~ – 2.60 V vs Fc/Fc^+) in both DMF and acetonitrile with 0.5 M $TEABF_4$ (see supporting information). This irreversibility is attributed to the detrimental effect of hydrogen on stability of radical anion. Further studies focused on establishing whether the 1- or 2-position is the optimal site for substitution on the benzotriazole nitrogen to improve radical anion stability. 1-

Methylbenzotriazole (**2a**) and 2-methylbenzotriazole (**2b**) were synthesized via the reaction of benzotriazole with methyl iodide and then separation of the two isomers by chromatography on silica gel. Their reductive electrochemistry was interrogated via CV under the previously described conditions. Two metrics were used to preliminarily evaluate redox stability: (1) the peak height ratio (i_{pc}/i_{pa}) upon the initial CV scan and (2) the decay of peak current intensity (and appearance of new peaks) upon 5 continuous scans.

As shown in Figure 8.2, the CVs of **2a** and **2b** in acetonitrile (MeCN, the most common solvent for non-aqueous redox flow batteries with a potential limit of ~ -3.3 V) show low reduction potentials of -2.85 and -2.69 V vs Fc/Fc^+, respectively. However, the peak height ratios for the initial CV scans are 0.79 and 0.58, respectively, indicating poorly reversible reductions under these conditions. This is confirmed in the 5 continuous CV scans, which show significant erosion of the peak intensity, 29% and 59.2 %, as well as the appearance of new peaks at ~-0.50 V (**2a**) and ~-2.25 V and -1.12 V (**2b**), respectively.

We next moved to N,N-dimethylformamide (DMF) as a solvent based on literature reports showing improved redox stability of **BzNNN** derivatives in this medium.[24,25,34] As shown in Figure 1, the redox potentials of **2a** and **2b** in DMF are -2.91 and -2.71 V vs Fc/Fc^+, respectively, which are nearly identical to those in MeCN. However, the peak height ratios for the reduction peaks are much closer to 1 in DMF, at 0.87 and 0.91, respectively. Furthermore, 5 continuous CV scans shows similar erosion of peak intensity for **2a** (24.2 %) but significantly less for **2b** (8.6 %) in DMF. Overall, these studies show that DMF is the optimal solvent for electrochemical cycling and that methylation at the 2-position of **BzNNN** results in significantly enhanced redox stability compared to the 1-substituted analogue. However, the radical anion of **2b** shows instability upon further evaluation of the one electrochemical reduction event.

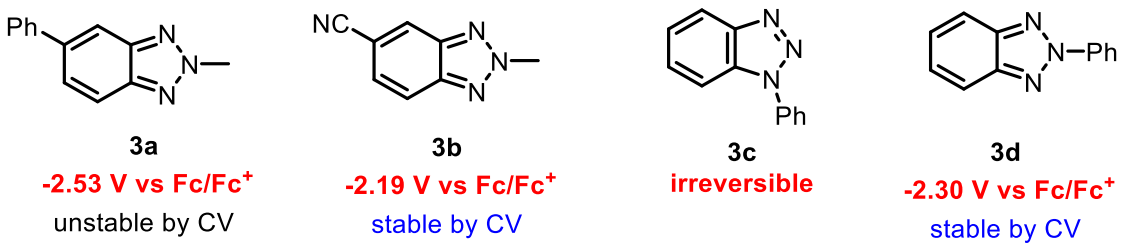

Figure 8.3. Versatile substitutions on benzotriazole core

We next sought to strategically introduce substituents to stabilize the radical anion in this system and thus enhance the reductive cycling performance (Figure 8.3). The general idea is to decrease the energy level of the radical anion either through extended resonance (3a, 3c, and 3d) or attaching electron withdrawing substituents (3b). Meanwhile, it is important to tailor the molecular structure for the optimal balance between stability and potential. The advantage of the benzotriazole derivatives is that there are two sites for modification: the aryl ring of the heterocycle and the substituent on nitrogen.

Analogous to the previous study on 5 position substitutions of **BZNSN**[31], We first synthesized derivatives bearing phenyl (**3a**) or cyano (**3b**) substitutions on 5 position in order to evaluate the impact of either resonance stabilization or strong inductive electron withdrawing on redox properties of the **BzNNN** core. **3a** was synthesized and characterized by Ryan Walser-Kuntz. The derivatives **3a** were synthesized via literature procedures[35]. **3b** was prepared through an S_N2 reaction between 5-cyano-1H-benzotriazole and methyl iodide. Through CV study in DMF, although **3a** also shows a reversible reduction at -2.53 V vs Fc/Fc^+, it is accompanied by a very close second irreversible reduction that destabilizes the first reduction and thus makes **3a** an undesired candidate. On the other hand, **3b** shows a more positively shifted reversible reduction

peak at -2.19 V vs Fc/Fc^+ with a peak height ratio of 0.93 and no observable decay in peak density for 5 continuous cycles, exhibiting good stability for CV time scale (Table 8.1).

Table 8.1. CV data of all compounds

compound	solvent	$E_{1/2}$[a]	i_{pa}/i_{pc}	decay of CV peak[b]
2a	MeCN	-2.85 V	0.79	29.0%
2a	DMF	-2.69 V	0.87	24.2%
2b	MeCN	-2.91 V	0.58	59.2%
2b	DMF	-2.71 V	0.91	8.6%
3a	DMF	-2.53 V	0.70	13.4%
3b	DMF	-2.19 V	0.93	0%
3c	DMF	irreversible	n/a	n/a
3d	DMF	-2.30 V	1.00	0%

[a] 5 mM substrate in 0.5 M $TEABF_4$/MeCN or DMF and referenced to Fc/Fc^+; scan rate of 100 [b] after 5 cycles

We next studied the impact of substitutions on nitrogen (1 and 2 positions) to the redox behavior. Consistent with a previous literature study,[36] **3c** shows irreversible reduction in CV in DMF while **3d** shows reversible reduction peak at -2.30 V vs Fc/Fc^+ with a peak height ratio of 1.00 and no observable decay in peak density for 5 continuous cycles, confirming the better stability of 2-substituted compounds under these conditions (Table 8.1).

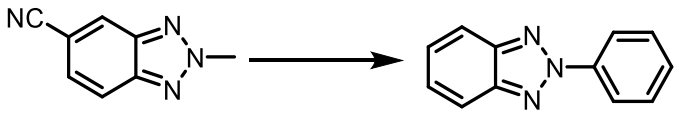

3b
-2.19 V vs Fc/Fc^+
unstable by charging-discharging

3d
-2.30 V vs Fc/Fc^+
stable

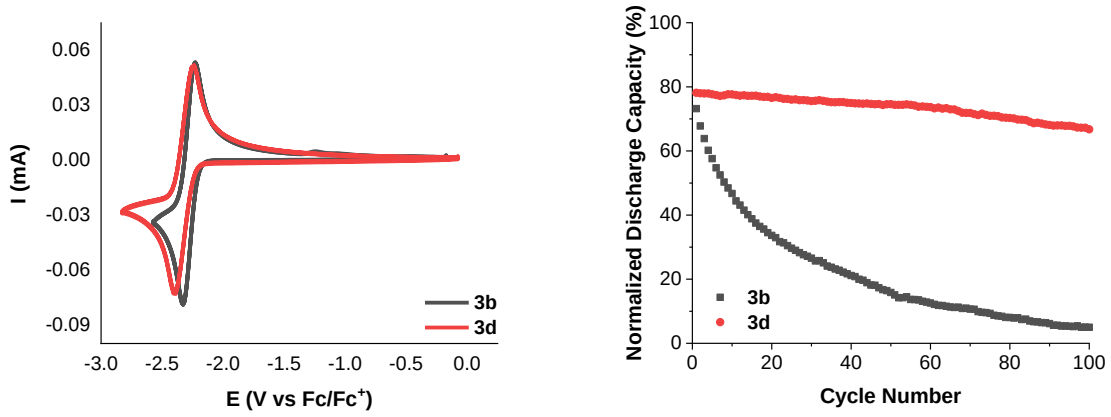

Figure 8.4. **Left**: 5 continuous CV scans of **3b** and **3d**; CVs conducted with 5 mM solutions of the redox active molecules in 0.5 M $TEABF_4$/DMF at 100 mV/s scan rate; **Right:** H-cell charge and discharge experiment of **3b** and **3d**

We next compared capacity retention between **3b** and **3d** during bulk charge-discharge cycling in a static H-cell (Figure 8.4, right). These experiments were conducted in a three-electrode H-cell separated with a fine glass frit with reticulated vitreous carbon (RVC) working and counter electrodes.[37] One-electron cycling was conducted with a 5 mM solution of the appropriate anolyte **3b** or **3d** in 0.5 M $TEABF_4$/DMF on both the working and counter electrode sides of the cell. After the initial charge, the solution on the counter electrode side was exchanged for a fresh solution of **3b or 3d** in 0.5 M $TEABF_4$/DMF to enable symmetrical one-electron cycling. The working side was charged at a rate of 5 mA using voltaic cutoffs in order to achieve the maximum state-of-charge (SOC). The discharged capacity on the working electrode side was monitored versus cycle number to assess capacity retention. The material utilization of **3b** is 74 % and 78 % for **3d**. The coulombic efficiency is 93% for **3b** and 97% or **3d**. The results show compound **3d** has much better capacity retention (85 % after 100 cycles) than that of **3b** (6.8 % after 100 cycles).

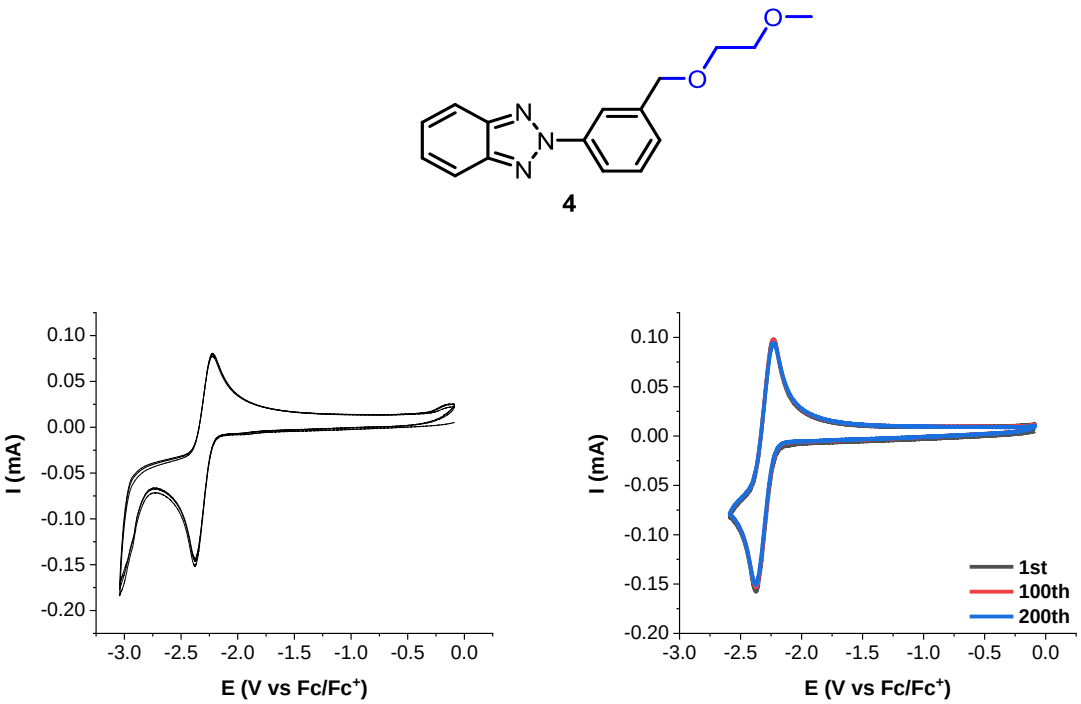

Figure 8.5. **Left**: full CV scan of **4** (3 cycles); **Right:** 200 continuous CV scans of **4**; CVs conducted with 10 mM solutions of the redox active molecules in 0.25 M LiTFSI/DMF at 100 mV/s scan rate

Compound **3d** was thus selected to further optimize its solubility for high concentration cycling. An oligoethylene oxide group (OEO) is incorporated on the meta position to the nitrogen in order to increase solubility while having minimal effects on the redox activity of the molecule. The new compound **4** is a liquid that is miscible with DMF, showing suitable solubility for high energy density devices. CV study of **4** exhibits a second irreversible peak slightly closer to the first desired couple than that of the compound **3d** due to weak inductively electron-withdrawing effect from the OEO chain, which might influence cycling performance (Figure 8.5, left). Fortunately, 200 continuous CV scans of the isolated first reversible couple confirms its high stability by showing no significant change of current intensity (Figure 8.5, right). The same charging-

discharging H-cell experiment was also conducted on **4** and the result shows comparable stability with **3d**, making **4** a good candidate for higher concentration cycling.

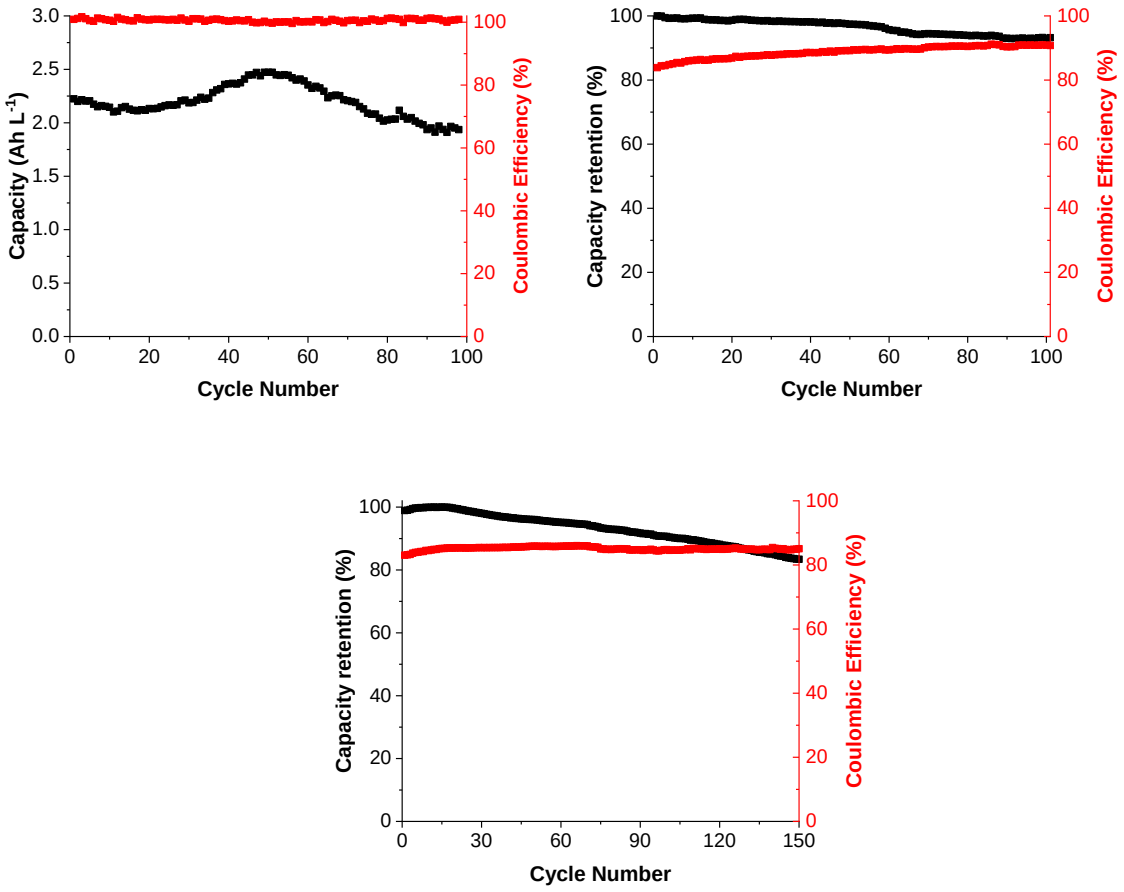

Figure 8.6. **Up left**: galvanostatic test using LATP solid membrane (0.1 M in 1 M LiTFSI/DMF); **Up right:** static mode cycling with Daramic 175 (0.1 M in 1M $TEABF_4$/ DMF) and **Down**: 0.3 M in 1M $TEABF_4$/ DMF

We next collaborated with Dr. Guihua Yu's group at University of Texas Austin for evaluating the optimal compound **4** in more battery related environment. The previous bulk electrolysis setup is only suitable for low concentration cycling test due to the large cell resistance. In order for evaluation of cycling stability at higher concentration, compound **4** was then paired with Li and tested in a home-made cylinder cell. A solid LATP separator was used in order to

exclude the influence of crossover on cycling performance. For over 100 cycles, the cycling of 0.1 M solution of **4** in 1 M LiTFSI/DMF shows about 85% capacity retention at 0.1 mA/ cm^2. This experiment shows the good cycling stability of **4** at battery-related concentration in a relatively isolated setup. To further test the compound under more realistic conditions, a 50/50 mixture of **4** (anolyte) and ferrocene (catholyte) in 1M $TEABF_4$/ DMF was tested in static mode using Daramic 175 as the membrane. The battery was first tested at 0.1 M, showing 93% capacity retention over 100 cycles at 10 mA/ cm^2. Notably, this battery gives a relatively high battery potential of 2.3 V even with a catholyte of low oxidation potential. Moreover, when cycled at higher concentration of 0.3 M at 10 mA/ cm^2, the battery still exhibits good capacity retention of 83% after 150 cycles. Overall, these experiments show good cycling performance of **4** with ferrocene at both low and high concentration.

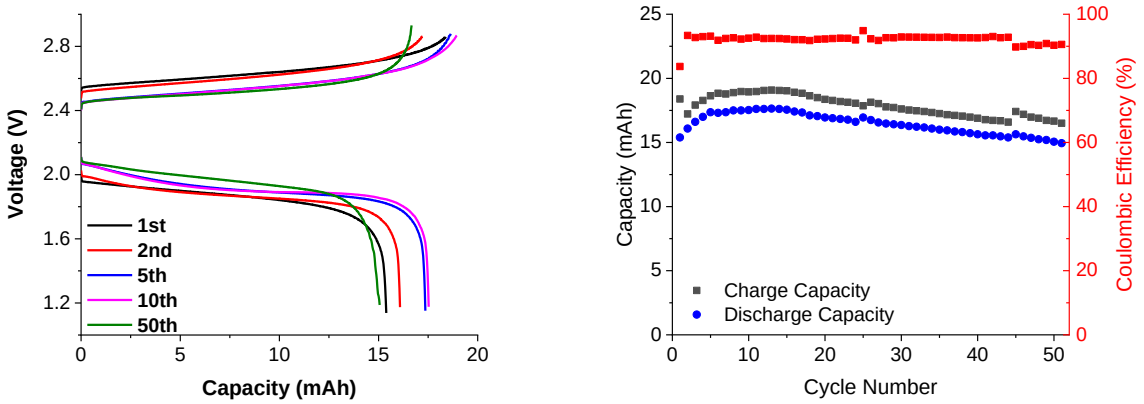

Figure 8.7. **Left**: charge-discharge curve of flow battery (0.1 M in 1M LiTFSI / DMF); **Right:** Capacity retention and coulombic efficiency of the flow battery

However, when we transferred these conditions to flow battery test, the battery of 0.1 M active materials shows fast capacity decay and fast increase of voltage polarization. This can potentially come from more side reactions due to interactions with more complicated parts of the

set-up (e.g., tubing, connectors, reservoirs, and other parts in the cell). When we switched the supporting salts from $TEABF_4$ to LiTFSI, the cycling performance was significantly improved, exhibiting 86% capacity retention over 50 cycles at 25 mA/ cm^2. This implies LiTFSI might enhance the stability of highly energetic radical anion. The battery achieves a peak power density of 125 mW/ cm^2 with high material utilization and the coulombic efficiency. When using dimethoxy benzene derivative (DBMMB) as the catholyte, although with fast capacity decay, the battery potential is up to 3 V, one of the highest potentials reported for non-aqueous redox flow batteries.[25,38,39] The maximum power density can reach 180 mW/ cm^2, which is higher than most of the reported non-aqueous RFBs and comparable to some demonstrated aqueous organic RFBs.[23,25]

8.3 Conclusion

To conclude, through rational molecular design, we have developed a promising anolyte with simple synthesis, extremely low potential, high solubility, and stable cycling performance. To our best knowledge, this work represents the anolyte with lowest redox potential reported for non-aqueous RFB, paving the way for high energy density devices.[20,21,25,27,39] Future work will be focused on tailoring the molecular structure to be compatible with more broad solvent and catholyte choices in order to achieve stable cycling at high cell potentials.

8.4 Experimental Procedures and Characterization of Compounds

8.4.1 Synthetic Procedures

General Information. All commercial chemicals were used as received unless stated otherwise. Anhydrous CH_2Cl_2, THF were obtained from an Innovative Technology, Inc. (now rebranded to Inert) solvent purification system. Reactions were performed under a nitrogen atmosphere.**2a** and **2b** were prepared according to the previous procedures.[40] **3a** and **3b** was prepared by another

Sanford Lab member (Ryan Walser-Kuntz). **3d** was prepared according to a previous report.[41] NMR spectra were obtained on Varian VNMRs 700, Varian VNMRs 500, Varian Inova 500, or Varian MR400 spectrometers. ^{1}H and ^{13}C NMR chemical shifts are reported in parts per million (ppm) relative to TMS, with the residual solvent peak used as an internal reference. High-resolution mass spectroscopy (HRMS) was performed on a Micromass AutoSpec Ultima Magnetic Sector Mass Spectrometer using electrospray ionization (ESI).

Synthesis of **4**: According to the previous report, **4** was prepared through a two-step procedure. Step 1: 15 mL acetonitrile solution of 1-Iodo-3-[(2 methoxyethoxy)methyl]benzene[42] (5 g, 17 mmol) was added to a 20 mL vial, equipped with a magnetic stir bar. m-CPBA (3.5 g, 20 mmol) was added in one portion, followed by the dropwise addition of TFA (1.3 mL, 17 mmol). Vial was sealed with Teflon screw cap, the reaction was stirred for 50 min at 55°C. 1,3,5-trimethoxybenzene (2.8 g, 17 mmol) was added in one portion, and the mixture was stirred at 55°C for 15 min. The postreaction mixture was concentrated under reduced pressure and triturated with excess diethyl ether and used without further purification. Step 2: To a flame dried round bottom flask (250 mL) equipped with a magnetic stir bar, benzotriazole (1.7 g, 14 mmol), diaryliodonium salt (from step 1) (9.6 g, 17 mmol), and Na_2CO_3 (1.8 g, 17 mmol) were added under nitorgen atmosphere. The flask was equipped with reflux condenser and anhydrous and degassed toluene (80 mL) was added to the flask. The mixture was stirred at 100°C for 24 hours. The postreaction mixture was allowed to reach at the ambient temperature. Next, water was added to the mixture and organics were extracted with dichloromethane (100 mL x 2). Organic layer was dried over sodium sulfate and volatiles were removed under reduced pressure. The residue was purified by silica-gel flash chromatography (10 % ethyl acetate in hexane, R_f = 0.2) to obtain colorless oil (1.8 g, yield 37%)

^{1}H NMR (700 MHz, Chloroform-*d*) δ 8.35 (m, 1H), 8.27 (m, 1H), 7.97 – 7.89 (m, 2H), 7.54 (t, *J* = 7.8 Hz, 1H), 7.48 (m, 1H), 7.46 – 7.38 (m, 2H), 4.74 – 4.66 (s, 2H), 3.73 – 3.65 (m, 2H), 3.65 – 3.58 (m, 2H), 3.41 (s, 3H). ^{13}C NMR (176 MHz, Chloroform-*d*) δ 145.15, 140.55, 140.29, 129.69, 128.27, 127.35, 119.96, 119.95, 118.51, 72.90, 72.11, 69.83, 59.25. HRMS (EI) *m/z* calcd for $C_{16}H_{17}N_3O_2$ (**4**): 283.1321, found: 283.1326.

8.4.2 Electrochemistry Experimental Procedures

General methods and materials. Acetonitrile and N,N-Dimethylformamide (anhydrous, 99.8%) were obtained from Sigma Aldrich and used as received. Tetraethylammonium tetrafluoroborate ($TEABF_4$; electrochemical grade) was obtained from Sigma Aldrich and dried under high vacuum for 48 h at 70 °C before being transferred to a N_2-filled glovebox. A 0.50 M stock solution of $TEABF_4$ in acetonitrile and DMF were prepared in a N_2-filled glovebox and dried over 3Å molecular sieves for at least two days prior to use. Daramic-175 membrane was generously provided by Daramic company and used as received.

Cyclic voltammetry. Cyclic voltammetry (CV) was performed in a N_2-filled glovebox with a Biologic VSP multichannel potentiostat/galvanostat using a three-electrode electrochemical cell, consisting of a glassy carbon disk working electrode (0.071 cm^2, BASi), a Ag/Ag^+ reference electrode (BASi) with 0.01 M $AgBF_4$ (Sigma) and 0.5 M $TEABF_4$ in acetonitrile or DMF, and a platinum wire counter electrode.

H-cell cycling. Bulk charge/discharge measurements were carried out in a N_2-filled glovebox with a BioLogic VSP galvanostat in a custom glass H-cell with an ultrafine fritted glass separator (P5, Adams and Chittenden). The working and counter electrodes were reticulated vitreous carbon (100 ppi, ~70 cm^2 surface area, Duocel). A Ag/Ag^+ reference electrode was used on the working side of the H-cell. The electrolyte contained 5 mM active species and 0.50 M $TEABF_4$ in DMF. Both

chambers of the H-cell were loaded with 5 mL electrolyte solution and were stirred continuously during cycling at a current of 5 mA. Voltage cutoffs of +0.5 V higher than $E_{1/2}$ as the upper limit and -0.5 V lower than $E_{1/2}$ as the lower limit were employed.

The lithium-hybrid cell, static cell and flow cell were tested by Dr. Leyuan Zhang from Professor Guihua Yu's group at University of Texas, Austin and the similar procedures can be found in literature.[23,25]

8.5 References

(1) Rugolo, J.; Aziz, M. J. Electricity Storage for Intermittent Renewable Sources. *Energy Environ. Sci.* **2012**, *5* (5), 7151–7160. https://doi.org/10.1039/C2EE02542F.

(2) Barnhart, C. J.; Dale, M.; Brandt, A. R.; Benson, S. M. The Energetic Implications of Curtailing versus Storing Solar- and Wind-Generated Electricity. *Energy Environ. Sci.* **2013**, *6* (10), 2804–2810. https://doi.org/10.1039/C3EE41973H.

(3) Wang, W.; Luo, Q.; Li, B.; Wei, X.; Li, L.; Yang, Z. Recent Progress in Redox Flow Battery Research and Development. *Advanced Functional Materials* **2013**, *23* (8), 970–986. https://doi.org/10.1002/adfm.201200694.

(4) Leung, P.; Li, X.; León, C. P. de; Berlouis, L.; Low, C. T. J.; Walsh, F. C. Progress in Redox Flow Batteries, Remaining Challenges and Their Applications in Energy Storage. *RSC Adv.* **2012**, *2* (27), 10125–10156. https://doi.org/10.1039/C2RA21342G.

(5) Noack, J.; Roznyatovskaya, N.; Herr, T.; Fischer, P. The Chemistry of Redox-Flow Batteries. *Angewandte Chemie International Edition* **2015**, *54* (34), 9776–9809. https://doi.org/10.1002/anie.201410823.

(6) Zhao, Y.; Ding, Y.; Li, Y.; Peng, L.; Byon, H. R.; Goodenough, J. B.; Yu, G. A Chemistry and Material Perspective on Lithium Redox Flow Batteries towards High-Density

Electrical Energy Storage. *Chem. Soc. Rev.* **2015**, *44* (22), 7968–7996. https://doi.org/10.1039/C5CS00289C.

(7) Wei, X.; Pan, W.; Duan, W.; Hollas, A.; Yang, Z.; Li, B.; Nie, Z.; Liu, J.; Reed, D.; Wang, W.; Sprenkle, V. Materials and Systems for Organic Redox Flow Batteries: Status and Challenges. *ACS Energy Lett.* **2017**, *2* (9), 2187–2204. https://doi.org/10.1021/acsenergylett.7b00650.

(8) Wei, X.; Xu, W.; Vijayakumar, M.; Cosimbescu, L.; Liu, T.; Sprenkle, V.; Wang, W. TEMPO-Based Catholyte for High-Energy Density Nonaqueous Redox Flow Batteries. *Advanced Materials* **2014**, *26* (45), 7649–7653. https://doi.org/10.1002/adma.201403746.

(9) Winsberg, J.; Hagemann, T.; Muench, S.; Friebe, C.; Häupler, B.; Janoschka, T.; Morgenstern, S.; Hager, M. D.; Schubert, U. S. Poly(Boron-Dipyrromethene)—A Redox-Active Polymer Class for Polymer Redox-Flow Batteries. *Chem. Mater.* **2016**, *28* (10), 3401–3405. https://doi.org/10.1021/acs.chemmater.6b00640.

(10) Zhang, C.; Zhang, L.; Ding, Y.; Peng, S.; Guo, X.; Zhao, Y.; He, G.; Yu, G. Progress and Prospects of Next-Generation Redox Flow Batteries. *Energy Storage Materials* **2018**, *15*, 324–350. https://doi.org/10.1016/j.ensm.2018.06.008.

(11) Kwon, G.; Lee, S.; Hwang, J.; Shim, H.-S.; Lee, B.; Lee, M. H.; Ko, Y.; Jung, S.-K.; Ku, K.; Hong, J.; Kang, K. Multi-Redox Molecule for High-Energy Redox Flow Batteries. *Joule* **2018**, *2* (9), 1771–1782. https://doi.org/10.1016/j.joule.2018.05.014.

(12) Zhang, J.; Yang, Z.; Shkrob, I. A.; Assary, R. S.; Tung, S. on; Silcox, B.; Duan, W.; Zhang, J.; Su, C. C.; Hu, B.; Pan, B.; Liao, C.; Zhang, Z.; Wang, W.; Curtiss, L. A.; Thompson, L. T.; Wei, X.; Zhang, L. Annulated Dialkoxybenzenes as Catholyte Materials for Non-Aqueous

Redox Flow Batteries: Achieving High Chemical Stability through Bicyclic Substitution. *Adv. Energy Mater.* **2017**, *7* (21), 1701272. https://doi.org/10.1002/aenm.201701272.

(13) VanGelder, L. E.; Schreiber, E.; Matson, E. M. Physicochemical Implications of Alkoxide "Mixing" in Polyoxovanadium Clusters for Nonaqueous Energy Storage. *J. Mater. Chem. A* **2019**, *7* (9), 4893–4902. https://doi.org/10.1039/C8TA12306C.

(14) VanGelder, L. E.; Kosswattaarachchi, A. M.; Forrestel, P. L.; Cook, T. R.; Matson, E. M. Polyoxovanadate-Alkoxide Clusters as Multi-Electron Charge Carriers for Symmetric Non-Aqueous Redox Flow Batteries. *Chem. Sci.* **2018**, *9* (6), 1692–1699. https://doi.org/10.1039/C7SC05295B.

(15) A. Kowalski, J.; D. Casselman, M.; Preet Kaur, A.; D. Milshtein, J.; F. Elliott, C.; Modekrutti, S.; Harsha Attanayake, N.; Zhang, N.; R. Parkin, S.; Risko, C.; R. Brushett, F.; A. Odom, S. A Stable Two-Electron-Donating Phenothiazine for Application in Nonaqueous Redox Flow Batteries. *Journal of Materials Chemistry A* **2017**, *5* (46), 24371–24379. https://doi.org/10.1039/C7TA05883G.

(16) Escalante-García, I. L.; Wainright, J. S.; Thompson, L. T.; Savinell, R. F. Performance of a Non-Aqueous Vanadium Acetylacetonate Prototype Redox Flow Battery: Examination of Separators and Capacity Decay. *J. Electrochem. Soc.* **2015**, *162* (3), A363–A372. https://doi.org/10.1149/2.0471503jes.

(17) Carino, E. V.; Staszak-Jirkovsky, J.; Assary, R. S.; Curtiss, L. A.; Markovic, N. M.; Brushett, F. R. Tuning the Stability of Organic Active Materials for Nonaqueous Redox Flow Batteries via Reversible, Electrochemically Mediated Li+ Coordination. *Chem. Mater.* **2016**, *28* (8), 2529–2539. https://doi.org/10.1021/acs.chemmater.5b04053.

(18) Silcox, B.; Zhang, J.; Shkrob, I. A.; Thompson, L.; Zhang, L. On Transferability of Performance Metrics for Redox-Active Molecules. *J. Phys. Chem. C* **2019**, *123* (27), 16516–16524. https://doi.org/10.1021/acs.jpcc.9b02230.

(19) Kwon, G.; Lee, K.; Lee, M. H.; Lee, B.; Lee, S.; Jung, S.-K.; Ku, K.; Kim, J.; Park, S. Y.; Kwon, J. E.; Kang, K. Bio-Inspired Molecular Redesign of a Multi-Redox Catholyte for High-Energy Non-Aqueous Organic Redox Flow Batteries. *Chem* **2019**, *5* (10), 2642–2656. https://doi.org/10.1016/j.chempr.2019.07.006.

(20) Sevov, C. S.; Fisher, S. L.; Thompson, L. T.; Sanford, M. S. Mechanism-Based Development of a Low-Potential, Soluble, and Cyclable Multielectron Anolyte for Nonaqueous Redox Flow Batteries. *J. Am. Chem. Soc.* **2016**, *138* (47), 15378–15384. https://doi.org/10.1021/jacs.6b07638.

(21) Duan, W.; Huang, J.; Kowalski, J. A.; Shkrob, I. A.; Vijayakumar, M.; Walter, E.; Pan, B.; Yang, Z.; Milshtein, J. D.; Li, B.; Liao, C.; Zhang, Z.; Wang, W.; Liu, J.; Moore, J. S.; Brushett, F. R.; Zhang, L.; Wei, X. "Wine-Dark Sea" in an Organic Flow Battery: Storing Negative Charge in 2,1,3-Benzothiadiazole Radicals Leads to Improved Cyclability. *ACS Energy Lett.* **2017**, *2* (5), 1156–1161. https://doi.org/10.1021/acsenergylett.7b00261.

(22) Huang, J.; Cheng, L.; Assary, R. S.; Wang, P.; Xue, Z.; Burrell, A. K.; Curtiss, L. A.; Zhang, L. Liquid Catholyte Molecules for Nonaqueous Redox Flow Batteries. *Advanced Energy Materials* **2015**, *5* (6), 1401782. https://doi.org/10.1002/aenm.201401782.

(23) Zhang, C.; Qian, Y.; Ding, Y.; Zhang, L.; Guo, X.; Zhao, Y.; Yu, G. Biredox Eutectic Electrolytes Derived from Organic Redox-Active Molecules: High-Energy Storage Systems. *Angewandte Chemie International Edition* **2019**, *58* (21), 7045–7050. https://doi.org/10.1002/anie.201902433.

(24) Zhang, C.; Niu, Z.; Ding, Y.; Zhang, L.; Zhou, Y.; Guo, X.; Zhang, X.; Zhao, Y.; Yu, G. Highly Concentrated Phthalimide-Based Anolytes for Organic Redox Flow Batteries with Enhanced Reversibility. *Chem* **2018**, *4* (12), 2814–2825. https://doi.org/10.1016/j.chempr.2018.08.024.

(25) Zhang, L.; Qian, Y.; Feng, R.; Ding, Y.; Zu, X.; Zhang, C.; Guo, X.; Wang, W.; Yu, G. Reversible Redox Chemistry in Azobenzene-Based Organic Molecules for High-Capacity and Long-Life Nonaqueous Redox Flow Batteries. *Nature Communications* **2020**, *11* (1), 3843. https://doi.org/10.1038/s41467-020-17662-y.

(26) Wei, X.; Duan, W.; Huang, J.; Zhang, L.; Li, B.; Reed, D.; Xu, W.; Sprenkle, V.; Wang, W. A High-Current, Stable Nonaqueous Organic Redox Flow Battery. *ACS Energy Lett.* **2016**, *1* (4), 705–711. https://doi.org/10.1021/acsenergylett.6b00255.

(27) Griffin, J. D.; Pancoast, A. R.; Sigman, M. S. Interrogation of 2,2′-Bipyrimidines as Low-Potential Two-Electron Electrolytes. *J. Am. Chem. Soc.* **2021**, *143* (2), 992–1004. https://doi.org/10.1021/jacs.0c11267.

(28) Hu, B.; Liu, T. L. Two Electron Utilization of Methyl Viologen Anolyte in Nonaqueous Organic Redox Flow Battery. *Journal of Energy Chemistry* **2018**, *27* (5), 1326–1332. https://doi.org/10.1016/j.jechem.2018.02.014.

(29) Wei, X.; Xu, W.; Huang, J.; Zhang, L.; Walter, E.; Lawrence, C.; Vijayakumar, M.; Henderson, W. A.; Liu, T.; Cosimbescu, L.; Li, B.; Sprenkle, V.; Wang, W. Radical Compatibility with Nonaqueous Electrolytes and Its Impact on an All-Organic Redox Flow Battery. *Angewandte Chemie International Edition* **2015**, *54* (30), 8684–8687. https://doi.org/10.1002/anie.201501443.

(30) Zhao, Y.; Yu, Z.; A. Robertson, L.; Zhang, J.; Shi, Z.; R. Bheemireddy, S.; A. Shkrob, I.; Z, Y.; Li, T.; Zhang, Z.; Cheng, L.; Zhang, L. Unexpected Electrochemical Behavior of an Anolyte Redoxmer in Flow Battery Electrolytes: Solvating Cations Help to Fight against the Thermodynamic–Kinetic Dilemma. *Journal of Materials Chemistry A* **2020**, *8* (27), 13470–13479. https://doi.org/10.1039/D0TA02214D.

(31) Huang, J.; Duan, W.; Zhang, J.; A. Shkrob, I.; S. Assary, R.; Pan, B.; Liao, C.; Zhang, Z.; Wei, X.; Zhang, L. Substituted Thiadiazoles as Energy-Rich Anolytes for Nonaqueous Redox Flow Cells. *Journal of Materials Chemistry A* **2018**, *6* (15), 6251–6254. https://doi.org/10.1039/C8TA01059E.

(32) Patel, D. G. (Dan); Feng, F.; Ohnishi, Y.; Abboud, K. A.; Hirata, S.; Schanze, K. S.; Reynolds, J. R. It Takes More Than an Imine: The Role of the Central Atom on the Electron-Accepting Ability of Benzotriazole and Benzothiadiazole Oligomers. *J. Am. Chem. Soc.* **2012**, *134* (5), 2599–2612. https://doi.org/10.1021/ja207978v.

(33) Qi, F.; Jiang, K.; Lin, F.; Wu, Z.; Zhang, H.; Gao, W.; Li, Y.; Cai, Z.; Woo, H. Y.; Zhu, Z.; Jen, A. K.-Y. Over 17% Efficiency Binary Organic Solar Cells with Photoresponses Reaching 1000 Nm Enabled by Selenophene-Fused Nonfullerene Acceptors. *ACS Energy Lett.* **2021**, *6* (1), 9–15. https://doi.org/10.1021/acsenergylett.0c02230.

(34) Wang, X.; Chai, J.; Lashgari, A.; Jiang, J. J. Azobenzene-Based Low-Potential Anolyte for Nonaqueous Organic Redox Flow Batteries. *ChemElectroChem* **2021**, *8* (1), 83–89. https://doi.org/10.1002/celc.202001035.

(35) Schellhammer, C. W.; Schroeder, J.; Joop, N. Über alykylierungen von benzotriazol-derivaten. *Tetrahedron* **1970**, *26* (2), 497–510. https://doi.org/10.1016/S0040-4020(01)97845-7.

(36) Pedersen, S. U.; Lund, H.; Mattinen, J.; Göndös, G.; Wittman, G.; Gera, L.; Bartók, M.; Pelczer, I.; Dombi, G. Electrochemical Reduction of Some Benzotriazoles in Protic and Aprotic Media. *Acta Chem. Scand.* **1988**, *42b*, 319–323. https://doi.org/10.3891/acta.chem.scand.42b-0319.

(37) Sevov, C. S.; Samaroo, S. K.; Sanford, M. S. Cyclopropenium Salts as Cyclable, High-Potential Catholytes in Nonaqueous Media. *Advanced Energy Materials* **2017**, *7* (5), 1602027. https://doi.org/10.1002/aenm.201602027.

(38) Yan, Y.; Robinson, S. G.; Sigman, M. S.; Sanford, M. S. Mechanism-Based Design of a High-Potential Catholyte Enables a 3.2 V All-Organic Nonaqueous Redox Flow Battery. *J. Am. Chem. Soc.* **2019**, *141* (38), 15301–15306. https://doi.org/10.1021/jacs.9b07345.

(39) Geysens, P.; Li, Y.; Vankelecom, I.; Fransaer, J.; Binnemans, K. Highly Soluble 1,4-Diaminoanthraquinone Derivative for Nonaqueous Symmetric Redox Flow Batteries. *ACS Sustainable Chem. Eng.* **2020**, *8* (9), 3832–3843. https://doi.org/10.1021/acssuschemeng.9b07244.

(40) Singh, D.; Silakari, O. Sodium Hydrogen Exchanger Inhibitory Activity of Benzotriazole Derivatives. *European Journal of Medicinal Chemistry* **2017**, *126*, 183–189. https://doi.org/10.1016/j.ejmech.2016.10.005.

(41) Roshandel, S.; Lunn, M. J.; Rasul, G.; Muthiah Ravinson, D. S.; Suri, S. C.; Prakash, G. K. S. Catalyst-Free Regioselective N ^{2} Arylation of 1,2,3-Triazoles Using Diaryl Iodonium Salts. *Org. Lett.* **2019**, *21* (16), 6255–6258. https://doi.org/10.1021/acs.orglett.9b02140.

(42) Shiraki, M.; Takahashi, H.; Nogami, T. Crystals of Glycine Derivative and Pharmaceutical Use Thereof. US20140128605A1, May 8, 2014

Chapter 9 Summary and Outlook

In summary, this thesis research focuses on the design, synthesis and characterization of redox active organic materials and their application as energy storage materials for non-aqueous redox flow batteries. New catholytes and anolytes were developed through the combination of rational molecular design, computation predication and structure-property analysis. On the catholyte side, great progress has been made to realize high performance new materials through tailoring the properties of the cyclopropenium scaffold. Compared to the field five years ago, our research has led to the discovery of new generation materials with about 600 mV potential increase, materials with both two electron transfers and extremely high potentials, materials with high energy capacity and materials that show no crossover in a battery setup with anion-exchange membrane. With these materials, we were able to assemble batteries with the highest potential difference, the highest energy density while without crossover, and the most stable cycling in the field. On the anolyte side, our research has pushed the potential limit to 300 mV lower than current state-of-the-art by discovering the benzotriazole based materials. With further molecular engineering of their solubility and stability, the optimal compound was able to be cycled stably in a flow cell set up. Looking forward, our group will continue working on benzotriazole based materials and there are two potential directions: 1) these materials have been tailored to be stable in DMF but not in MeCN based electrolyte. In order for broader scope of catholyte selections, it is potentially interesting to make these materials more stable in acetonitrile. 2) rational molecular engineering can lead to new materials with even lower reduction potential to increase energy density of the resulting batteries.